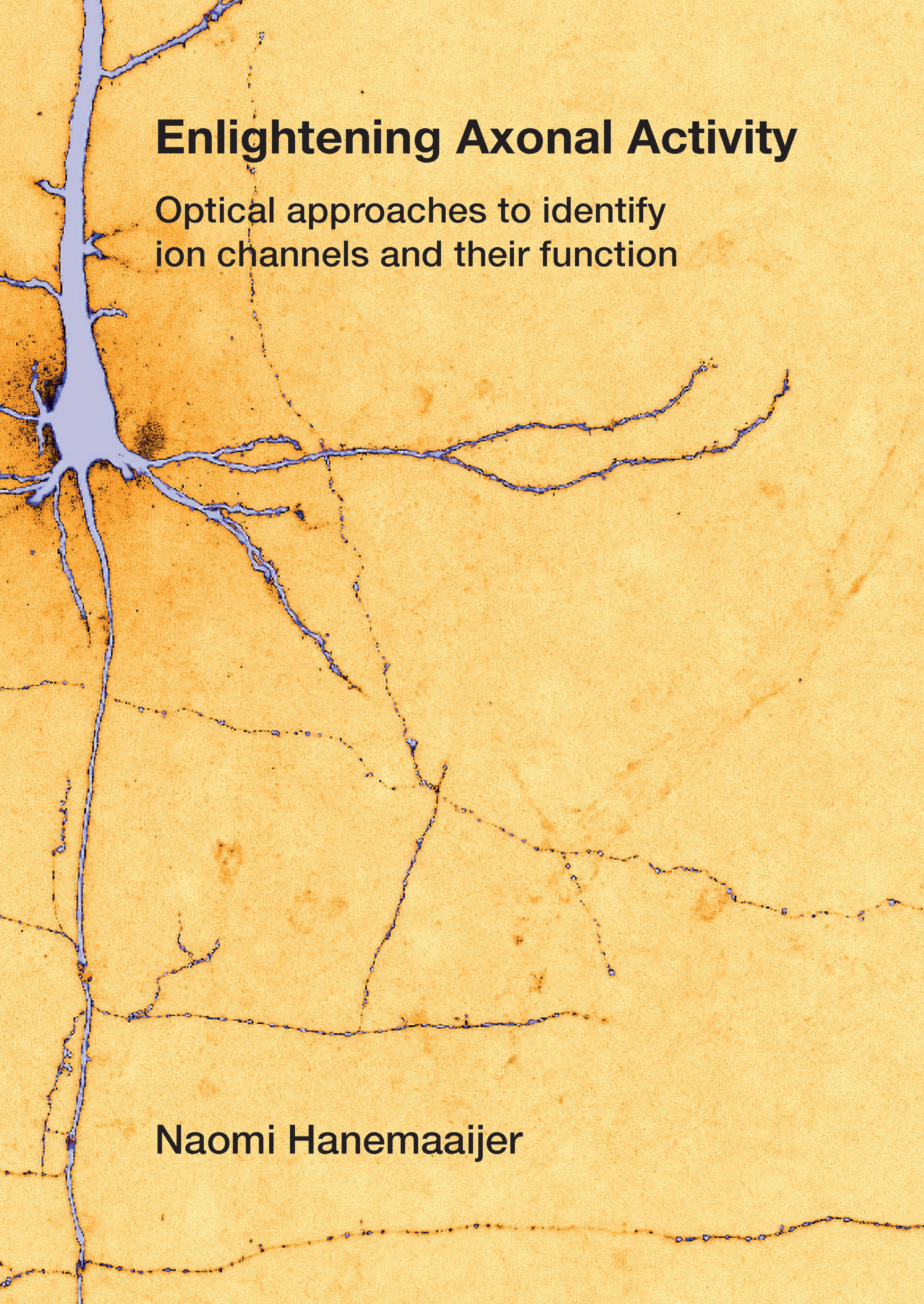

Enlightening Axonal Activity

Optical approaches to identify ion channels and their function

Naomi Hanemaaijer

Enlightening axonal activity

Optical approaches to identify ion channels and their function

ISBN: 978-94-6421-849-7

Cover: “The route through the brain” by Naomi Hanemaaijer

Printed by: Ipskamp Printing

This work originates as part of the research program Neurophotonics (16NEPH02) of the Foundation for Fundamental Research on Matter (FOM), and falls as of April 1st, 2017 under the responsibility of Foundation for Nederlandse Wetenschappelijk Onderzoek Instituten (NWO-I), which is part of the Dutch Research Council (NWO). In addition, this work was also financed by the Dutch Research Council (NWO Vici 865.17.003).

Enlightening axonal activity
Optical approaches to identify ion channels and their function

Axonale activiteit belichten
Optische methodes om ion kanalen en hun werking te identificeren

(met een samenvatting in het Nederlands)

Proefschrift

ter verkrijging van de graad van doctor aan de
Universiteit Utrecht
op gezag van de
rector magnificus, prof.dr. H.R.B.M. Kummeling,
ingevolge het besluit van het college voor promoties
in het openbaar te verdedigen op

vrijdag 30 september 2022 des middags te 4.15 uur

door

Naomi Anne Karen Hanemaaijer

geboren op 1 april 1991
te Leiden

Promotoren:

Prof. dr. M.H.P. Kole
Prof. dr. L.C. Kapitein

Copromotor:
Dr. M.A. Popovic

To my parents

Table of contents

Chapter 1 General Introduction 9

Chapter 2 Ca^{2+} entry through Na_V channels generates submillisecond axonal Ca^{2+} signaling 31

Chapter 3 Axonal BK-channel mediated action potential repolarization revealed by holographic voltage recordings 87

Chapter 4 Robust adaptive optics for localization microscopy deep in complex tissue 139

Chapter 5 General Discussion 181

Appendix Summary 203

Nederlandse samenvatting 205

Curriculum Vitae 207

Acknowledgements 211

Chapter 1

General Introduction

Fundamental to all our thoughts and actions are ions carrying charge flowing between the intra- or extracellular space to build electrical potentials. At synapses, the electrical potentials cause the release of chemical neurotransmitters, which subsequently initiate the flow of ions through the membrane of the postsynaptic cell. It's a fascinating collaboration between electrical and chemical signals, that never ceases to amaze.

The primary electrical signal, or *action potential* (AP), was recorded for the first time intracellularly in 1939 by Alan Hodgkin and Andrew Huxley in the squid giant axon (Hodgkin and Huxley, 1939). The squid giant axon, with its ~1 mm diameter, was an ideal model to study ion fluxes and their role in neuronal electrical signaling, due to the ability to control intra- and extracellular ion concentrations and to insert an electrode inside the axon. The active flow of ions during an AP was first visually detected in 1950, by studying radioactively labeled particles in the squid giant axon, revealing that specifically sodium (Na^+), potassium (K^+) and calcium (Ca^{2+}) ions, migrate in and out of cells during rest and activity (Rothenberg, 1950). By passive and active transport of ions through the membrane, neurons maintain a gradient of high K^+ inside and high Na^+ outside the cell, resulting in a negative intracellular resting potential. When a cell receives excitatory input, the precisely timed sequential opening of voltage-gated Na^+ (Na_V) and K^+ (K_V) channels results in an AP: the rapid de- and repolarization of the membrane. In a series of seminal papers, Hodgkin and Huxley mathematically described the voltage-dependency of the currents underlying the AP (Hodgkin and Huxley, 1952a, 1952d, 1952b, 1952c; Hodgkin et al., 1952).

The axon initial segment AP bridges neuronal in- and output

Neurons are morphologically complex, with intricate dendritic and axonal arborizations and consequently varying potentials between neuronal regions (see **Figure 1a**). Neurons are polarized: they have distinct regions for receiving and sending signals (Rasband, 2010). Information is received on synapses, mostly located on the dendrites. Excitatory synaptic input causes relatively small depolarizations which are amplified by Na_V channels in the soma and axon (Stuart and Sakmann, 1995). The cell body, or soma, contains the nucleus and connects all dendrites to the axon, the output neurite that weighs synaptic input and conveys APs to the downstream targets. In some neurons (up to 60%, depending on cell type and brain region) the axon exits a basal dendrite, providing a privileged pathway for

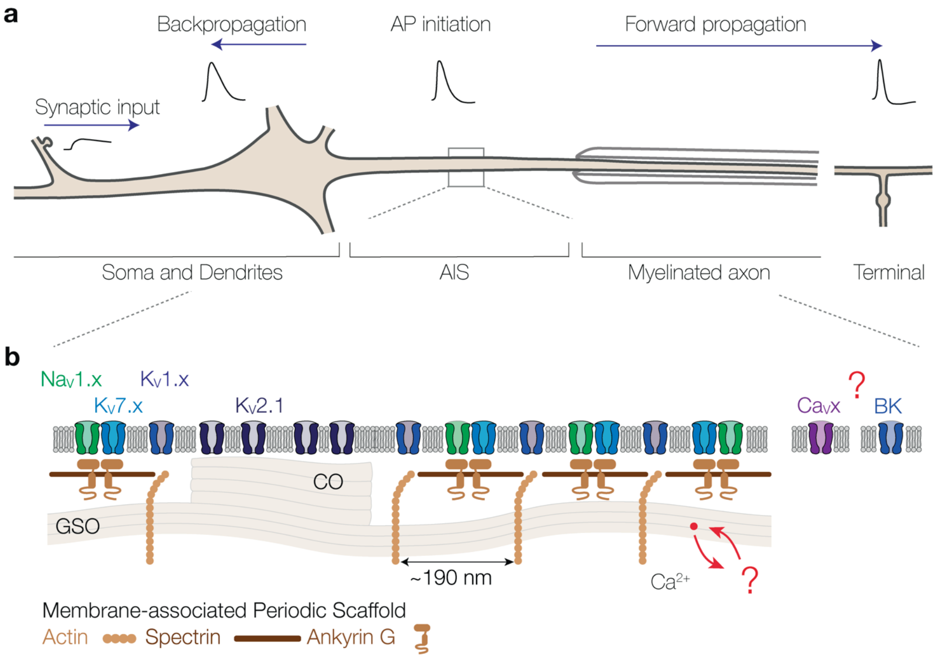
a
Backpropagation
AP initiation
Forward propagation
Synaptic input
Soma and Dendrites
AIS
Myelinated axon
Terminal
b
Na$_V$1.x
K$_V$1.x
K$_V$7.x
K$_V$2.1
Ca$_V$x
?
BK
CO
GSO
~190 nm
Ca^{2+}
?
Membrane-associated Periodic Scaffold
Actin
Spectrin
Ankyrin G

Figure 1. AP initiation and ion channel clustering at the AIS
a. Schematic of a pyramidal neuron. The neuron is a polarized cell that integrates synaptic input (left) along the somatodendritic compartment. Input in weighed and converged to an AP at the AIS, which is subsequently propagated antidromically into the soma and dendrites and orthodromically into the axon proper, where it causes neurotransmitter release in the presynaptic terminals. **b**. An insert from **a** presenting the membrane-associated periodic scaffold and associated ion channels at the AIS. Na$_V$1.x and K$_V$7.x are anchored to the cytoskeleton through AnkyrinG, whereas K$_V$1.x colocalizes with actin rings. K$_V$2.1 clusters at AnkyrinG-defficient hotspots where cisternal organelles (CO), stacked endoplasmic reticulum, closely associate to the membrane. The L5 AIS also contains a unique organization of endoplasmic reticulum along the entire length of the AIS: the Giant Saccular Organelle (GSO), hypothesized to regulate Ca^{2+} levels, which is investigated in Chapter 2. Whether Ca$_V$ and BK channels (right) are present at the AIS is discussed in Chapter 2 and 3.

synaptic input to weigh to the AP initiation (Kole and Brette, 2018; Thome et al., 2014). Most neurons contain one axon, although through elaborate branching it can divide in a multitude of arbors, span up to ~1 meter distance in humans when projecting to the spinal cord or connect to thousands of other neurons across different brain regions. The first 10-60 µm of the axon is called the axon initial segment (AIS, see **Figure 1b**) and was first described as a distinct region based on dense granular material and bundled microtubules visible in electron microscopy (Palay et al., 1968). The AIS is now recognized by the presence of the scaffolding proteins AnkyrinG and ßIV-spectrin (Leterrier, 2018), which cluster a high-density clustering of Na$_V$ channels to the AIS (Zhou et al., 1998), as shown by autoradiography using the Na$_V$ channel-binding ^{125}I-scorpion toxin (Catterall, 1981), immunohistochemistry (Lorincz and Nusser, 2008), freeze-fracture electron microscopy immunogold labeling (Lorincz and Nusser, 2010) and patch clamp recordings (Kole et al., 2008). The AIS also clusters a variety of K^+ channels, such as K$_V$1.1 and 1.2, which contribute to the repolarization phase of the AP, and K$_V$7.2 and 7.3, which stabilize the axonal membrane potential and facilitate axonal excitability (Battefeld et al., 2014; Kole et al., 2007; Lorincz and Nusser, 2008).

This high-density of ion channels make the AIS an excitable hotspot and indeed, early work based on somatically recorded intracellular potentials in spinal motoneurons from toads and cats described that APs may initiate in the AIS (Coombs et al., 1957; Fatt, 1957; Fuortes et al., 1957; Otani and Araki, 1955). Later dual somatic and axonal whole-cell recordings in rat L5 pyramidal neurons and whole-cell recordings *in vivo* in ferrets confirmed that the axonal AP always preceded the somatic AP, supporting the notion that the axon is the final locus for synaptic integration (Kole and Stuart, 2012; Kole et al., 2007; Shu et al., 2007a; Stuart and Sakmann, 1994; Stuart et al., 1997a). While recording from two locations provides more insight into the temporal sequence of potentials, the use of a fluorescent voltage reporter provides more defined spatial evidence of initiation. Palmer and Stuart recorded the AP waveform simultaneously from a long stretch of primary axon including the myelinated internode (Palmer and Stuart, 2006). This optical approach offered spatial detail about the initiation and propagation of the AP through the axon: the AP is initiated in the distal AIS of pyramidal neurons, ~35 µm from the soma, and re-initiated at the nodes of Ranvier, which show earlier onset latency of the AP compared to the internodes. The location and morphology of the AIS dynamically alters the cell’s input-output relationship (Kuba et al., 2006) and shows activity-dependent plasticity (Grubb and Burrone, 2010; Grubb et al., 2011; Jamann et al., 2021). Given its prominent role in the electrical behavior of a neuron, AIS pathology is linked to a variety of diseases, such as epilepsy and autism spectrum disorder (Huang and Rasband, 2018).

The AP shape and role differs between neuronal compartments

Initiation and propagation of the AP is a complex process both temporally and spatially. After initiation in the AIS, the AP propagates antidromically (backward) into the somatodendritic compartment and orthodromically (forward) into the axon, where it is carried to the downstream targets. Historically, the AP is viewed as a binary ‘all-or-none’ signal, however the shape and function of the AP differs widely between cellular compartments. In the axon terminals, the AP duration directly relates to the amplitude of the postsynaptic signal and therefore the shape is regulated strictly (Borst and Sakmann, 1996, 1999; Geiger and Jonas, 2000; Hoppa et al., 2014). In addition, the precise arrival time of the AP is important, and the axonal AP is generally narrow, ~250 μs in the L5 pyramidal neuron, as discussed in **Chapter 3** (Kole et al., 2007). On the other hand, the backpropagating AP functions to open slower somatodendritic Ca_V channels where the elevated Ca^{2+} levels finetune synaptic connections (Waters et al., 2005). Since these processes take place on a much slower time scale, the exact timing of the backpropagating AP is less important and it becomes increasingly wider and smaller with distance from the soma (Stuart et al., 1997b). Given the different functions and temporal precision of the AP in different cellular compartments, the exact shape of the AP is of high importance in the axon.

The local shape of the AP is defined by active and passive properties of the neuron: the composition of ion channels and biophysical properties, respectively (Bean, 2007). One important passive property depends on the membrane: the membrane is a lipid bilayer between two conducting media and, from an electrical point of view, acts both as a capacitor and an insulator. Membrane capacitance (C_m) increases with diameter and slows down the change in voltage when current is injected. In addition, the conducting media have a resistance (R_a), which is proportional to the distance between two locations and inversely proportional to the diameter the neurite and causes a reduction in the voltage signal. The soma is relatively large (~30 μm) compared to the axon, whose diameter tapers from a few μm to ~1 μm along the AIS. The depolarization associated with AP initiation in the AIS mostly travels antidromically to the soma, due to the lower R_a in the direction of the soma. Because of this resistive coupling between soma and axon, a voltage gradient develops between these regions (Brette, 2013; Goethals and Brette, 2020; Kole and Brette, 2018). In addition, the large size of the soma gives it a large capacity and makes it act like a current sink, which slows down the depolarization. Contrarily, the orthodromic AP traveling into the axon proper encounters a much smaller diameter membrane, so the higher R_a reduces the current flowing to the axon, but due to the lower C_m the membrane depolarizes quickly. Furthermore, the myelin sheath acts as a coupled capacitor that takes up part of the charge and induces saltatory conduction in space and time (Cohen et al., 2020).

The active properties of the membrane depend on the local composition of ion channels, which is highly diverse between neuronal regions. For example, the high density of Na_V channels make the AIS an excitable hotspot, as discussed previously. In the AIS and nodes of Ranvier, a complex cytoskeletal architecture enables high density coupling of ion channels. This molecular build-up of the AIS is receiving wide attention in the last decade, especially since the development of superresolution microscopy.

Superresolution microscopy identified nanoscale AIS architecture

In 1994 Stefan Hell introduced the concept of superresolution light microscopy, which vastly improved the diffraction limit of $d = \lambda / 2NA$, as approximated by Ernst Karl Abbe in 1873, from ~250 nm to tens of nanometers (Abbe, 1873; Hell and Wichmann, 1994; Klar et al., 2000). The original superresolution method developed by Stefan Hell, Stimulated emission depletion (STED), is based on an excitation beam and a depletion beam, practically reducing the size of the excitation focal spot. Hell's discovery led to a surge of new imaging techniques, such as Stochastic Optical Reconstruction Microscopy (STORM), SIM, and adaptive optics (Prakash et al., 2022). STORM uses the stochastic blinking of molecules to localize single molecules and reconstruct the sample with a lateral resolution of ~20 nm (Linde et al., 2011). These new imaging techniques initiated the exploration of the ultrastructure of neurons. One important breakthrough was the use of STORM to visualize the periodicity of the cytoskeletal proteins and Na_V channels in the axon, with actin rings being interleaved and spaced by spectrin molecules at ~190 nm distance (see **Figure 1b**, Xu et al., 2013). Since then, the nanoscale architecture of the AIS and nodes, termed the Membrane-associated Periodic Scaffold (MPS), has been dissected to a highly detailed level (D'Este et al., 2017; Leterrier, 2018). Na_V and K_V7 channels are clustered at the MPS through a shared AnkyrinG binding motif, whereas K_V1 channels anchor to the

MPS through a different scaffolding partner and cluster at actin rings (see **Figure 1b**, D'Este et al., 2017; Pan et al., 2006; Xu et al., 2013).

Surprisingly, Kv2 channels do not cluster at the MPS, but instead appear at AnkyrinG-deficient hotspots adjacent to the intracellular cisternal organelles, a formation of stacked endoplasmic reticulum (King et al., 2014). The L5 pyramidal neuron AIS in particular contains a unique organization of cisternal organelles along its entire length: the giant saccular organelle, which is hypothesized to be involved in regulating Ca^{2+} levels (see **Figure 1b**, Antón-Fernández et al., 2013). Ca^{2+} release from these internal stores is a Ca^{2+} dependent process and live experiments suggested the presence of Cav channels at the AIS (Bender and Trussell, 2009). However, Cav channels are difficult to visualize, and it is unknown whether they associate to the MPS or are organized at the AIS otherwise. BK channels, a special type of K^+ with a large peak conductance, have been visualized at the paranodes of Purkinje neurons (Hirono et al., 2015), but further structural information is limited, although pharmacological experiments suggests that BK channels are also present at the AIS and nodes of L5 pyramidal neuron (Roshchin et al., 2018; Yu et al., 2010). Superresolution imaging techniques are extended with electron microscopy and proximity-biotinylation to further tease apart the nano-architecture of the axonal cytoskeleton (Hamdan et al., 2020; Vassilopoulos et al., 2019). With the expanding knowledge about the ultrastructure of the AIS, it becomes increasingly relevant to connect the high-resolution structural information with functional measurements to obtain a better understanding of the structure-function relationship in neurons. Bridging functional and structural information is a big challenge. Functional experiments require intact and thick sections of tissue, but superresolution microscopy is compromised by the scattering properties of biological tissue. An optical approach to overcome this challenge and perform superresolution reconstruction of cells used for functional investigation will be addressed in **Chapter 4**.

Experimental approaches to study ion channel activity

In the 1950s, Alan Hodgkin and Andrew Huxley developed and applied voltage-clamp recordings from the squid giant axon while varying the ionic concentrations of the intra- and extracellular solutions. This seminal work provided the first mathematical description of the Na^+ influx and K^+ outflux through voltage-gated ion channels (Hodgkin and Huxley, 1952a, 1952d, 1952b, 1952c; Hodgkin et al., 1952). Since then, the behavior and function of ion channels has been studied using a variety of methods, such as electrophysiology to describe the activation mechanisms and voltage-dependency of ion channels (Berkefeld et al., 2006; Rush et al., 2005; Yang et al., 2019), combined with pharmacology to identity the presence and role of an ion channel (Battefeld et al., 2014; Kole et al., 2007; Shu et al., 2007b), immunofluorescence to visualize the relative distribution of the subtypes (Boiko et al., 2003; Caldwell et al., 2000; Hu et al., 2009; Tian et al., 2014; Wart et al., 2007) and computational simulations to isolate the relative subcellular contribution of subtypes (Hu et al., 2009).

In addition to the electrical and computational methods described above, ion channel activity can also be visualized through optical recordings of ion indicators. Ion indicators are bioluminescent or fluorescent molecules that covalently bind an ion, which causes a confirmational change and a subsequent shift or amplitude change in the excitation or emission spectrum of the molecule (see **Figure 2a**). The emitted photons are an indirect reporter of dye molecules bound to the ion and thus report the ion concentration in the cell. In 1971, Baker et al. loaded the squid giant axon with the bioluminescent molecule aequorin, that emits blue light upon binding Ca^{2+}, and recorded the ‘glow’ of the molecule with a photomultiplier (see **Figure 2b**, Baker et al., 1971). With this molecule, Baker at al. confirmed the voltage-dependent entry of Ca^{2+} in the axon and even suggested a slight permeation of Ca^{2+} through Nav channels, which will be discussed in more detail in **Chapter 2**. A few years later, several smaller and more readily available Ca^{2+} dyes were reported that detected small changes in intracellular Ca^{2+} concentration (Brown et al., 1975). Since then, the possibilities to optically record Ca^{2+} have expanded and fluorescent indicators for other ions, such as Na^+, have also been developed (Minta and Tsien, 1989). One unavoidable disadvantage of using fluorescent indicators is that the reporters inherently buffer the ion that you study, which will influence its downstream signaling. Nonetheless, optical recordings are a valuable tool for subcellular investigations of ion fluxes such as at the AIS or dendritic spines (Bender and Trussell, 2009; Yuste and Denk, 1995). The development of faster cameras enables simultaneous recording of two ions (Miyazaki and Ross, 2015; Miyazaki et al., 2019) and in combination with low-affinity dyes even allow direct optical recordings of Ca^{2+} and Na^+ currents (see **Figure 2c**, Filipis and Canepari, 2021; Jaafari et al., 2014; Ouares et al., 2016). In addition, the development of two-photon microscopy and genetically encoded dyes has also opened the field of *in vivo* measurement of Ca^{2+} in neurons (Masatoshi, 2020). 50 years since Baker et al. experimented with the Ca^{2+} reporter aequorin, Ca^{2+} imaging is the ‘workhorse’ of neuroscience and recently researchers even succeeded, by applying temporal beam multiplexing, to record the Ca^{2+} dynamics of a dazzling 1 million neurons in a living brain (Demas et al., 2021).

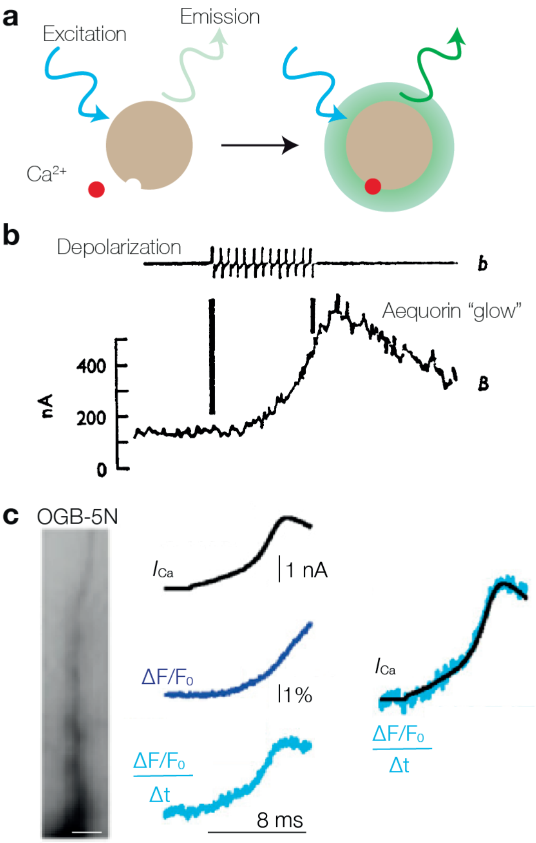

Figure 2. Optical methods to record Ca^{2+} levels and currents
a. Schematic of a fluorescent molecule excited by blue light and emitted green light, with increased emission upon binding Ca^{2+}. **b**. The first optical recording of intracellular Ca^{2+} from a squid giant axon from Baker et al., Journal of Physiology (1971). The axon was filled with the bioluminescent molecule aequorin and stimulated with a train of depolarizing pulses. The light emission or glow from aequorin was recorded on a photonmultiplier. **c**. Left, the apical dendrite of a CA1 hippocampal neuron filled with the low-affinity Ca^{2+} dye OGB-5N. Scale bar is 20 µm. Right, simultaneous recording of Ca^{2+} current and the OGB-5N fluorescence ($\Delta F/F_0$) at 20 kHz, while pharmacologically blocking Na^+ and K^+ currents. The derivative of the change in fluorescence is equal to the electrically recorded Ca^{2+} current, showing the feasibility to optically record currents. From Jaafari et al., Biophysical Journal (2014). This method is employed in Chapter 2.

Optical voltage recordings to investigate subcellular AP characteristics

In the same decennium that Baker et al. experimented with aequorin, several researchers at Yale University and the Marine Biological Laboratory developed a method to directly visualize the membrane potential. They optically recorded an AP for the first time with the dye merocyanine in the squid giant axon (see **Figure 3a**, Davila et al., 1973) and soon after also in a much smaller single neuron from the leech segmental ganglion (Salzberg et al., 1973). A newer merocyanine-oxazolon dye allowed simultaneous recording from multiple neurons and had sufficient signal-to-noise ratio to detect subthreshold events (Salzberg et al., 1997). Thereafter, the search for voltage indicators with higher signal size and more rapid kinetics led to the development of JPW1114, which allowed voltage recording in single cells in brain slices (Antic and Zecevic, 1995). Due to its high signal-to-noise ratio and microsecond activation kinetics, this dye is still wide used today, including in **Chapter 2** and **3**. Optical voltage recordings were vital in the investigation of the dendritic integration of pre- and postsynaptic signal but also in the spatiotemporal characteristics of axonal AP initiation and propagation (see **Figure 3b, c**, Canepari et al., 2007, 2008; Foust et al., 2010, 2011; Palmer and Stuart, 2006; Popovic et al., 2011). An in-depth review of the historical development and the broad field of further applications of voltage imaging has been described previously (Canepari et al., 2015). As with Ca^{2+} imaging, the development of optical voltage dyes also sparked the search for a genetically encoded indicator (Dimitrov et al., 2007; Siegel and Isacoff, 1997). Voltage imaging *in vivo* has somewhat different requirements for an indicator: where a synthetic dye is generally used to study subcellular V_M and should thus faithfully report the potential, genetically encoded dyes are often used to detect the occurrence of APs, making signal size more important than speed or voltage-linearity. The development of these indicators has resulted in a wide range of dyes, some most useful for detecting spikes in vivo and others are best suited to record subthreshold events (Jin et al., 2012; Kannan et al., 2018; Piatkevich et al., 2019). Combined with optogenetic stimulation, we can now perform an ‘all-optical electrophysiology’ (Adam et al., 2019; Hochbaum et al., 2014; Scanziani and Häusser, 2009).

In studies of subcellular activity, optical voltage recordings form a valuable complementary method to electrophysiology. While electrophysiological recordings offer

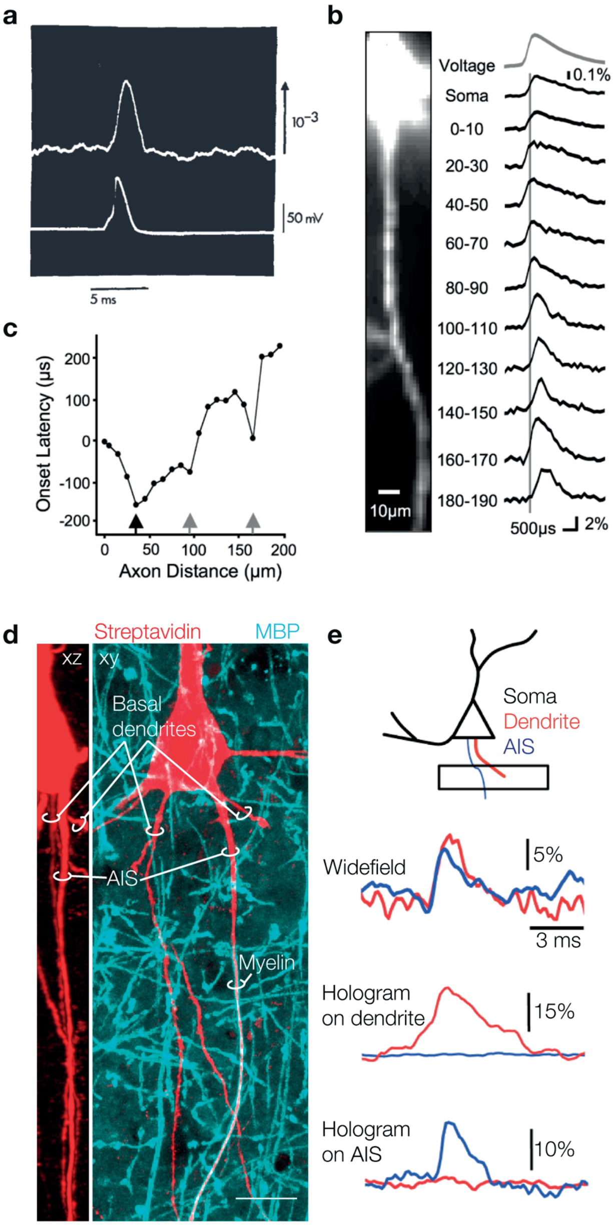

Figure 3. Optical voltage recordings reveal axonal AP characteristics
a. The first optical recording of an AP from the squid giant axon, using the molecule merocyanide, from Davila et al., Nature New Biology (1973). **b**. Optical voltage recordings from the layer 5 pyramidal neuron using the dye JPW3028, from Palmer and Stuart, The journal of Neuroscience (2006). Left, the baseline fluorescence of a JPW filled cell, right, voltage signals were recorded over 10 μm stretches of axon. **c**. Onset latency of the data in b plotted over distance from the soma reveals AP initiation in the distal AIS (black arrow) and reinitiation at the nodes of Ranvier (grey arrows). **d**. A biocytin-filled L5 pyramidal neuron stained with streptavidin (red) and myelin basic protein (cyan). Note the close distance in xy and in xz between the AIS and basal dendrites. Scale bar is 20 μm. **e**. Optical voltage recordings reveal dendrite and AIS AP shape differences only when holographic illumination is used, from Foust et al., Neurophotonics (2015). In widefield illumination (top trace), the AIS and dendrite are excited simultaneously and the signals interfere. This method is employed in Chapter 3.

high temporal resolution, exquisite signal to noise ratio and subcellular access (Kole and Popovic, 2016), patch pipettes can approach a cell in a limited number of locations and are not able to reach small structures (< 1 μm), such as axonal branches, or patches of membrane covered by myelination. Contrarily, optical voltage recordings allow simultaneous measurements from multiple areas, including the myelinated axon (see

Figure 3bc, Cohen et al., 2020; Foust et al., 2010; Palmer and Stuart, 2006; Popovic et al., 2011).

Optical voltage recordings are challenging. Due to the rapidity of an AP, high acquisition rates (>kHz) are imperative, and in order to receive sufficient signal per pixel, high light intensities are required, and spatial resolution is often sacrificed over temporal resolution. In addition, methods to increase spatial accuracy, such as confocal and two-photon microscopy, require scanning of the excitation beam over the tissue. This is not feasible with voltage-sensitive dye imaging, because it either slows down the acquisition rate or drastically reduces dwell time per pixel. Wide-field one photon illumination is therefore preferred but comes with a disadvantage: the excitation light is scattered by the opaque biological tissue, causing interfering signal from neurites that are out-of-focus or near the region of interest (see **Figure 3d**). This is especially problematic in neurons due to their highly ramified 3D anatomy and overlapping or adjacent neurites in the field of view and consequently mixing of fluorescence emission from separate neurites. Inspired by the development of multiple optical tweezers, a holographic approach to divide a beam of light (Curtis et al., 2002), Foust et al. published a method to overcome these obstacles by patterning excitation light to a region of interest (ROI, see **Figure 3e**, Foust et al., 2015). A spatial light modulator in the excitation light path applies a phase modulation to the excitation beam which is translated to an amplitude pattern in the focal plane and reduces excitation of the background and of neuronal parts that are not of interest (Gerchberg and Saxton, 1972). This method was published previously as an approach to uncage compounds simultaneously in distinct spots and shows a higher confinement of the beam in z, so regions out-of-focus receive lower light intensities (Lutz et al., 2008). When used for voltage imaging, Foust et al. observed improved signal accuracy, since interfering emission from non-ROIs no longer disrupts the signal. This method is especially advantageous when imaging small neurites next to larger structures, such as the AIS next to the soma or spines next to the apical dendrite (Foust et al., 2015; Tanese et al., 2017). The development of light patterned imaging has technically advanced the temporal and spatial resolution with which recordings from the axon can be made and will be further discussed in **Chapter 3**.

In this thesis, electrophysiological recordings, advanced live-cell imaging and superresolution structural reconstructions are combined to bridge the structure to function relationship of axonal activity.

Thesis outline

In this thesis, several advanced optical approaches, often combined with electrophysiology, were used to study ion channel signaling within and around the axon initial segment.

In **Chapter 2**, we combined electrophysiology with live imaging to study the activity dependent Ca^{2+} levels in the AIS and investigated the entry routes for Ca^{2+}. We observed Ca^{2+} increase in response to subthreshold stimulation and AP firing, that was partly Ca^{2+} release from internal stores, partly entered the membrane through Ca_V channels and, surprisingly, a large fraction of Ca^{2+} entered through Na_V channels. We used high-speed imaging with a low-affinity Ca^{2+} dye to optically record the Ca^{2+} current and observed that its activation kinetics resembled Na_V channel gating. We concluded that in addition to Ca_V channels a Na_V-mediated Ca^{2+} entry provides a submillisecond Ca^{2+} signaling pathway.

In **Chapter 3**, we employed a light patterning approach to obtain optical voltage recordings from the axon with high temporal and spatial resolution. In combination with calibration of the fluorescent signal and data fitting to obtain more accurate measures, we quantified the diversity of AP shape in axonal regions and investigated the mechanisms responsible for the differences in AP repolarization. BK channels in the distal AIS are activated efficiently by nanodomain coupling with Ca_V channels and are required for high-frequency firing.

In **Chapter 4**, we described a combination of adaptive optics and STORM microscopy that enabled superresolution microscopy deep inside biological tissue. We used adaptive optics to correct for aberrations caused by the tissue and thus increase localization precision. We were able to resolve the molecular nanoscale organization of cytoskeletal proteins at the AIS of a neuron we used for path-clamp recording, as a proof-of-principle of this approach to bridge functional assays with superresolution reconstructions.

References

Abbe, E. (1873). Beiträge zur Theorie des Mikroskops und der mikroskopischen Wahrnehmung. Archiv Für Mikroskopische Anatomie *9*, 413–468.

Adam, Y., Kim, J.J., Lou, S., Zhao, Y., Xie, M.E., Brinks, D., Wu, H., Mostajo-Radji, M.A., Kheifets, S., Parot, V., et al. (2019). Voltage imaging and optogenetics reveal behaviour-dependent changes in hippocampal dynamics. Nature *569*, 413–417.

Antic, S., and Zecevic, D. (1995). Optical signals from neurons with internally applied voltage-sensitive dyes. J Neurosci *15*, 1392–1405.

Antón-Fernández, A., Rubio-Garrido, P., DeFelipe, J., and Muñoz, A. (2013). Selective presence of a giant saccular organelle in the axon initial segment of a subpopulation of layer V pyramidal neurons. Brain Structure and Function *220*, 869–884.

Baker, P.F., Hodgkin, A.L., and Ridgway, E.B. (1971). Depolarization and calcium entry in squid giant axons. J Physiology *218*, 709–755.

Battefeld, A., Tran, B.T., Gavrilis, J., Cooper, E.C., and Kole, M.H.P. (2014). Heteromeric Kv7.2/7.3 channels differentially regulate action potential initiation and conduction in neocortical myelinated axons. The Journal of Neuroscience *34*, 3719–3732.

Bean, B.P. (2007). The action potential in mammalian central neurons. Nature Reviews Neuroscience *8*, 451–465.

Bender, K.J., and Trussell, L.O. (2009). Axon Initial Segment Ca2+ Channels Influence Action Potential Generation and Timing. Neuron *61*, 259–271.

Berkefeld, H., Sailer, C.A., Bildl, W., Rohde, V., Thumfart, J.-O., Eble, S., Klugbauer, N., Reisinger, E., Bischofberger, J., Oliver, D., et al. (2006). BK_{Ca}-Cav Channel Complexes Mediate Rapid and Localized Ca^{2+}-Activated K^+ Signaling. Science *314*, 615–620.

Boiko, T., Wart, A.V., Caldwell, J.H., Levinson, S.R., Trimmer, J.S., and Matthews, G. (2003). Functional Specialization of the Axon Initial Segment by Isoform-Specific Sodium Channel Targeting. J Neurosci *23*, 2306–2313.

Borst, J.G.G., and Sakmann, B. (1996). Calcium influx and transmitter release in a fast CNS synapse. Nature *383*, 431–434.

Borst, J.G.G., and Sakmann, B. (1999). Effect of changes in action potential shape on calcium currents and transmitter release in a calyx-type synapse of the rat auditory brainstem. Philosophical Transactions of the Royal Society B: Biological Sciences *354*, 347–355.

Brette, R. (2013). Sharpness of spike initiation in neurons explained by compartmentalization. PLoS Computational Biology *9*, e1003338.

Brown, J., Cohen, L.B., Weer, P. de, Pinto, L.H., Ross, W.N., and Salzberg, B.M. (1975). Rapid changes of intracellular free calcium concentration. Biophysical Journal *11*, 1155–1160. https://doi.org/10.1016/s0006-3495(75)85891-7.

Caldwell, J.H., Schaller, K.L., Lasher, R.S., Peles, E., and Levinson, S.R. (2000). Sodium channel Na(v)1.6 is localized at nodes of ranvier, dendrites, and synapses. PNAS *97*, 5616–5620.

Canepari, M., Djurisic, M., and Zecevic, D. (2007). Dendritic signals from rat hippocampal CA1 pyramidal neurons during coincident pre- and post-synaptic activity: a combined voltage- and calcium-imaging study. The Journal of Physiology *580*, 463–484.

Canepari, M., Vogt, K., and Zecevic, D. (2008). Combining Voltage and Calcium Imaging from Neuronal Dendrites. Cellular and Molecular Neurobiology *28*, 1079–1093.

Marco Canepari, Dejan Zecevic, and Olivier Bernus (2015). Membrane Potential Imaging in the Nervous System and Heart. 516.

Catterall, W. (1981). Localization of sodium channels in cultured neural cells. J Neurosci *1*, 777–783.

Cohen, C.C.H., Popovic, M.A., Klooster, J., Weil, M.-T., Möbius, W., Nave, K.-A., and Kole, M.H.P. (2020). Saltatory Conduction along Myelinated Axons Involves a Periaxonal Nanocircuit. Cell *180*, 1–28.

Coombs, J.S., Curtis, D.R., and Eccles, J.C. (1957). The generation of impulses in motoneurones. J Physiology *139*, 232–249.

Curtis, J.E., Koss, B.A., and Grier, D.G. (2002). Dynamic holographic optical tweezers. Opt Commun *207*, 169–175.

Davila, H.V., Salzberg, B.M., Cohen, L.B., and Waggoner, A.S. (1973). A Large Change in Axon Fluorescence that Provides a Promising Method for Measuring Membrane Potential. Nat New Biology *241*, 159–160.

Demas, J., Manley, J., Tejera, F., Barber, K., Kim, H., Traub, F.M., Chen, B., and Vaziri, A. (2021). High-speed, cortex-wide volumetric recording of neuroactivity at cellular resolution using light beads microscopy. Nat Methods *18*, 1103–1111.

D'Este, E., Kamin, D., Balzarotti, F., and Hell, S.W. (2017). Ultrastructural anatomy of nodes of Ranvier in the peripheral nervous system as revealed by STED microscopy. Proceedings of the National Academy of Sciences *114*, E191–E199.

Dimitrov, D., He, Y., Mutoh, H., Baker, B.J., Cohen, L., Akemann, W., and Knöpfel, T. (2007). Engineering and Characterization of an Enhanced Fluorescent Protein Voltage Sensor. Plos One *2*, e440.

Fatt, P. (1957). Sequence of Events in Synaptic Activation of a Motoneurone. J Neurophysiol *20*, 61–80.

Filipis, L., and Canepari, M. (2021). Optical measurement of physiological sodium currents in the axon initial segment. Journal of Physiology *599*, 2020.07.20.211839.

Foust, A.J., Popovic, M.A., Zecevic, D., and McCormick, D.A. (2010). Action Potentials Initiate in the Axon Initial Segment and Propagate through Axon Collaterals Reliably in Cerebellar Purkinje Neurons. Journal of Neuroscience *30*, 6891–6902.

Foust, A.J., Yu, Y., Popovic, M.A., Zecevic, D., and McCormick, D.A. (2011). Somatic Membrane Potential and Kv1 Channels Control Spike Repolarization in Cortical Axon Collaterals and Presynaptic Boutons. Journal of Neuroscience *31*, 15490–15498.

Foust, A.J., Zampini, V., Tanese, D., Papagiakoumou, E., and Emiliani, V. (2015). Computer-generated holography enhances voltage dye fluorescence discrimination in adjacent neuronal structures. Neurophotonics *2*, 021007.

Fuortes, M.G.F., Frank, K., and Becker, M.C. (1957). Steps in the Production of Motoneuron Spikes. J Gen Physiology *40*, 735–752.

Geiger, J.R.P., and Jonas, P. (2000). Dynamic control of presynaptic Ca(2+) inflow by fast-inactivating K(+) channels in hippocampal mossy fiber boutons. Neuron *28*, 927–939.

Gerchberg, R., and Saxton, W.O. (1972). A Practical Algorithm for the Determination of Phase from Image and Diffraction Plane Pictures. *35*, 237–246.

Goethals, S., and Brette, R. (2020). Theoretical relation between axon initial segment geometry and excitability. Elife *9*, e53432.

Grubb, M.S., and Burrone, J. (2010). Activity-dependent relocation of the axon initial segment fine-tunes neuronal excitability. Nature *465*, 1070–1074.

Grubb, M.S., Shu, Y., Kuba, H., Rasband, M.N., Wimmer, V.C., and Bender, K.J. (2011). Short- and Long-Term Plasticity at the Axon Initial Segment. J Neurosci *31*, 16049–16055.

Hamdan, H., Lim, B.C., Torii, T., Joshi, A., Konning, M., Smith, C., Palmer, D.J., Ng, P., Leterrier, C., Oses-Prieto, J.A., et al. (2020). Mapping axon initial segment structure and function by multiplexed proximity biotinylation. Nat Commun *11*, 100.

Hell, S.W., and Wichmann, J. (1994). Breaking the diffraction resolution limit by stimulated emission: stimulated-emission-depletion fluorescence microscopy. Opt Lett *19*, 780.

Hirono, M., Ogawa, Y., Misono, K., Zollinger, D.R., Trimmer, J.S., Rasband, M.N., and Misonou, H. (2015). BK Channels Localize to the Paranodal Junction and Regulate Action Potentials in Myelinated Axons of Cerebellar Purkinje Cells. Journal of Neuroscience *35*, 7082–7094.

Hochbaum, D.R., Zhao, Y., Farhi, S.L., Klapoetke, N., Werley, C.A., Kapoor, V., Zou, P., Kralj, J.M., Maclaurin, D., Smedemark-Margulies, N., et al. (2014). All-optical electrophysiology in mammalian neurons using engineered microbial rhodopsins. Nat Methods *11*, 825–833.

Hodgkin, A.L., and Huxley, A.F. (1939). Action Potentials Recorded from Inside a Nerve Fibre. Nature *144*, 710–711.

Hodgkin, A.L., and Huxley, A.F. (1952a). A quantitative description of membrane current and its application to conduction and excitation in nerve. J Physiology *117*, 500–544.

Hodgkin, A.L., and Huxley, A.F. (1952b). The components of membrane conductance in the giant axon of Loligo. J Physiology *116*, 473–496.

Hodgkin, A.L., and Huxley, A.F. (1952c). The dual effect of membrane potential on sodium conductance in the giant axon of Loligo. J Physiology *116*, 497–506.

Hodgkin, A.L., and Huxley, A.F. (1952d). Currents carried by sodium and potassium ions through the membrane of the giant axon of Loligo. J Physiology *116*, 449–472.

Hodgkin, A.L., Huxley, A.F., and Katz, B. (1952). Measurement of current-voltage relations in the membrane of the giant axon of Loligo. J Physiology *116*, 424–448.

Hoppa, M.B., Gouzer, G., Armbruster, M., and Ryan, T.A. (2014). Control and Plasticity of the Presynaptic Action Potential Waveform at Small CNS Nerve Terminals. Neuron *84*, 778–789.

Hu, W., Tian, C., Li, T., Yang, M., Hou, H., and Shu, Y. (2009). Distinct contributions of Nav1.6 and Nav1.2 in action potential initiation and backpropagation. Nature Publishing Group *12*, 996–1002.

Huang, C.Y., and Rasband, M.N. (2018). Axon initial segments: structure, function, and disease. Ann Ny Acad Sci *1420*, 46–61.

Jaafari, N., Waard, M.D., and Canepari, M. (2014). Imaging Fast Calcium Currents beyond the Limitations of Electrode Techniques. Biophysical Journal *107*, 1280–1288.

Jamann, N., Dannehl, D., Lehmann, N., Wagener, R., Thielemann, C., Schultz, C., Staiger, J., Kole, M.H.P., and Engelhardt, M. (2021). Sensory input drives rapid homeostatic scaling of the axon initial segment in mouse barrel cortex. Nature Communications 1–14.

Jin, L., Han, Z., Platisa, J., Wooltorton, J.R.A., Cohen, L.B., and Pieribone, V.A. (2012). Single Action Potentials and Subthreshold Electrical Events Imaged in Neurons with a Fluorescent Protein Voltage Probe. Neuron *75*, 779–785.

Kannan, M., Vasan, G., Huang, C., Haziza, S., Li, J.Z., Inan, H., Schnitzer, M.J., and Pieribone, V.A. (2018). Fast, in vivo voltage imaging using a red fluorescent indicator. Nature Methods *15*, 1–14.

King, A.N., Manning, C.F., and Trimmer, J.S. (2014). A unique ion channel clustering domain on the axon initial segment of mammalian neurons. Journal of Comparative Neurology *522*, 2594–2608.

Klar, T.A., Jakobs, S., Dyba, M., Egner, A., and Hell, S.W. (2000). Fluorescence microscopy with diffraction resolution barrier broken by stimulated emission. Proc National Acad Sci *97*, 8206–8210.

Kole, M.H.P., and Brette, R. (2018). The electrical significance of axon location diversity. Current Opinion in Neurobiology *51*, 52–59.

Kole, M.H.P., and Popovic, M.A. (2016). Patch-Clamp Recording from Myelinated Central Axons. (Springer New York), pp. 123–138.

Kole, M.H.P., and Stuart, G.J. (2012). Signal processing in the axon initial segment. Neuron *73*, 235–247.

Kole, M.H.P., Letzkus, J.J., and Stuart, G.J. (2007). Axon Initial Segment Kv1 Channels Control Axonal Action Potential Waveform and Synaptic Efficacy. Neuron *55*, 633–647.

Kole, M.H.P., Ilschner, S.U., Kampa, B.M., Williams, S.R., Ruben, P.C., and Stuart, G.J. (2008). Action potential generation requires a high sodium channel density in the axon initial segment. Nature Neuroscience *11*, 178–186.

Kuba, H., Ishii, T.M., and Ohmori, H. (2006). Axonal site of spike initiation enhances auditory coincidence detection. Nature *444*, 1069–1072.

Leterrier, C. (2018). The Axon Initial Segment: An Updated Viewpoint. Journal of Neuroscience *38*, 2135–2145.

Linde, S. van de, Löschberger, A., Klein, T., Heidbreder, M., Wolter, S., Heilemann, M., and Sauer, M. (2011). Direct stochastic optical reconstruction microscopy with standard fluorescent probes. Nat Protoc 6, 991–1009.

Lorincz, A., and Nusser, Z. (2008). Cell-Type-Dependent Molecular Composition of the Axon Initial Segment. J Neurosci 28, 14329–14340.

Lorincz, A., and Nusser, Z. (2010). Molecular identity of dendritic voltage-gated sodium channels. Science 328, 906–909.

Lutz, C., Otis, T.S., DeSars, V., Charpak, S., DiGregorio, D.A., and Emiliani, V. (2008). Holographic photolysis of caged neurotransmitters. Nat Methods 5, 821–827. https://doi.org/10.1038/nmeth.1241.

Masatoshi, I. (2020). Genetically Encoded Calcium Indicators to Probe Complex Brain Circuit Dynamics in vivo. Neurosci Res *169*, 2–8.

Minta, A., and Tsien, R.Y. (1989). Fluorescent indicators for cytosolic sodium*. J Biol Chem *264*, 19449–19457.

Miyazaki, K., and Ross, W.N. (2015). Simultaneous Sodium and Calcium Imaging from Dendrites and Axons. ENeuro *2*, 1–10.

Miyazaki, K., Lisman, J.E., and Ross, W.N. (2019). Improvements in Simultaneous Sodium and Calcium Imaging. Frontiers in Cellular Neuroscience *12*, ENEURO.0050-15.2016-10.

Otani, T., and Araki, T. (1955). Response of Single Motoneurons to Direct Stimulation in Toad's Spinal Cord. Journal of Physiology.

Ouares, K.A., Jaafari, N., and Canepari, M. (2016). A generalised method to estimate the kinetics of fast Ca2+ currents from Ca2+ imaging experiments. J Neurosci Meth *268*, 66–77.

Palay, S.L., Sotelo, C., Peters, A., and Orkand, P.M. (1968). The Axon Hillock and the Initial Segment. J Cell Biology *38*, 193–201.

Palmer, L.M., and Stuart, G.J. (2006). Site of action potential initiation in layer 5 pyramidal neurons. The Journal of Neuroscience *26*, 1854–1863.

Pan, Z., Kao, T., Horvath, Z., Lemos, J., Sul, J.-Y., Cranstoun, S.D., Bennett, V., Scherer, S.S., and Cooper, E.C. (2006). A Common Ankyrin-G-Based Mechanism Retains KCNQ and Na V Channels at Electrically Active Domains of the Axon. J Neurosci *26*, 2599–2613.

Piatkevich, K.D., Bensussen, S., Tseng, H., Shroff, S.N., Lopez-Huerta, V.G., Park, D., Jung, E.E., Shemesh, O.A., Straub, C., Gritton, H.J., et al. (2019). Population imaging of neural activity in awake behaving mice. Nature *574*, 1–28.

Popovic, M.A., Foust, A.J., McCormick, D.A., and Zecevic, D. (2011). The spatio-temporal characteristics of action potential initiation in layer 5 pyramidal neurons: a voltage imaging study. The Journal of Physiology *589*, 4167–4187.

Prakash, K., Diederich, B., Heintzmann, R., and Schermelleh, L. (2022). Super-resolution microscopy: a brief history and new avenues. Philosophical Transactions Royal Soc *380*, 20210110.

Rasband, M.N. (2010). The axon initial segment and the maintenance of neuronal polarity. Nature Reviews Neuroscience *11*, 1–11.

Roshchin, M.V., Matlashov, M.E., Ierusalimsky, V.N., Balaban, P.M., Belousov, V.V., Kemenes, G., Staras, K., and Nikitin, E.S. (2018). A BK channel–mediated feedback pathway links single-synapse activity with action potential sharpening in repetitive firing. Sci Adv *4*, eaat1357.

Rothenberg, M.A. (1950). Studies on permeability in relation to nerve function II. ionic movements across axonal membranes. Biochim Biophys Acta *4*, 96–114.

Rush, A.M., Dib-Hajj, S.D., and Waxman, S.G. (2005). Electrophysiological properties of two axonal sodium channels, Na v1.2 and Na v1.6, expressed in mouse spinal sensory neurones. The Journal of Physiology *564*, 803–815.

Salzberg, B.M., Davila, H.V., and Cohen, L.B. (1973). Optical Recording of Impulses in Individual Neurones of an Invertebrate Central Nervous System. Nature *246*, 508–509.

Salzberg, B.M., Grinvald, A., Cohen, L.B., Davila, H.V., and Ross, W.N. (1977). Optical recording of neuronal activity in an invertebrate central nervous system: simultaneous monitoring of several neurons. J Neurophysiol *40*, 1281–1291. https://doi.org/10.1152/jn.1977.40.6.1281.

Scanziani, M., and Häusser, M. (2009). Electrophysiology in the age of light. Nature *461*, 930–939.

Shu, Y., Duque, A., Yu, Y., Haider, B., and McCormick, D.A. (2007a). Properties of Action-Potential Initiation in Neocortical Pyramidal Cells: Evidence From Whole Cell Axon Recordings. J Neurophysiol *97*, 746–760.

Shu, Y., Yu, Y., Yang, J., and McCormick, D.A. (2007b). Selective control of cortical axonal spikes by a slowly inactivating K+ current. Proc National Acad Sci *104*, 11453–11458.

Siegel, M.S., and Isacoff, E.Y. (1997). A Genetically Encoded Optical Probe of Membrane Voltage. Neuron *19*, 735–741.

Stuart, G.J., and Sakmann, B. (1994). Active propagation of somatic action potentials into neocortical pyramidal cell dendrites. Nature *367*, 69–72.

Stuart, G.J., and Sakmann, B. (1995). Amplification of EPSPs by axosomatic sodium channels in neocortical pyramidal neurons. Neuron *15*, 1065–1076.

Stuart, G., Schiller, J., and Sakmann, B. (1997a). Action potential initiation and propagation in rat neocortical pyramidal neurons. J Physiology *505*, 617–632.

Stuart, G., Spruston, N., Sakmann, B., and Häusser, M. (1997b). Action potential initiation and backpropagation in neurons of the mammalian CNS. Trends Neurosci *20*, 125–131.

Tanese, D., Weng, J.-Y., Zampini, V., Sars, V.D., Canepari, M., Rozsa, B., Emiliani, V., and Zecevic, D. (2017). Imaging membrane potential changes from dendritic spines using computer-generated holography. Neurophotonics *4*, 031211.

Thome, C., Kelly, T., Yanez, A., Schultz, C., Engelhardt, M., Cambridge, S.B., Both, M., Draguhn, A., Beck, H., and Egorov, A.V. (2014). Axon-Carrying Dendrites Convey Privileged Synaptic Input in Hippocampal Neurons. Neuron *83*, 1418–1430.

Tian, C., Wang, K., Ke, W., Guo, H., and Shu, Y. (2014). Molecular identity of axonal sodium channels in human cortical pyramidal cells. Front Cell Neurosci *8*, 297.

Vassilopoulos, S., Gibaud, S., Jimenez, A., Caillol, G., and Leterrier, C. (2019). Ultrastructure of the axonal periodic scaffold reveals a braid-like organization of actin rings. Nat Commun *10*, 5803.

Wart, A.V., Trimmer, J.S., and Matthews, G. (2007). Polarized distribution of ion channels within microdomains of the axon initial segment. J Comp Neurol *500*, 339–352.

Waters, J., Schaefer, A., and Sakmann, B. (2005). Backpropagating action potentials in neurones: measurement, mechanisms and potential functions. Prog Biophysics Mol Biology *87*, 145–170.

Xu, K., Zhong, G., and Zhuang, X. (2013). Actin, spectrin, and associated proteins form a periodic cytoskeletal structure in axons. Science *339*, 452–456.

Yang, J., Xiao, Y., Li, L., He, Q., Li, M., and Shu, Y. (2019). Biophysical Properties of Somatic and Axonal Voltage-Gated Sodium Channels in Midbrain Dopaminergic Neurons. Front Cell Neurosci *13*, 317.

Yu, Y., Maureira, C., Liu, X., and McCormick, D.A. (2010). P/Q and N channels control baseline and spike-triggered calcium levels in neocortical axons and synaptic boutons. The Journal of Neuroscience *30*, 11858–11869.

Yuste, R., and Denk, W. (1995). Dendritic spines as basic functional units of neuronal integration. Nature *375*, 682–684.

Zhou, D., Lambert, S., Malen, P.L., Carpenter, S., Boland, L.M., and Bennett, V. (1998). AnkyrinG Is Required for Clustering of Voltage-gated Na Channels at Axon Initial Segments and for Normal Action Potential Firing. J Cell Biology *143*, 1295–1304.

Chapter 2

Ca^{2+} entry through Na_V channels generates submillisecond axonal Ca^{2+} signaling

Naomi A. K. Hanemaaijer[1, 2 #], Marko A. Popovic[1, 3 #], Xante Wilders[1], Sara Grasman[1], Oriol Pavón Arocas[1, 4] and Maarten H. P. Kole[1,2 *]

Published in *eLife* **9**, 353–32 (2020).

Affiliations

[1] Department of Axonal Signaling, Netherlands Institute for Neuroscience (NIN), Royal Netherlands Academy of Arts and Sciences (KNAW), Meibergdreef 47, 1105 BA, Amsterdam, The Netherlands.

[2] Cell Biology, Neurobiology and Biophysics, Department of Biology, Faculty of Science, Utrecht University, Padualaan 8, 3584 CH, Utrecht, The Netherlands.

[3] Present address: Molecular Cell Biology and Immunology, Amsterdam UMC, Location VUmc, Gustav Mahlerlaan 665, 1082 MK, Amsterdam, The Netherlands.

[4] Present address: Sainsbury Wellcome Centre for Neural Circuits and Behaviour, University College London, UK.

[#] These authors contributed equally to this work.

Abstract

Calcium ions (Ca^{2+}) are essential for many cellular signaling mechanisms and enter the cytosol mostly through voltage-gated calcium channels. Here, using high-speed Ca^{2+} imaging up to 20 kHz in the rat layer 5 pyramidal neuron axon we found that activity-dependent intracellular calcium concentration ($[Ca^{2+}]_i$) in the axonal initial segment was only partially dependent on voltage-gated calcium channels. Instead, $[Ca^{2+}]_i$ changes were sensitive to the specific voltage-gated sodium (Na_V) channel blocker tetrodotoxin. Consistent with the conjecture that Ca^{2+} enters through the Na_V channel pore, the optically resolved I_{Ca} in the axon initial segment overlapped with the activation kinetics of Na_V channels and heterologous expression of $Na_V1.2$ in HEK-293 cells revealed a tetrodotoxin-sensitive $[Ca^{2+}]_i$ rise. Finally, computational simulations predicted that axonal $[Ca^{2+}]_i$ transients reflect a 0.4% Ca^{2+} conductivity of Na_V channels. The findings indicate that Ca^{2+} permeation through Na_V channels provides a submillisecond rapid entry route in Na_V-enriched domains of mammalian axons.

Introduction

Ca^{2+} ions crossing the neuronal plasma membrane are critically involved in depolarization and distribute in the cytosol in spatial microdomains and organelles to regulate a wide range of processes ranging from gene expression to fast transmitter release (Berridge, 2006; Neher and Sakaba, 2008). In axons, voltage-gated Ca^{2+} (Ca_V) channels at presynaptic terminals open in response to a single action potential (AP), raising intracellular Ca^{2+} concentrations ($[Ca^{2+}]_i$) in nanodomains from ~50 nM up to ~10 μM to increase transmitter vesicle release rates by the power of ~4 (Helmchen et al., 1997; Schneggenburger and Neher, 2000). In response to APs, large and local $[Ca^{2+}]_i$ transients are typically also observed in the axon initial segment (AIS) and nodes of Ranvier (Callewaert et al., 1996; Bender and Trussell, 2009; Yu et al., 2010; Gründemann and Clark, 2015; Zhang and David, 2016; Clarkson et al., 2017). At these sites, Ca^{2+} currents have been implicated in AP initiation and propagation by a local depolarizing action of the inward current or by activating the large conductance, Ca^{2+}- and voltage-dependent K^+ (BK_{Ca}) channels modulating burst firing probability and limiting frequency-dependent AP failure rates (Bender and Trussell, 2009; Yu et al., 2010; Hirono et al., 2015). The Ca_V channel subtypes identified in axons are both cell- and species-dependent and include the T-, P/Q- or N-type

Ca_V channels (Callewaert et al., 1996; Bender and Trussell, 2009; Yu et al., 2010; Gründemann and Clark, 2015; Zhang and David, 2016). At the AIS in particular the T-type Ca^{2+} channel mediates AP-dependent Ca^{2+} influx (Bender and Trussell, 2009; Martinello et al., 2015; Fukaya et al., 2018; Jin et al., 2019). However, in prefrontal cortical pyramidal neuron AIS about 70% of the AP-evoked $[Ca^{2+}]_i$ remains unaffected following pharmacological block of T-type Ca_V channels (Clarkson et al., 2017). Furthermore, evidence for a clustering of T-type Ca_V channels at the AIS remains ambiguous and immunofluorescence or immuno-gold labeling studies show a density which is comparable to somatodendritic or spine compartments (McKay et al., 2006; Martinello et al., 2015).

Several other mechanisms may contribute to axoplasmic $[Ca^{2+}]_i$ elevations in the AIS. Firstly, Ca^{2+} levels could rise due to Ca^{2+}-induced Ca^{2+} release from intracellular sources such as the endoplasmic reticulum (ER). Most AISs contain ER cisternae organelles consisting of stacks of membranes expressing the store-operated ryanodine receptor (RyR), inositol 1,4,5-triphosphate receptor 1(IP_3R1) and sarcoplasmic ER Ca^{2+} ATPase (SERCA) pumps (Benedeczky et al., 1994; King et al., 2014; Antón-Fernández et al., 2015). The coupling of transmembrane Ca^{2+} entry with intracellular store release may generate a local activity-dependent rise of $[Ca^{2+}]_i$. However, a contribution of ER stores to AIS $[Ca^{2+}]_i$ remains to be directly demonstrated. Secondly, near the peak of the AP the electrogenic Na^+-Ca^{2+} exchanger (NCX) reverses direction and imports Ca^{2+}. A reverse mode of operation has not only been implicated in pathological $[Ca^{2+}]_i$ elevations in axons during hypoxia and injury (Stys et al., 1991; Iwata et al., 2004), but also occurs during trains of APs in nodes and neighboring internodes (Zhang and David, 2016). Finally, one pathway that until so far has yet to be directly examined in mammalian cortical axons are the voltage-gated Na^+ (Na_V) channels. Studies in the squid giant axon combining electrophysiological recordings with Ca^{2+} imaging showed that an early component of depolarization-induced Ca^{2+} entry is tetrodotoxin (TTX)-sensitive (Baker et al., 1971; Meves and Vogel, 1973; Brown et al., 1975). Using voltage-clamp recordings from axons and perfusing distinct ionic solutions provided a quantitative estimate that Na_V channels may pass divalent Ca^{2+} ions with permeability ratios for P_{Ca}/P_{Na} up to 0.10 (Hille, 1972; Meves and Vogel, 1973). Ca^{2+} permeability of Na_V channels has also been shown to occur in cardiac cells and hippocampal neurons (Akaike and Takahashi, 1992; Aggarwal et al., 1997; Santana et al., 1998) but whether this extends to the cortical axons remains to be examined.

Here, using wide-field Ca^{2+} imaging with a high-speed CCD camera enabling detection of $[Ca^{2+}]_i$ changes at high sensitivity and high temporal resolution (Jaafari et al., 2014; Ait Ouares et al., 2016), we explored the various pathways of Ca^{2+} entry in axons of rat thick-tufted neocortical layer 5 (L5) pyramidal neurons. We found that during subthreshold membrane depolarizations $[Ca^{2+}]_i$ transients were highly compartmentalized to the AIS and nodes of Ranvier. While in the AIS $[Ca^{2+}]_i$ transients were amplified by ER store release the trigger was only modestly accounted for by Ca_V channels. The largest fraction of activity-dependent $[Ca^{2+}]_i$ was TTX-sensitive and overlapped with the rapid gating of Na_V channels. Experiments in HEK-293 cells transfected with the human $Na_V1.2$ channel confirmed that TTX-sensitive Na^+ currents were sufficient to generate $[Ca^{2+}]_i$ elevations. Together, the data suggest that $[Ca^{2+}]_i$ dynamics in the mammalian AIS are predominantly mediated by a rapid Ca^{2+} entry through Na_V channels.

Results

Activity-dependent compartmentalized Ca^{2+} entry in layer 5 axons

Thick-tufted L5 pyramidal neurons, also called L5B or pyramidal tract neurons, are the largest pyramidal neurons in the cortex and integrate synaptic inputs from all cortical layers, playing a central to cognitive tasks including perception (Groh et al., 2010; Ramaswamy and Markram, 2015; Takahashi et al., 2016). Their large axons (~1.5 μm in diameter) send long-range output projections to the thalamus, striatum and spinal cord, but within the cortex branch sparsely and have a trajectory perpendicular to the pia providing an excellent anatomical arrangement to image and record from. To optically record the spatial profile of axonal $[Ca^{2+}]_i$ we made somatic whole-cell patch-clamp recordings from thick-tufted L5 pyramidal neurons filled with the high-affinity Ca^{2+} indicator Oregon Green BAPTA 1 (OGB-1, 100 μM) and imaged epifluorescence signals along the proximal region of the main axon (**Figure 1**). We first used subthreshold depolarizations evoked by artificial excitatory postsynaptic potentials (a-EPSPs, 100 Hz, peak depolarization 17.0 ± 0.6 mV, $n = 15$; **Figure 1a**). Examination of the spatial profile revealed that Ca^{2+} signals were observed in the AIS and hot spots separated with regular distances along the axon (locations

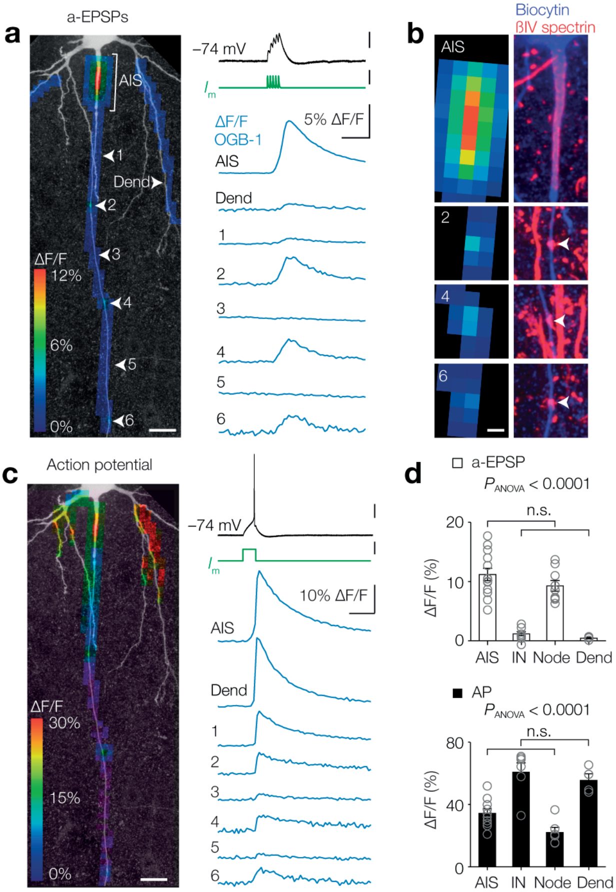

Figure 1. Activity-dependent compartmentalized Ca^{2+} entry in layer 5 axons

a. Left, Color-coded maximal ΔF/F of OGB-1 imaged in a L5 pyramidal neuron axon in response to an a-EPSP (five current injections at 100 Hz) overlaid with a z-projection of biocytin-streptavidin (grey) of the same neuron. White arrowheads indicate regions of interest from which example traces are shown on the right. Scale bar, 20 μm. Right, ΔF/F traces from locations specified left. For illustrative purposes, ΔF/F traces represent averages of ~400 trials. Top to bottom scale bars, 10 mV, 1 nA, 5% ΔF/F, 100 ms. **b**. Left, higher magnification of the regions of interest shown in **a**. Right, maximal z-projection of biocytin-streptavidin (blue) and ßIV spectrin (red). White arrows indicate nodes or Ranvier. Sites with a-EPSP-evoked $[Ca^{2+}]_i$ transients were all positive to ßIV spectrin (n = 15 AISs and 23 nodes from n = 15 axons). Scale bar, 5 μm. **c**. Same axon and locations as in **a** with color-coded maximal ΔF/F in response to an AP. Scale bars, 20 mV, 0.5 nA, 10% ΔF/F, 100 ms and 20 μm. **d**. Top, Population data for peak ΔF/F in response to a-EPSPs in the AIS (n = 13), first internode (IN, n = 9), the first Node (n = 9) and basal dendrite (Dend, n = 4), one-way ANOVA with Tukey's multiple comparisons test, P < 0.0001, Bottom, peak ΔF/F in response to a single AP in the AIS (n = 10), first internode (IN, n = 6), the first Node (n = 6) and basal dendrite (Dend, n = 4), one-way ANOVA with Tukey's multiple comparisons test, P < 0.0001. Open circles represent individual cells and bars show the population mean ± s.e.m. Data available in Figure 1–source data 1. See also Figure 1–figure supplement 1.

2, 4 and 6; **Figure 1a**). In order to examine whether the $[Ca^{2+}]_i$ hot spots corresponded to nodes of Ranvier, we post-hoc stained for βIV-spectrin and biocytin, and found a high degree of overlap between subthreshold $[Ca^{2+}]_i$ rise and spectrin-enriched sites (**Figure 1b**). In the same cells we examined the spatial profile of $\Delta[Ca^{2+}]_i$ in response to a single AP evoked with a brief square current injection (**Figure 1c**). As expected from back- and forward-propagating APs with much higher depolarizations (~100 mV), large $[Ca^{2+}]_i$ transients were observed widespread throughout all axonal and somatodendritic domains. Population analysis showed that AP-induced $[Ca^{2+}]_i$ transients were similar between AIS and nodes (one-way ANOVA followed by Tukey's multiple comparison test, $P < 0.0001$, differences between all groups were significant ($P < 0.05$) except between AIS and node ($P = 0.13$) and between internode (IN) and dendrites ($P = 0.85$); **Figure 1c, d**). Interestingly, also during a-EPSPs the $[Ca^{2+}]_i$ transients in the AIS and the first nodes were highly comparable, while $[Ca^{2+}]_i$ signals in the internodal and dendritic domains were an order of magnitude smaller (one-way ANOVA with Tukey's multiple comparison test, $P < 0.0001$, differences between all groups were significant ($P < 0.0001$), except between AIS and node ($P = 0.38$) and IN and Dend ($P = 0.97$); **Figure 1a, d**). Similar experiments in L5 neocortical pyramidal neurons in slices from human temporal cortex also revealed a-EPSP evoked $\Delta[Ca^{2+}]_i$ in the AIS, but not in the dendrite, suggesting that subthreshold sensitive $[Ca^{2+}]_i$ transients are conserved across mammalian species (**Figure 1–figure supplement 1**). Together, these results show that activity-dependent $[Ca^{2+}]_i$ transients are spatiotemporally compartmentalized and Ca^{2+} entry dynamics are similar in the axoplasm of the AIS and nodes.

Giant saccular organelle amplifies activity-dependent $[Ca^{2+}]_i$ transients in the AIS

The thick-tufted L5 pyramidal neuron AIS contains a unique variant of cisternal organelle characterized by a continuous tubular organization of smooth ER, called the giant saccular organelle (Antón-Fernández et al., 2015). Cisternal organelles with smooth ER express synaptopodin (synpo), RyR, the IP_3 receptor 1, and SERCA that are thought to contribute to Ca^{2+} release, buffering and storage (Bas Orth et al., 2007; King et al., 2014). We hypothesized that these organelles could generate Ca^{2+}-induced Ca^{2+}-release, thereby contributing to domain-selective activity-dependent $[Ca^{2+}]_i$ transients (**Figure 1**). Triple immunostaining for synpo, Ankyrin G and biocytin confirmed that the cisternal organelle was present along the entire axis of the AIS and spatially overlapped with the subthreshold-evoked $[Ca^{2+}]_i$ transients (*n* = 19; **Figure 2a, b**). However, while subthreshold depolarization-induced Ca^{2+} transients were present in the nodes, synaptopodin expression was not detectable there (*n* = 10 nodes; **Figure 1** and **2a**). To experimentally test whether AIS Ca^{2+}-store release contributes to activity-dependent $[Ca^{2+}]_i$ transients we performed experiments with standard intracellular solution and subsequently re-patched the same cell with a solution containing ryanodine (200 µM, blocking RyR-mediated Ca^{2+} release) and heparin (5 mg/ml, competitively inhibiting IP_3-evoked Ca^{2+} release; **Figure 2c**). Blocking Ca^{2+} release significantly lowered ΔF/F Ca^{2+} peak transients in the AIS, both for the subthreshold- and AP-evoked $[Ca^{2+}]_i$ changes (a-EPSP, 53.2% reduction, $P = 0.006$; AP, 34.3% reduction, $P = 0.02$, one-tailed ratio paired t-tests, $n = 5$; **Figure 2d**). Consistent with the AIS-specific location of the giant saccular organelle, store blockers had no effect on AP-evoked $\Delta[Ca^{2+}]_i$ in the basal dendrite ($P = 0.48$, $n = 3$; **Figure 2d**). Furthermore, since the stores contribute significantly to AIS Ca^{2+} levels, blocking store release could act as a low-pass filter for Ca^{2+} level kinetics, reducing rise and decay times. However, blocking Ca^{2+}-store release did not alter the rise- or decay time kinetics in the AIS (τ_{act}, $P = 0.52$; τ_{de-act}, $P = 0.18$, two-tailed paired *t*-tests, $n = 5$; **Figure 2e**). These data suggest that the giant saccular organelle amplifies activity-dependent $[Ca^{2+}]_i$ changes selectively in the AIS.

Ca_V channels and NCX have a limited role in activity-dependent Ca^{2+} entry at the AIS

Ca^{2+} release from internal stores is likely triggered by Ca^{2+} entry from outside and via neuronal voltage-dependent plasmalemmal routes. To test whether AIS $[Ca^{2+}]_i$ changes require Ca^{2+} from the extracellular space, we bath applied 2.5 mM of the Ca^{2+} chelator EGTA which effectively lowered the extracellular Ca^{2+} concentration ($[Ca^{2+}]_o$) from 2 mM to ~437 nM, thereby reducing the driving force for Ca^{2+} (see **Materials and Methods**). Ca^{2+} imaging at the AIS (OGB-1, 100 µM) showed that EGTA almost fully abolished the subthreshold-evoked $\Delta[Ca^{2+}]_i$ (90.7% reduction, one-tailed ratio paired t-test, $P = 0.0031$, $n = 4$; **Figure 3a, b**). Similarly, the AP-generated $\Delta[Ca^{2+}]_i$ was almost extinguished after bath application of EGTA (92.8% reduction, $P = 0.0011$, $n = 4$; **Figure 3a, b**).

Next, we hypothesized that the transmembrane pathway for Ca^{2+} entry in the AIS during subthreshold stimuli could in particular be explained by the low-voltage gated Ca_V channels

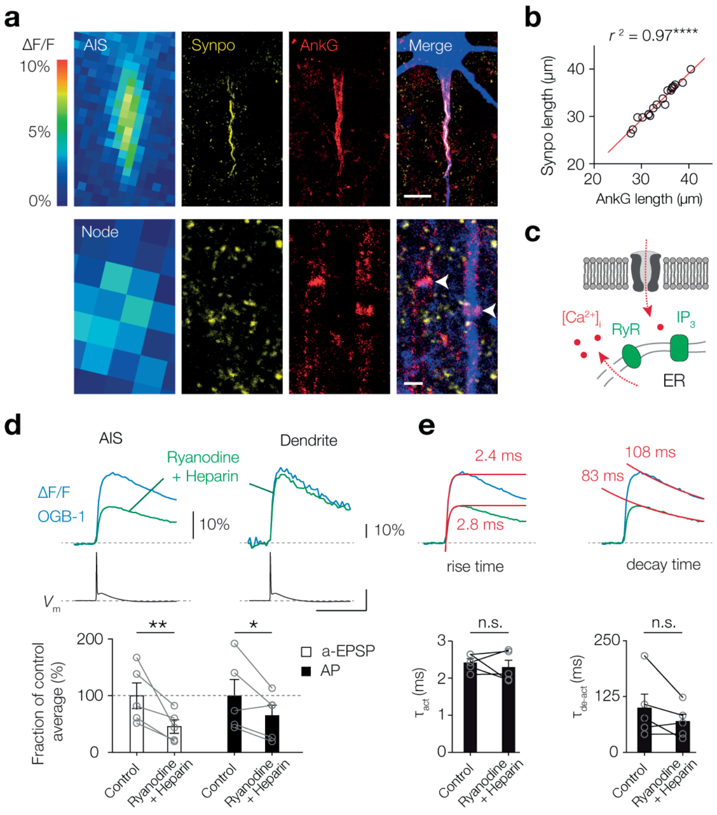

Figure 2. Giant saccular organelle amplifies activity-dependent $\Delta[Ca^{2+}]_i$ in the AIS

a. Example color-coded maximal ΔF/F profile (100 µM OGB-1) in response to a-EPSPs in the AIS (top) and Node (bottom) compared to z-projections for synaptopodin (Synpo, yellow), Ankyrin-G (AnkG, red) and biocytin/streptavidin (blue) of the same axon. White arrows indicate the locations of nodes, in the imaged axon (blue) and a neighboring one without Synpo. The many small synpo puncta are likely co-localized with subclasses of spines (Benedeczky et al., 1994; Bas Orth et al., 2007). Scale bars, 10 µm and 1 µm. **b**. The length of synaptopodin (Synpo) fluorescence linearly scales with Ankyrin G length. Red trace, linear regression fit with $y = 1.005x - 0.95$, $r^2 = 0.966$, ****$P < 0.0001$, $n = 19$. **c**. Schematic of Ca^{2+}-induced Ca^{2+} release by internal ER stores. **d**. Top, example ΔF/F (OGB-1) transients from AIS (left) and dendrite (right) in response to an AP (V_M, black) in control conditions (blue) and re-patched with blockers (green). Scale bars, 10% ΔF/F, 50 mV and 50 ms. Bottom, population data of the peak ΔF/F in the AIS in response to a-EPSP (white bars) and AP (black bars) before and after store release block, one-tailed ratio paired t-tests, **$P = 0.0060$, *$P = 0.021$, $n = 5$. Open circles and connecting lines represent paired recordings from individual cells and bars show the population mean ± s.e.m. **e**. Top, Ca^{2+} transients fitted with a single exponential function (red) to the rise (left) and decay time (right) in response to an AP, red number indicates the τ. Bottom, comparison of the rise and decay time (two-tailed paired t-tests, τ_{act}, $P = 0.52$, $\tau_{de\text{-}act}$, $P = 0.18$, $n = 5$). Open circles and connecting lines represent paired recordings from individual cells and bars show the population mean ± s.e.m. Data available in Figure 2–source data 1.

(T- and R-type). However, bath application of the T-type ($Ca_V3.1$-3) blockers TTA-P2 (1 µM, a highly selective blocker (Choe et al., 2011)) or nickel (Ni^{2+}, 100 µM) did not significantly reduce Ca^{2+} signals (one-tailed ratio paired *t*-tests; TTA-P2, $P = 0.17$, $n = 4$; Ni^{2+}, $P = 0.063$, $n = 5$; **Figure 3b, c**). We next blocked R-type Ca_V channels, by puffing SNX-482 (500 nM) locally to the AIS, but this did not lead to a reduction in subthreshold $[Ca^{2+}]_i$ rise either (SNX-482, $P = 0.11$, $n = 3$). Furthermore, consistent with their more depolarized voltage range of activation, the L-type channels did not affect subthreshold $\Delta[Ca^{2+}]_i$ (20 µM isradipine bath application, $P = 0.14$; 10 µM nimodipine bath application, $P = 0.41$, both $n = 4$; **Figure 3b**) and the block of N-type and P/Q-type channels, by local puff application of ω-conotoxin MVIIC (2 µM) to the AIS, also failed to reduce Ca^{2+} signals ($P = 0.42$, $n = 5$; **Figure 3b**). Furthermore, a combined block of T- and L-type channels did not affect the peak ΔF/F in the AIS (TTA-P2 and isradipine bath application, $P = 0.12$, $n = 3$; **Figure 3b**).

Although application of the T-type blockers TTA-P2 and Ni^{2+} was ineffective to block subthreshold $[Ca^{2+}]_i$ rise, in the same neurons it did reduce the peak ΔF/F evoked by a single AP by almost 20% (1 µM TTA-P2 bath application, 18.7%, $P = 0.021$, $n = 4$; 100 µM Ni^{2+} bath application, 19.7% block, $P = 0.013$, $n = 5$; **Figure 3b, c**). In addition, isradipine reduced the AP-evoked $\Delta[Ca^{2+}]_i$ in the AIS by 14.9% (20 µM isradipine bath appication, $P = 0.0070$, $n = 4$) and the alternative L-type blocker nimodipine showed a non-significant blocking trend (10 µM nimodipine bath application, $P = 0.060$, $n = 4$; **Figure 3b**). A combined application of T- and L-type channel blockers (1 µM TTA-P2 and 20 µM isradipine bath application) caused a 27.2% reduction of peak ΔF/F, showing a sublinear summation of two blocking agents (TTA-P2 and isradipine, $P = 0.0071$, $n = 5$; **Figure 3b**). In contrast, the R-type Ca_V channel blocker SNX-482 (500 nM puff application) did not reduce the AP-evoked $\Delta[Ca^{2+}]_i$ (SNX-482, $P = 0.29$, $n = 3$; **Figure 3b**). Local application of the N- and P/Q-type blocker ω-conotoxin MVIIC (2 µM puff application) showed a non-significant trend to block the peak ΔF/F (6.8%, ω-conotoxin MVIIC, $P = 0.064$, $n = 5$; **Figure 3b**). As a positive control experiment, we imaged a collateral bouton of the same neuron and used local puff application of ω-conotoxin MVIIC which almost completely abolished the peak ΔF/F by 91.5%, consistent with the presence of Ca_V channel subtypes in presynaptic terminals ($P = 0.021$, $n = 3$; **Figure 3b**). Finally, given the unexpected

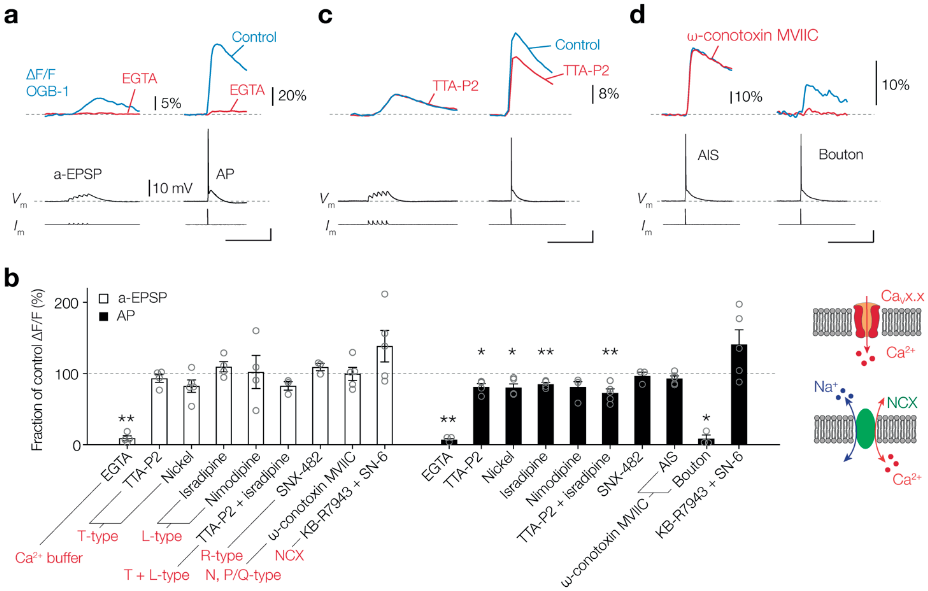

Figure 3. Ca_V channels play a partial role in activity-dependent Ca^{2+} entry at the AIS
a. Top, example traces of ΔF/F (100 μM OGB-1) in the AIS evoked by an a-EPSP (left) and AP (right), before (blue) and after (red) bath application of EGTA (2.5 mM). Bottom, somatic V_M and current-clamp protocols. Scale bars bottom right, 20 mV, 100 ms. **b**. Left, population data for the effect of an extracellular Ca^{2+} buffer, Ca_V channel blockers and NCX on the peak $\Delta[Ca^{2+}]_i$ signal in the AIS in response to an a-EPSP (open bars) and AP stimulation (closed bars). Data are shown as ratio to the pre-drug peak Ca^{2+} responses measured in the same neuron. One-tailed ratio paired t-tests, $^*P < 0.05$ and $^{**}P < 0.01$. Open circles represent individual cells and the bars show the mean ± s.e.m. Right, schematics of Ca^{2+} entry in the axoplasm via Ca_V channels (top) or NCX (bottom). **c**. Top, example traces of ΔF/F in the AIS evoked by an a-EPSP (left) and AP (right), before (blue) and after (red) bath application of TTA-P2 (1 μM). Bottom, somatic V_M and current-clamp protocols. Scale bar, 20 mV, 100 ms. **d**. Top, example traces of ΔF/F evoked by an AP in the AIS (left) and presynaptic bouton of the same neuron (right), before (blue) and after (red) puff application of ω-conotoxin MVIIC (2 μM). Bottom, somatic V_M and current-clamp protocols. Scale bar, 20 mV, 100 ms. Data available in Figure 3–source data 1.

remaining $[Ca^{2+}]_i$ transients in the AIS in the presence of Ca_V channel blockers, we hypothesized that NCX may contribute to activity-dependent $[Ca^{2+}]_i$ increase in the AIS. At the resting membrane potential NCX exports Ca^{2+} from the cytoplasm to maintain $[Ca^{2+}]_i$ near ~50 nM, however Na^+ entry may promote instantaneous Ca^{2+} influx by a reverse mode of operation (Yu and Choi, 1997; Stys and Lopachin, 1998) (**Figure 3b**). To examine its contribution, we pharmacologically blocked NCX by combined bath application of KB-R7943 (20 μM) and SN-6 (10 μM). The results showed, however, no change in the subthreshold nor AP-evoked $\Delta[Ca^{2+}]_i$ (two-tailed ratio paired t-tests, a-EPSP, $P = 0.16$; AP,

$P = 0.13$, $n = 5$, respectively; **Figure 3b**).

In summary, these data show that while transmembrane Ca^{2+} influx from the extracellular space is required for activity-evoked $\Delta[Ca^{2+}]_i$, none of the Ca_V channels played a role in the subthreshold depolarization, whereas T- and L-type Ca_V channels partially contributed to the AP-evoked influx.

Subthreshold- and AP-evoked Ca^{2+} *entry at the AIS requires TTX-sensitive channels*

What could be the source of the remaining component of Ca^{2+} influx at the AIS? Both in hippocampal neurons and heart muscle cells, Ca^{2+} currents have been described which are not blocked by Ni^{2+} nor by other known Ca_V channel antagonists, but instead are sensitive to the highly selective Na_V channel blocker tetrodotoxin (TTX), and therefore called $I_{Ca(TTX)}$ (Akaike and Takahashi, 1992; Aggarwal et al., 1997). In Na^+-free extracellular solution $I_{Ca(TTX)}$ resembles the Na^+ current and activates at potentials as negative as –70 mV while peaking at –30 mV (Akaike and Takahashi, 1992). To examine the presence of $I_{Ca(TTX)}$ in L5 axons we took advantage of the low-affinity indicator Oregon Green BAPTA 5N (OGB-5N, 1 mM; **Figure 4a**), which gives smaller fluorescent signals but is linear over a wider range of $[Ca^{2+}]_i$ compared to OGB-1 (K_d 20 μM vs. 170 nM, respectively). We used the voltage-clamp configuration and injected depolarizing ramps of 50 ms with increasing slopes (from 0.0 to 0.55 mV ms^{-1}) with a maximum peak at ~95% of the AP threshold (**Figure 4b**), thereby studying the same depolarization range and duration as the a-EPSPs used in **Figures 1–3**. The results showed that Ca^{2+} influx was strongly compartmentalized to the AIS and nodal axolemma (**Figure 4a**) consistent with the a-EPSP evoked OGB-1 transients (**Figure 1**). Remarkably, bath application of TTX almost completely abolished $[Ca^{2+}]_i$ elevations, even at depolarizations above the AP threshold (at –54.5 mV, 92.8% block, Cohen's *d*: 1.88, two-way ANOVA, $P < 0.0001$, $n = 4$; **Figure 4b, c**). As an alternative to TTX we used the quaternary amine Na_V channel inhibitor QX-314, which plugs the open state of the Na_V channel from the internal side. Similar to TTX, with 6 mM QX-314 added to the pipette solution voltage ramps did not evoke Ca^{2+} transients (at –54.5 mV, 94.8% block, Cohen's *d*: 1.92, control vs. QX-314, $P < 0.0001$, $n = 4$, TTX vs. QX-314, $P = 0.97$, $n = 4$; **Figure 4c**). Although QX-314 at this concentration has been reported

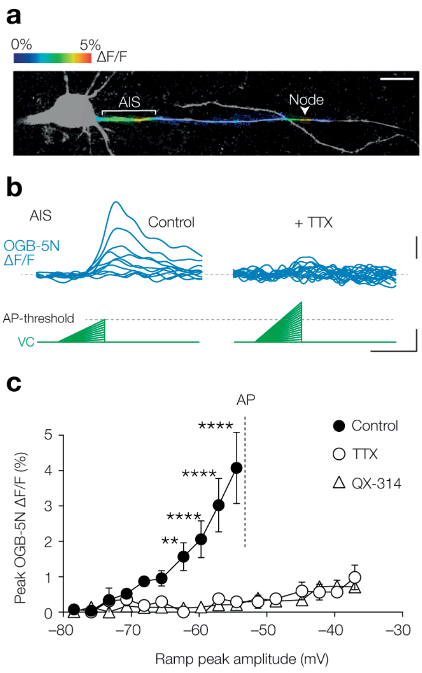

Figure 4. Subthreshold $[Ca^{2+}]_i$ changes are TTX sensitive

a. Example image of color-coded maximal ΔF/F (1 mM OGB-5N) along the proximal axon in response to a voltage ramp from –78.5 mV to maximally –54.5 mV. Acquisition rate was 125 Hz. The color-coded image is overlaid with a maximal z-projection of a confocal scan of biocytin/streptavidin staining (grey) of the same axon. Note the compartmentalized Ca^{2+} influx at the AIS and node (indicated by a white arrow). Scale bar, 20 µm. **b**. Example traces of OGB-5N ΔF/F reveals increasing Ca^{2+} responses to voltage ramps with increasing incline in control (left) but not in TTX (1 µM, right). Traces filtered with one-pass binomial (three point). Scale bars, 1% ΔF/F, 10 mV and 50 ms. **c**. Population data for maximal OGB-5N ΔF/F versus voltage ramp peaks in control (closed circles, n = 4), in TTX (open circles, n = 4) or QX-314 (open triangles, 6 mM, n = 4). Two-way ANOVA with Tukey's multiple comparisons test, $^{**}P < 0.01$, $^{****}P < 0.0001$. AP threshold is indicated with a gray line. Data are shown as mean ± s.e.m. Data available in Figure 4–source data 1.

to also block voltage-gated Ca^{2+} currents (Talbot and Sayer, 1996), subthreshold-evoked $[Ca^{2+}]_i$ was not mediated by Cav channels (**Figure 3b**). The near complete block by two distinct Nav channel blockers therefore indicates an important role of Nav channels in mediating subthreshold axonal Ca^{2+} influx.

We next investigated whether Nav channels also contribute to AP-evoked $\Delta[Ca^{2+}]_i$ (**Figure 5a**). To be able to distinguish between a putative role of Nav channels to pass Ca^{2+} ions and their role in generating the depolarization of ~100 mV we first imaged Ca^{2+} at the AIS in current-clamp, subsequently applied 1 µM TTX and imaged Ca^{2+} transients evoked by the recorded AP waveform injected as a voltage command ('AP-clamp'). The results showed a near complete abolishment of $\Delta[Ca^{2+}]_i$ in the presence of TTX (one-way ANOVA with Tukey's multiple comparisons test, CC vs. VC, 89.5% reduction, $P < 0.0001$, $n = 7$; **Figure 5a, b**). However, this $[Ca^{2+}]_i$ peak amplitude reduction could also be due to an incomplete voltage- and space-clamp of the AIS for fast voltage transients. The small diameter of the axon has a high axial resistance, acting as a low-pass filter for the antidromic AIS action potentials (Hamada et al., 2016) which also may attenuate the orthodromic voltage spread into the axon. To examine the possibility that axonal APs are attenuated in the somatic AP clamp configuration, we optically recorded JPW3028, a fast fluorescent voltage indicator that remains stable over long recording periods and is highly linear over a large voltage range (~250 mV, **Figure 5–figure supplement 1**). Consistent with the voltage loss, when we injected the AP-clamp in the soma in the presence of TTX and optically recorded V_m in the AIS, we observed a significant ~2-fold reduction in the AP peak amplitude (one-way ANOVA with Tukey's multiple comparisons test, VC vs. CC, $P = 0.014$; **Figure 5a, c**). To restore peak depolarization in the presence of TTX and reliably compare the Ca^{2+} transients

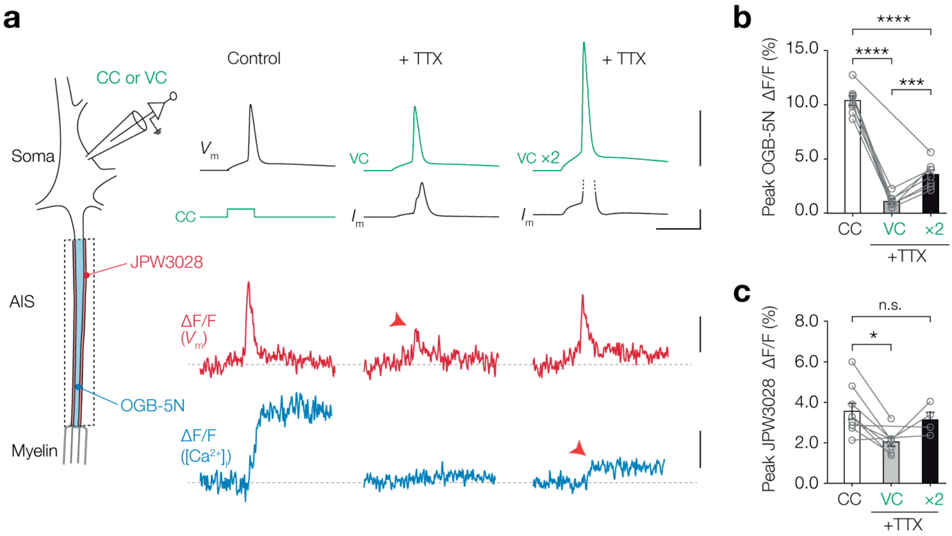

Figure 5. AP-evoked $[Ca^{2+}]_i$ changes are TTX sensitive

a. Left, schematic of the experimental setup; electrophysiological recording from the soma and fluorescence recording from AIS. Right, example traces from electrophysiology (recorded traces in black, applied commands in green), ΔF/F JPW3028 (red) for voltage imaging and ΔF/F OGB-5N (blue) for Ca^{2+} imaging. Left panel shows example traces from a current clamp recording, middle panel was performed in AP-clamp in the presence of TTX (1 μM) and right panel was performed in AP-clamp scaled two-fold (VC×2) in the presence of TTX. The JPW3028 and OGB-5N experiments were performed separately. Scale bars from top to bottom, 100 mV, 5 nA, 5 ms, 2% ΔF/F and 5% ΔF/F. **b**. Peak OGB-5N ΔF/F in response to an AP (n = 8), AP clamp + TTX (VC, n = 7) and double AP clamp + TTX (VC×2, n = 8). One-way ANOVA with Tukey's multiple comparisons test, ***P = 0.0005, ****P < 0.0001, n = 8. Circles and connecting lines represent paired recordings in individual cells and bars show the population mean ± s.e.m. **c**. Peak JPW3028 ΔF/F in response to an AP (n = 9), AP clamp + TTX (VC, n = 7) and double AP clamp + TTX (VC×2, n = 4). One-way ANOVA with Tukey's multiple comparisons test, *P = 0.014. Circles and connecting lines represent paired recordings in individual cells and bars show the population mean ± s.e.m. Data available in Figure 5–source data 1. See also Figure 5–figure supplement 1.

evoked by equal depolarization, we doubled the amplitude of the somatic AP-clamp (VC ×2). With this protocol both the peak depolarization and AP half-width in the AIS were indistinguishable from the control APs (peak JPW, VC ×2 vs. CC, one-way ANOVA with Tukey's multiple comparisons test, $P = 0.75$, $n = 4$, **Figure 5c,** half-width in JPW, VC ×2 vs. CC, one-way ANOVA with Tukey's multiple comparisons test, $P = 0.36$, $n = 4$, not shown) and TTX blocked 65.5% of the AP-evoked $\Delta[Ca^{2+}]_i$ (peak OGB-5N, Cohen's *d*: 5.49, VC ×2 vs. CC, $P < 0.0001$, $n = 8$; **Figure 5b**). Taken together, these data suggest that a large fraction of both subthreshold-depolarization and AP-evoked Ca^{2+} influx enters the cytoplasm through TTX-sensitive channels at the AIS.

Axonal $[Ca^{2+}]_i$ follows gating kinetics of Na_V channels

Whether $I_{Ca(TTX)}$ is carried by a specific TTX-sensitive Ca_V channel or reflects Ca^{2+} permeating directly through the Na_V channel remains debated (Santana et al., 1998; Cruz et al., 1999; Heubach et al., 2000; Chen-Izu et al., 2001; Guatimosim et al., 2001). We hypothesized that if Ca^{2+} ions enter the AIS cytoplasm by flowing through Na_V channels, $I_{Ca(TTX)}$ should reflect the biophysical properties of I_{Na} including activation kinetics. To measure submillisecond rapid events with fluorescence in the small axon (diameter ~1.5 µm), we optimized multiple imaging parameters enabling us to acquire AIS fluorescence at 20 kHz (see **Materials and Methods**). Using a Na^+-sensitive indicator (sodium-binding benzofuran isophthalate, SBFI, 1 mM) in combination with OGB-5N (1 mM) showed that the two indicators were indistinguishable in their rising phase during an AP, suggesting that Ca^{2+} entry at the AIS may be as rapid as Na^+ entry (**Figure 6–figure supplement 1**).

In order to quantify the kinetics of I_{Na} and I_{Ca} more directly, we next used a voltage-clamp approach. Near ~20 ºC and –40 mV, Na_V channels open at least one order of magnitude faster compared to the T-type Ca_V channels (~200 µs (Schmidt-Hieber & Bischofberger, 2010) vs. ~5 ms (Perez-Reyes et al., 1998), respectively) which may be sufficiently different to compare against the kinetics of optically recorded $[Ca^{2+}]_i$ at the AIS. To determine the specific activation kinetics of I_{Na} and T-type I_{Ca} (I_{CaT}) in L5 pyramidal neurons we measured total inward current ($I_{Na} + I_{Ca}$,) by depolarizing the soma with a step depolarization to –35 mV and subsequently pharmacologically isolated Na^+ and Ca^{2+} current components by bath application of 1 µM TTX or 100 µM Ni^{2+}, respectively (**Figure**

6a). The activation time constant of the total inward current was identical to I_{Na} (single exponential fit $\tau_{total} = 438.2$ µs vs. $\tau_{Na} = 440.3$ µs, one-way ANOVA with Tukey's multiple comparison test, $P > 0.999$, $n = 6$), whereas the total current was substantially faster in

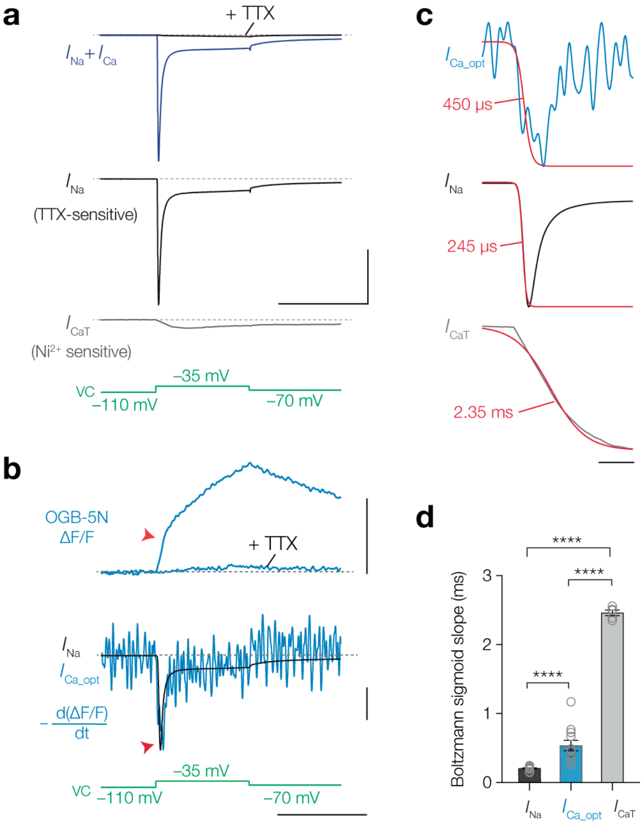

Figure 6. Temporal derivative of AIS $[Ca^{2+}]_i$ mirrors the opening kinetics of Na_V channels
a. Top to bottom, total inward current in response to a voltage-clamp step to –35 mV (blue) and after application of 1 µM TTX (black), I_{Na}; the difference between the total current and the TTX-sensitive current, I_{CaT}, obtained after application of 100 µM Ni^{2+}, voltage clamp protocol (green). Scale bars, 10 nA and 50 ms. **b**. Top to bottom: ΔF/F OGB-5N of an AIS imaged at 20 kHz before and after application of 1 µM TTX, the electrically recorded somatic I_{Na} of the same neuron overlaid with the first temporal derivative of ΔF/F (–d(ΔF/F)/dt) representing I_{Ca_opt}, voltage clamp protocol. Optically and electrically recorded traces filtered with a 3-point binomial filter for 100 iterations. Red arrows indicate the rapid component visible in the ΔF/F and in the overlaid I_{Na} and I_{Ca_opt}. Scale bars, 20% ΔF/F, $10\%^{-1}$ / 6.3 nA and 50 ms. **c**. Top to bottom: I_{Ca_opt}, I_{Na} and I_{CaT} fit with a Boltzmann sigmoid function (red). Slope values are indicated. Scale bar, 5 ms. **d**. Population data for the slope values for I_{Na} (n = 17), I_{Ca_opt} (n = 10) and I_{CaT} (n = 5). One-way ANOVA with Tukey's multiple comparisons test, ****$P < 0.0001$. Open circles represent individual cells, bars indicate the population mean ± s.e.m. Data available in Figure 6–source data 1. See also Figure 6–figure supplement 1.

comparison to I_{CaT} (τ_{total} = 438.2 µs vs. τ_{CaT} = 4.8 ms, $P < 0.0001$, $n = 5$; **Figure 6a**). The initial fraction of the inward current was thus primarily generated by I_{Na}. The large difference in gating could provide a temporal window to distinguish Ca^{2+} entry via Na_V channels or T-type Ca_V channels. Theoretical and experimental work show that low-affinity Ca^{2+} indicators, like OGB-5N, are capable of tracking rapidly activating Ca^{2+} currents when imaged at high speed, the first time derivative of ΔF/F ($d_{\Delta F/F\ dt^{-1}}$) overlaps with electrically recorded I_{Ca}, providing a mean to optically resolve the time course of I_{Ca} (Sabatini and Regehr, 1998; Jaafari et al., 2014; Ait Ouares et al., 2016).

Imaging OGB-5N (1 mM) at 20 kHz in the AIS we observed that ΔF/F comprised of two separate time courses, a fast initial rise followed by a slower rising phase (**Figure 6b)**. Both $[Ca^{2+}]_i$ transients were almost completely abolished by TTX, leaving only a small transient reflecting putatively I_{CaT} ($n = 6$). We quantitatively compared the activation time constants of I_{Na}, I_{Ca_opt} ($d\Delta F/F\ dt^{-1}$) and I_{CaT} by resampling the electrically recorded I_{Na} and I_{CaT} to 20 kHz and filtering both electrical and optical traces identically (see **Materials and Methods**). Multiple hallmarks of I_{Na} matched with I_{Ca_opt}: both traces showed a rapid inward component, followed by inactivation and a persistent component (**Figure 6b, c**). In comparison, I_{CaT} lacked both the rapid activation and inactivation time constants (**Figure 6a, c**). Given the lower signal-to-noise ratio in the optical traces we fitted Boltzmann sigmoid functions to the rising phase to compare the slopes of the optical and electrically recorded currents (**Figure 6c**). The average slope of I_{Ca_opt} was significantly faster compared to the activation of I_{CaT} (~500 µs vs. ~2.5 ms, respectively, one-way ANOVA with Tukey's multiple comparison test, $P < 0.0001$) and slower compared to I_{Na} (~500 µs vs. ~ 200 µs, I_{Ca_opt} vs. I_{Na} $P < 0.0001$; **Figure 6c, d**). The small difference between I_{Na} and I_{Ca_opt} may be explained by the equilibration time of OGB-5N (~200 µs) (Ait Ouares et al., 2016), local differences between Na_V channels in the soma and AIS or the presence of Ca^{2+}-store release in the AIS. Together, the findings indicate that the current mediating $[Ca^{2+}]_i$ at the AIS resembles Na_V channel kinetics.

Calcium influx through $Na_V1.2$ channels

The results suggest that Ca^{2+} ions could enter the cytoplasm by permeation through the Na_V channel pore. Previous studies showed Ca^{2+} influx through the cardiac $Na_V1.5$ channel (Cruz et al., 1999; Guatimosim et al., 2001). To examine whether Na_V isoforms of the axon initial segment also enable Ca^{2+} influx we performed experiments in HEK-293 cells which were transfected with the human gene *SCN2A* encoding $Na_V1.2$ channel ($Na_V1.2$) with auxiliary β1 and β2 subunits and EGFP tag (**Methods**; **Figure 7a**). Whole-cell recording revealed Na^+ currents in $EGFP^+$ cells but not in non-transfected cells (average peak current density –115.7 ± 28.4 pA/pF, $n = 10$ vs. –3.7 ± 1.9 pA/pF at –20 mV, $n = 5$, respectively; **Figure 7b**). The inward currents were completely abolished by 1 µM TTX (96.1 ± 1.3%, $n = 7$, one-tailed Wilcoxon matched-pairs signed rank test, $P = 0.0078$, **Figure 7c**) and the voltage-dependence of activation and inactivation revealed midpoints at –25.4 ± 2.1 mV and –74.1 ± 3.9 mV, respectively ($n = 10$, **Figure 7d**, **e**), consistent with previous work (Ben-Shalom et al., 2017), indicating a highly selective expression of $Na_V1.2$ channels. Next, we filled the transfected cells with 100 µM OGB-1 and imaged the fluorescence changes in response to a train of depolarizing pulses (200 Hz for 1 s, –120 to –30 mV steps; **Figure 7f**). We observed an increase in ΔF/F in every HEK-293 cell, indicating an influx of Ca^{2+} (average peak 0.46 ± 0.18% ΔF/F, range: 0.06–1.4% ΔF/F, $n = 7$; **Figure 7f–h**). To test whether the $[Ca^{2+}]_i$ increase required Na_V channel opening we bath applied TTX (1 µM), revealing a significant decrease in the peak ΔF/F (92.1 ± 3.8% reduction, one-tailed Mann Whitney test, $P = 0.012$, $n = 4$; **Figure 7h**). The results indicate that molecular expression and opening of $Na_V1.2$ channels suffices to cause transmembrane Ca^{2+} influx.

Estimating Ca^{2+} conductivity of Na_V channels with computational modeling

Our findings are in agreement with the depolarization-induced Ca^{2+} entry in the squid axon which is tetrodotoxin (TTX)-sensitive and reflected a 1% conductivity of Na_V channels for Ca^{2+} ions (Baker et al., 1971). To estimate the conductivity ratios (g_{Ca}/g_{Na}) in L5 axons we performed computational simulations. Ca^{2+} entry through Na_V channels was implemented by adding an ohmic Ca^{2+} ion mechanism into a mathematical 8-state Na_V channel model that calculated the current carried by Ca^{2+} ($I_{Ca(Na)}$) and Na^+ (I_{Na}) (see **Materials and Methods**). A single compartment containing I_{Na} and $I_{Ca(Na)}$ together with high voltage-gated and T type-gated Ca_V channel models (I_{CaH} and I_{CaT}, respectively) showed that with an

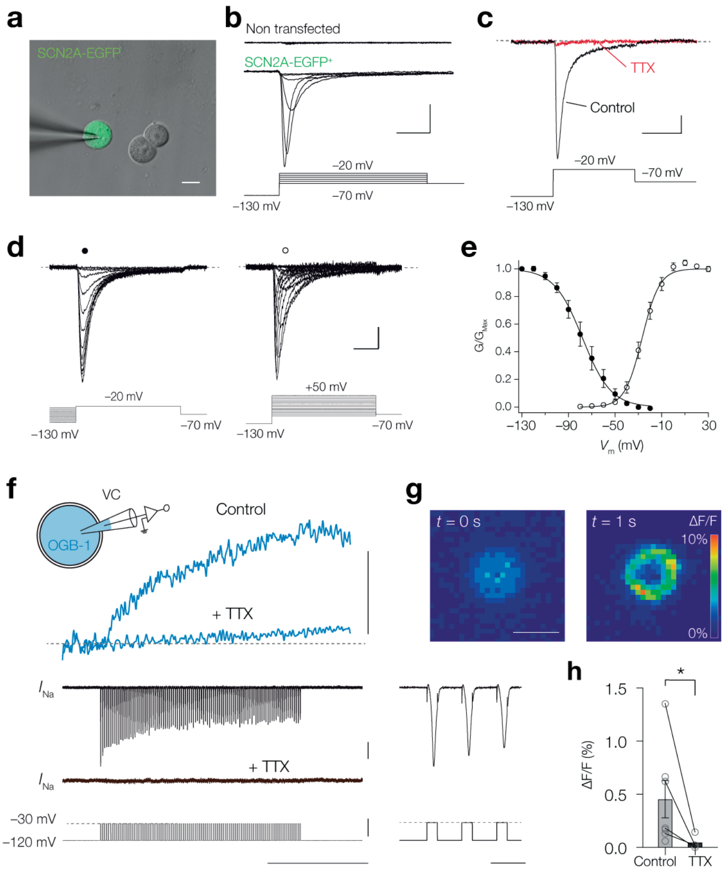

Figure 7. Na$_V$1.2 channels mediate a Ca^{2+} influx

a. Combined brightfield and fluorescence image of a whole-cell recording from a SCN2A-EGFP$^+$ HEK-293 cell (green). Scalebar, 10 µm. **b**. Example traces of I_{Na} recorded in response to depolarizing voltage command potentials (bottom) for a non-transfected (top) and SCN2A-EGFP$^+$ cell (middle), scale bars indicate 0.5 nA and 5 ms. **c**. Peak I_{Na} traces before (black) and after TTX application (red) in response to a depolarizing voltage step (bottom), scale bars indicate 100 pA and 10 ms. **d**. Example current traces of steady-state inactivation (left) and activation protocols (right), scale bars indicated 100 pA and 5 ms. **e**. Population data for steady-state activation and inactivation curves, circles and error bars indicate mean ± s.e.m. Lines represent Boltzmann fits to the mean data. **f**. Schematic of the experiment: a SCN2A-EGFP$^+$ HEK-293 cell was recorded in voltage-clamp and filled with OGB-1 (0.1 mM) after which a train of depolarizing pulses (–120 to –30 mV, 200 Hz, 1 second) was applied, top to bottom, ΔF/F before and after bath application of 1 µM TTX (blue), the recorded currents and voltage command potentials, right, magnification of the first three action currents, scale bars from top to bottom represent 1% ΔF/F, 0.5 nA, 100 mV, 500 ms and 10 ms. **g**. Color-coded average ΔF/F of 100 frames before onset (left) and at the end (right) of the voltage command, scale bar indicates 10 µm. **h**. OGB-1 ΔF/F is significantly higher in control (n = 7) than after application of TTX (n = 4), one-tailed Mann Whitney test, P = 0.0121. Data available in Figure 7–source data 1.

axonal AP waveform $I_{Ca(Na)}$ is activated during the first microseconds of AP onset, rapidly inactivates and is temporally separated from I_{CaH} and I_{CaT} (**Figure 8–figure supplement 1**). Next, to estimate the g_{Ca}/g_{Na} we used a published multicompartmental model of the L5 pyramidal neuron (**Figure 8a**, including detailed reconstructions of the AIS and nodal domains (see **Figure 2a** within (Hamada et al., 2016)). Based on multiple experimentally recorded parameters we constrained the model AP and found that a peak conductance density of Na_V channels of 16,000 and 850 pS μm^{-2} in the AIS and soma, respectively, reproduced the recorded AP and matched with AP-evoked $\Delta[Na^+]_i$ imaged in the AIS (see **Materials and Methods** and **Figure 8a**). Subsequently, $[Ca^{2+}]_i$ was simulated based on mathematical equations representing Ca^{2+} diffusion and extrusion, endogenous stationary Ca^{2+} buffers (taken together as κ_s) and was supplemented with the buffering capacities of the specific Ca^{2+} indicators (Fink et al., 2000) (see **Materials and Methods**). The Ca^{2+} extrusion threshold and rates were adjusted to approximate the experimentally imaged peak and decay time course of measured OGB-5N ΔF/F in the AIS (**Figure 8–figure supplement 2)**. To determine the absolute rise in $[Ca^{2+}]_i$ produced exclusively by Na_V channels, we performed additional experiments in which we imaged $[Ca^{2+}]_i$ while blocking Ca_V channels that contributed to AP-evoked $\Delta[Ca^{2+}]_i$: T- and L-type calcium channels (bath application of 1 µM TTA-P2 and 20 µM isradipine, respectively, see **Figure 3b**). Using calibrated ratiometric bis-Fura-2 (200 µM) imaging, we found that during 1 AP, Ca^{2+} entry though Na_V channels induces a peak $\Delta[Ca^{2+}]_i$ of 55.6 nM ($n = 4$; **Figure 8b**, **Figure 8–figure supplement 2**). Since ~35% of AP-evoked $\Delta[Ca^{2+}]_i$ is caused by internal store amplification (**Figure 2d**) ~36 nM is mediated by transmembrane Ca^{2+} entry via Na_V channels (**Figure 8b**). We subsequently simulated these experiments in the multicompartmental model by removing Ca_V channels and including the buffering properties of 200 µM bis-Fura-2. Varying endogenous buffering (κ_s) between 1 and 100 we updated g_{Ca}/g_{Na} to obtain a 36 nM rise of free $[Ca^{2+}]_i$ at the AIS. A κ_s of ~100 corresponds to dendritic buffering capacities (Cornelisse et al., 2007), while axonal buffering capacities are reported to be lower (10 – 40, (Klingauf and Neher, 1997; Jackson and Redman, 2003; Delvendahl et al., 2015)). When changing κ_s between 10 – 40 the g_{Ca}/g_{Na} ratio was 0.38% (κ_s =10: 0.37%, κ_s = 40: 0.39%; **Figure 8c**).

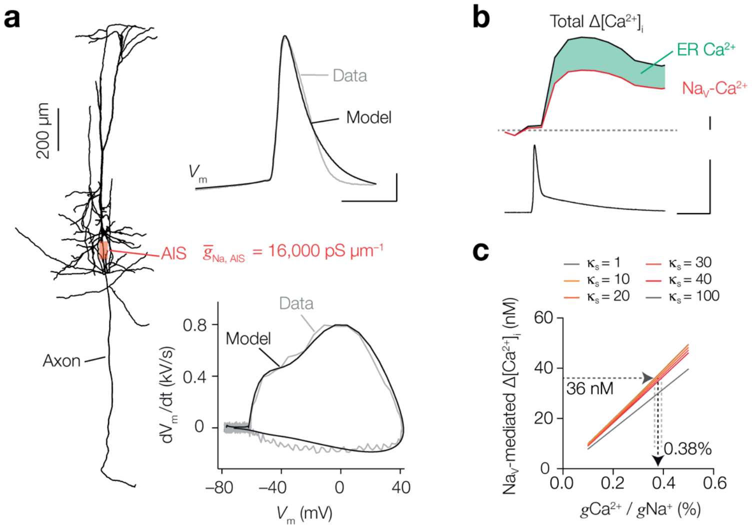

Figure 8. Computational simulation of Ca^{2+} conductivity by Na_V channels predicts a conductivity ratio of 0.38%

a. Left, morphology of the conductance-based multi-compartmental model. Right, Na_V channel density in the AIS was estimated by optimizing to $\Delta[Na^+]_i$, V_M (top) and phase-plane plot (bottom) in simulation (black) to the experimental data (gray). Scale bars, 200 µm, 20 mV and 0.5 ms. **b**. Example trace of calibrated ratiometric imaging of bis-Fura2 to measure absolute changes in $\Delta[Ca^{2+}]_i$ in response to a single AP (bottom), the experiment was performed in the presence of T- and L-type Ca_V blockers, so $\Delta[Ca^{2+}]_i$ is mediated by Na_V channels (red) and amplified by internal store release (35%, green), scale bars indicate 10 nM, 100 mV and 10 ms. **c**. Dependence of Na_V-mediated peak AP $\Delta[Ca^{2+}]_i$ on conductance ratio (gCa/gNa) for varying endogenous buffer capacities (κ_s = 1–100). $\Delta[Ca^{2+}]_i$ was measured and modeled in a cell with 200 µM bis-Fura2 present and T- and L-type Ca_V channels blocked. See also Figure 8–figure supplement 1 and figure supplement 2.

Spatiotemporal distribution of Ca^{2+} entry routes under physiological conditions

Using the 0.38% conductivity ratio we next evaluated how Ca^{2+} currents through Nav and Cav channels spatiotemporally varied across the neuronal compartments without the buffering capacities of externally applied Ca^{2+} dyes (**Figure 9a, b** and **Figure 8–figure supplement 2**). The simulations showed that the AP-evoked $\Delta[Ca^{2+}]_i$ reached a peak concentration of ~800 nM in the AIS (**Figure 9a, b**). Due to the high density of Nav channels in the AIS they contribute to the majority of $\Delta[Ca^{2+}]_i$ and cause a rise of $[Ca^{2+}]_i$ within submillisecond from the start of the AP (450 nM < 150 µs from AP threshold, red arrow in **Figure 9b**). These results are likely to provide an underestimate of the total $\Delta[Ca^{2+}]_i$ since in the model Ca^{2+} release from giant saccular organelle was not simulated, which would result in a total AP-evoked $\Delta[Ca^{2+}]_i$ of ~1.2 µM. In the basal dendritic branches the AP has a slower rise time and broader half-width, causing dendritic [Ca^{2+}]$_i$ to accumulate slower and to higher concentrations, consistent with our experimental findings (**Figure 1**). Because the dendritic Na$_V$ channel density is substantially lower, their contribution to the total [Ca^{2+}]$_i$ is negligible. The distinct contribution of Na$_V$ and Ca$_V$ channels to [Ca^{2+}]$_i$ is clearly visible when comparing the different Ca^{2+} currents in the AIS, showing that the majority of the total I_{Ca} during an AP is carried by $I_{Ca(Na)}$ (**Figure 9c**). Simulations predict that the $I_{Ca(Na)}$ rapidly inactivates during the AP while I_{Ca} activates more slowly and has an incomplete inactivation during the AP repolarization, likely becoming the dominant contribution to [Ca^{2+}]$_i$ during the afterdepolarization and high-frequency spike generation (**Figure 9c** and **Figure 8–figure supplement 1**).

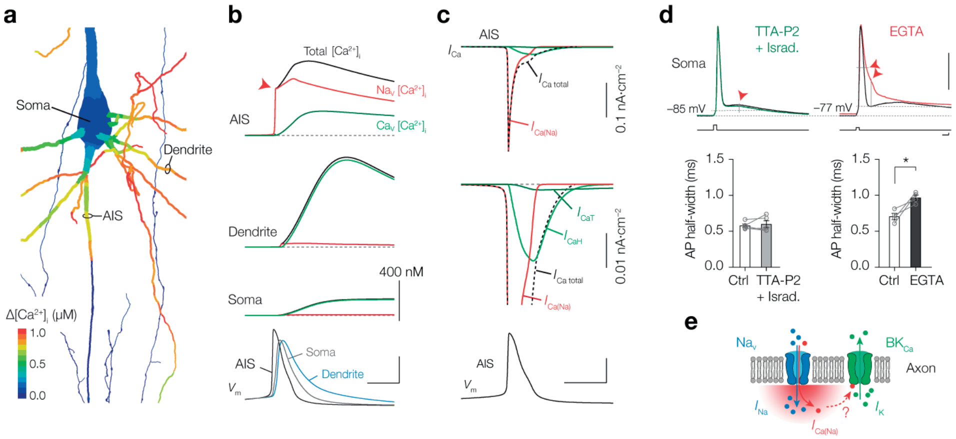

Figure 9. Na$_V$ channels produce submillisecond near-micromolar [Ca^{2+}]$_i$ at the AIS
a. Color coded shape plot of simulated [Ca^{2+}]$_i$ in the axon, dendrites and soma activated by an AP in current clamp without Ca^{2+} indicator. **b**. The modeled [Ca^{2+}]$_i$ in the AIS, Soma and Dendrite (locations specified in **a**). The total [Ca^{2+}]$_i$ (black) is divided in a Na$_V$ channel mediated (red) and Ca^{2+}-channel (Ca$_V$) mediated (green) fraction. Bottom, V_M in the same compartments. Scale bars, 400 nM for all [Ca^{2+}]$_i$ plots, 50 mV and 1 ms. **c**. Top, I_{Ca} in response to an AP (bottom) in the AIS. Middle, I_{Ca} on expanded scale. Ca^{2+} extrusion contributes to I_{Ca} total, but is not shown. Scale bars bottom, 50 mV and 1 ms. **d**. Top, example traces of somatic APs in control (black) and after bath application of TTA-P2 and Isradipine (green, left) and EGTA (red, right). Resting membrane potential and AP voltage threshold are indicated by the dotted grey lines. Red arrows indicate the significant changes in ADP (with TTA-P2 + Isradipine) and AP width and AHP (with EGTA). Capacitance transients are removed for clarity. Scale bars indicate 50 mV, 2.5 nA, 1 ms. Bottom, population data of AP half-width before and after blocking T– and L–type Ca$_V$ channels (left, P = 0.61, two-tailed paired t-test, n = 5) and before and after preventing Ca^{2+} influx by bath application of EGTA (right, *P = 0.035, two-tailed paired t-test, n = 4), see also Table 1. **e**. Schematic of Ca^{2+} permeation through a Na$_V$ channel activating a Ca^{2+}–dependent BK channel.

Our experiments and computational simulations show that $[Ca^{2+}]_i$ changes mediated by Ca_V or Na_V channels act at distinct spatiotemporal scales. To experimentally test the differential impact of Ca^{2+} influx on the AP waveform, we analyzed the somatically recorded APs when using distinct blockers most effective in modulating $[Ca^{2+}]_i$ in the AIS (**Figure 3**). Blocking both T- and L-type Ca_V channels, contributing to ~27% to AP-evoked Ca^{2+} at the AIS (**Figure 3**), significantly reduced the afterdepolarization and showed a trend to reduce the afterhyperpolarization (ADP, $P = 0.039$ and AHP, $P = 0.055$, respectively, two-tailed paired t-tests, $n = 5$), without affecting other AP properties ($P > 0.30$; **Figure 9d** and **Table 1**). In contrast, when lowering $[Ca^{2+}]_o$ with EGTA, which abolished all AIS Ca^{2+} influx (**Figure 3**), the AP half-width significantly increased and the AHP was strongly abolished (AP half-width, $P = 0.035$ and AHP, $P = 0.043$, two-tailed paired t-tests, $n = 4$; **Figure 9d**, **Table 1**). These results are consistent with the temporal differences in AP-evoked AIS $[Ca^{2+}]_i$ and suggest that Na_V-mediated Ca^{2+} entry may act to open BK_{Ca} channels (**Figure 9e**), thereby driving K^+ efflux and facilitating axonal AP repolarization.

Discussion

In the present study we identified Ca^{2+} permeation through Na_V channels as a source for activity-dependent Ca^{2+} entry in mammalian axons. The findings were supported by independent and converging lines of evidence, ranging from anatomical compartmentalized $[Ca^{2+}]_i$ transients at sites with high Na_V channel densities, a pharmacological block by TTX, an overlap of optically recorded I_{Ca} with Na_V channel gating and molecular evidence for Ca^{2+} influx mediated by the $Na_V1.2$ channel. In axonal domains Na_V channels are thus not only involved in electrically generating the upstroke of the action potential, but also contribute to cytoplasmic Ca^{2+} signaling.

Ca^{2+} entry in the L5 pyramidal neuron AIS was in part mediated by T- and L-type Ca_V channels (**Figure 3** and **Figure 5**) in keeping with previous studies showing that Ca_V channel subtypes mediate activity-dependent Ca^{2+} changes in both central- and peripheral nervous system axons (Callewaert et al., 1996; Bender and Trussell, 2009; Yu et al., 2010; Gründemann and Clark, 2015; Zhang and David, 2016; Clarkson et al., 2017). However, when quantifying the specific fraction of block Ca_V channels explained only ~35% of the total Ca^{2+} entry during a single AP (**Figure 3**). These results are consistent with recent 2-

photon Ca^{2+} imaging from the prefrontal cortical pyramidal neuron AIS, showing that ~70% of the $[Ca^{2+}]_i$ transients evoked by a train of three APs remains in the presence of T-type Ca_V channel block (Clarkson et al., 2017). Here, we found that for APs the remaining ~65% of $[Ca^{2+}]_i$ increase is actually TTX-sensitive and this accounted even for >90% of the subthreshold-induced $[Ca^{2+}]_i$ changes (**Figure 4** and **Figure 5**). That Ca^{2+} enters through Na_V channels builds on landmark studies showing that the initial component of depolarization-induced Ca^{2+} entry in the squid giant axon is tetrodotoxin (TTX)-sensitive (Baker et al., 1971; Meves and Vogel, 1973; Brown et al., 1975). Squid axons even generate rapid spikes in the sole presence of Ca^{2+} ions (Watanabe et al., 1967). A TTX-sensitive Ca^{2+} current has also been identified in hippocampal neurons (Akaike and Takahashi, 1992) and more extensively investigated in cardiac myocytes (Aggarwal et al., 1997; Santana et al., 1998; Cruz et al., 1999; Heubach et al., 2000; Chen-Izu et al., 2001). The incomplete selectivity of toxins and blockers for Ca^{2+} channels continued, however, to cast doubt about the precise identity of the TTX-sensitive Ca^{2+} current (Cruz et al., 1999; Chen-Izu et al., 2001; Sun et al., 2008). Indeed, an alternative explanation for some of the present results is that TTX blocks a Ca_V channel subtype. This has been reported at very high concentrations (30 μM) for $Ca_V3.3$ (Sun et al., 2008), which is higher than what we used (1 μM). Although we cannot exclude the presence of a TTX-sensitive Ca_V channel at the AIS that is not blocked by one of the compounds used in the pharmacological screening (**Figure 3**), our optically recorded I_{Ca} provides biophysical evidence that the TTX-sensitive Ca^{2+} current follows the same rapid activation time course as the Na^+ channel pore, incompatible with T-type channel kinetics (**Figure 6**). Importantly, in further support that Na_V channels give rise to cytoplasmic Ca^{2+} changes, heterologous expression of α- and β-subunits of $Na_V1.2$, known to be expressed in the rodent and human AIS (Garrido et al., 2003; Hu et al., 2009; Tian et al., 2014), showed that the channel proteins expressed in isolation were sufficient to mediate Ca^{2+} influx (**Figure 7**). These results are in support of the findings by Lederer and colleagues showing that heterologous expression of $hNa_V1.5$ channel produces depolarization-evoked $[Ca^{2+}]_i$, if expressed with its β subunits (Cruz et al., 1999; Guatimosim et al., 2001).

From an evolutionary point of view, some Ca^{2+} permeation of Na_V channels is not surprising. Na_V channels evolved from the Ca_V channel superfamily and share molecular structure both in their pore sequence and intracellular regulatory domains (Zakon, 2012; Ben-Johny et al., 2014). Furthermore, the Born radii for Na^+ and Ca^{2+} are comparable (1.68 and 1.73 Å, respectively) and Ca^{2+} ions are known to enter the Na_V channel pore to block Na^+ permeation in a concentration-dependent manner (Lewis, 1979; Armstrong and Cota, 1999). Interestingly, single residue mutations in the selectivity filter of Na_V channels suffices to increase Ca^{2+} ion permeation (Heinemann et al., 1992; Naylor et al., 2016). Our calculations indicate that the conductivity of the Na_V channel for Ca^{2+} is ~0.4% (**Figure 7**). If we assume there exists proportionality between permeability and conduction we can apply the equation of permeability ~conductance/concentration × valency^2 (Baker et al., 1971; Meves and Vogel, 1973). With our extracellular solutions $[Ca^{2+}]_o/[Na^+]_o$ being 0.0148 and the valence ratio $(Ca^{2+}/Na^+)^2$ being 4 we can calculate that Na_V channels in mammalian axons have a P_{Ca}/P_{Na} ratio of 0.06. Notably, the value is in range of direct recordings for P_{Ca}/P_{Na} in the sciatic nerve and squid axons (0.10 and 0.14 (Hille, 1972; Meves and Vogel, 1973)) as well as recordings from $Na_V1.5$ channels revealing P_{Ca}/P_{Na} ratios of ~0.04 (Cruz et al., 1999). Such permeability is orders of magnitude lower than P_{Ca}/P_{Na} ratios of acetylcholine receptors or NMDA receptors (1.0 and 17, respectively) (Lewis, 1979; Iino et al., 1997). An independence of Na^+ and Ca^{2+} ions, modeled as ohmic conductances, will be a major simplification of the Na_V channel under multi-ion conditions. Molecular dynamic studies of Na_V channels showed that ionic interactions between Na^+ and Ca^{2+} at the channel pore are complex (Corry, 2013; Boiteux et al., 2014; Naylor et al., 2016). The energy barrier of the selectivity filter strongly favors Na^+ ions but can be flexible, changing in conformational states and consistent with modest Ca^{2+} permeation (Corry, 2013; Boiteux et al., 2014; Naylor et al., 2016). In future experiments it will be interesting to obtain more detailed permeability ratios (P_{Ca}/P_{Na}) by recording changes in E_{rev} with varying intra- and extracellular concentrations, fitting the data to mathematical solutions such as the electro-diffusion theory of Goldman-Hodgkin-Katz (GHK) extended with surface charge potentials (Lewis, 1979; Campbell et al., 1988), or using Eyring–Läuger theory based on individual ionic rate constants (Läuger, 1973). Such experiments would be in particular interesting to be performed for $Na_V1.6$, the main isoform expressed in axonal domains (Lorincz and Nusser, 2010; Kole and Stuart, 2012).

Although the Ca^{2+} conductivity of the channels is small it achieves near–micromolar Ca^{2+} changes in axons as Na_V channels are clustered to very high densities (~1,000 channels μm^{-2}) at the AIS and nodes of Ranvier (Neumcke and Stämpfli, 1982; Lorincz and Nusser, 2010; Kole and Stuart, 2012). Consistent with this idea, our imaging experiments showed that also nodes of Ranvier produced subthreshold-activated Ca^{2+} entry (**Figure 1** and **Figure 4**), suggesting that Na_V channel mediated Ca^{2+} entry could play similar roles in these domains. At the AIS, the rapid opening of high densities of Na_V channels along the membrane surface may further act as a trigger to amplify $[Ca^{2+}]_i$ via the activation of ryanodine receptors, mediating ER store release of Ca^{2+} from the giant saccular organelle, which extends continuously along the AIS of thick-tufted L5 pyramidal neurons (**Figure 2**).

The rapid inactivation of Na_V channels compared to the slow inactivation of Ca_V channels will lead to voltage- and time-dependent changes in the relative contribution of Na_V and Ca_V channels to $[Ca^{2+}]_i$. In axons, a single AP will mostly lead to Na_V-mediated Ca^{2+} entry while an increasing number of APs, or longer sustained depolarization, will lead to increased contribution from Ca_V channels. Indeed, Ca^{2+} entry via Ca_V channels has been identified as a major contributor to Ca^{2+} entry in sciatic nerve or Purkinje axons during trains of APs or prolonged depolarization for hundreds of milliseconds (Callewaert et al., 1996; Zhang and David, 2016). However, *in vivo* recordings from L5 pyramidal neurons show that they typically fire sparsely and on average ~1–4 Hz (De Kock et al., 2007) and the half-width of axonal APs is about ~300 µs (Kole et al., 2007). In this view, Na_V-mediated Ca^{2+} entry may be the main source for activity-dependent $[Ca^{2+}]_i$ in the excitable domains of axons under physiological conditions.

What could be the functional role of Na_V-mediated Ca^{2+} entry in axon initial segments and nodes of Ranvier? One downstream target of submembranous axoplasmic $[Ca^{2+}]_i$ may be regulation of Na_V inactivation kinetics via their Ca^{2+}/calmodulin domain at their C-terminus as has been demonstrated for multiple Na_V subtypes, including $Na_V1.2$ and $Na_V1.6$ (Sarhan et al., 2012; Reddy Chichili et al., 2013; Ben-Johny et al., 2014; Wang et al., 2014). Another target of Na_V-mediated Ca^{2+} could be to open axonal large-conductance BK_{Ca} channels. The BK_{Ca} channel opens with the cooperative action of membrane voltage and $[Ca^{2+}]_i \geq 10$ µM to contribute to the repolarization of APs and shorten their duration (Berkefeld et al., 2010). Across cell types there are considerable variations in the magnitude and time course of BK_{Ca} currents due to differences in nanodomain coupling with Ca_V channel isoforms. BK_{Ca} channels are exclusively activated by P/Q-type Ca_V channels in cerebellar Purkinje neurons with short AP durations (Womack et al., 2004), but in rat chromaffin cells with wider APs, BK_{Ca} channels are coupled with the Q- and slower activating L-type Ca_V channels (Prakriya and Lingle, 1999). Also in in L5 pyramidal neurons BK_{Ca} activation substantially shortens the duration of somatic APs from ~1 ms to ~600 μs (Yu et al., 2010; Bock and Stuart, 2016; Roshchin et al., 2018). Considering the brief duration of axonal APs in the L5 pyramidal neurons (~300 μs (Kole et al., 2007)) Na_V channels may provide both a precisely-timed voltage-dependent activation, via Na^+ current, as well as a $[Ca^{2+}]_i$ signaling pathway, producing a $[Ca^{2+}]_i$ rise <150 μs (**Figure 9**), to rapidly open BK_{Ca} channels and shape axonal AP repolarization. In agreement with this conjecture our data show that T- and L-type Ca_V channels are too slow to mediate somatic AP repolarization, leaving open the possibility that a Na_V-BK_{Ca} channel nanodomain coupling provides the required Ca^{2+} signal. Firm evidence for such interaction would require mutating the selectivity filter of Na_V channels to abolish Ca^{2+} but not Na^+ permeation. Two-photon Ca^{2+} uncaging experiments already showed that the $[Ca^{2+}]_i$ rise at the first node of Ranvier in L5 axons opens nodal BK_{Ca} channels to shorten the AP duration and facilitate the generation of high firing rates in the proximal axon (Roshchin et al., 2018). Further downstream from the initiation site nodal BK_{Ca} channels in Purkinje axons play a role in augmenting the hyperpolarization following APs and facilitate recovery from Na_V inactivation to prevent propagation failures (Hirono et al., 2015). The dual permeation of axonal Na_V channels for Na^+ and Ca^{2+} ions may thus serve a common function; mediating the rapid electrical upstroke of the AP and via Ca^{2+} signaling activating K^+ efflux to recover from inactivation and accelerating Na_V channel availability for the next AP, representing a fine-tuning specifically to the needs of axonal AP generation and conduction fidelity.

Acknowledgements

The authors are indebted to Stefan Hallermann (Univ. Leipzig), Christian Lohmann (NIN–KNAW) and Christiaan de Kock (CNCR, VU) for critically reading earlier versions of the manuscript. We thank Huib Mansvelder (CNCR, VU) for sharing the human tissue. Part of the work was supported by the National Multiple Sclerosis Society (RG 4924A1/1) and the

Netherlands Organization for Scientific Research (NWO), including an NWO Vici grant 865.17.003 and a Program Grant 16NEPH02 of the Foundation for Fundamental Research on Matter (FOM) to M.K. O.P.A. was supported by the Erasmus + Traineeship Program and the Graduate School of Systemic Neurosciences.

Competing Interests

The authors declare that there are no competing interests.

Author Contributions

MK conceived the research. NH performed the electrophysiological and imaging experiments to measure the contribution of the Giant Saccular Organelle (Figure 2), the various $\mathrm{Ca^{2+}}$ entry pathways (Figure 3, together with MP), the AP-dependent $\mathrm{Ca^{2+}}$ entry through $\mathrm{Na_V}$ channels (Figure 5), the temporal separation of $\mathrm{Ca_V}$ and $\mathrm{Na_V}$ mediated $\mathrm{Ca^{2+}}$ entry (Figure 6, together with MP), the $\mathrm{Na_V}$ mediated $\mathrm{Ca^{2+}}$ entry in $\mathrm{Na_V1.2}$ expressing HEK-cells (Figure 7) and the NEURON simulations (Figure 8 and 9, together with MP and MK). MP performed the electrophysiological and imaging experiments to study the compartmentalization of $\mathrm{Ca^{2+}}$ entry (Figure 1, together with OPA), the various $\mathrm{Ca^{2+}}$ entry pathways (Figure 3, together with NH), the subthreshold $\mathrm{Na_V}$ mediated $\mathrm{Ca^{2+}}$ entry (Figure 4), the temporal separation of $\mathrm{Ca_V}$ and $\mathrm{Na_V}$ mediated $\mathrm{Ca^{2+}}$ entry (Figure 6, together with NH) and the NEURON simulations (Figure 8 and 9, together with NH and MK). XW performed the HEK cells transfections and electrophysiological characterization (Figure 7). SG performed the staining and analysis of the GSO – AIS location (Figure 2). OPA performed the electrophysiological and imaging experiments to study the compartmentalization of $\mathrm{Ca^{2+}}$ entry (Figure 1, together with MP). NH and MP wrote the software for analysis and made the figures. MK performed the funding acquisition, project administration and wrote the first version of the manuscript with later editions from NH and MP.

References

Aggarwal R, Shorofsky SR, Goldman L, Balke CW (1997) Tetrodotoxin-blockable calcium currents in rat ventricular myocytes; a third type of cardiac cell sodium current. The Journal of Physiology 505 (Pt 2):353–369.

Ait Ouares K, Jaafari N, Canepari M (2016) A generalised method to estimate the kinetics of fast Ca(2+) currents from Ca(2+) imaging experiments. J Neurosci Methods 268:66–77.

Akaike N, Takahashi K (1992) Tetrodotoxin-sensitive calcium-conducting channels in the rat hippocampal CA1 region. The Journal of Physiology 450:529–546.

Antón-Fernández A, Rubio-Garrido P, DeFelipe J, Muñoz A (2015) Selective presence of a giant saccular organelle in the axon initial segment of a subpopulation of layer V pyramidal neurons. Brain Struct Funct 220:869–884.

Armstrong CM, Cota G (1999) Calcium block of Na+ channels and its effect on closing rate. Proc Natl Acad Sci USA 96:4154–4157.

Baker PF, Hodgkin AL, Ridgway EB (1971) Depolarization and calcium entry in squid giant axons. The Journal of Physiology 218:709–755.

Bas Orth C, Schultz C, Müller CM, Frotscher M, Deller T (2007) Loss of the cisternal organelle in the axon initial segment of cortical neurons in synaptopodin-deficient mice. J Comp Neurol 504:441–449.

Battefeld A, Popovic MA, van der Werf D, Kole MHP (2018) A Versatile and Open-Source Rapid LED Switching System for One-Photon Imaging and Photo-Activation. Front Cell Neurosci 12:530.

Ben-Johny M, Yang PS, Niu J, Yang W, Joshi-Mukherjee R, Yue DT (2014) Conservation of Ca2+/calmodulin regulation across Na and Ca2+ channels. Cell 157:1657–1670.

Ben-Shalom R, Keeshen CM, Berrios KN, An JY, Sanders SJ, Bender KJ (2017) Opposing Effects on NaV1.2 Function Underlie Differences Between SCN2A Variants Observed in Individuals With Autism Spectrum Disorder or Infantile Seizures. Biol Psychiatry 82:224–232.

Bender KJ, Trussell LO (2009) Axon initial segment Ca2+ channels influence action potential generation and timing. Neuron 61:259–271.

Benedeczky I, Molnár E, Somogyi P (1994) The cisternal organelle as a Ca(2+)-storing compartment associated with GABAergic synapses in the axon initial segment of hippocampal pyramidal neurones. Exp Brain Res 101:216–230.

Berkefeld H, Fakler B, Schulte U (2010) Ca2+-activated K+ channels: from protein complexes to function. Physiol Rev 90:1437–1459.

Berridge MJ (2006) Calcium microdomains: organization and function. Cell Calcium 40:405–412.

Bers DM, Patton CW, Nuccitelli R (2010) A practical guide to the preparation of Ca(2+) buffers. Methods Cell Biol 99:1–26.

Bock T, Stuart GJ (2016) The Impact of BK Channels on Cellular Excitability Depends on their Subcellular Location. Front Cell Neurosci 10:206.

Boiteux C, Vorobyov I, Allen TW (2014) Ion conduction and conformational flexibility of a bacterial voltage-gated sodium channel. Proceedings of the National Academy of Sciences 111:3454–3459.

Brown JE, Cohen LB, De Weer P, Pinto LH, Ross WN, Salzberg BM (1975) Rapid changes in intracellular free calcium concentration. Detection by metallochromic indicator dyes in squid giant axon. Biophys J 15:1155–1160.

Callewaert G, Eilers J, Konnerth A (1996) Axonal calcium entry during fast "sodium" action potentials in rat cerebellar Purkinje neurones. The Journal of Physiology 495 (Pt 3):641–647.

Campbell DL, Giles WR, Hume JR, Noble D, Shibata EF (1988) Reversal potential of the calcium current in bull-frog atrial myocytes. The Journal of Physiology 403:267–286.

Carnevale NT, Hines ML (2006) The NEURON Book. Cambridge University Press.

Chen-Izu Y, Sha Q, Shorofsky SR, Robinson SW, Wier WG, Goldman L, Balke CW (2001) I(Ca(TTX)) channels are distinct from those generating the classical cardiac Na(+) current. Biophys J 81:2647–2659.

Choe W, Messinger RB, Leach E, Eckle V-S, Obradovic A, Salajegheh R, Jevtovic-Todorovic V, Todorovic SM (2011) TTA-P2 is a potent and selective blocker of T-type calcium channels in rat sensory neurons and a novel antinociceptive agent. Molecular Pharmacology 80:900–910.

Clarkson RL, Liptak AT, Gee SM, Sohal VS, Bender KJ (2017) D3 Receptors Regulate Excitability in a Unique Class of Prefrontal Pyramidal Cells. J Neurosci 37:5846–5860.

Cornelisse LN, van Elburg RAJ, Meredith RM, Yuste R, Mansvelder HD (2007) High speed two-photon imaging of calcium dynamics in dendritic spines: consequences for spine calcium kinetics and buffer capacity. PLoS ONE 2:e1073.

Corry B (2013) Na(+)/Ca(2+) selectivity in the bacterial voltage-gated sodium channel NavAb. PeerJ 1:e16.

Cruz JS, Santana LF, Frederick CA, Mattei LN, Malhotra YD, Isom LL, Kass RS, Xia J, An R-H, Lederer WJ (1999) Whether" slip-mode conductance" occurs. Science 284:711a6–711a13 Available at: https://science.sciencemag.org/content/284/5415/709.16.

De Kock CPJ, Bruno RM, Spors H, Sakmann B (2007) Layer- and cell-type-specific suprathreshold stimulus representation in rat primary somatosensory cortex. The Journal of Physiology 581:139–154.

Delvendahl I, Jablonski L, Baade C, Matveev V, Neher E, Hallermann S (2015) Reduced endogenous Ca2+ buffering speeds active zone Ca2+ signaling. Proceedings of the National Academy of Sciences 112:E3075–E3084.

Edelstein AD, Tsuchida MA, Amodaj N, Pinkard H, Vale RD, Stuurman N (2014) Advanced methods of microscope control using μManager software. J Biol Methods 1.

Fink CC, Slepchenko B, Moraru II, Watras J, Schaff JC, Loew LM (2000) An image-based model of calcium waves in differentiated neuroblastoma cells. Biophys J 79:163–183.

Fukaya R, Yamada R, Kuba H (2018) Tonotopic Variation of the T-Type Ca2+ Current in Avian Auditory Coincidence Detector Neurons. J Neurosci 38:335–346.

Garrido JJ, Giraud P, Carlier E, Fernandes F, Moussif A, Fache M-P, Debanne D, Dargent B (2003) A targeting motif involved in sodium channel clustering at the axonal initial segment. Science 300:2091–2094.

Groh A, Meyer HS, Schmidt EF, Heintz N, Sakmann B, Krieger P (2010) Cell-type specific properties of pyramidal neurons in neocortex underlying a layout that is modifiable depending on the cortical area. Cerebral Cortex 20:826–836.

Gründemann J, Clark BA (2015) Calcium-Activated Potassium Channels at Nodes of Ranvier Secure Axonal Spike Propagation. Cell Rep 12:1715–1722.

Grynkiewicz G, Poenie M, Tsien RY (1985) A new generation of Ca2+ indicators with greatly improved fluorescence properties. J Biol Chem 260:3440–3450.

Guatimosim S, Sobie EA, Cruz JS, Martin LA, Lederer WJ (2001) Molecular identification of a TTX-sensitive Ca(2+) current. Am J Physiol, Cell Physiol 280:C1327–C1339.

Hallermann S, de Kock CPJ, Stuart GJ, Kole MHP (2012) State and location dependence of action potential metabolic cost in cortical pyramidal neurons. Nat Neurosci 15:1007–1014.

Hamada MS, Goethals S, de Vries SI, Brette R, Kole MHP (2016) Covariation of axon initial segment location and dendritic tree normalizes the somatic action potential. Proceedings of the National Academy of Sciences 113:14841–14846.

Hamada MS, Popovic MA, Kole MHP (2017) Loss of Saltation and Presynaptic Action Potential Failure in Demyelinated Axons. Front Cell Neurosci 11:45.

Heinemann SH, Terlau H, Stühmer W, Imoto K, Numa S (1992) Calcium channel characteristics conferred on the sodium channel by single mutations. Nature 356:441–443.

Helmchen F, Borst JG, Sakmann B (1997) Calcium dynamics associated with a single action potential in a CNS presynaptic terminal. Biophys J 72:1458–1471.

Heubach JF, Köhler A, Wettwer E, Ravens U (2000) T-Type and tetrodotoxin-sensitive Ca(2+) currents coexist in guinea pig ventricular myocytes and are both blocked by mibefradil. Circ Res 86:628–635.

Hille B (1972) The permeability of the sodium channel to metal cations in myelinated nerve. J Gen Physiol 59:637–658.

Hines ML, Carnevale NT (2001) NEURON: a tool for neuroscientists. The Neuroscientist 7:123–135.

Hirono M, Ogawa Y, Misono K, Zollinger DR, Trimmer JS, Rasband MN, Misonou H (2015) BK Channels Localize to the Paranodal Junction and Regulate Action Potentials in Myelinated Axons of Cerebellar Purkinje Cells. J Neurosci 35:7082–7094.

Hu W, Tian C, Li T, Yang M, Hou H, Shu Y (2009) Distinct contributions of Na(v)1.6 and Na(v)1.2 in action potential initiation and backpropagation. Nat Neurosci 12:996–1002.

Iino M, Ciani S, Tsuzuki K, Ozawa S, Kidokoro Y (1997) Permeation properties of Na+ and Ca2+ ions through the mouse epsilon2/zeta1 NMDA receptor channel expressed in Xenopus oocytes. J Membr Biol 155:143–156.

Iwata A, Stys PK, Wolf JA, Chen X-H, Taylor AG, Meaney DF, Smith DH (2004) Traumatic axonal injury induces proteolytic cleavage of the voltage-gated sodium channels modulated by tetrodotoxin and protease inhibitors. J Neurosci 24:4605–4613.

Jaafari N, De Waard M, Canepari M (2014) Imaging fast calcium currents beyond the limitations of electrode techniques. Biophys J 107:1280–1288.

Jackson MB, Redman SJ (2003) Calcium dynamics, buffering, and buffer saturation in the boutons of dentate granule-cell axons in the hilus. J Neurosci 23:1612–1621.

Jin X, Chen Q, Song Y, Zheng J, Xiao K, Shao S, Fu Z, Yi M, Yang Y, Huang Z (2019) Dopamine D2 receptors regulate the action potential threshold by modulating T-type calcium channels in stellate cells of the medial entorhinal cortex. The Journal of Physiology 597:3363–3387.

King AN, Manning CF, Trimmer JS (2014) A unique ion channel clustering domain on the axon initial segment of mammalian neurons. J Comp Neurol 522:2594–2608.

Klingauf J, Neher E (1997) Modeling buffered Ca2+ diffusion near the membrane: implications for secretion in neuroendocrine cells. Biophys J 72:674–690.

Kole MHP, Letzkus JJ, Stuart GJ (2007) Axon initial segment Kv1 channels control axonal action potential waveform and synaptic efficacy. Neuron 55:633–647.

Kole MHP, Stuart GJ (2012) Signal processing in the axon initial segment. Neuron 73:235–247.

Langer J, Rose CR (2009) Synaptically induced sodium signals in hippocampal astrocytes in situ. The Journal of Physiology 587:5859–5877.

Läuger P (1973) Ion transport through pores: a rate-theory analysis. Biochim Biophys Acta 311:423–441.

Lewis CA (1979) Ion-concentration dependence of the reversal potential and the single channel conductance of ion channels at the frog neuromuscular junction. The Journal of Physiology 286:417–445.

Lorincz A, Nusser Z (2010) Molecular identity of dendritic voltage-gated sodium channels. Science 328:906–909.

Mainen ZF, Sejnowski TJ (1996) Influence of dendritic structure on firing pattern in model neocortical neurons. Nature 382:363–366.

Martinello K, Huang Z, Luján R, Tran B, Watanabe M, Cooper EC, Brown DA, Shah MM (2015) Cholinergic afferent stimulation induces axonal function plasticity in adult hippocampal granule cells. Neuron 85:346–363.

McKay BE, McRory JE, Molineux ML, Hamid J, Snutch TP, Zamponi GW, Turner RW (2006) Ca(V)3 T-type calcium channel isoforms differentially distribute to somatic and dendritic compartments in rat central neurons. Eur J Neurosci 24:2581–2594.

Meves H, Vogel W (1973) Calcium inward currents in internally perfused giant axons. The Journal of Physiology 235:225–265.

Miyazaki K, Ross WN (2015) Simultaneous Sodium and Calcium Imaging from Dendrites and Axons. eNeuro 2.

Naylor CE, Bagnéris C, DeCaen PG, Sula A, Scaglione A, Clapham DE, Wallace BA (2016) Molecular basis of ion permeability in a voltage-gated sodium channel. EMBO J 35:820–830.

Neher E, Sakaba T (2008) Multiple roles of calcium ions in the regulation of neurotransmitter release. Neuron 59:861–872.

Neumcke B, Stämpfli R (1982) Sodium currents and sodium-current fluctuations in rat myelinated nerve fibres. The Journal of Physiology 329:163–184.

Perez-Reyes E, Cribbs LL, Daud A, Lacerda AE, Barclay J, Williamson MP, Fox M, Rees M, Lee JH (1998) Molecular characterization of a neuronal low-voltage-activated T-type calcium channel. Nature 391:896–900.

Prakriya M, Lingle CJ (1999) BK channel activation by brief depolarizations requires Ca2+ influx through L- and Q-type Ca2+ channels in rat chromaffin cells. J Neurophysiol 81:2267–2278.

Ramaswamy S, Markram H (2015) Anatomy and physiology of the thick-tufted layer 5 pyramidal neuron. Front Cell Neurosci 9:233.

Reddy Chichili VP, Xiao Y, Seetharaman J, Cummins TR, Sivaraman J (2013) Structural basis for the modulation of the neuronal voltage-gated sodium channel NaV1.6 by calmodulin. Sci Rep 3:2435.

Roshchin MV, Matlashov ME, Ierusalimsky VN, Balaban PM, Belousov VV, Kemenes G, Staras K, Nikitin ES (2018) A BK channel-mediated feedback pathway links single-synapse activity with action potential sharpening in repetitive firing. Sci Adv 4:eaat1357.

Sabatini BL, Regehr WG (1998) Optical measurement of presynaptic calcium currents. Biophys J 74:1549–1563.

Santana LF, Gómez AM, Lederer WJ (1998) Ca2+ flux through promiscuous cardiac Na+ channels: slip-mode conductance. Science 279:1027–1033.

Sarhan MF, Tung C-C, Van Petegem F, Ahern CA (2012) Crystallographic basis for calcium regulation of sodium channels. Proceedings of the National Academy of Sciences 109:3558–3563.

Schindelin J, Arganda-Carreras I, Frise E, Kaynig V, Longair M, Pietzsch T, Preibisch S, Rueden C, Saalfeld S, Schmid B, Tinevez J-Y, White DJ, Hartenstein V, Eliceiri K, Tomancak P, Cardona A (2012) Fiji: an open-source platform for biological-image analysis. Nat Meth 9:676–682.

Schmidt-Hieber C, Bischofberger J (2010) Fast sodium channel gating supports localized and efficient axonal action potential initiation. J Neurosci 30:10233–10242.

Schneggenburger R, Neher E (2000) Intracellular calcium dependence of transmitter release rates at a fast central synapse. Nature 406:889–893.

Stys PK, Lopachin RM (1998) Mechanisms of calcium and sodium fluxes in anoxic myelinated central nervous system axons. Neuroscience 82:21–32.

Stys PK, Waxman SG, Ransom BR (1991) Na(+)-Ca2+ exchanger mediates Ca2+ influx during anoxia in mammalian central nervous system white matter. Ann Neurol 30:375–380.

Sun H, Varela D, Chartier D, Ruben PC, Nattel S, Zamponi GW, Leblanc N (2008) Differential interactions of Na+ channel toxins with T-type Ca2+ channels. J Gen Physiol 132:101–113.

Takahashi N, Oertner TG, Hegemann P, Larkum ME (2016) Active cortical dendrites modulate perception. Science 354:1587–1590.

Talbot MJ, Sayer RJ (1996) Intracellular QX-314 inhibits calcium currents in hippocampal CA1 pyramidal neurons. J Neurophysiol 76:2120–2124.

Testa-Silva G, Verhoog MB, Linaro D, de Kock CPJ, Baayen JC, Meredith RM, De Zeeuw CI, Giugliano M, Mansvelder HD (2014) High bandwidth synaptic communication and frequency tracking in human neocortex. PLoS Biol 12:e1002007.

Tian C, Wang K, Ke W, Guo H, Shu Y (2014) Molecular identity of axonal sodium channels in human cortical pyramidal cells. Front Cell Neurosci 8:297.

Wang C, Chung BC, Yan H, Wang H-G, Lee S-Y, Pitt GS (2014) Structural analyses of Ca^{2+}/CaM interaction with NaV channel C-termini reveal mechanisms of calcium-dependent regulation. Nat Commun 5:4896.

Watanabe A, Tasaki I, Singer I, Lerman L (1967) Effects of Tetrodotoxin on Excitability of Squid Giant Axons in Sodium-Free Media. Science 155:95–97.

Womack MD, Chevez C, Khodakhah K (2004) Calcium-activated potassium channels are selectively coupled to P/Q-type calcium channels in cerebellar Purkinje neurons. J Neurosci 24:8818–8822.

Yu SP, Choi DW (1997) Na(+)-Ca2+ exchange currents in cortical neurons: concomitant forward and reverse operation and effect of glutamate. Eur J Neurosci 9:1273–1281.

Yu Y, Maureira C, Liu X, McCormick D (2010) P/Q and N channels control baseline and spike-triggered calcium levels in neocortical axons and synaptic boutons. J Neurosci 30:11858–11869.

Zakon HH (2012) Adaptive evolution of voltage-gated sodium channels: the first 800 million years. Proceedings of the National Academy of Sciences 109 Suppl 1:10619–10625.

Zhang Z, David G (2016) Stimulation-induced Ca(2+) influx at nodes of Ranvier in mouse peripheral motor axons. The Journal of Physiology 594:39–57.

Supplemental Figures

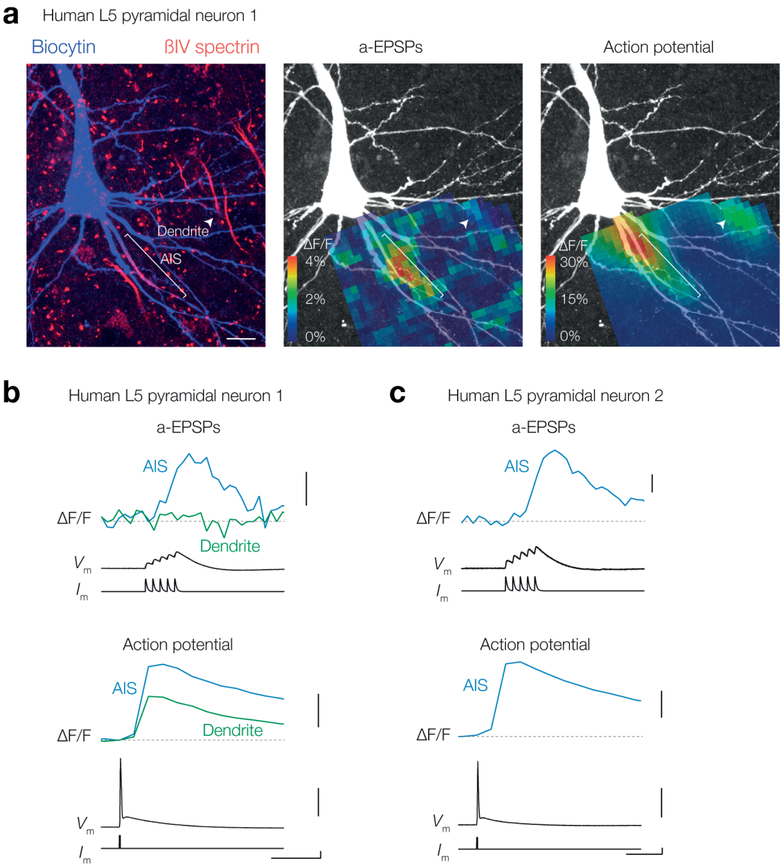
a
Human L5 pyramidal neuron 1
Biocytin
ßIV spectrin
a-EPSPs
Action potential
Dendrite
AIS
ΔF/F
4%
2%
0%
ΔF/F
30%
15%
0%
b
Human L5 pyramidal neuron 1
a-EPSPs
AIS
ΔF/F
Dendrite
Vm
Im
Action potential
AIS
ΔF/F
Dendrite
Vm
Im
c
Human L5 pyramidal neuron 2
a-EPSPs
AIS
ΔF/F
Vm
Im
Action potential
AIS
ΔF/F
Vm
Im

Figure 1–figure supplement 1. EPSP-evoked evoked Δ[Ca^{2+}]$_i$ in human layer 5 pyramidal neuron AIS

a. *Left*, *z*-projection of a human temporal lobe layer 5 pyramidal neuron stained with biocytin / streptavidin (blue) and βIV-spectrin (red). *Middle* and *right*, peak ΔF/F (OGB-1, 100 μM) overlaid with a *z*-projection of biocytin-streptavidin (white) in response to an a-EPSP and AP (*right*). Note that not all regions visible in the confocal scan (left) are from the same focal plane and thus visible in the ΔF/F plot. The AIS (white line) and a part of a basal dendrite (white arrow) were in focus. Scale bar, 10 μm. **b**. Example traces from AIS (blue) and dendrite (green) in response to an a-EPSP (*top*) and AP (*bottom*) from locations indicated in **a**. Note the absence of a-EPSP evoked Ca^{2+} influx in the dendrite. From top to bottom scale bars, 1% ΔF/F, 10% ΔF/F, 10 mV, 1 nA and 50 ms. **c**. Example ΔF/F traces from another neuron AIS (blue) in response to an a-EPSP (*top*) and AP (*bottom*). From top to bottom scale bars, 1% ΔF/F, 10% ΔF/F, 10 mV, 1 nA and 50 ms.

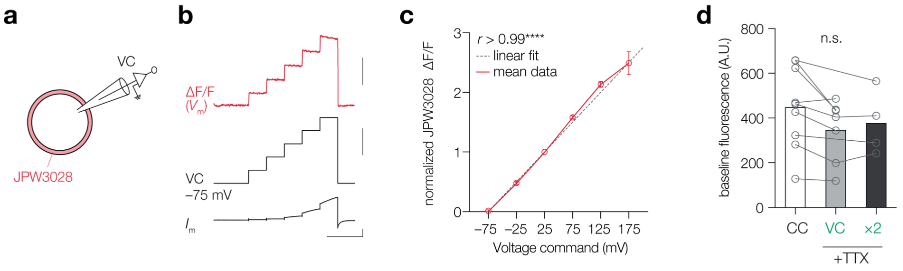

Figure 5–figure supplement 1. JPW3028 fluorescence linearly increases with membrane potential over a wide range of voltages.

a. Schematic of the experiment; whole-cell voltage clamp of HEK-293 cells filled with 0.8 mM JPW3028. **b**. *Top*, example ΔF/F JPW3028 trace (red), *middle*, voltage command potentials, *bottom*, recorded current. Slow outward rectification was visible with depolarizing steps >150 mV. Scale bars, from top to bottom: 1% ΔF/F, 100 mV, 2 nA, 200 ms. **c**. Mean ΔF/F of the first 20 frames of each voltage step normalized to ΔF/F of the 100 mV step plotted versus the applied voltage revealed a highly linear relationship between V_m and ΔF/F, with r indicating Pearson's correlation coefficient, $****P < 0.0001$, $n = 3$. Grey dotted line is a linear fit between voltage –75 and +25 (approximate V_m range of an AP), data plotted as mean (red line and open circles) ± s.e.m. **d**. The baseline fluorescence of JPW presented in Figure 5 remained stable throughout the recording. One-way ANOVA, $P = 0.45$, Tukey's multiple comparisons test, CC ($n = 9$) vs. VC ($n = 7$), $P = 0.44$, CC vs. VC×2 ($n = 4$), $P = 0.74$, VC vs. VC×2, $P = 0.95$. Data available in **Figure 5–source data 1**.

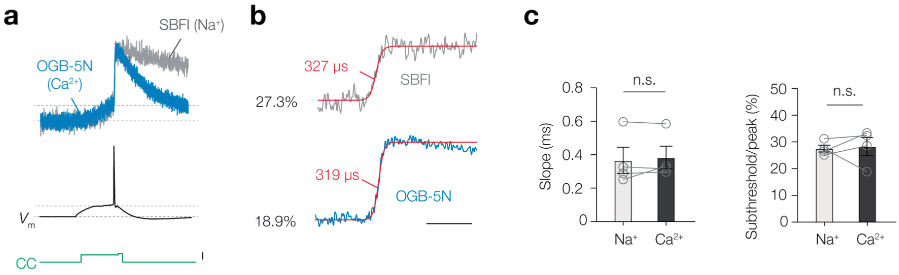

Figure 6–figure supplement 1. AP-evoked Ca^{2+} and Na$^+$ entry follow identical kinetics **a.** Neurons were co-loaded with OGB-5N (1 mM) and SBFI (1 mM) indicators to acquire Ca^{2+} (blue) and Na$^+$ (grey) signals from the same AIS region at a rate of 20 kHz. The current-clamp step protocol (green) consisted of a 50 ms subthreshold square pulse followed by a brief 5 ms pulse at the end triggering an AP. Both subthreshold and AP evoked signals are visible for $[Ca^{2+}]_i$ and $[Na^+]_i$. Scale bar, 500 pA. **b.** The example traces from **a**. fitted with a sigmoidal function (red) with slopes values indicated (red). The percentages indicate the subthreshold-activated fraction of ion flux (ΔF/F prior to the AP normalized peak ΔF/F). Scale bar, 10 ms. **c.** Population data of the rise times and subthreshold/peak ratio difference of Ca^{2+} and Na$^+$ indicators. Slope, Wilcoxon matched-pairs signed rank test, $n = 4$, $P > 0.999$, ratio subthreshold to peak, two-tailed paired *t*-test, $n = 4$, $P = 0.83$. Open circles and connecting lines represent individual cells and bars show the mean ± s.e.m. Data available in **Figure 6–source data 1**.

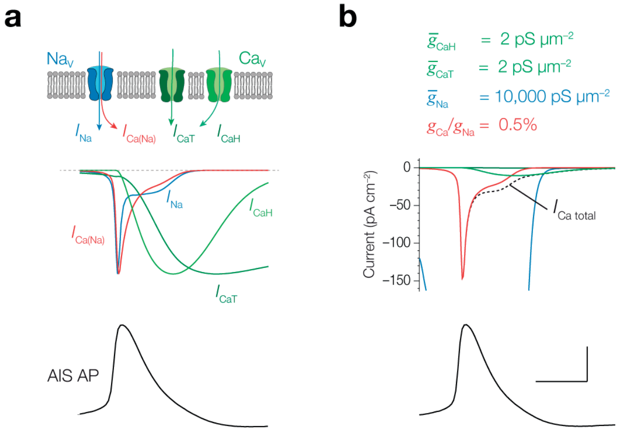

Figure 8–figure supplement 1. I_{Ca} compared to $I_{Ca(Na)}$ in a single compartment model
a. *From top to bottom,* schematic of a Na$_V$ channel mediating Na$^+$ and Ca^{2+} current (I_{Na} and $I_{Ca(Na)}$) and a Ca$_V$ channel mediating I_{CaT} and I_{CaH}, peak normalized simulated currents (I_{Na}, $I_{Ca(Na)}$, I_{CaH} and I_{CaT}) in a single compartment activated by an AIS AP waveform. Currents are normalized to peak amplitude. Note that $I_{Ca(Na)}$ is ~10-fold more rapid compared to I_{CaH} and I_{CaT}. The difference in shape of $I_{Ca(Na)}$ and I_{Na} reflects the different driving forces. Since the equilibrium potential for Ca^{2+} (+140 mV) is higher than for Na$^+$ (+55 mV), the driving force for $I_{Ca(Na)}$ is less affected during the voltage trajectory of the AP. **b**. Absolute current amplitudes comparing $I_{Ca(Na)}$ to I_{CaH} and I_{CaT} as well as the total I_{Ca} for typical channel densities (as noted above) and 0.5% conductivity ratio. I_{Na} is clipped to visually compare the Ca^{2+} currents. Note that $I_{Ca(Na)}$ dominates the Ca^{2+} charge for rapid action potentials. Scale bars, 50 mV and 0.5 ms.

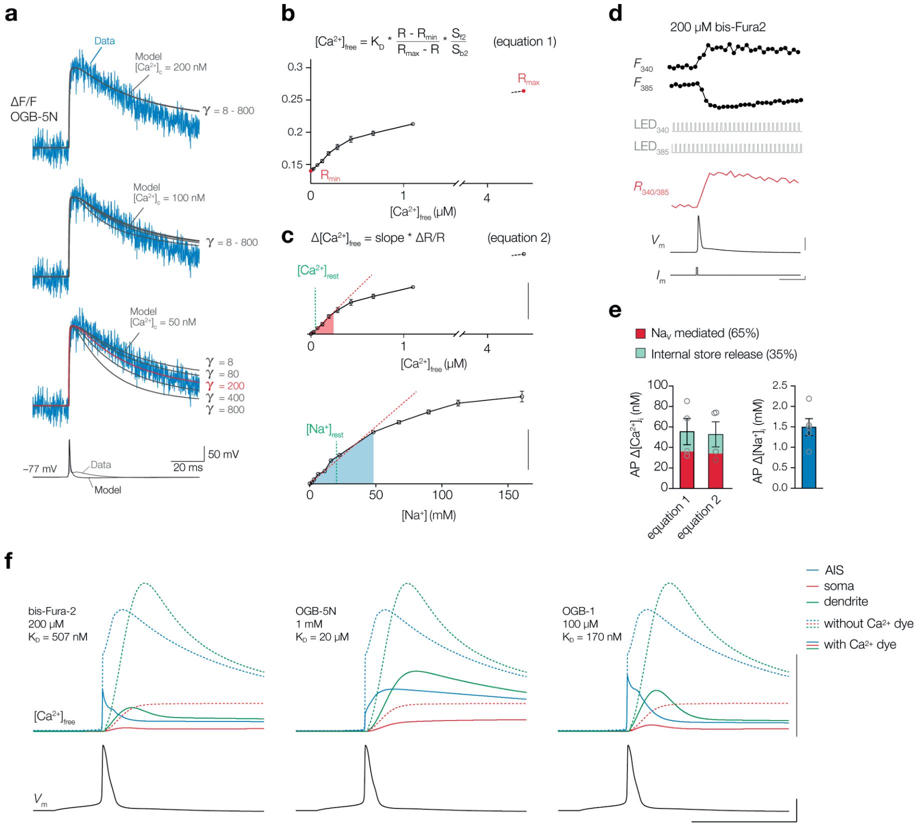

Figure 8–figure supplement 2. Calibration and modeling of $[Ca^{2+}]_i$

a. ΔF/F OGB-5N (1 mM, 20 kHz) traces from a representative cell AIS used to optimize Ca^{2+} extrusion in the model. Imaged ΔF/F (blue) overlaid with the simulated ΔF/F (grey) with varying Ca^{2+} extrusion thresholds ($[Ca^{2+}]_c$) and flux densities (γ) in the membrane. The optimal fit is indicated in red. **b**. Calibration of ratiometric bis-Fura-2 (bF2) signals to solutions with known $[Ca^{2+}]$ to determine K_D, R_{min} and R_{max} used in equation 1, which was subsequently used to convert ratiometric signals into absolute $\Delta[Ca^{2+}]_i$. Data shown as mean ± s.e.m (3 repetitions). **c**. The relationship between changes in fluorescence ratio ΔR/R normalized to the ratio in Ca^{2+}-free or Na^{+}-free solutions, used in equation 2. Data shown as mean ± s.e.m (3 repetitions), red dashed line is a linear fit through the mean $\Delta R/R_{bF2}$ (0–193 nM, 6 concentrations) and $\Delta R/R_{SBFI}$ (0–48 mM, 8 concentrations). Scale bars, 40% and 100%. **d**. Example traces of a ratiometric bF2 recording. Top to bottom: fluorescence transients from the AIS upon excitation with 340 and 385 nm (average of 38 trials), TTL pulses triggering the LEDs, fluorescence ratio R340/385, somatic AP and current injection. Scale bars, 40 mV, 4 nA and 10 ms. **e**. Absolute increase in $[Ca^{2+}]_i$ and $[Na^+]_i$ in the AIS after 1 AP in the presence of 200 μM bF2 and 1.5 mM SBFI, respectively, separate for the 2 Ca^{2+} calibration methods from **b** and **c**. Bar and error bars represent the mean ± s.e.m., open circles are individual cells. **f**. Simulation of distinct Ca^{2+} dyes on the $[Ca^{2+}]_i$, adjusting the K_D and concentration of the simulated exogenous buffer, shown for the AIS (blue), soma (red) and dendrites (green) (locations as specified in **Figure 9a**) in response to an AP (bottom). Note that OGB-5N, due to its low-affinity, buffers $[Ca^{2+}]_i$ more linear in comparison to bis-Fura-2 and OGB-1. Scale bars from top to bottom, 500 nM, 50 mV and 5 ms.

Table 1. Effect of Ca^{2+} entry on AP waveform

	RMP (mV)	AP threshold (mV)	AP amplitude (mV)	AP half-width (μs)	AHP (mV)	ADP (mV)
Control	–77.4 ± 2.5	–67.1 ± 3.0	110.9 ± 12.5	612.7 ± 24.7	5.6 ± 2.1	7.6 ± 2.5
TTA-P2 + isradipine	–76.0 ± 2.9	–65.0 ± 4.1	109.3 ± 3.3	634.5 ± 49.6	3.2 ± 2.9	4.6 ± 3.3
Paired t-tests ($n = 5$)	$P = 0.32$	$P = 0.30$	$P = 0.33$	$P = 0.61$	$P = 0.055$	$P = 0.039$*
Control	–70.4 ± 1.6	–59.3 ± 3.9	102.4 ± 1.8	753.8 ± 45.9	3.7 ± 3.8	6.5 ± 3.4
EGTA	–71.8 ± 3.6	–65.4 ± 1.8	103.5 ± 2.4	1031.5 ± 39.6	25.5 ± 4.3	11.7 ± 1.5
Paired t-tests ($n = 4$)	$P = 0.69$	$P = 0.19$	$P = 0.27$	$P = 0.035$*	$P = 0.043$*	$P = 0.17$

Overview of mean and s.e.m. of AP properties compared between control and toxin experiments recorded at the soma. RMP, resting membrane potential, AHP, fast afterhyperpolarization, ADP, afterdepolarization. The APs were elicited by large and brief current injections (~6 nA for 0.5 ms) to obtain temporally aligned APs between trials and image OGB-1 fluorescence (Figure 3). AP amplitude, AHP and ADP were measured relative to the AP threshold. If the AHP or ADP was not detectable as a local peak, the membrane potential at the time point as in control was used (see EGTA example **Figure 9d**). *P* values are results of two-tailed paired *t*-tests before and after toxin application. Data available in **Table 1–source data 1**.

Materials and Methods

Ethical approval

All animal experiments were performed in compliance with the European Communities Council Directive 2010/63/EU effective from 1 January 2013. They were evaluated and approved by the national CCD authority (license AVD8010020172426) and by the KNAW animal welfare and ethical guidelines and protocols (DEC NIN 14.49, DEC NIN 12.13, IvD NIN 17.21.01 and 17.21.03). Written informed consent was obtained from patients and all procedures on human tissue were performed with the approval of the Medical Ethical Committee of the Amsterdam UMC, location VuMC and in accordance with Dutch license procedures and the Declaration of Helsinki. All data were anonymized.

Tissue collection

Young-adult male Wistar rats (RjHan:WI) were used at an age between P21 and P35 (Charles River Laboratories and Janvier labs). Animals were deeply anaesthetized by 3% isoflurane inhalation, decapitated and 300 µm parasagittal slices containing the primary somatosensory cortex were cut with a Vibratome (1200S, Leica Microsystems B.V.) within ice-cold artificial cerebrospinal fluid (ACSF) of the following composition (in mM): 125 NaCl, 3 KCl, 25 glucose, 25 $NaHCO_3$, 1.25 $Na_2H_2PO_4$, 1 $CaCl_2$, 6 $MgCl_2$, saturated with 95% O_2 and 5% CO_2 (pH 7.4). Following a recovery period at 35 °C for 35–45 minutes slices were stored at room temperature in the ACSF. Human slices were obtained from non-pathological cortex removed for the surgical treatment of deeper brain structures for mesial temporal lobe epilepsy. After resection, a block of the temporal lobe was placed within 30 seconds in ice-cold artificial cerebrospinal fluid (ACSF) slicing solution which contained in (mM): 110 choline chloride, 26 $NaHCO_3$, 10 D-glucose, 11.6 sodium ascorbate, 7 $MgCl_2$, 3.1 sodium pyruvate, 2.5 KCl, 1.25 NaH_2PO_4, and 0.5 $CaCl_2$ (300 mOsm) and transported to the laboratory, as described in detail previously (Testa-Silva et al., 2014). Transition time between resection of the tissue and preparation of the slices was < 15 minutes. Neocortical slices (~350 µm thickness) were cut in an ice-cold slicing solution, stored for 30 minutes at 34 °C, and afterwards switched to room temperature in standard ACSF. Slices were subsequently transported (< 15 min) towards the NIN (KNAW) in continuously carbogenated ACSF.

Cell lines

Human embryonic kidney 293 cells (HEK 293T/17 cell line, CRL-11268 obtained from ATCC) were cultured in growth medium consisting of equal parts of Dulbecco's modified Eagle's medium (DMEM) (DMEM Glutamax, Gibco, Thermo Fisher Scientific) and Ham's F10 nutrient mix (Gibco, Thermo Fisher Scientific), supplemented with 10% fetal calf serum (FCS) and 1% penicillin–streptomycin. The STR profile is available at ATCC and the mycoplasma status was not confirmed. Cells were split twice a week by trypsinization and grown at 37 °C with a humidified atmosphere containing 5% CO_2. Human *SCN2A* (D-splice variant), encoding for the alpha subunit of the $Na_V1.2$ channel was cloned in pcDNA3.1-IRES-GFP, and *SCN1B/SCN2B*, encoding for beta subunits 1 and 2, was cloned into pcDNA3.1. These vectors were described previously (Ben-Shalom et al., 2017) and obtained from Genscript (Genscript, USA). The constructs were amplified in Stbl3 bacteria (Genscript, USA) and were purified using the GeneJET Plasmid Maxiprep kit (ThermoFisher, USA) according to the manufacturer's protocols. The plasmids were transiently transfected into 70% confluent HEK-293 cells plated in 12-well plates. Per well, the transfection cocktail contained 500 ng pcDNA3.1-SCN2A-IRES-GFP, 290 ng pcDNA3.1-SCN1B- IRES-SCN2B and 5 μL of polyethylenimine (PEI) diluted in 100 μL 1% saline, incubated for 20 minutes at room temperature before addition to the culture medium. Cells were incubated with 100 μL of transfection cocktail in 1 mL of culture medium for 24 hours at 37 °C in a humidified atmosphere containing 5% CO2. Cells were trypsinised and used for electrophysiological recording typically 48 hours after transfection.

Electrophysiological recording from neurons

For patch-clamp recording, slices were transferred to a customized upright microscope (BX51WI, Olympus Nederland BV). The transmitted light path consisted of a custom made 850 nm Light Emitting Diode (LED) light source (LZ1-10R602, LED Engin, CA), collimated using an aspheric condenser lens (ACL50832U-B, Thorlabs, Germany) and adapted to the microscope lamp port using a custom 3D printed adapter and passed through an oblique or Dodt illumination condenser (WI-OBCD, Olympus). The top 50 μm of the slice surface was visualized using an optical pathway consisting of a 60× water immersion objective (N.A. 1.0, LUMPLFLN60XW, Olympus or N.A. 1.1, LUMPLFLN60XW, Olympus), 2× intermediate zoom attachment (U-ECA, Olympus), camera splitter (U-TRU, Olympus) with inbuilt 180 mm tube lens on the back port and a 0.63× demagnifier (U-TV0.63XC, Olympus) projected the final image onto a high resolution CCD camera (CoolSNAP-EZ, Photometrics), which was operated using μManager (Edelstein et al., 2014). Based on the bright-field image large L5 neurons with an intact axon parallel and close to the surface were targeted for recording. Current-clamp recordings were made with Dagan BVC-700A amplifiers (Dagan Corporation, MN, USA) or AxoClamp 900A (Molecular Devices Limited, UK). An Axopatch 200B (Molecular Devices) was used for voltage-clamp and AP-clamp experiments. The microscope bath was perfused with oxygenated (95% O_2, 5% CO_2) ACSF consisting of (in mM): 125 NaCl, 3 KCl, 25 glucose, 25 $NaHCO_3$, 1.25 $Na_2H_2PO_4$, 2 $CaCl_2$, and 1 $MgCl_2$. Patch pipettes were pulled from borosilicate glass (Harvard Apparatus, Edenbridge, Kent, UK) pulled to an open tip of 3 – 6 MΩ resistance. For all current-clamp, subthreshold voltage-clamp ramp and AP-clamp recordings the intracellular solution contained (in mM): 130 K-Gluconate, 10 KCl, 4 Mg-ATP, 0.3 Na_2-GTP, 10 HEPES and 10 Na_2-phosphocreatine (pH 7.25 adjusted with KOH, 280 mOsmol kg^{-1}). The liquid junction potential difference of –13.5 mV was corrected in all recordings. For morphological reconstruction, 5 mg ml^{-1} biocytin was routinely added. Voltage recordings were analogue low-pass filtered at 10 kHz (Bessel) and digitally sampled at 100 kHz using A-D converter (ITC-18, HEKA Elektronik Dr. Schulze GmbH, Germany) and data acquisition software Axograph X (v.1.5.4, Axograph Scientific, NSW, Australia). Bridge-balance and capacitances were fully compensated based on small current injections leading to minimal voltage errors. The recording temperature was 33 ± 1 °C. Only cells with a stable bridge-balance (< 25 MΩ), resting membrane potential and AP shape throughout the recording session were included in the analysis.

For voltage-clamp recordings of I_{Na} and I_{Ca} (**Figure 5**) the bath was perfused with oxygenated (95% O_2, 5% CO_2) extracellular recording solution consisting of (in mM): 100 NaCl, 3 KCl, 25 glucose, 25 $NaHCO_3$, 1.25 $Na_2H_2PO_4$, 2 $CaCl_2$, 1 $MgCl_2$, 5 4-AP, 20 TEA-Cl, 0.02 CNQX, 0.05 D-AP5, 0.02 ZD-7288, 0.01 XE991 and 0.003 Gabazine (SR-95531). The intracellular solution contained (in mM): 130 CsCl, 10 TEA-Cl, 10 HEPES, 4 Mg-ATP, 5 Na_2-phosphocreatine and 0.3 Na_2-GTP (pH 7.25 adjusted with CsOH, 280 mOsmol kg^{-1}). A liquid junction potential of –5.6 mV was applied to the recordings. Series resistance was routinely compensated to >75% and the linear leak and capacitance off-line subtracted using a P/9 protocol with 10-fold scaled pulses. Current recordings were analogue low-pass filtered at 10 kHz (Bessel) and digitally sampled at 100 kHz using A-D converter (ITC-18, HEKA Elektronik Dr. Schulze GmbH, Germany) and data acquisition software Axograph X (v.1.5.4, Axograph Scientific, NSW, Australia). To improve voltage-clamp of the large and rapid Na^+ currents the recordings were made at room temperature (~20 °C).

Electrophysiological recordings from HEK-293 cells

For recordings from HEK-293 cells they were transferred to a recording chamber which was continuously perfused with extracellular solution, containing (in mM): 135 NaCl, 4.5 KCl, 2 $CaCl_2$, 1 MgCl, 10 HEPES and 11 Glucose. The intracellular solution contained (in mM): 110 CsF, 10 NaCl, 20 EGTA and 10 HEPES. In the OGB-1 experiments, we added 100 µM OGB-1, EGTA was omitted and CsF raised to 120 mM instead of 110 mM. The liquid junction potential difference of –10 mV was corrected for. Whole-cell patch-clamp recordings were made ~48 hours after transfection. Cells were recorded at room temperature (~20 °C) and continuously perfused with extracellular solution at a flow rate of 1.5 mL·min$^{–}$1. Patch pipettes were pulled to a resistance of 2–3 MΩ. Round, isolated cells with a diameter >10 µm, a smooth cell surface and a moderate EGFP fluorescent signal were selected for recordings (**Figure 7a**). HEK-293 cells had an average capacitance of 9.19 ± 0.70 pF (n = 16). The holding potential was –70 mV and voltage dependence of activation of $Na_V1.2$ was determined by an activating protocol consisting of a hyperpolarizing pulse to –130 mV (20 ms) followed by step pulses from –80 mV to +50 mV with increments of 10 mV for 20 ms. In some recordings, the hyperpolarization was at –150 mV followed by voltage pulses from –100 to 90 mV with increments of 10 mV. Voltage dependence of inactivation was assessed with voltage pulses from –130 mV to –30 mV with increments of 10 mV for 100 ms duration, followed by a depolarizing pulse to –10 mV for 20 ms. In some recordings, voltage pulses were made from –150 to –50 mV, followed by a depolarizing pulse to –20 mV. A P/5 leak subtraction protocol (10-fold scaling) was used to subtract remaining capacitive and leak currents. Series resistance was not compensated.

Blockers and toxins

EGTA and blockers were added to the appropriate concentration to the ACSF and perfused.

The extracellular Ca^{2+} ($[Ca^{2+}]_o$) was lowered by bath application of 2.5 mM EGTA and using the online maxchelator tool (https://somapp.ucdmc.ucdavis.edu/) (Bers et al., 2010) we calculated the remaining $[Ca^{2+}]_o$ to be 437 nM, based on a recording temperature of 35 °C, a pH of 7.4 and an ionic strength of 0.15 M of the free ions in our solution. To limit hyperexcitability in the presence of EGTA, we added synaptic blockers to the ACSF in all conditions (20 μM CNXQ and 50 μM D-AP5) and kept the a-EPSP voltage peak amplitude constant by reducing the amplitude of the current injections in both control and EGTA measurements (**Figure 2**). To prevent precipitation of Ni^{2+} we used phosphate-free extracellular solutions for the Ni^{2+} experiments, containing (in mM): 126.25 NaCl, 3 KCl, 25 glucose, 25 $NaHCO_3$, 2 $CaCl_2$, 1 $MgCl_2$ and 0.1 Ni^{2+}. A >10% increase in fluorescence baseline was observed in some experiments (3 out of 8 recordings), which were subsequently excluded. Two blockers (SNX-478 and ω-conotoxin MVIIC) were not perfused but were locally puffed using a Picospritzer III (Intracel) for 3 seconds ending 0.5 s before imaging to avoid vibration artifacts. Bovine serum albumin (0.1 mg/ml) was added to the rACSF before ω-conotoxin MVIIC was introduced to minimize non-specific binding of the drug.

Ca^{2+} and Na^+ imaging

To optically record $[Ca^{2+}]_i$ and $[Na^+]_i$ in axons, membrane impermeable Ca^{2+} and/or Na^+ indicators were added to intracellular solutions. For Ca^{2+} we used OGB-1 (100 μM), OGB-5N (1 mM) or bis-Fura-2 (200 μM) and for Na^+ imaging we used sodium-binding benzofuran isophthalate (SBFI, 1 – 1.5 mM). Patch pipettes were first filled with dye-free solution for half of the tapered part of the pipette tip, then backfilled with the dye-containing solution. Fluorescence intensity at the AIS was monitored during dye loading and imaging started only when the indicators were fully equilibrated (typically after 0.5–1 h). Optical recordings of Ca^{2+} or Na^+ dye fluorescence changes were obtained with wide-field epifluorescence microscopy. Fluorescence was collected by the same 60× water immersion objective, passed through the microscope tube lens (U-TR30IR, Olympus) and projected onto a rapid data-acquisition camera with relatively low spatial resolution (80 × 80 pixels) but high dynamic range (14 bits) and low read noise (NeuroCCD-SM, RedShirtImaging LLC, Decatur, GA) via a 0.1× or 0.35× demagnifier. The CCD frame corresponded to an area of approximately 320 or 91 μm^2 in the object plane with each individual pixel receiving light from an area of ~4×4 or 1.1×1.1 μm^2, respectively. High-speed recordings (20 kHz) were always performed with the 0.35 demagnifier and with 3×3 binning of pixels on the chip, the ultimate pixel sizes in these recordings were ~3.4×3.4 μm^2. The two recordings from human cells were performed under a 100× NA 1.1 Nikon objective (MRL07920) in combination with a 0.1 demagnifier, resulting in a pixel size of ~2.4×2.4 μm^2 (see **Figure 1–figure supplement 1**).

The epifluorescence light path consisted of an excitation LED light source, which were collimated using ACL5040U-A aspheric lens (Thorlabs, Germany) and the appropriate excitation filter, dichroic mirror and emission filter. For OGB-1 and OGB-5N excitation a 470 nm LED was used (SP-01-B4, Luxeon Star LEDs, Canada), the excitation light was filtered with 475/30 nm (475 nm center wavelength, 30 nm wide) excitation filter, reflected to the preparation by a dichroic mirror with a central wavelength of 500 nm and the fluorescence light was passed through a 520 nm barrier filter (U-MWB2 cube, Olympus). For SBFI excitation, LED light (365 nm LED, LZ1-10UV00, Ledengin, USA) was filtered by 357/44 nm filter (FF01-357/44-25, Semrock), a dichroic mirror with edge at 415 nm (Di03-R405-t1-25×36, Semrock) reflected excitation light to the sample and the emission light was then passed through a long-pass colored glass filter with the edge at 400 nm (FGL400, Thorlabs). For combined Na^+ and Ca^{2+} imaging (**Figure 6–figure supplement 1**), the light from the 365 and 470 LEDs was combined by a dichroic mirror with edge at 458 nm (FF458-Di02, Semrock) and the filter set switched between trials. Light was directed through a fluorescence illuminator (BX-RFA, Olympus) equipped with a rectangular field stop providing an open area of 150×250 µm to reduce phototoxicity (U-RFSS, Olympus). The cell body was positioned just outside the field stop and the axon in the middle parallel to the long side (see e.g. **Figure 1**).

The critical benefit of epifluorescence measurements over two-photon imaging is increased light collection (~90% quantum efficiency, low-read noise of the CCD camera) enabling a high sensitivity and temporal fidelity. We optimized all imaging parameters to obtain maximal signal to noise ratio, which allowed us to image at the maximum acquisition rate of 20 kHz. In addition to the light collection optimization and selective targeting of superficial neurons, multiple trials were averaged to improve signal-to-noise ratio (typically

20-40). Fluorescence signals were temporally aligned to the electrophysiological voltage or current signals. For optical recording of I_{Ca}, which requires the transformation of ΔF/F into the first time derivative, Ca^{2+} binding to the indicator must be proportional to $[Ca^{2+}]_i$ and the endogenous buffering capacity to be low. Based on the submillisecond equilibration time of OGB-5N and imaging at the maximally possible frame rate of 20 kHz it was recently shown that in CA1 hippocampal neurons these conditions are met and optically recorded I_{Ca} tracks electrically recorded I_{Ca}, enabling the identification of Ca_V channel subtypes in dendrites (Jaafari et al., 2014). Considering the low buffering capacities of endogenous buffers in the axon ($\kappa_s \approx 20$) (Jackson and Redman, 2003; Delvendahl et al., 2015), we employed this technique in the AIS. Ca^{2+} imaging in HEK-293 cells was performed with 0.1 mM OGB1 added to the HEK-293 cell intracellular solution (from which EGTA was omitted). The fluorescence was recorded during a 200 Hz 1 s train of depolarizing pulses from –120 to –30 or –20 mV (corrected for liquid junction potential).

Voltage imaging

Voltage imaging in neurons was performed as reported previously (Hamada et al., 2017). Neurons were filled with intracellular solution containing JPW3028 (0.8 mM) for typically 1h at room temperature, after which the patch pipette was retracted and the dye was left to diffuse into the lipid membranes for 1–4 h. Subsequently the bath temperature was increased to 35 °C and the cell was re-patched with normal intracellular solution. A 530 nm LED (SP-05-G4, Luxeon Star LEDs, Canada) was used for excitation of the dye. The excitation light was filtered with a 530/20 nm filter (BP510-550, Olympus), reflected to the sample by a dicroic mirror with a center wavelength of 570 nm (DM570, Olympus) and the emission light filtered by a 590 longpass filter (BA590, Olumpys). Data were collected at 20 kHz and low-pass filtered by a binomial filter (1 pass) and averaged over 20–30 trials. Voltage imaging in HEK-293 cells was performed identically, with the only exception being that the experiments were performed at 20 °C and the dye diffused equally in the small round cells, so imaging experiments were initiated 20 minutes after obtaining whole-cell configuration. The cells were maintained at –75 mV holding potential and the fluorescence of JPW3028 recorded at 1 kHz. The voltage command consisted of 100 ms steps of 50 mV increasing steps with a maximal step of +250 mV relative to holding potential. The average ΔF/F per voltage step was defined as the first 20 frames of each bleach corrected and normalized voltage step.

Imaging data analysis

Imaging data analysis was performed using Neuroplex (Redshirt imaging), Axograph and Excel. Fluorescence signals were always background-subtracted. To correct for bleach effects, every 5th trial was recorded without current injection. A first order exponential was fitted to the average of the bleach trials and normalized to the peak. The average of the signal trials was divided by this trace to correct for bleach decay. Values for each ROI were defined as a fractional fluorescence change ($\Delta F/F_{baseline}$), where $F_{baseline}$ is the raw intensity average of 10 frames before the signal (subthreshold or AP) was initiated. Pixels were color coded with "physics" color scheme from FIJI image processing software (NIH, USA) (Schindelin et al., 2012). For both OGB-1 and OGB-5N, we recorded the fluorescence in response to subthreshold stimuli, single APs and multiple APs. The $\Delta F/F$ response to subthreshold stimuli and a single AP was always below dye saturation. For OGB-1, we recorded trains of APs and observed that a single AP was 25 ± 2.7 % of dye saturation (n = 8) and for OGN-5N, we observed a linear increase from 1 to 3 APs (n = 3), indicating that the fluorescence of a single AP was far from dye saturation.

Optical current measurements

To compare kinetics between electrically and optically recorded currents, electrical currents were first downsampled to 20 kHz (optical acquisition rate). The optical trace was differentiated and then inverted (to mimic I_{Na}, which is conventionally depicted as a negative, inward current). All current traces were then filtered with a 3-window binomial filter of 50-150 iterations (generally 100). The traces were baselined to the current before the onset of the fast current and normalized to the peak of the current. Because the I_{Ca_opt} traces were too noisy to be fitted with a single exponential fit, conventionally used to obtain activation rise time, we used a Boltzmann sigmoid function to obtain the slopes of the traces.

$$y = bottom + \frac{(top - bottom)}{1 + e^{\left(\frac{x - x_0}{k}\right)}}$$

We fitted all traces using Axograph and the slope values (k) were used to compare activation kinetics. Although the I_{Na} peak amplitude recorded at the soma highly varied between neurons (–36.61 ± 6.53 nA), the slope was nearly constant (207 ± 0.007 µs, n = 17).

Ratiometric imaging

To estimate the absolute $[Na^+]_i$ and $[Ca^{2+}]_i$ in response to a single AP, we used a ratiometric imaging approach. Patch pipettes were front filled with clear intracellular solution and back-filled with intracellular solution containing 1.5 mM SBFI (Invitrogen) or 200 µM bis-Fura-2 hexapotassium salt (bF2, Biotium). Fluorescent emission of ratiometric indicators depends on the ionic concentration and the excitation wavelength where an increase in $[Ca^{2+}]_i$ produces an increase in bF2 fluorescence with the wavelength of 340 nm but a decrease with 385 nm. On the other hand, with SBFI an increase in $[Na^+]_i$ decreases SBFI fluorescence at 340 nm but no change at 385 nm excitation wavelength. Using the ratio (R) corrects for differences in cytosolic volume or dye concentration differences along imaged compartments (Langer and Rose, 2009). The sources of excitation light were two LEDs (Thorlabs) with peaks at 340 nm and 385 nm, fitted with band pass excitation filters at 340/22 and 387/11 nm (FF01-340/22-25 and FF01-387/11-25, Semrock) and combined by a dichroic mirror with a central wavelength of 376 nm (FF376-Di01-25x36, Semrock). The excitation light was reflected to the sample by a dichroic mirror with a central wavelength at 405 nm (Di01-R405-25x36, Semrock) and passed through the objective (60×, NA1.1, Olympus) to the sample. The fluorescent emission signals were passed through a 420 long pass filter (Thorlabs). Ratiometric imaging was performed by alternatingly triggering each LED at the frame rate of the camera, as described previously (Miyazaki and Ross, 2015). This was achieved by combining custom designed Arduino/Parallax machines with Cyclops LED drivers. These hardware solutions allowed us to digitally control the voltage driving the LED, thus having maximum control over excitation light intensity. Fluorescence emission signals originating from each LED were separated with custom written software (FrameSplitter.txt (Battefeld et al., 2018)). The camera operated at 0.5-1.0 kHz, resulting in a ratiometric frame rate of 0.25–0.5 kHz. Per experiment the fluorescent signals were averaged for 40 to 120 trials. The ratio R was defined as F_1/F_2, where F_1 and F_2 are the background-subtracted fluorescence intensities at excitation with 340 nm and 385 nm, respectively.

Calibration of ratiometric imaging

In order to scale ratiometric bF2 signals to absolute changes in Ca^{2+} concentration, we used the standard equation for ratiometric measurements (equation 1 in **Figure 8–figure supplement 2**) (Grynkiewicz et al., 1985), which depends on K_D, the dissociation constant, R_{min} and R_{max}, the ratio in zero and dye-saturating Ca^{2+}, respectively and the scaling factor (S_{f2}/S_{b2}), defined as the fluorescence intensity at excitation with 385 nm of zero Ca^{2+} divided by saturating Ca^{2+}. These values were determined in an *ex situ* calibration, by measuring the ratiometric signal of solutions containing 0 Ca^{2+} and a high $[Ca^{2+}]$ (**Figure 8–figure supplement 2**). The solutions closely mimicked intracellular solutions and contained (in mM): 110 K-gluconate, 4.4 or 21 KCl, 0 or 10 $CaCl_2$, 3.8 or 5.36 $MgCl_2$, 10 HEPES, 4 Mg-ATP, 0.3 Na_2-GTP, 10 Na_2-phosphocreatine, 10 EGTA, and 0.2 bF2. The final free $[Ca^{2+}]$ depends on interaction between Ca^{2+}, Mg^{2+} and EGTA and was calculated using the maxchelator tool (Bers et al., 2010)

$[Ca^{2+}]_{min}$ was 0 and $[Ca^{2+}]_{max}$ was 4.39 µM. We repeated the entire calibration experiment 3 times. In our experimental setting, the K_D of bF2 was 507.3 ± 5.7 nM, which matches with the reported value of 525 nM in the presence of Mg^{2+} (Thermofischer, 2015). We then performed ratiometric imaging in the AIS in response to a single AP. $\Delta R/R$ was calculated by dividing every ratio by the average of the baseline ratio before the onset of the AP (similar to the conventional $\Delta F/F$). We used the K_D as determined from our calibration experiments. The R_{min} was scaled to be ~95% of $R_{baseline}$ to result in resting $[Ca^{2+}]_i$ of 50 nM and R_{max} as established in the calibration experiments. If the LED intensity of the cellular recording was different from the calibration intensity used during the calibration experiments, the R_{max} was corrected linearly, assuming that R_{min} / R_{max} was constant. These experiments showed that after a single AP, $[Ca^{2+}]_{free}$ in the AIS rises with 55.6 ± 12.6 nM (see **Figure 8–figure supplement 2**).

Because R_{min} and R_{max} were not measured *in situ* we verified the $\Delta[Ca^{2+}]_{free}$ with an alternative analysis that is independent of the exact values for K_D, R_{min} and R_{max} (equation 2 in **Figure 8–figure supplement 2**) (Langer and Rose, 2009). In this approach, changes in fluorescence ratio $\Delta R/R_0$ (%) are plotted versus $[Ca^{2+}]_{free}$, showing a nearly linear increase in $\Delta R/R_0$ (%) for low $[Ca^{2+}]_{free}$ (see **Figure 8–figure supplement 2**). A linear fit to the region of $[Ca^{2+}]_i$ between 0 and 193 nM indicated that a 1% increase in $\Delta R/R_{bF2}$

corresponded to a $\Delta[Ca^{2+}]_i$ of ~10.4 nM ($R^2 = 0.99$, 6 concentrations, $n = 3$ repetitions). We measured an AP-evoked $\Delta[Ca^{2+}]_{free}$ of 52.5 ± 12.2 nM (**Figure 8–figure supplement 2**), in good support of the standard Ca^{2+} measurement approach. We analyzed the ratiometric SBFI data only using this second approach, which is standard for SBFI measurements (Langer and Rose, 2009). The two base calibration solutions contained (in mM): 130 K-Gluconate or Na-Gluconate, 10 KCl of NaCl, 0.3 $Tris_2$-GTP or Na_2-GTP, 10 HEPES, 4 Mg^{2+}ATP, 10 $Tris_2$-phospocreatine or Na_2-phospocreatine, and 1.5 SBFI, pH 7.25 adjusted with Tris base. These two base solutions provided a range of 0 – 160.6 mM $[Na^+]$. When normalized to the ratio obtained in Na^+-free solution (R_0), a 1% increase in $\Delta R/R_{SBFI}$ corresponded to a $\Delta[Na^+]_i$ of 0.35 mM for $\Delta[Na^+]_i$ between 0 and 48 mM ($R^2 = 0.98$; 8 concentrations, $n = 3$ repetitions, **Figure 8–figure supplement 2**). An AP evoked a $\Delta[Na^+]_i$ of 1.49 ± 0.2 mM (**Figure 8–figure supplement 2**).

Immunofluorescence staining

Following imaging experiments, the slices were fixed using 4% PFA in 0.1 M phosphate-buffered saline (PBS), pH 7.4 for 20 minutes and stored in 0.1 M PBS, pH 7.4 at 4 C°. For triple immunohistological labeling the slices were washed three times in PBS and then incubated in a blocking solution (10% normal goat serum, 0.5% Triton X-100 in PBS) at room temperature for two hours, followed by 24 h incubation at room temperature in the blocking solution containing primary antibodies: streptavidin Alexa-488 conjugate (1:500; Invitrogen), primary antibody for giant saccular organelle Synaptopodin (rabbit; 1:500; Sigma-Aldrich Chemie) and antibody for AIS marker: Ankyrin G (mouse; 1:100; Neuromab) or ßIV-spectrin (mouse; 1:250; Neuromab, see also Key Resources Table). The slices were 3x washed in 0.1 M PBS and then incubated with secondary antibodies: Alexa-555 goat anti rabbit IgG (1:500; Invitrogen) and Alexa 633 goat anti mouse IgG (1:500; Invitrogen). Subsequently, the slices were 3x washed in 0.1 M PBS and mounted with Vectashield mounting media with 4,6-diamidino-2-phenylindole (DAPI; Vector Laboratories). Images (bit depth, 8) were collected as described previously (Hamada et al., 2016). To align confocal images and the Ca^{2+} fluorescence images of the RedShirt CCD camera (**Figure 1**, **2** and **4**) we used the original calibrated images of the two systems. The maximum Ca^{2+} fluorescence image was calibrated within the original optical path. We overlaid the maximum Ca^{2+} fluorescence image of the RedShirt camera and the maximum projection of the streptavidin image of the neuron morphology from confocal microscopy within ImageJ and applied only a rotation translation to visually match the two images based on the AP-evoked Ca^{2+} signals spreading into dendrites and axons.

Model simulations with single compartment

All model simulations were performed with NEURON (v.7.5) (Hines and Carnevale, 2001). A single compartment was created with length and diameter dimensions of 10 µm and *nseg* = 10, with specific membrane capacitance of 1.0 µF cm^{-2}, specific membrane resistance of 25 kΩ cm^2 and specific axial resistivity of 150 Ω cm. The resting membrane potential set to –77 mV using e_pass. Conductance models for Ca^{2+} were based on the high-voltage activated (CaH) and a T-type Ca_V channel model (CaT) obtained from ModelDB (https://senselab.med.yale.edu/ModelDB/) (Mainen and Sejnowski, 1996). Ca^{2+} conductivity of Na_V channels was modeled by including a standard ohmic Ca^{2+} ion mechanism with a reversal potential (*eca*) of +140 mV into a mathematical 8-state Na^+ conductance model, computing simultaneously voltage- and time-dependence of the Ca^{2+} current $I_{Ca(Na)}$ and I_{Na} based on experimentally constrained rate constants of somatodendritic and axonal I_{Na} (Schmidt-Hieber and Bischofberger, 2010). The kinetics of the voltage-gated conductance models was examined by fitting the current rise times with an exponential function for a –35 mV command potential, resampling the simulated traces to 20 kHz. The results showed that the I_{Na} in the model activated with 240 µs and $I_{Ca(Na)}$ (0.5% conductivity ratio) with 280 µs. In comparison, I_{CaT} activated with 4.88 ms and I_{CaH} with 6.51 ms. These time constants are well in range of the experimentally determined values for the TTX- and Ni^{2+}-sensitive components recorded at the soma (**Figure 5**). For **Figure 8–figure supplement 1** we used an AP recorded from the L5 pyramidal neuron AIS at 100 kHz (threshold-to-peak, 94 mV; half-width duration of 285 µs (Hallermann et al., 2012) as the command potential in VectorPlay linked to the SEClamp function in NEURON (with R_s being infinitely small). Single compartmental models were run at *dt* of 10 µs at a nominal temperature of 33 °C.

Model simulations with a multicompartmental model

Conductance-based multi-compartmental simulations were performed with an anatomically realistic reconstructed rat L5 pyramidal neuron (NeuroMorpho.Org ID:

NMO_75667, Neuron Name 2014-04-01_1). The morphology was acquired with a confocal microscope at 2048 × 2048 pixels (1.0 µm *z*-steps, Leica SP8) using a 40× oil-immersion objective (NA 1.3) scanning both the biocytin-streptavidin fluorescence and the ßIV-spectrin fluorescence. Uncompressed image stacks (~20 GB) were imported and reconstructed into Neurolucida (v.10, MBF Bioscience Inc., Germany), compartmentalized for the AIS and nodes as described previously (Hamada et al., 2016) and imported with the 3D import tool in NEURON (Carnevale and Hines, 2006). Multicompartmental simulations were performed to estimate the detailed ionic accumulation, concentration and diffusion in the proximal sites of the axon and match our experimental recordings as close as possible. Ca^{2+} diffusion, buffering and pump (cdp) mechanisms were implemented based on the algorithms described in the NEURON book (Chapter 9, example 9.8 in (Carnevale and Hines, 2006)) and on a previously published Ca^{2+} model (Fink et al., 2000) (available at ModelDB, accession number 125745, https://senselab.med.yale.edu/ModelDB/). We implemented cdp.mod (Fink et al., 2000) with the following alterations: we removed all SERCA related parameters, updated some starting values to our experimental conditions and extended the models to report not only $[Ca^{2+}]_i$, but also to simulate the Ca^{2+} indicator response ΔF/F, using the equation:

$$\mathrm{F} = \frac{[dye]_{free} + c * [\mathrm{Ca}^{2+} + \mathrm{buffer}]}{[dye]_{total}}$$

With *c* being a constant to scale simulated ΔF/F. Because the equation was used to match the simulation to experimental data with regard to the temporal dynamics of Ca^{2+} extrusion, the absolute amplitude of ΔF/F was not used and *c* was set to a nominal value of 6. The different Ca^{2+} indicators used experimentally were implemented by adjusting the concentration of the exogenous buffer, and its known or measured K_D. Static Ca^{2+} buffering properties of endogenous organelles (κ_s) were simulated with a TBufs of 100 – 400 µM and KDs of 10 µM, to mimic a κ_s of 10 – 40 (Jackson and Redman, 2003; Delvendahl et al., 2015).

To constrain the peak Na^+ conductance densities ($\bar{g}_{Na}$) we injected a 3 ms square current pulse in the somatic compartment and iteratively adjusted $\bar{g}_{Na}$ and $\bar{g}_K$. We varied both their peak conductance densities as well as the voltage-dependence of activation of Na_V and K_V

channels by constraining the model AP to the experimentally recorded AP of the same neuron, with the aim to match the AP both in the *V-t* as well as the phase-plane dimensions recorded and simulated at 100 kHz (**Figure 7c**). To further constrain $\bar{g}_{Na}$ we compared the AP-evoked $[Na^+]$ with the experimental recordings using the ratiometric indicator SBFI, yielding a $\Delta[Na^+]_i$ of on average ~1.5 ± 0.2 mM (*n* = 5, imaged at 0.5 kHz; **Figure 8–figure supplement 2**). Ca_V channels were incorporated based on previously published models (Mainen and Sejnowski, 1996) and Ca_V channel conductance was separated in high- and low-voltage (T-type) activated channels and was varied between 2 and 4 pS μm^{-2} in the AIS, 8 and 4 pS μm^{-2} in the soma and ranged between 0.5 and 4 pS μm^{-2} in the dendrites.

Statistics and data availability

All statistical tests were done in GraphPad Prism 8 (version 8.1.2, GraphPad Software, Inc.). Sample sizes for the pharmacological experiments were estimated based on the following assumptions: to observe a 50% block (based on (Bender and Trussell, 2009)) with 25% standard deviation (relative to mean) with a power of 0.8 and a type I error probability of 0.05, we would need a minimum of 4 paired recordings per treatment (PS Software version 3.1.6).

The cutoff significance level (*P*) was 0.05. Control peak ΔF/F values at the AIS in response to both subthreshold and AP signals were tested for normality. Since both data sets passed the D’Agostino & Pearson normality test, parametric tests were used to test all differences between peak OGB-1 ΔF/F. To compare the spatial differences in signals amplitude we used one-way ANOVA multiple comparisons with Tukey correction for false positives. A linear regression was used to assess the synaptopodin and AIS marker length (Ankyrin G or ß4-spectrin) relationship. We used one-tailed ratio (compared log differences in the data set) paired *t*-test when analyzing all our toxin data. Differences between toxin and control give a measure of absolute reduction; differences between logarithms give a measure of relative reduction log toxin – log control = log (toxin/control). One tailed test was used on the premise that toxins reduce Ca^{2+} signals. The exception was the effect of NCX for which we used a two-tailed ratio paired t-test. The OGB-5N peaks in response to subthreshold depolarizations passed the D’Agostino & Pearson normality test and to compare the effects of TTX and QX-314 on subthreshold Ca^{2+} responses we used two-way-ANOVA with Sidak’s correction for false positives. The following data sets passed the Shapiro-Wilk test for normality, so we compared the means using parametric tests: rise and decay times of OGB1 before and after Ca^{2+} store release block, peak ΔF/F JPW3028, peak ΔF/F OGB-5N and slopes of I_{Na}, I_{Ca_opt} and I_{Ca}, the ratio of subthreshold peak to AP peak between sodium (SBFI) and calcium (OGB-5N) fluorescence. The following data did not pass the Shapiro-Wilk test for normality, so we compared the means using nonparametric tests: the slope AP peak between sodium (SBFI) and calcium (OGB-5N) fluorescence, the peak I_{Na} and peak OGB-1 ΔF/F In HEK-293 cells. All data generated or analyzed are in the manuscript or supporting files. The source data files are provided for Figures 1 to 7 and Table 1. The NEURON model morphology is available at NeuroMorpho.Org ID: NMO_75667, Neuron Name 2014-04-01_1 and the mod file used to model Ca^{2+} diffusion and buffering is available at ModelDB, accession 125745 (https://senselab.med.yale.edu/ModelDB/), with adjustments described in ‘Model simulations with a multicompartmental model’.

Chapter 3

Axonal BK channel-mediated action potential repolarization revealed by holographic voltage recordings

Naomi A.K. Hanemaaijer[1,2], Kieran P. Higgins[1,2], Koen Kole[1], Arthur P.J. de Jong[2], Harold D. MacGillavry[2], Maarten H.P. Kole[1,2]

in preparation

Affiliations

[1] Department of Axonal Signaling, Netherlands Institute for Neuroscience (NIN), Royal Netherlands Academy of Arts and Sciences (KNAW), Netherlands
[2] Cell Biology, Neurobiology and Biophysics, Department of Biology, Faculty of Science, Utrecht University, Netherlands

Abstract

Rapid and faithful action potential repolarization is critical to ensure precise signaling and high-frequency action potential firing and is in part mediated by large conductance K^+ (BK) channels. Whether BK channels shape repolarization in the axon initial segment (AIS), where action potential initiation occurs, is not well understood. Here, using holographic illumination to pattern excitation light, we optically recorded and calibrated voltage at high spatiotemporal resolution, and studied the properties of action potential repolarization along the AIS, myelinated internode(s) and first node of Ranvier. We measured a gradient of voltage-gated potassium channels from the soma into the proximal axon setting the action potential width, whereas axonal BK channels contributed predominantly to the fast afterhyperpolarization. Using CRISPR/Cas9 genome editing, we labelled BK channels in the L5 mouse pyramidal neuron and confirmed their presence in the soma and axons. Finally, BK channels were critical to enable high-firing frequencies and required Ca^{2+} entry through voltage gated Ca^{2+} channels with which they formed nanodomains. The findings suggest highly organized Ca^{2+}- BK signaling in the axon to enable high-frequency burst firing.

Introduction

The thick-tufted layer 5 (L5) pyramidal neuron, also referred to as pyramidal tract or extratelencephalic neuron (Kalmbach et al., 2021), located in the primary somatosensory cortex of the rodent, integrates feedforward sensory input from the thalamus with higher-order cortical information, and forms the main output stream to the thalamus, striatum, superior colliculus and pontine and tactile nuclei in the pons (Ramaswamy and Markram, 2015). To encode whisker touch, the L5 pyramidal neuron generates bursts of action potentials (APs) at frequencies up to 300 Hz (Kock et al., 2021; Kole, 2011; Williams and Stuart, 1999; Xu et al., 2012). To fire at high frequencies, biophysical mechanisms for fast and faithful AP repolarization are paramount since it prepares the membrane for a rapid subsequent spike by limiting the time- and voltage-dependent inactivation of the voltage-gated sodium (Na_V) channels. Rapid repolarization of APs is a prominent hallmark of the axon initial segment (AIS), where APs are initiated before they forward propagate into the axon proper and back along the somatodendritic membrane (Kole et al., 2007; Palmer and Stuart, 2006; Shu et al., 2007; Stuart and Sakmann, 1994; Stuart et al., 1997). In the distal AIS, the local AP recorded in whole-cell patch-clamp exhibit a fast afterhyperpolarization (fAHP) of up to ~20 mV in amplitude relative to the AP voltage threshold (Kole and Stuart, 2008; Kole et al., 2007; Shu et al., 2007). Consistent with this shape, current- and voltage-clamp recordings from L5 pyramidal neuron AIS revealed very high densities of voltage-gated potassium (K$_V$) channels of the subtype K$_V$1.1, 1.2 and 1.6, blocked by 4-aminopyridine (4-AP) or dendrotoxin I, accounting for a narrowing of the AP halfwidth to ~250 µs and decoupling the axonal AP from the somatic AP waveform (Kole et al., 2007; Lorincz and Nusser, 2008; Shu et al., 2007). However, whether other conductances are contributing to the AP repolarization in the proximal axon of L5 pyramidal neurons is not well understood.

One important K^+ conductance responsible for the repolarization of single APs is the large-conductance and calcium (Ca^{2+})-activated channel (BK$_{Ca}$ or BK). BK channels are widely expressed in many brain areas, including cerebral cortex, and subcellular regions, including soma, dendrites and presynaptic terminals, as shown by immunoreactivity in mouse (Sausbier et al., 2005) and *in situ* hybridization in rat brain (Knaus et al., 1996). RNA sequencing in mice and human shows that the pore-forming α-subunit of BK channels as well as the β4 subunit is expressed in all excitatory cortical neurons, including the layer 5 PT neuron (AllenInstitute, 2022; Yao et al., 2021). Mutations to the *KCNMA1* gene, coding for the α-subunit of the BK channel, have been linked to neurological pathologies including seizures, movement disorders and developmental delay (Bailey et al., 2019; Typlt et al., 2013). The BK channel has a single-channel conductance of ~180 - 260 pS, an order of magnitude larger than most K$_V$ channels, and is expected to have a large impact on excitability with even a low density of channel numbers (Kang et al., 1996; Womack and Khodakhah, 2002). In the CA1 pyramidal neuron, BK channels mediated the AP width and fAHP, which facilitates high-frequency spike generation (Gu et al., 2007). Previous electrophysiological recordings using local and global pharmacological block have shown that BK channels also prominently contribute to excitability of L5 pyramidal neurons (Benhassine and Berger, 2008; Bock and Stuart, 2016; Gómez et al., 2021; Yu et al., 2010). After evoking individual APs by current injections, the BK channels in the soma, but not those in the apical dendritic tree, increase the rate of repolarization, narrowing AP width and increasing the fAHP (Benhassine and Berger, 2008; Bock and Stuart, 2016; Roshchin et al., 2018). This is consistent with their fast activation kinetics (~1 ms), based on single-channel recording, and immuno-EM identification of BK channels in the L5 pyramidal neuron somata (Benhassine and Berger, 2005; Kang et al., 1996; Kaufmann et al., 2010). Direct axon recordings from L5 pyramidal neurons in ferrets suggested that the BK channels also contribute to the AP repolarization in the AIS (Yu et al., 2010), but whether this extends to other species or the activation mechanisms of axonal BK channels remain unknown.

Importantly, BK channel activation is not only dependent on voltage, but also on intracellular Ca^{2+} levels, which move the voltage-dependence of activation from +200 mV to more hyperpolarized voltages (Berkefeld et al., 2006; Womack and Khodakhah, 2002). The membrane depolarization during the upstroke of the AP opens voltage gated Ca^{2+} (Ca_V) channels, resulting in Ca^{2+} entry, which activates BK channels and causes a large outflux of K^+. Together with the voltage-dependence of the BK channels this Ca_V -mediated Ca^{2+} entry forms a negative feedback loop of membrane de- and repolarization. In various cell types and brain regions, functional coupling of BK channels with Ca_V channel subtypes into nanodomains, has been described (Gutzmann et al., 2019; Hirono et al., 2015; Irie and Trussell, 2017; Marrion and Tavalin, 1998). Nanodomain coupling speeds BK activation and increases fidelity and has been shown structurally by immunogold labeling, such as between P/Q and BK channels in the somata of Purkinje cells (Indriati et al., 2013). We previously investigated AIS Ca^{2+} entry using calibrated ratiometric Ca^{2+} imaging and showed $[Ca^{2+}]_i$ transients up to 1 µM for individual APs and with submillisecond activation speed in the AIS (Hanemaaijer et al., 2020). The rapid and large cytoplasmic rise in $[Ca^{2+}]_i$ could provide a crucial activating pathway for BK channels. Consistent with this idea, local Ca^{2+} uncaging or Iberiotoxin applications to the axon suggest a prominent contribution of axonal BK channels to somatic AP repolarization in L5 pyramidal neurons (Roshchin et al., 2018).

To study how axonal BK channels contribute to local AP repolarization in various regions of the proximal axon, we used high-speed voltage imaging and assessed the AP waveform along the axolemma including myelinated internodes (Cohen et al., 2020; Foust et al., 2010; Popovic et al., 2011, 2012). We employed holographic illumination of the axon, with a patterned excitation beam to limit light exposure and scattering of light to areas outside of the axon such as the soma and out-of-focus basal dendrites and increased confinement of the beam in *z* (Foust et al., 2015, Lutz et al., 2008). The optimized accuracy of the signal, in combination with a voltage calibration approach, allowed us to optically resolve the fAHP along the axon and quantify AP repolarization features. We observed spatially distinct contributions of Kv1 and BK channels to the axonal AP repolarization. Axonal BK channels were activated efficiently and rapidly by Ca^{2+} entering the membrane through voltage-gated Ca^{2+} (Cav) channels, with which they formed nanodomains. BK channels were required to produce high-frequency output of L5 pyramidal neurons, suggesting axonal Ca^{2+} - BK coupling mechanisms to fire at high frequencies. Furthermore, we used the CRISPR/Cas9 knock-in approach ORANGE to label endogenous BK channels in the L5 mouse pyramidal neurons and observed BK channel expression in the soma and axons.

Results

Holographic illumination reliably reveals axonal AP repolarization

To record the detailed shape of the AP in the soma and proximal axon, we combined patch-clamp recording from the soma with optical voltage recording from the axon in acute rat brain slices, using a liquid crystal on silicon–spatial light modulator (LCOS-LSM, X13138-04, Hamamatsu) enabling holographic illumination to restrict excitation light to regions of interest (**Figure 1a, b, Supplemental Figure 1**)(Foust et al., 2015). We selected thick-tufted L5 pyramidal neurons with an axon parallel to the optical imaging plane and filled the neurons with the voltage sensitive dye JPW3028 for ~45 min (n = 105 neurons from N = 74 rats, **Figure 1c**). We used computer-generated hologram to restrict light to the first 90 µm of the proximal axon including the AIS and ~45 µm of the myelinated internode (**Figure 1b, d**). Using an 8 ms current injection we elicited single APs and recorded the membrane potential (V_M) electrically from the soma and optically from the axon at 20 kHz and 3.4 µm pixels, generally averaging 12 trials. The optical AP transients were calibrated using a hyperpolarization pulse method to convert fluorescence to absolute V_M (**Supplemental Figure 2**), as described previously (Cohen et al., 2020). In a subset of experiments, we post hoc fixed the brain slices and stained for intracellular applied biocytin (streptavidin), myelin basic protein (MBP) and the AIS and nodal marker Ankyrin-G or ßIV-spectrin to confirm the positions of the AIS and myelin sheath within the imaged axons (AIS onset: 3.0 ± 0.4 µm, AIS length: 45.2 ± 1.3 µm, n = 19, **Figure 1c**).

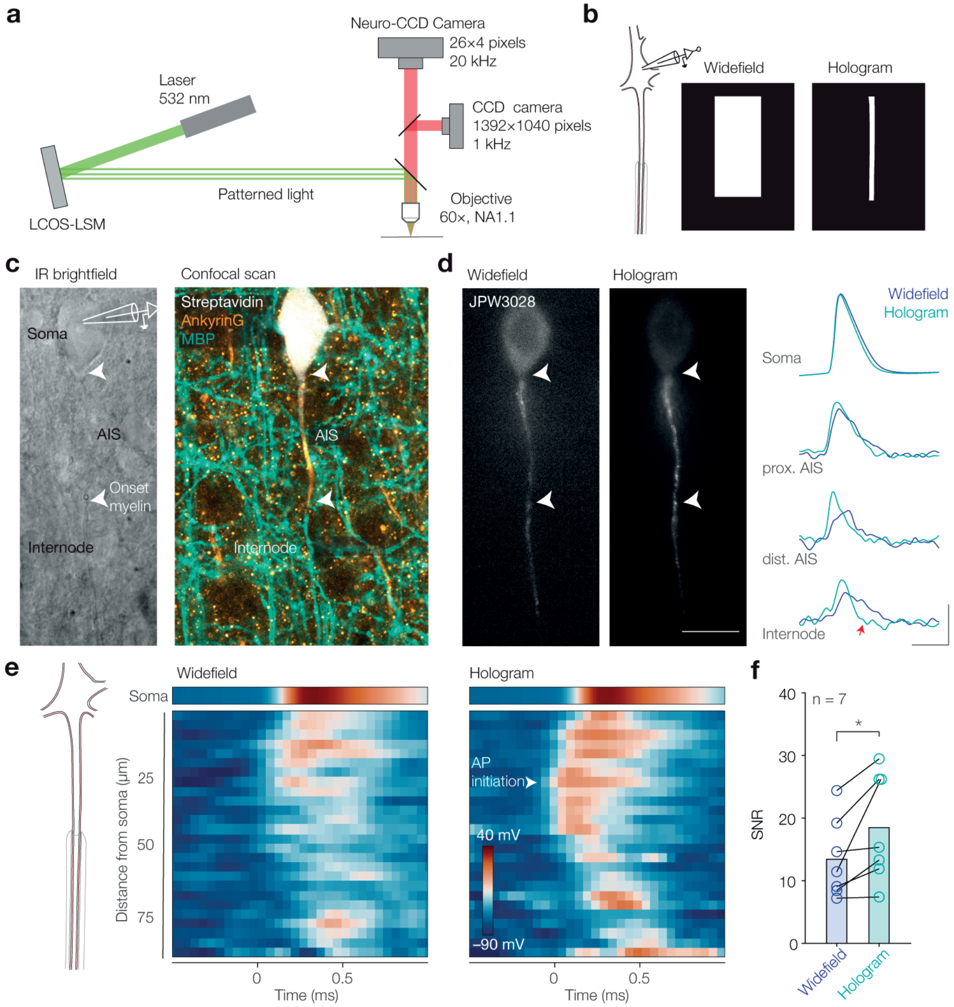

Figure 1. Holographic illumination reveals axonal AP repolarization kinetics
a. Schematic of the optical system: a 532 nm laser excited the tissue and an LCOS-SLM shaped the wavefront of the excitation beam. The light was reflected to the sample using a dichroic mirror. The emitted fluorescence was recorded on a low spatial but high temporal resolution CCD camera. A second CCD camera with low temporal but high spatial resolution was used for patching. See also Supplemental Figure 1. **b**. Left, a schema of a neuron with a patch-pipette and JPW in the membrane. Middle, the pattern shaped by the SLM to mimic widefield illumination. Note that the border of the light pattern is on the edge of the axon: the soma is not excited directly. Right, an example pattern that is used to restrict light to the axon. **c**. A bright-field image of a patched layer 5 pyramidal neuron. White arrows indicate the onset of the AIS and the onset of the myelination. Cells with an axon parallel to the optical plane, as visible in the myelination, were selected. Right, a confocal scan of the same cell, with streptavidin staining of the biocytin filled cell in grey, AnkyrinG in orange and MBP in cyan. – figure legends continues on the next page

We tested the improvement of the holographic patterns by comparing the recording to one obtained in a pseudo widefield excitation (see **Methods** and **Figure 1b, d, e**). Holographic illumination showed a steeper rise and fall of the AP and a fAHP became visible in the axon (**Figure 1b, d, e**). Furthermore, in this example the AP initiation site could be identified at ~27 µm from the soma, corresponding to AP initiation in the distal AIS (Kole et al., 2007; Palmer and Stuart, 2006; Popovic et al., 2011). The improved discrimination of rapid falling kinetics of the axonal AP can be explained by the fact that holography excitation reduces light scattering to the large and bright soma and limits out-of-focus dye emission from in nearby basal dendrites. Since the AP kinetics in soma and dendrites are slower than in the axon, excitation of these regions and the axon simultaneously increases the apparent width of the axonal AP (Foust et al., 2015). Holography allows imaging with higher light intensities without increasing unwanted background emission and thus allows imaging with increasing signal to noise ratio. Consistent with the reduced light scattering and increased excitation, we observed an improved spatial profile of the back- and forward propagation of the voltage wave into the soma and into the internode, respectively, together with a significant increase in the signal-to-noise ratio (widefield: 13.5, hologram: 18.6, paired t-test: $p = 0.035$, $n = 7$, **Figure 1f**). We therefore employed these holography-improved optical recordings to study AP repolarization in the (myelinated) proximal axon.

Spatiotemporal profile of the forward propagating axonal AP

We recorded single APs and quantitatively compared various parameters of the AP from the optical recordings along the AIS and internode at 3.4 µm precision (see **Figure 2a, b, c**). In a subset of recordings, we additionally recorded the AP in the first node of Ranvier

d. The fluorescence of the cell in **c** when excited with a widefield (left) or hologram (middle) pattern. White arrows indicate the onset of the AIS and myelin as in **c**. Note the difference in the background intensity and emission from the soma, even though it is not directly excited in either condition. Right, V_M recorded electrically from the soma (top) and optically from the axon when excited in widefield (dark blue) and with a hologram (light blue). Note the sharper rise and fall of the AP in hologram illumination and the appearance of the AHP, indicated by the red arrow. Scale bars from top to bottom are 50 mV and 1 ms. **e**. Color-coded voltage plots of optical voltage recordings in widefield (middle) and holographic (right) illumination with left, a schematic of a neuron indicating the location of the plots. Calibrated color scale runs from –90 to +40 mV. **f**. Quantitative comparison of the average AIS signal to noise ratio (SNR) for widefield versus holographic illumination. Widefield = 13.5 ± 6.3, Hologram = 18.6 ± 8.6, paired t-test, $p = 0.035$, $n = 7$ cells).

and adjacent internodes at 6.8 µm precision (*n* = 10, **Figure 2a, b**). Although the temporal resolution (20 kHz) and the SNR with optical voltage recordings is much smaller than electrophysiological recordings (~100 kHz), it allows simultaneous recordings from a large

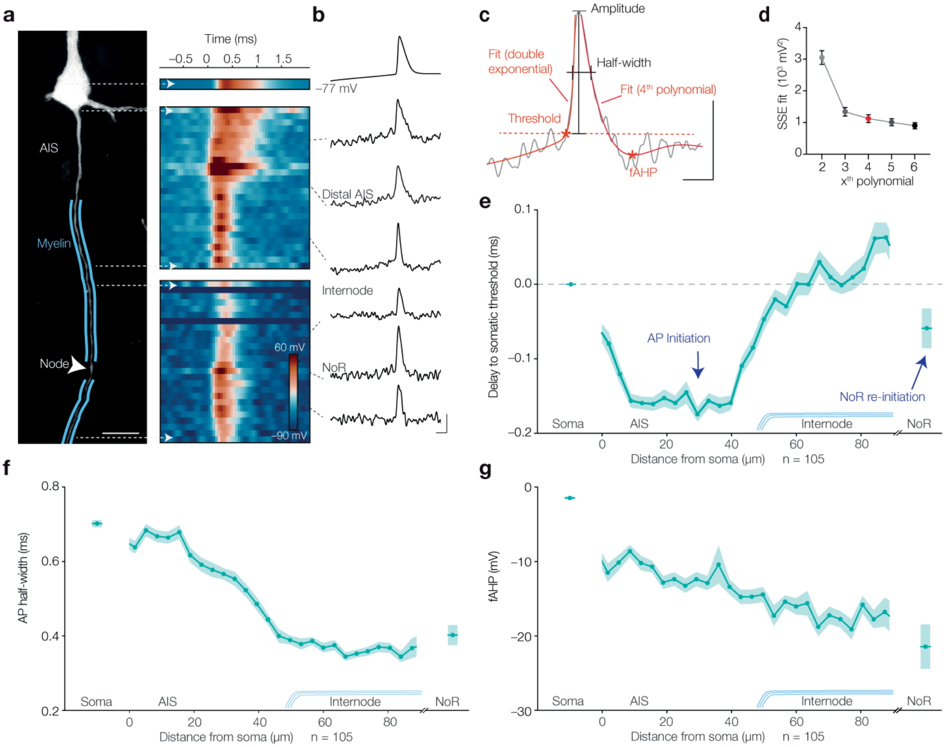

Figure 2. Voltage imaging in AIS and node reveals subcellular diversity in AP repolarization

a. Left, streptavidin staining of a biocytin-filled cell with the AIS, myelin and node of Ranvier indicated. Right, color-coded electrically (top) and optically recorded V_M. Middle and bottom were recorded sequentially. Location of the recordings correspond to the position of the plots relative to the image on the left, see white arrows. Scale bar is 20 µm. **b**. Single pixel traces as **a**, pixel indicated with grey dotted lines. Scale bars from top to bottom are 50 mV and 1 ms. **c**. The third trace from the top from **b** with a double exponential fit to the depolarization phase of the AP and a fourth polynomial fit to the repolarization phase of the AP. Indicated are several quantified parameters: AP threshold, amplitude, half-width and the fAHP. Scale bars from top to bottom are 50 mV and 1 ms. **d**. The sum of squared errors of increasing polynomial fits to the repolarization phase. The 4th polynomial was used to quantify the fAHP. See also Supplemental Figure 3. **e**. The delay from somatic threshold plotted over distance from the soma. Data from the NoR is from separate recordings (n = 10). AP initiation and re-initiation are indicated with dark blue arrows. Location of soma, AIS, myelinated internode and NoR relative to the x-axis indicated. **f**. AP half-width and **g**. fAHP plotted over distance from the soma. Data from the NoR is from separate recordings (n = 10). See also Supplemental Figure 3 for statistics. Location of Soma, AIS, myelinated internode and NoR relative to the x-axis indicated.

path of one single axon, unperturbed by cytoplasmic washout and provides V_M information from membrane sites inaccessible to patch pipettes, such as the myelinated internodal axolemma. To overcome the lower SNR of optical voltage recordings and obtain reliable estimates for the AP voltage threshold and the fast afterhyperpolarization (fAHP) amplitude, we fitted the rising phase of the AP with a double exponential function and the falling phase with 4th order polynomial functions (**Figure 2c, d** and **Supplemental Figure 3**). Despite the lack of models to support these fits, the results revealed an excellent overlap with the V_M dynamics and the obtained parameter estimates had a similar variance when compared to those of electrophysiological data (see **Supplemental Figure 4**).

We spatially averaged traces from the proximal AIS (prox. AIS), distal AIS (dist. AIS) and quantified several features of the AP from multiple regions in the soma and axon. In keeping with earlier voltage imaging studies and patch clamp recordings of the AP in L5 pyramidal neuron axons (Kole et al., 2007; Palmer and Stuart, 2006; Popovic et al., 2011; Shu et al., 2007), we observed AP initiation in the distal AIS (on average at ~30 µm from the soma) and re-initiation in the first Node of Ranvier (**Figure 2e**). The AP spread rapidly through the AIS and antidromically invaded the soma, which due to its large capacity depolarized more slowly, and orthodromically into the internodal aoxolemma, where invasion of the AP is also slower due to charging of the myelin membrane acting as a coupled capacitor (Cohen et al., 2020). In addition, we observed a steep decrease in the AP halfwidth with distance from the soma, even within the AIS, confirming previous axonal patch-clamp recordings (prox. AIS, on average 709 µs, dist. AIS: 535 µs, n = 105, **Figure 2f**, **Supplemental Figure 4**)(Kole et al., 2007). Interestingly, the AP half-width was even narrower within the myelinated internode where it remained constant over ~45 µm and on average 379 µs (n = 105), comparable to the width at the node of Ranvier (on average 403 µs, n = 10). Similarly, we observed a gradual increase of the fAHP with distance from the soma, with the fAHP being –14.7 mV in the myelinated internode, compared to –9.3 mV and –10.9 mV in the proximal and distal AIS, respectively (n = 105 cells). In the node, the fAHP was even lower: –21.5 mV (n = 10 cells, **Figure 2g**). In contrast, the AP peak amplitude was on average 98.3 mV in nodal regions. See **Supplemental Figure 4** for a statistical comparison of the parameters between these regions. These data show that sub-millisecond differences in AP shape along the proximal axon can be reliably quantified with holographic voltage recordings at high spatial and temporal resolution, enabling the investigation of local AP repolarization mechanisms.

4-AP sensitive channels contribute to AP repolarization increasingly with distance from the soma

Voltage gated K_V1 channels contribute to AP repolarization in the AIS and axon proper and the relative impact on the AP when blocking these channels increases with distance from

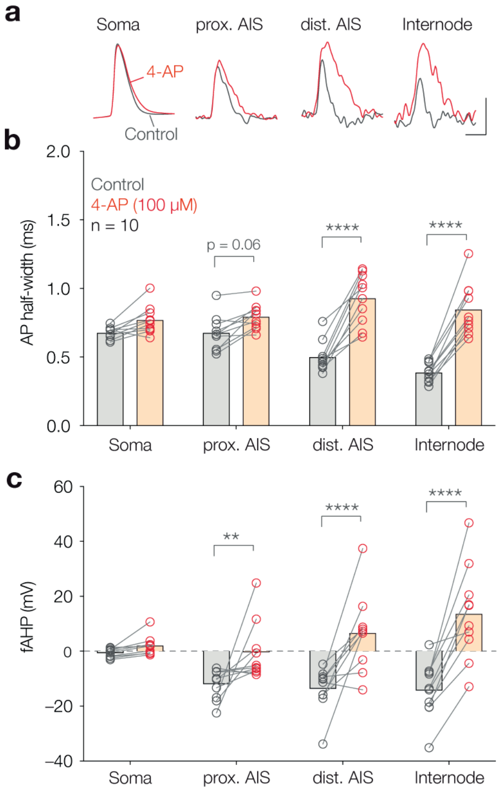

Figure 3. The contribution of 4-AP sensitive channels increases with distance from the soma

a. Example traces from the electrically recorded V_M in the soma and optically recorded V_M in the axon in Control (grey) and after bath application of 100 µM 4-AP (red). Scale bars are 1 ms and 50 mV. **b**. Population data for the AP half-width in Control (grey) and after bath application of 100 µm 4-AP (red). Paired recordings indicated with grey lines. Two-way ANOVA, condition effect: $p < 0.0001$, interaction location x condition: $p < 0.0001$, multiple comparison statistics indicated by stars, n = 10 cells. **c**. Same as **b** for the fAHP. Two-way ANOVA, condition effect: $p = 0.0011$, interaction between location and condition: $p < 0.0001$, multiple comparison statistics indicated by stars, n = 10 cells.

the soma (Kole et al., 2007; Sabater et al., 2021), but how Kv1 channels contribute to AP repolarization in the myelinated axon is not yet quantified. To test whether holographic illumination enables the identification of pharmacological block of axonal Kv1 channels we first examined the stability of optical recordings over time. In control recordings in ACSF we observed no differences in AP amplitude, threshold, AP half-width or fAHP between recordings made at 20 minutes or 40 minutes delay (mixed models, condition, and interaction term not significant for any of the tested parameters, see **Supplemental Figure 5**). Next, we recorded the somatic and axonal AP and subsequently bath applied 100 µM 4-AP, blocking Kv1.x and Kv3.x channels (**Figure 3a**). After a wait period of > 10 min, we observed a significant effect of 4-AP on AP width (two-way ANOVA, $p < 0.0001$, $n = 10$,) and an interaction between location and the drug (interaction term, $p < 0.0001$, $n = 10$, **Figure 3b**). The AP half-width was significantly increased in the distal AIS (control: 499 µs, 4-AP: 927 µs, $p < 0.0001$) and internode (control: 387 µs, 4-AP: 846 µs, $p < 0.0001$). In addition, we observed a significant and location dependent reduction in the fAHP (two-way ANOVA, $p = 0.0011$, $n = 10$; interaction term, $p < 0.0001$, $n = 10$, see **Figure 3c**). More specifically, the fAHP was decreased in the prox. AIS (control: –11.9 mV, 4-AP: –0.36 mV, $p = 0.0015$), dist. AIS (control: –13.6 mV, 4-AP: +6.6 mV, $p < 0.0001$) and internode (control: –14.3 mV, 4-AP: +13.6 mV, $p < 0.0001$). These findings not only confirm that 4-AP sensitive Kv1 and/or Kv3 type channels contribute to the AIS membrane repolarization (Kole et al., 2007), but also demonstrate that APs are actively repolarized by the juxtaparanodal Kv channels positioned below the myelin sheath.

BK channels contribute to different phases of the AP repolarization in a location dependent manner

Next, we investigated the role of BK channels to the repolarization of a single AP in the soma and axon, by using the BK channel blocker Iberiotoxin (IbTx)(Galvez et al., 1990). When the α subunit of the BK channel is accompanied by the ß4 subunit, the blocking effect of IbTx is slower than when only the α subunit is present. In the presence of the ß4 subunit, IbTx blocks ~50% and ~ 90% of the BK current after 2 and 7 minutes, respectively (Meera et al., 2000). Single-cell RNA sequencing in mouse and human shows that the α subunit is expressed in both excitatory and inhibitory neurons, whereas the β4 subunit is mostly expressed in excitatory neurons, including the PT L5 pyramidal neuron, and the β2 subunit

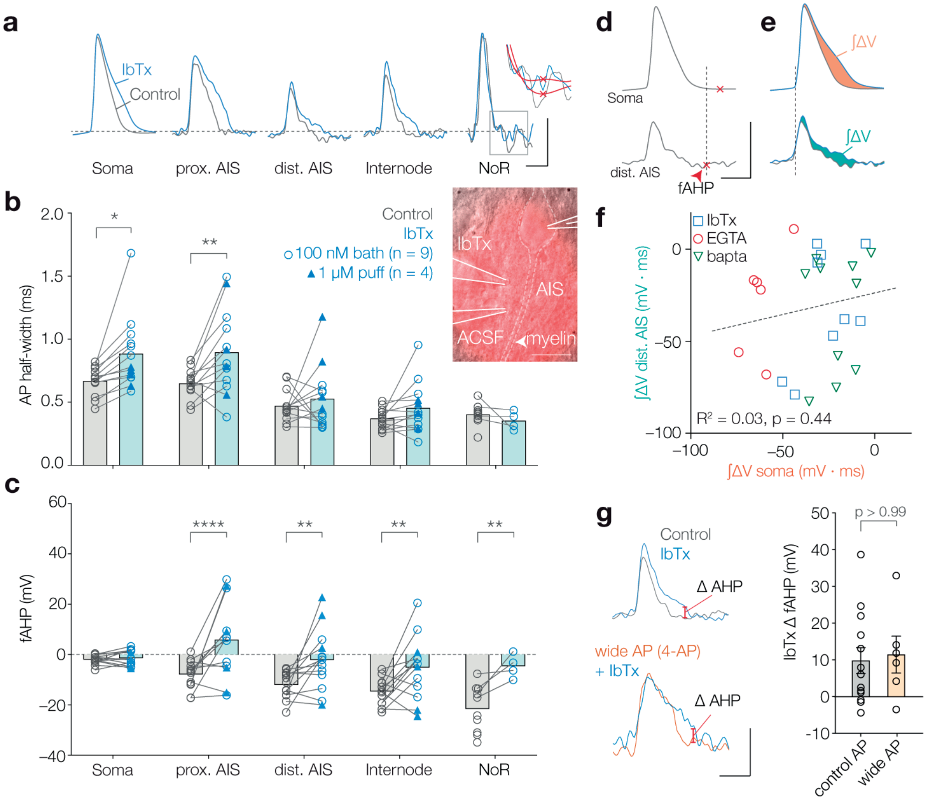

Figure 4. BK channels contribute to different phases of AP repolarization depending on axonal location

a. Example traces from the electrically recorded V_M in the soma and optically recorded V_M in the axon in Control (grey) and after bath application of 100 nM Iberiotoxin (blue). See insert for a zoom in on the nodal fAHP. Scale bars from top to bottom are 50 mV and 1 ms. **b**. Population data for the AP half-width in Control (grey) and after bath application of 100 nM Iberiotoxin (blue circles) or 1 µM puff application (blue triangles). Paired recordings indicated with grey lines. Two-way ANOVA, condition effect: p = 0.0010, interaction between location and condition: p = 0.14, multiple comparison statistics indicated by stars, n = 13 cells. Example of puff experiment in the insert right, with patch pipette and two puff pipettes containing ACSF and IbTx indicated to show the spread of the puffed solutions, scale bar is 20 µm. **c**. Same as **b** for the fAHP. Two-way ANOVA, condition effect: p = 0.0036, interaction between location and condition: p = 0.0056, multiple comparison statistics indicated by stars, n = 13 cells. **d**. Example traces from a showing that the axonal fAHP, indicated by the red cross, precedes the somatic AHP. Scale bars from top to bottom are 50 mV and 1 ms. **e**. The effect of BK channels on the AP was measured as the integral of the difference ∫ΔV between control and IbTx in the soma (orange) and distal AIS (green). **f**. The ∫ΔV between control and several conditions with minimized BK channels activity: IbTx (blue square, 100 nM bath application), EGTA (red circle, 2.5 mM bath application) and bapta (green triangle, 10 mM intracellular application). The effect of BK channels block ∫ΔV on somatic (orange) and axonal (blue) AP is independent. There was no correlation between the soma and distal AIS. Simple linear regression, R^2: 0.026, p = 0.43. – figure legend continues on the next page is preferentially expressed in interneurons (AllenInstitute, 2022; Yao et al., 2021), suggesting that to block most BK channels in the L5 pyramidal neuron a sufficiently long waiting period is required. In line with previous studies of BK channels in the L5 pyramidal neuron (Bock and Stuart, 2016; Roshchin et al., 2018), we observed a significant broadening of the somatically recorded AP after 10 minutes IbTx application (**Supplemental Figure 6**). Paxilline, an alternative BK channel blocker not affected by ß subunits (Sanchez and McManus, 1996), similarly increased the AP half-width (100 nM IbTx 956 µs, 10 µM paxilline: 843 µs, Kruskas Wallis test, multiple comparisons: $p > 0.99$, see **Supplemental Figure 6**). The data indicate that >10-minutes bath application of 100 nM IbTx completely blocked BK channels.

Following a baseline recording, we applied IbTx in the bath solution (100 nM, $n = 9$ cells, **Figure 4a**) or focally to the AIS via a puff pipette (1 µM in the puff pipette, $n = 4$ cells, **Figure 4b**). Puff application of ACSF had no effect on AP with or fAHP in any region (two-way ANOVA: AP width: $p = 0.65$, fAHP: $p = 0.16$, $n = 5$, data not shown). Bath or puff application of IbTx significantly affected the AP width (two-way ANOVA: $p = 0.0010$, $n = 13$, **Figure 4b**). Specifically, the AP width was increased in the soma (control: 669 µs, IbTx: 884 µs, $p = 0.012$) and in the prox. AIS (control: 650 µs, IbTx: 897 µs, $p = 0.0031$), but not the distal AIS and internodes ($p > 0.63$). The effect of IbTx on the fAHP showed a different spatial profile (two-way ANOVA: $p = 0.0036$, interaction condition x location: $p = 0.0056$, $n = 13$, **Figure 4c**), with a significant decrease in the prox. AIS (control: –7.9 mV, IbTx: +6.0 mV, $p < 0.0001$), dist. AIS (control: –12.0 mV, IbTx: –2.1 mV, $p = 0.0015$) and internode (control: –14.6 mV, IbTx: –5.2 mV, $p = 0.0026$). In a separate set of experiments, we recorded the effect of bath application of IbTx on the AP shape in the node. Similar to the distal AIS, 100 nM IbTx did not affect the nodal AP half-width (control: 403 µs, $n = 10$, IbTx: 354 µs, Mann-Whitney test, $n = 4$, $p = 0.37$), but reduced the fAHP (control: –21.5 mV, $n = 10$, IbTx: –4.6 mV, $n = 4$, $p = 0.004$, Mann-Whitney test, see **Figure**

g. BK channels in distal AIS are not activated more by a wider than a normal AP. We compared the effect of IbTx (blue) to the fAHP in distal AIS in case of a normal AP (grey) and a larger, wider AP caused by application of 100 µM 4-AP (orange). Scale bars from top to bottom are 50 mV and 1 ms. Right: two-way ANOVA, condition: $p = 0.97$, multiple comparison for fAHP in distal AIS: $p > 0.99$, normal AP: $n = 13$, wide AP: $n = 6$.

4a, b, c). Together, the data suggest that BK channels contribute to AP repolarization in the soma and axon. In the soma and proximal AIS, BK channels mostly contribute to the width of the AP, whereas in distal AIS, internode and node, BK channels increase the fAHP.

Uncoupling of somatic and AIS AP

Are BK channels present in the axon or could the observed effect in the axon be passive voltage reflection of the wider AP in the soma? To answer this question, we first tested the coupling of the somatic AP and axonal AP in control conditions by correlating AP width and fAHP in the soma and distal AIS. The fAHP in soma and the AP width in distal AIS did not correlate ($r = –0.03$, $p = 0.79$, $n = 105$), corresponding to the axonal AP fAHP preceding the somatic fAHP by ~400 µs (fAHP delay from threshold soma: 2.38 ms, distal AIS 1.98 ms, (see **Figure 4d**). In addition, we found significant, but weak correlations for somatic AP and axonal AP width (Spearman correlation, $r = 0.45$, $p < 0.0001$, $n = 105$, data not shown) and somatic AP width with axonal fAHP ($r = 0.24$, $p = 0.013$, $n = 105$). The somatic fAHP was significantly, but weakly correlated with the AIS fAHP ($r = 0.41$, $p < 0.0001$, $n = 105$). The data suggest that only a small fraction of the variability in axonal repolarization is caused by the repolarization of the somatic AP and thus that the two regions are electrically only loosely coupled (Brette, 2013; Kole and Brette, 2018). Next, we checked if the IbTx effect in the AIS could be explained by a wider somatic AP by testing if the effect of blocking BK channels in the two regions was dependent. We quantified the degree of a BK block effect by taking the integral of the difference between the control and IbTx AP: $\int \Delta V_{\mathrm{IbTx}}$ (**Figure 4e**). We only included recordings where we bath applied IbTx and to strengthen the analysis, we included recordings where we blocked BK channel activation by removing extracellular or intracellular Ca^{2+}, through application of 2.5 mM extracellular EGTA and 10 mM intracellular bapta, respectively. A linear regression showed insignificant, weak correlations for these conditions individually, as well as combined (simple linear regression, IbTx $R^2 = 0.24$, $p = 0.18$, $n = 9$, EGTA: $R^2 = 0.36$, $p = 0.21$, $n = 6$, bapta: $R^2 = 0.02$, $p = 0.70$, $n = 10$, combined: $R^2 = 0.03$, $p = 0.44$, $n = 25$, **Figure 4e**). The data show that BK block acted independently in the soma and axon and thus that the IbTx effect in the axon cannot be explained as passive reflection from the soma, suggesting that BK channels are present and active in the axon.

BK channels are maximally active during a single AP

BK channels are both voltage and Ca^{2+} dependent and require a combination of depolarization and high intracellular Ca^{2+} levels to activate (Berkefeld et al., 2006). In the mossy fiber bouton, BK channels are not activated by a control AP of ~ 1 ms, however a wider AP, mediated by first blocking Kv3 channels, did activate BK channels (Alle et al., 2011). Given the narrow AP in the dist. AIS (535 μs), we hypothesized that the depolarization trajectory of a single AP may not be sufficient to activate all BK channels and that we would observe a bigger effect of IbTx with a larger and wider AP. To test this hypothesis, we used 4-AP application to enlarge the AP in the axon, leading to a higher amplitude, wider AP and decreased fAHP (**Figure 3b,c**). We surmised that in addition to the increased membrane depolarization, Ca^{2+} levels in the axon would also rise higher, providing conditions were BK channels would open maximally. Next, we added IbTx to the bath and recorded the AP again (**Supplemental Figure 7a)**. IbTx had an additional effect on the AP width in the soma and prox. AIS (two-way ANOVA multiple comparisons between 4-AP and 4-AP + IbTx: Soma: $p = 0.0012$ and prox. AIS, $p < 0.0001$, **Supplemental Figure 7b**). IbTx also had an additional effect on the fAHP in the distal AIS and internode (two-way ANOVA multiple comparisons between 4-AP and 4-AP + IbTx: dist. AIS: $p = 0.044$ and internode, $p = 0.0032$, **Supplemental Figure 7c**). The data shows that the effect of blocking BK channels was additive to $K_V1.x$ channels. Next, we tested if a 4-AP mediated larger AP in the distal AIS activated more BK channels (**Figure 4e**). The absolute change in fAHP caused by IbTx was not different when it was relative to control (+9.9 mV) and to a 4-AP-mediated larger AP (+11.6 mV, two-way ANOVA multiple comparisons: $p > 0.99$). This shows that BK channels are not differently activated by a larger AP and surprisingly, that they are maximally activated by a normal AP, suggesting highly efficient activation of BK channels during the trajectory of an axonal AP.

Rapid BK channel activation requires Ca_V channels

The unexpected complete activation of BK channels in the distal AIS with a small and narrow AP (59 mV and 535 μs) suggested that BK channels are activated by a rapid and highly efficient Ca^{2+} route. To compare the activation kinetics of BK channels between AIS and soma, we quantified the temporal delay of BK channel onset and peak activation. We subtracted the APs measured in IbTx from control to obtain the BK mediated ΔV and fitted a double exponential fit to the activation of the BK channel-mediated ΔV (see **Figure 5a**). The onset of ΔV was significantly earlier in the distal AIS compared to the soma (soma: 439 µs, n = 13, dist. AIS: 190 µs, n = 11, unpaired t-test: p = 0.0039, **Figure 5a**). The difference in onset delay suggests that the two regions have separate BK channels activation

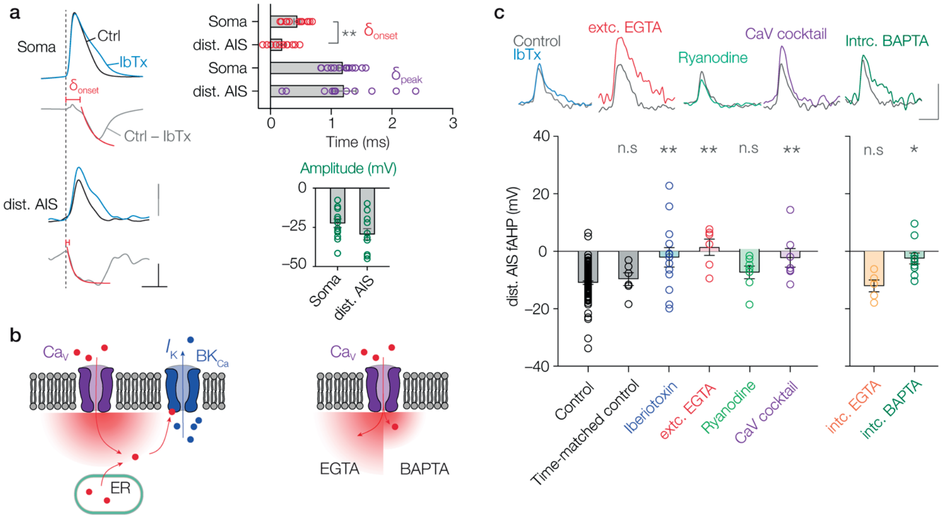

Figure 5. AIS BK channels activate rapidly and rely on nanodomain coupled Ca_V channels
a. BK channels are activated more rapidly in distal AIS than soma, but delay from threshold to peak and peak amplitude is not different. Left: the activation of BK channels was quantified by subtracting the IbTx AP (blue) from the control AP (grey) in the soma (top) and distal AIS (bottom). From the subtracted trace, we quantified the BK onset by fitting a double exponential curve to the activation (red). Scale bars from top to bottom are 50 mV, 20 mV and 1 ms. Right top: population data for the onset delay (red, unpaired t-test: p = 0.00439), peak delay (purple, paired t-test: p = 0.92) and peak amplitude (green, paired t-test: p = 0.13). **b**. Left, schematic of Ca^{2+} pathways that could potentially activate BK channels, indicated are Ca^{2+} entry from the extracellular space through Ca_V channels (purple) and Ca^{2+} release from intracellular stores (ER). Right: schematic of the effect of intracellular EGTA and BAPTA application, BAPTA has a ~150× faster binding kinetics than EGTA, resulting in a smaller intracellular Ca^{2+} spread. **c**. The amplitude of the fAHP in the distal AIS during various pharmacological interventions. Top: example traces from in control (grey) and after application of IbTx (blue), extracellular EGTA (red), ryanodine (green), a Ca_V channel block cocktail (purple), intracellular BAPTA (green). Scale bars from top to bottom are 50 mV and 1 ms. Bottom: population data of amplitude of the fAHP in the distal AIS, treatment: time-matched control (blue, n = 6, p = 0.81), IbTx (blue, 100 nM bath or 1 µM puff, n = 13, p = 0.0015), extracellular EGTA (red, 2.5 mM, n = 6, p = 0.0029), ryanodine (green, 10 µM, n = 7, p = 0.95), a Ca_V channel block cocktail (purple, 200 µM Cadmium, 100 µM Nickel and 1 µM ω-conotoxin MVIIC, n = 7, p = 0.0058), intracellular EGTA (10 mM, n = 5, p = 0.88), intracellular BAPTA (10 mM, n = 10, p = 0.027). Statistics are multiple comparisons of two-way ANOVA's for each treatment on location and condition.

routes, with the axon BK channels relying on a more rapid or efficient route. The delay to the peak was identical between these regions (soma: 1.19 ms, n = 13, dist. AIS: 1.21 ms, n = 11, unpaired t-test: p = 0.92), as was peak amplitude (soma: –22.3 mV, n = 13, dist. AIS: –29.3 mV, n = 11, unpaired t-test: p = 0.13, **Figure 5a**). The delay from threshold to the peak BK channel activity was identical in these regions, but because of the difference in the AP width (soma: 702 µs, dist. AIS: 535 µs), the maximum BK activation was more visible in other characteristics of the AP: the half-width and fAHP, respectively.

Our data showed that BK channels in the distal AIS are activated rapidly (~200 µs) and fully by an AP. Since BK channels are dependent on high Ca^{2+} levels (~10 µM) to activate in the AP voltage range (Berkefeld et al., 2006), we suspected that they are efficiently activated by a Ca^{2+} source (**Figure 5b**). We hypothesized that there are several Ca^{2+} source candidates that could provide the Ca^{2+} to activate BK channels. Firstly, BK channels could be activated by Ca^{2+} released from the endoplasmic reticulum. The L5 pyramidal neuron contains a unique organization of cisternal organelle along the entire length the AIS: the giant saccular organelle, which amplifies Ca^{2+} levels by ~35% (Antón-Fernández et al., 2013; Hanemaaijer et al., 2020). Functional coupling of BK channel with Ca^{2+} induced Ca^{2+} release has previously been described in cartwheel cells from the dorsal cochlear nucleus (Irie and Trussell, 2017). Secondly, Ca_V channel mediated BK channels activation by has been described, such as L-type channel in adrenal chromaffin cells (Marcantoni et al., 2010), N-type in hippocampal (Marrion and Tavalin, 1998) or P/Q in cartwheel cells (Irie and Trussell, 2017). Thirdly, previously we described Na_V channel mediated Ca^{2+} entry in the AIS, which could also provide a rapid BK channel activation pathway (Hanemaaijer et al., 2020).

We focused on the locus of AP initiation: the distal AIS, where IbTx reduced the fAHP (**Figure 4c** and **Figure 5c**). We first tested the dependence of BK channels on Ca^{2+} entry and bath applied 2.5 mM EGTA, effectively lowering [Ca^{2+}] from 2 mM to ~450 nM (see **Methods**). This significantly reduced the fAHP in the distal AIS (control: –11.2 mV, extr. EGTA: +1.4 mV, n = 6, p = 0.0029, **Figure 5c**). This suggest that Ca^{2+} entry from the extracellular space is necessary to activate BK channels. We then tested if BK channels were activated by Ca^{2+} induced Ca^{2+} release from internal stores. However, when we blocked ryanodine receptor mediated Ca^{2+} release from the ER by applying 10 µM ryanodine, we observed no effect on the fAHP (two-way ANOVA: $p = 0.62$, **Figure 5c**), suggesting that Ca^{2+} release from the ER does not activate BK channels in distal AIS. Next, we tested if Ca^{2+} entered the axon through Ca_V channels. When we applied a broad cocktail of T-, L-, P/Q-, N-, and R-type Ca_V channel blockers (200 µM Cadmium, 100 µM Nickel and 1 µM ω-conotoxin MVIIC), the fAHP was significantly reduced in the distal AIS (control: –11.7 mV, Ca_V cocktail: –2.0 mV, $n = 7$, $p = 0.0058$, **Figure 6c**). The effect of IbTx on the dist. AIS fAHP was identical to the effect of blocking Ca_V channels (IbTx: +9.9. mV, $n = 13$, Ca_V channels cocktail: +9.4 mV, $n = 7$, unpaired t-test, $p = 0.93$), suggesting that solely Ca_V channels provide the Ca^{2+} to activate BK channels.

BK channels form nanodomains with Ca_V channels

BK channels can be found in nanodomains with voltage gated Ca^{2+} channels or internal Ca^{2+} stores to activate reliably (Irie and Trussell, 2017; Muller et al., 2007). The proximity of a Ca^{2+} source to a BK channel can be tested by comparing the effect of intracellular application of the Ca^{2+} buffer BAPTA or EGTA. Both Ca^{2+} buffers have similar steady-state binding affinities with Ca^{2+}, but very different binding rate constants, with BAPTA binding Ca^{2+} approximately 150 times faster than EGTA, resulting in a smaller distance spread from the Ca^{2+} source (**Figure 5b**) (Naraghi and Neher, 1997). This difference can be used to estimate the distance between a Ca^{2+} source and a BK channel. Generally, if an effect of BAPTA and EGTA is observed, the distance of between the Ca^{2+} source and the BK channel is >100 µm and termed a microdomain. If there is no effect of EGTA, but only of BAPTA, the Ca^{2+} source and BK channel must be in close proximity: a nanodomain, generally defined as ~20-50 µm. If no effect of BAPTA is observed, the distance between the BK channel and its Ca^{2+} source is assumed to be even smaller (Marrion and Tavalin, 1998). To test if BK channels form domains with a Ca^{2+} source in the L5 cortical pyramidal neurons, we measured the AP shape in the soma and axon in a control condition and then repatched the same cells with intracellular solution containing 10 mM EGTA or 10 mM BAPTA. We observed no effect on the fAHP after application of EGTA (fAHP, two-way ANOVA multiple comparisons, $p = 0.86$, $n = 5$, **Figure 5c**). However, intracellular application of the faster buffer BAPTA did significantly decrease the fAHP in the distal AIS (control: –9.1 mV, BAPTA: –2.5 mV, $p = 0.027$, **Figure 5c**). The data suggest that in the distal AIS, BK channels are efficiently activated by Ca^{2+} entry through nanodomain coupled Ca_V channels.

BK channels are required for high-frequency bursts

What could be the result of the highly efficient BK channel activation? We hypothesized that BK channels might be involved in enabling burst firing in the L5 pyramidal neurons, as they do in hippocampal CA1 neurons (Gu et al., 2007). To test this hypothesis, we patched S1 L5 pyramidal neuron and injected 300 ms steps of current (0.5 – 1 nA) to elicit trains of APs before and after bath application of IbTx (see **Figure 6a**). We did not see an effect of IbTx on the tonic firing frequency (mixed model, $p = 0.28$, $n = 14$, see **Figure 6b**). However, when we bath applied 100 nM IbTx, we did observe a significant effect on the firing frequency between the first two APs (two-way ANOVA, $p = 0.0081$, $n = 14$, **Figure 6c**). Specifically, after IbTx, the firing frequency in response to 0.9 and 1 nA was significantly reduced (0.9 nA, control: 111.1 Hz, IbTx: 62.27 Hz, $p = 0.0001$, 1 nA, control: 128.5 Hz, IbTx: 65.55 Hz, $p < 0.0001$). The effect of blocking BK channels is limited to high current injections, that in control conditions elicit > 100 Hz firing. This suggests that BK channels are required to fire at high (>100 Hz) frequencies. Next, we stimulated the cells to fire at specific frequencies, by injecting current at intervals between 20 – 500 Hz, and again quantified the firing frequency of the first two APs (see **Figure 6d**). In control conditions, the cells could faithfully uphold a firing frequency up until 300 Hz. When we bath applied 100 nM IbTx, the cells were not affected up until 200 Hz, however at 300 Hz the firing frequency was significantly reduced (control: 297.4 Hz, IbTx: 254.9 Hz, mixed model multiple comparisons, $p < 0.0001$, see **Figure 6e**). In neither condition could the cells uphold 500 Hz firing frequency, and with IbTx application the firing frequency was lower than in control (control: 270.0 Hz, IbTx: 229.5 Hz, mixed model multiple comparisons, $p = 0.0010$). Taken together, the data show that BK channels are critically involved in high-frequency burst firing.

BK channels are present in the soma and axons of L5 mouse pyramidal neurons

Finally, we aimed to complement the functional investigation of axonal BK channels with structural information on the exact presence and location of the channels. The channel can be present in low densities, that may be below a detectable level when one uses

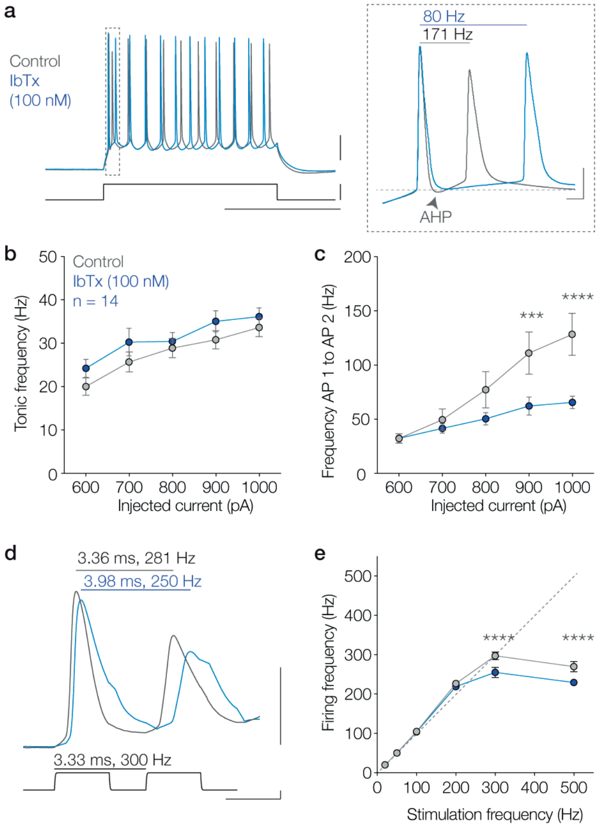

Figure 6. BK channels are required for high-frequency firing

a. A 400 ms current injection elicited a train of APs in Control (grey) and after bath application of 100 nM IbTx (blue). Insert shows a zoom in of the first two APs. Note the higher fAHP and the longer interspike interval after IbTx application. Scale bars from top to bottom are 20 mV, 1 nA and 200 ms. **b**. The tonic firing frequency from the 2nd to the last AP elicited by increasing current injections in Control (grey) and after bath application of 100 nM IbTx (blue). Mixed effects analysis, condition effect, p = 0.28, n = 14 cells. **c**. The firing frequency between the first two APs elicited by increasing current injections in Control (grey) and after bath application of 100 nM IbTx (blue). Two-way ANOVA, condition effect p = 0.0081, multiple comparison statistics indicated by stars, n = 14 cells. **d**. APs in response to 300 Hz current injection in Control (grey) and after bath application of 100 nM IbTx (blue), indicated on the top are the interspike intervals and corresponding frequencies. **e**. Population data for the firing frequency in response to stimulation frequency in Control (grey) and after bath application of 100 nM IbTx (blue). Mixed effects analysis, condition effect p = 0.0012, multiple comparison statistics indicated by stars, n = 14 cells.

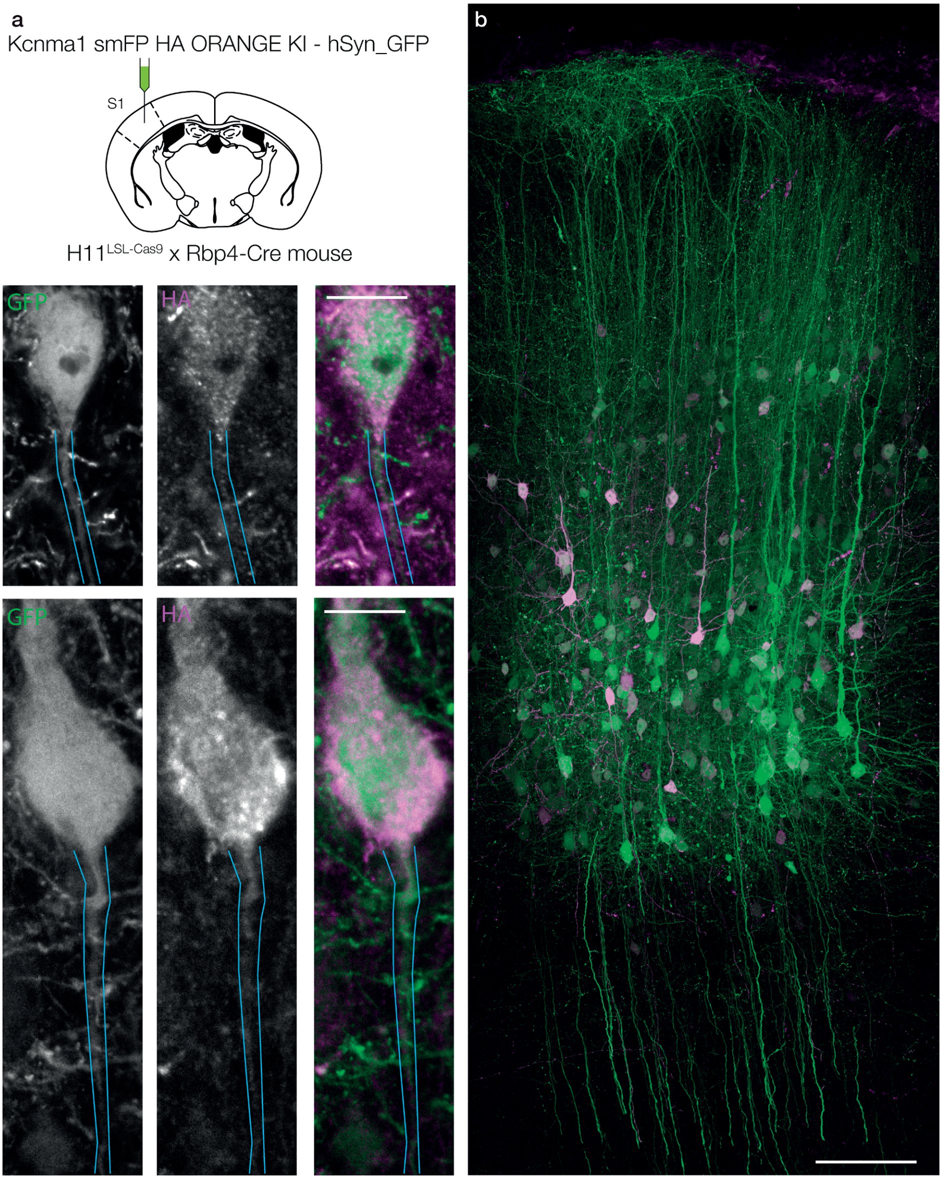
a
Kcnma1 smFP HA ORANGE KI - hSyn_GFP
S1
H11^LSL-Cas9 x Rbp4-Cre mouse
GFP
HA
GFP
HA
b

Figure 7. CRISPR/Cas9 labelling shows BK channels in the mouse L5 soma and axon
a. An AAV1 containing Kcnma1 smFP HA ORANGE KI - hSyn_GFP was injected in S1 in the layer 5 of the transgenic H11$^{LSL\text{-}Cas9}$ x Rbp4-Cre mouse and the tissue harvested after three weeks of expression. **b**. A scan of the injection site from pia (up) to L6 (down). The virus caused GFP expression in all transfected cells. In a subset of transfected cells the succesful knock-in of the HA gene in the locus of the BK channel caused the BK channel to be flagged by the HA tag, for which we stained wtih Alae 647. Scale bar is 100 μm. **c**. Two high-resolution scans of cells expressing both GFP and HA. Blue lines indicate the shape of the axon. GFP expression equally fills the cells, HA expression is uneven and more restricted to the cell membrane. Scale bar is 10 μm.

conventional immunohistochemistry. Instead, we used ORANGE, a CRISPR/Cas9 based gene editing technique, to label and visualize endogenous BK channels with the smHA tag (Willems et al., 2020). A major advantage of the smHA tag is that it contains multiple repetitions of the same epitopes that are recognized by the primary anti-HA antibody, which causes an amplification of the signal. We generated an HA knock-in construct for the BK channel (Kcnma1 smFP HA ORANGE KI - hSyn_GFP) and subcloned the construct in an AAV1 virus. We crossed the Rbp4-Cre mouse to the H11$^{\text{LSL-Cas9}}$ mouse to obtain animals with Cre and Cas9 expression restricted to the L5 pyramidal neurons. We chose mice as a model organism for these experiments, because these specific transgenic lines are not existent in rats. Next, we injected the construct carrying virus in S1 of the transgenic animals, which led to GFP expression in all transfected cells (**Figure 7a,b**). In addition, in a subset of cells, successful knock-in resulted in the insertion of the smHA gene in the locus of the BK gene of L5 pyramidal neurons. After 3 weeks of expression, the tissue was extracted and stained for HA. Preliminary results showed GFP expression restricted to the area of injection and HA expression in a subset of the transfected cells (**Figure 7b**). These data are the result of the first iteration of this approach and therefore must be interpreted cautiously. The preliminary results, on a closer inspection of individual cells with HA fluorescence, showed a general pattern of punctate fluorescence that is typical of BK channels, in the soma and the apical dendrite close to the soma, suggesting relatively high densities of BK channels in these regions (**Figure 7c**). In addition, a lower level of HA fluorescence was also observed in some primary axons, where the signal was strongest in close proximity to the soma, suggesting the presence of BK channels in the AIS of mice. Due to the limited availability of transgenic rat lines, we currently cannot repeat this approach in rats. In addition, future experiments, including a repetition in multiple animals, must be performed to obtain a quantification of the HA knock-in success rate and of the relative HA intensity in multiple cellular regions. Co-staining with AIS markers is required to investigate the relative location of BK channels within the AIS. Taking the need for repeated and follow-up experiments into consideration, the preliminary data do suggest that the BK channel is indeed present in the axon of the L5 pyramidal neuron of mice, which would correspond to the results of the functional presence of BK channels in the proximal AIS of the rat axon described earlier in this chapter.

Discussion

Using holographic illumination to optically measure the AP in the proximal axon of the L5 pyramidal neuron (**Figure 1**), we identified spatial gradients of AP repolarization mechanisms. AP repolarization strength increased with distance from the soma, apparent from the narrowing AP width and increase in fAHP (**Figure 2**). BK channels contributed to AP width proximal to the soma and the fAHP in the distal AIS, internode and node (**Figure 4**). BK channels in the distal AIS were activated by Ca_V channels coupled in nanodomains and the contribution of BK channels to AP repolarization was critical to fire in high-frequency bursts (**Figure 5 and 6**). Preliminary results of BK channel visualization confirmed the presence of BK channels in the proximal axon (**Figure 7**). Together, the data suggest highly organized Ca^{2+} - BK signaling in the AIS contributing to burst firing in the L5 pyramidal neuron.

We employed holographic imaging to obtain optical voltage recordings with high spatial and temporal resolution from regions inaccessible with a patch pipette (Foust et al., 2015). Exploiting the linear dependence of JPW fluorescence on voltage, we calibrated the data with a hyperpolarization pulse to obtain absolute voltage measures from the axon (Ehrenberg et al., 1987; Hanemaaijer et al., 2020). The calibration enabled the comparison of fAHP amplitude across different regions and pharmacological interventions. Because the SNR of optical voltage recordings remain orders of magnitude smaller than electrophysiological recordings, we tested various fits of the de- and repolarization phase to obtain more accurate measures of the voltage threshold and the fAHP. We measured the AP shape in the proximal axon of the L5 pyramidal neuron and confirmed the increase in the fAHP with distance from the soma, hitherto only recorded using direct axon patch-clamp recordings (**Figure 2**) (Kole et al., 2007; Shu et al., 2007). We confirmed and extended these findings, by providing simultaneous recordings from longer stretches of axon and evidence for local repolarization mechanisms in the myelinated axolemma. AP repolarization in the internode was rapid and relatively strong, apparent in the narrow AP width (379 μs) and large fAHP (–21.5 mV). Internode repolarization was mainly affected by 4-AP, which caused an increase in AP amplitude and width and a decrease in the fAHP, consisted with the presence of juxtaparanodal K_V1 channels (Salzer, 2003). However, we also observed a significant effect of BK channels on the internodal AP repolarization. In a previous publication, we described Ca^{2+} transients in response to single APs in the first internode, which may be linked to the strong BK activation in this region (Hanemaaijer et al., 2020).

We studied the activation mechanism of BK channels in more detail in the distal AIS, the locus of AP initiation. In the distal AIS, BK and Cav channels are coupled in nanodomains, which led to rapid (~200 µs) and efficient opening of BK channels (**Figure 4** and **5**). In a previous study, we identified three separate Ca^{2+} entry routes in the AIS: aside from Cav channels, release from internal stores and Nav channels contributed significantly to AIS Ca^{2+} levels (Hanemaaijer et al., 2020), although the relative size of each route may vary with species or in microstructures within the AIS (Lipkin et al., 2021). Interestingly, a cocktail of Cav channel blockers had an identical effect on the local AP as IbTx (**Figure 5**), suggesting that Cav channels are the sole source of Ca^{2+} activating BK channels in the distal AIS. Importantly, an alternative explanation for this result is a direct interaction between BK channels and the compounds in the cocktail of Cav channel blockers. We previously observed changes in baseline fluorescence of a Ca^{2+} indicator after we bath applied Ni^{2+} or Cd^{2+}, suggesting that these cations can enter the cytoplasm and potentially interact with BK channels directly (Hanemaaijer et al., 2020). Nickel (Ni^{2+}) and Cadmium (Cd^{2+}) are divalent cations, like Ca^{2+}, and block T-, R type and L, P/Q, R-type Cav channels, respectively. Divalent cations can interact with the BK channel pore in multiple locations and cause a concentration-dependent activation, block or altered Ca^{2+} affinity and this should be carefully considered when interpreting our results (Oberhauser et al., 1988; Zeng et al., 2005; Zhou et al., 2015). While Ni^{2+} does not directly interact with the channel, Cd^{2+} binding to BK channel causes activation of the channel at high intracellular concentrations (Oberhauser et al., 1988). In addition, both Ni^{2+} and Cd^{2+} can increase the Ca^{2+} affinity of the BK channel. This implies that even if Ni^{2+} and/or Cd^{2+} entered the cell in our Cav cocktail blocker experiments, they would have activated BK channels. Since we observed the opposite effect: the Cav blocker cocktail mimicked the effect of blocking BK channels, we concluded that the effect was caused by lack of Ca^{2+} entry through Cav channels, rather than a direct interaction with BK channels. Another alternative explanation for our results could be an indirect effect of Cd^{2+} dependent BK channel activation, which may have caused delayed inactivation of the channel, and which would also be reflected by a decreased fAHP. However, firstly, BK channels accompanied by the β4 subunit (the mayor

BK subunit expressed in L5 pyramidal neurons) do not inactivate, and secondly, BK channel inactivation is removed by hyperpolarization, which was a standard step in our experiments as part of the calibration protocol (Faber and Sah, 2003; Gonzalez-Perez and Lingle, 2016). Therefore, we do not expect that Cd^{2+} mediated BK channel inactivation can explain the effect on the AP repolarization we observed. Nonetheless, a repetition of these experiments with more specific CaV channel blockers, such as toxins, is necessary to exclude any effects caused by interactions between the blocker and the BK channel. Additional separate experiments with subtype-specific blockers could provide further detail about the CaV channel subtype coupled to BK channels in the L5 pyramidal neuron axon.

The data presented here imply that there is a specific structural mechanism that couples BK channels to CaV channels, but not other Ca^{2+} sources. Indeed, based on our BAPTA experiments, the two channels are coupled in a nanodomain. How the BK-CaV complex is localized to the AIS is not yet known. The cytoskeletal architecture of the AIS follows a periodic spacing, based on actin rings spatially separated ~190 nm by spectrin molecules (Leterrier, 2018). Several ion channels follow this periodicity, such as NaV, KV7 and KV1 channels, but this periodicity is not yet reported for BK or CaV channels (D’Este et al., 2017; Xu et al., 2013). In cerebellar Purkinje neurons, BK channels anchor to the paranodes through the scaffolding protein Caspr, which also follows the nanoscale periodicity at nodes and is also present at the AIS of cultured hippocampal neurons, potentially forming a scaffolding pathway for BK channels are the AIS (D’Este et al., 2017; Hirono et al., 2015; Ogawa et al., 2008). Not all AIS molecules are anchored to the periodic nanoscale, indeed the AIS cytoskeleton is regionally interrupted at AnkyrinG deficient and KV2.1 rich domains, where the cisternal organelle approach the membrane closely and which may correspond to Ca^{2+} microdomains (King et al., 2014; Lipkin et al., 2021; Sánchez-Ponce et al., 2012). In the Purkunje somata, CaV or BK channels colocalize in clusters with a diameter of a few hundred nm, but whether these clusters resemble the KV2.1 domains of the AIS is not known (Indriati et al., 2013). In synapses, the BK-CaV complex is clustered through scaffolding protein Shank and RIM, but these proteins have not yet been observed at the AIS (Gao et al., 2022; Sclip et al., 2018). Taken together, the structural coupling of CaV and BK channels and whether they are anchored to the AIS through the periodic nanoscale, KV2.1 domains or an alternative mechanism remains to be studied. Preliminary experiments using ORANGE to genetically tag BK channels showed their presence at the axon of L5 neurons in mice (Figure 7). This technique could be used to investigate the structural properties of BK channels and the axonal skeleton in more detail, for example by co-staining with AIS markers such as AnkyrinG and using superresolution microscopy to localize the BK channel in the AIS nanoscale. Recently, using conditional activation of knock-in expression, Droogers et al. developed a technique that allows tagging of multiple genes in the same tissue (Droogers et al., 2022). Combined with superresolution microscopy, this genetic approach opens up the possibility to visualize of BK and Cav channels simultaneously and investigate the structure of nanodomains in the axon.

The nanodomain coupling ensured a rapid and efficient activation of BK channels (**Figure 4** and **5**), which was necessary to uphold high firing frequencies, similar to the CA1 pyramidal neuron (Gu et al., 2007). Blocking BK channels increased the interspike interval between the first two APs at high current injected that initiated >100 Hz firing bursts in control. Bursting activity is functionally relevant in the L5 pyramidal neuron, because this cell type encodes whisker touch by firing a short burst in high frequency (Kock et al., 2021; Xu et al., 2012). What is the postsynaptic effect of the BK-mediated repolarization? Roshchin et al. recorded the postsynaptic response of two connected L5 pyramidal neurons in control and IbTx and found an increased paired pulse ratio, which they attributed to the increase AP width in the soma (Roshchin et al., 2018). Based on our results, this does not necessarily translate into a wider axonal AP, however we did not record the width of the second AP. Roshchin et al. applied IbTx to the bath, so the observed effect may also be due to BK channels present in the terminal (Roshchin et al., 2018). In addition, they fixed the ISI (10 ms), so the postsynaptic response did not incorporate the effect that BK block has on the ISI. The postsynaptic response is dependent on two factors: paired-pulse ratio and temporal summation. A shorter ISI naturally increases temporal summation but can simultaneously cause paired-pulse depression (Abbott and Regehr, 2004). In synaptically connected L5 neurons, the EPSPs caused by bursts show paired-pulse depression, but do lead to amplification and temporal summations of EPSPs (Williams and Stuart, 1999). This suggests that the increased ISI after BK channel block could increase the size of the second EPSP, but also temporally separate it from the first and reduce the likelihood of a postsynaptic AP. Out data suggest that nanoscale coupling of Cav and BK channels in the

AIS contributes to high frequency burst firing which may serve to induce temporal summation of postsynaptic signals and encode whisker touch in the somatosensory cortex.

Author Contributions

Naomi AK Hanemaaijer: Data curation, Software, Formal analysis, Validation, Investigation (electrophysiological and optical experiments), Visualization, Methodology, Writing - original draft, Writing - review and editing. Kieran P Higgins: Investigation (viral injections, perfusions, stainings). K Kole: Investigation (virus production). Arthur PH de Jong: Investigation (plasmid design and subcloning). Harold D MacGillavry: Funding acquisition and Supervision (plasmid design and subcloning). Maarten HP Kole: Conceptualization, Formal analysis, Supervision, Funding acquisition, Validation, Visualization, Methodology, Project administration, Writing - review and editing

References

Abbott LF, Regehr WG. 2004. Synaptic computation. *Nature* 431:796–803. doi:10.1038/nature03010

Alle H, Kubota H, Geiger JRP. 2011. Sparse But Highly Efficient Kv3 Outpace BKCa Channels in Action Potential Repolarization at Hippocampal Mossy Fiber Boutons. *J Neurosci* 31:8001–8012. doi:10.1523/jneurosci.0972-11.2011

AllenInstitute. 2022. ALLEN BRAIN MAP Transcriptomics Explorer. Dataset: Human - Multiple Cortical Areas - SMART-seq and Mouse - Whole Cortex & Hippocampus - 10x.

Antón-Fernández A, Rubio-Garrido P, DeFelipe J, Muñoz A. 2013. Selective presence of a giant saccular organelle in the axon initial segment of a subpopulation of layer V pyramidal neurons. *Brain Structure and Function* 220:869–884. doi:10.1007/s00429-013-0689-1

Bailey CS, Moldenhauer HJ, Park SM, Keros S, Meredith AL. 2019. KCNMA1-linked channelopathy. *J Gen Physiology* 151:1173–1189. doi:10.1085/jgp.201912457

Benhassine N, Berger T. 2008. Large-conductance calcium-dependent potassium channels prevent dendritic excitability in neocortical pyramidal neurons. *Pflügers Archiv - European J Physiology* 457:1133. doi:10.1007/s00424-008-0569-3

Benhassine N, Berger T. 2005. Homogeneous distribution of large-conductance calcium-dependent potassium channels on soma and apical dendrite of rat neocortical layer 5 pyramidal neurons. *Eur J Neurosci* 21:914–926. doi:10.1111/j.1460-9568.2005.03934.x

Berkefeld H, Sailer CA, Bildl W, Rohde V, Thumfart J-O, Eble S, Klugbauer N, Reisinger E, Bischofberger J, Oliver D, Knaus H-G, Schulte U, Fakler B. 2006. BK_{Ca}-Cav Channel Complexes Mediate Rapid and Localized Ca^{2+}-Activated K^+ Signaling. *Science* 314:615–620. doi:10.1126/science.1132915

Bers DM, Patton CW, Nuccitelli R. 2010. Chapter 1 - A Practical Guide to the Preparation of Ca2+ Buffers, Methods in Cell Biology. Elsevier Inc. doi:10.1016/b978-0-12-374841-6.00001-3

Bock T, Stuart GJ. 2016. The Impact of BK Channels on Cellular Excitability Depends on their Subcellular Location. *Frontiers in Cellular Neuroscience* 10:914–8. doi:10.3389/fncel.2016.00206

Brette R. 2013. Sharpness of spike initiation in neurons explained by compartmentalization. *PLoS computational biology* 9:e1003338. doi:10.1371/journal.pcbi.1003338

Cohen CCH, Popovic MA, Klooster J, Weil M-T, Möbius W, Nave K-A, Kole MHP. 2020. Saltatory Conduction along Myelinated Axons Involves a Periaxonal Nanocircuit. *Cell* 180:1–28. doi:10.1016/j.cell.2019.11.039

Crameri F, Shephard GE, Heron PJ. 2020. The misuse of colour in science communication. *Nat Commun* 11:5444. doi:10.1038/s41467-020-19160-7

D'Este E, Kamin D, Balzarotti F, Hell SW. 2017. Ultrastructural anatomy of nodes of Ranvier in the peripheral nervous system as revealed by STED microscopy. *Proceedings of the National Academy of Sciences* 114:E191–E199. doi:10.1073/pnas.1619553114

Droogers WJ, Willems J, MacGillavry HD, Jong APH de. 2022. Duplex Labeling and Manipulation of Neuronal Proteins Using Sequential CRISPR/Cas9 Gene Editing. *Eneuro* **9**:ENEURO.0056-22.2022. doi:10.1523/eneuro.0056-22.2022

Edelstein AD, Tsuchida MA, Amodaj N, Pinkard H, Vale RD, Stuurman N. 2014. Advanced methods of microscope control using μManager software. *Journal of Biological Methods* 1:10–10. doi:10.14440/jbm.2014.36

Ehrenberg B, Farkas DL, Fluhler EN, Lojewska Z, Loew LM. 1987. Membrane potential induced by external electric field pulses can be followed with a potentiometric dye. *Biophysical Journal* 51:833–837. doi:10.1016/s0006-3495(87)83410-0

Faber ESL, Sah P. 2003. Ca2+-activated K+ (BK) channel inactivation contributes to spike broadening during repetitive firing in the rat lateral amygdala. *J Physiology* 552:483–497. doi:10.1113/jphysiol.2003.050120

Foust AJ, Popovic MA, Zecevic D, McCormick DA. 2010. Action Potentials Initiate in the Axon Initial Segment and Propagate through Axon Collaterals Reliably in Cerebellar Purkinje Neurons. *Journal of Neuroscience* 30:6891–6902. doi:10.1523/jneurosci.0552-10.2010

Foust AJ, Zampini V, Tanese D, Papagiakoumou E, Emiliani V. 2015. Computer-generated holography enhances voltage dye fluorescence discrimination in adjacent neuronal structures. *Neurophotonics* 2:021007. doi:10.1117/1.nph.2.2.021007

Galvez A, Gimenez-Gallego G, Reuben JP, Roy-Contancin L, Feigenbaum P, Kaczorowski GJ, Garcia ML. 1990. Purification and characterization of a unique, potent, peptidyl probe for the high conductance calcium-activated potassium channel from venom of the scorpion Buthus tamulus. *J Biol Chem* 265:11083–11090. doi:10.1016/s0021-9258(19)38560-6

Gao L, Zhao J, Ardiel E, Hall Q, Nurrish S, Kaplan JM. 2022. Shank promotes action potential repolarization by recruiting BK channels to calcium microdomains. *Elife* 11:e75140. doi:10.7554/elife.75140

Gómez R, Maglio LE, Gonzalez-Hernandez AJ, Rivero-Pérez B, Bartolomé-Martín D, Giraldez T. 2021. NMDA receptor–BK channel coupling regulates synaptic plasticity in the barrel cortex. *Biorxiv* 2020.12.30.424719. doi:10.1101/2020.12.30.424719

Gonzalez-Perez V, Lingle CJ. 2016. Regulation of BK Channels by Beta and Gamma Subunits. *Annu Rev Physiol* 81:113–137. doi:10.1146/annurev-physiol-022516-034038

Gu N, Vervaeke K, Storm JF. 2007. BK potassium channels facilitate high-frequency firing and cause early spike frequency adaptation in rat CA1 hippocampal pyramidal cells. *J Physiology* 580:859–882. doi:10.1113/jphysiol.2006.126367

Gutzmann JJ, Lin L, Hoffman DA. 2019. Functional Coupling of Cav2.3 and BK Potassium Channels Regulates Action Potential Repolarization and Short-Term Plasticity in the Mouse Hippocampus. *Frontiers in Cellular Neuroscience* 13:553–14. doi:10.3389/fncel.2019.00027

Hamada MS, Goethals S, Vries SI de, Brette R, Kole MHP. 2016. Covariation of axon initial segment location and dendritic tree normalizes the somatic action potential. *Proceedings of the National Academy of Sciences of the United States of America* 113:14841–14846. doi:10.1073/pnas.1607548113

Hanemaaijer NA, Popovic MA, Wilders X, Grasman S, Arocas OP, Kole MHP. 2020. Ca2+ entry through NaV channels generates submillisecond axonal Ca2+ signaling. *eLife* 9:353–32. doi:10.7554/elife.54566

Hirono M, Ogawa Y, Misono K, Zollinger DR, Trimmer JS, Rasband MN, Misonou H. 2015. BK Channels Localize to the Paranodal Junction and Regulate Action Potentials in Myelinated Axons of Cerebellar Purkinje Cells. *Journal of Neuroscience* 35:7082–7094. doi:10.1523/jneurosci.3778-14.2015

Indriati DW, Kamasawa N, Matsui K, Meredith AL, Watanabe M, Shigemoto R. 2013. Quantitative Localization of Cav2.1 (P/Q-Type) Voltage-Dependent Calcium Channels in Purkinje Cells: Somatodendritic Gradient and Distinct Somatic Coclustering with Calcium-Activated Potassium Channels. *J Neurosci* 33:3668–3678. doi:10.1523/jneurosci.2921-12.2013

Irie T, Trussell LO. 2017. Double-Nanodomain Coupling of Calcium Channels, Ryanodine Receptors, and BK Channels Controls the Generation of Burst Firing. *Neuron* 96:856-870.e4. doi:10.1016/j.neuron.2017.10.014

Kalmbach BE, Hodge RD, Jorstad NL, Owen S, Frates R de, Yanny AM, Dalley R, Mallory M, Graybuck LT, Radaelli C, Keene CD, Gwinn RP, Silbergeld DL, Cobbs C, Ojemann JG, Ko AL, Patel AP, Ellenbogen RG, Bakken TE, Daigle TL, Dee N, Lee BR, McGraw M, Nicovich PR, Smith K, Sorensen SA, Tasic B, Zeng H, Koch C, Lein ES, Ting JT. 2021. Signature morpho-electric, transcriptomic, and dendritic properties of human layer 5 neocortical pyramidal neurons. *Neuron* 109:2914-2927.e5. doi:10.1016/j.neuron.2021.08.030

Kang J, Huguenard JR, Prince DA. 1996. Two types of BK channels in immature rat neocortical pyramidal neurons. *J Neurophysiol* 76:4194–4197. doi:10.1152/jn.1996.76.6.4194

Kaufmann WA, Kasugai Y, Ferraguti F, Storm JF. 2010. Two distinct pools of large-conductance calcium-activated potassium channels in the somatic plasma membrane of central principal neurons. *Neuroscience* 169:974–986. doi:10.1016/j.neuroscience.2010.05.070

King AN, Manning CF, Trimmer JS. 2014. A unique ion channel clustering domain on the axon initial segment of mammalian neurons. *Journal of Comparative Neurology* 522:2594–2608. doi:10.1002/cne.23551

Knaus H, Schwarzer C, Koch R, Eberhart A, Kaczorowski G, Glossmann H, Wunder F, Pongs O, Garcia M, Sperk G. 1996. Distribution of high-conductance Ca(2+)-activated K+ channels in rat brain: targeting to axons and nerve terminals. *J Neurosci* 16:955–963. doi:10.1523/jneurosci.16-03-00955.1996

Kock CPJ de, Pie J, Pieneman AW, Mease RA, Bast A, Guest JM, Oberlaender M, Mansvelder HD, Sakmann B. 2021. High-frequency burst spiking in layer 5 thick-tufted pyramids of rat primary somatosensory cortex encodes exploratory touch. *Commun Biology* 4:709. doi:10.1038/s42003-021-02241-8

Kole MHP. 2011. First Node of Ranvier Facilitates High-Frequency Burst Encoding. *Neuron* 71:671–682. doi:10.1016/j.neuron.2011.06.024

Kole MHP, Brette R. 2018. The electrical significance of axon location diversity. *Current opinion in neurobiology* 51:52–59. doi:10.1016/j.conb.2018.02.016

Kole MHP, Letzkus JJ, Stuart GJ. 2007. Axon Initial Segment Kv1 Channels Control Axonal Action Potential Waveform and Synaptic Efficacy. *Neuron* 55:633–647. doi:10.1016/j.neuron.2007.07.031

Kole MHP, Stuart GJ. 2008. Is action potential threshold lowest in the axon? *Nature Neuroscience* 11:1253–1255. doi:10.1038/nn.2203

Leterrier C. 2018. The Axon Initial Segment: An Updated Viewpoint. *Journal of Neuroscience* 38:2135–2145. doi:10.1523/jneurosci.1922-17.2018

Lipkin AM, Cunniff MM, Spratt PWE, Lemke SM, Bender KJ. 2021. Functional Microstructure of Ca V -Mediated Calcium Signaling in the Axon Initial Segment. J Neurosci 41:3764–3776. doi:10.1523/jneurosci.2843-20.2021

Lorincz A, Nusser Z. 2008. Cell-Type-Dependent Molecular Composition of the Axon Initial Segment. J Neurosci 28:14329–14340. doi:10.1523/jneurosci.4833-08.2008

Lutz C, Otis TS, DeSars V, Charpak S, DiGregorio DA, Emiliani V. 2008. Holographic photolysis of caged neurotransmitters. *Nat Methods* 5:821–827. doi:10.1038/nmeth.1241

Marcantoni A, Vandael DHF, Mahapatra S, Carabelli V, Sinnegger-Brauns MJ, Striessnig J, Carbone E. 2010. Loss of Cav1.3 Channels Reveals the Critical Role of L-Type and BK Channel Coupling in Pacemaking Mouse Adrenal Chromaffin Cells. J Neurosci 30:491–504. doi:10.1523/jneurosci.4961-09.2010

Marrion NV, Tavalin SJ. 1998. Selective activation of Ca2+-activated K+ channels by co-localized Ca2+ channels in hippocampal neurons. *Nature* 395:900–905. doi:10.1038/27674

Meera P, Wallner M, Toro L. 2000. A neuronal β subunit (KCNMB4) makes the large conductance, voltage- and Ca2+-activated K+ channel resistant to charybdotoxin and iberiotoxin. *Proc National Acad Sci* 97:5562–5567. doi:10.1073/pnas.100118597

Muller A, Kukley M, Uebachs M, Beck H, Dietrich D. 2007. Nanodomains of Single Ca2+ Channels Contribute to Action Potential Repolarization in Cortical Neurons. *Journal of Neuroscience* 27:483–495. doi:10.1523/jneurosci.3816-06.2007

Naraghi M, Neher E. 1997. Linearized Buffered Ca2+ Diffusion in Microdomains and Its Implications for Calculation of [Ca2+] at the Mouth of a Calcium Channel. *J Neurosci* 17:6961–6973. doi:10.1523/jneurosci.17-18-06961.1997

Oberhauser A, Alvarez O, Latorre R. 1988. Activation by divalent cations of a Ca2+-activated K+ channel from skeletal muscle membrane. *J Gen Physiology* 92:67–86. doi:10.1085/jgp.92.1.67

Ogawa Y, Horresh I, Trimmer JS, Bredt DS, Peles E, Rasband MN. 2008. Postsynaptic Density-93 Clusters Kv1 Channels at Axon Initial Segments Independently of Caspr2. *J Neurosci* 28:5731–5739. doi:10.1523/jneurosci.4431-07.2008

Palmer LM, Stuart GJ. 2006. Site of action potential initiation in layer 5 pyramidal neurons. *The Journal of neuroscience* 26:1854–1863. doi:10.1523/jneurosci.4812-05.2006

Popovic MA, Foust AJ, McCormick DA, Zecevic D. 2011. The spatio-temporal characteristics of action potential initiation in layer 5 pyramidal neurons: a voltage imaging study. *The Journal of Physiology* 589:4167–4187. doi:10.1113/jphysiol.2011.209015

Popovic MA, Gao X, Zecevic D. 2012. Voltage-sensitive dye recording from axons, dendrites and dendritic spines of individual neurons in brain slices. *Journal of Visualized Experiments* e4261. doi:10.3791/4261

Ramaswamy S, Markram H. 2015. Anatomy and physiology of the thick-tufted layer 5 pyramidal neuron. *Frontiers in Cellular Neuroscience* 9:1–29. doi:10.3389/fncel.2015.00233

Roshchin MV, Matlashov ME, Ierusalimsky VN, Balaban PM, Belousov VV, Kemenes G, Staras K, Nikitin ES. 2018. A BK channel–mediated feedback pathway links single-synapse activity with action potential sharpening in repetitive firing. *Sci Adv* 4:eaat1357. doi:10.1126/sciadv.aat1357

Salzer JL. 2003. Polarized Domains of Myelinated Axons. *Neuron* 40:297–318. doi:10.1016/s0896-6273(03)00628-7

Sanchez M, McManus OB. 1996. Paxilline Inhibition of the Alpha-subunit of the High-conductance Calcium-activated Potassium Channel. *Neuropharmacology* 35:963–968. doi:10.1016/0028-3908(96)00137-2

Sánchez-Ponce D, Blázquez-Llorca L, DeFelipe J, Garrido JJ, Muñoz A. 2012. Colocalization of α-actinin and Synaptopodin in the Pyramidal Cell Axon Initial Segment. *Cereb Cortex* 22:1648–1661. doi:10.1093/cercor/bhr251

Sausbier U, Sausbier M, Sailer CA, Arntz C, Knaus H-G, Neuhuber W, Ruth P. 2005. Ca2+-activated K+ channels of the BK-type in the mouse brain. *Histochem Cell Biol* 125:725. doi:10.1007/s00418-005-0124-7

Schindelin J, Arganda-Carreras I, Frise E, Kaynig V, Longair M, Pietzsch T, Preibisch S, Rueden C, Saalfeld S, Schmid B, Tinevez J-Y, White DJ, Hartenstein V, Eliceiri K, Tomancak P, Cardona A. 2012. Fiji: an open-source platform for biological-image analysis. *Nature Methods* 9:676–682. doi:10.1038/nmeth.2019

Sclip A, Acuna C, Luo F, Südhof TC. 2018. RIM-binding proteins recruit BK-channels to presynaptic release sites adjacent to voltage-gated Ca2+-channels. *Embo J* 37:e98637. doi:10.15252/embj.201798637

Shu Y, Duque A, Yu Y, Haider B, McCormick DA. 2007. Properties of Action-Potential Initiation in Neocortical Pyramidal Cells: Evidence From Whole Cell Axon Recordings. *J Neurophysiol* 97:746–760. doi:10.1152/jn.00922.2006

Stuart G, Schiller J, Sakmann B. 1997. Action potential initiation and propagation in rat neocortical pyramidal neurons. *J Physiology* 505:617–632. doi:10.1111/j.1469-7793.1997.617ba.x

Stuart GJ, Sakmann B. 1994. Active propagation of somatic action potentials into neocortical pyramidal cell dendrites. *Nature* 367:69–72. doi:10.1038/367069a0

Typlt M, Mirkowski M, Azzopardi E, Ruettiger L, Ruth P, Schmid S. 2013. Mice with Deficient BK Channel Function Show Impaired Prepulse Inhibition and Spatial Learning, but Normal Working and Spatial Reference Memory. *Plos One* 8:e81270. doi:10.1371/journal.pone.0081270

Willems J, Jong APH de, Scheefhals N, Mertens E, Catsburg LAE, Poorthuis RB, Winter F de, Verhaagen J, Meye FJ, MacGillavry HD. 2020. ORANGE: A CRISPR/Cas9-based genome editing toolbox for epitope tagging of endogenous proteins in neurons. *Plos Biol* 18:e3000665. doi:10.1371/journal.pbio.3000665

Williams SR, Stuart GJ. 1999. Mechanisms and consequences of action potential burst firing in rat neocortical pyramidal neurons. *J Physiology* 521:467–482. doi:10.1111/j.1469-7793.1999.00467.x

Womack MD, Khodakhah K. 2002. Characterization of large conductance Ca2+-activated K+ channels in cerebellar Purkinje neurons. *Eur J Neurosci* 16:1214–1222. doi:10.1046/j.1460-9568.2002.02171.x

Xu K, Zhong G, Zhuang X. 2013. Actin, spectrin, and associated proteins form a periodic cytoskeletal structure in axons. *Science* 339:452–456. doi:10.1126/science.1232251

Xu N, Harnett MT, Williams SR, Huber D, O'Connor DH, Svoboda K, Magee JC. 2012. Nonlinear dendritic integration of sensory and motor input during an active sensing task. *Nature* 492:247–251. doi:10.1038/nature11601

Yao Z, Velthoven CTJ van, Nguyen TN, Goldy J, Sedeno-Cortes AE, Baftizadeh F, Bertagnolli D, Casper T, Chiang M, Crichton K, Ding S-L, Fong O, Garren E, Glandon A, Gouwens NW, Gray J, Graybuck LT, Hawrylycz MJ, Hirschstein D, Kroll M, Lathia K, Lee C, Levi B, McMillen D, Mok S, Pham T, Ren Q, Rimorin C, Shapovalova N, Sulc J, Sunkin SM, Tieu M, Torkelson A, Tung H, Ward K, Dee N, Smith KA, Tasic B, Zeng H. 2021. A taxonomy of transcriptomic cell types across the isocortex and hippocampal formation. *Cell* 184:3222-3241.e26. doi:10.1016/j.cell.2021.04.021

Yu Y, Maureira C, Liu X, McCormick DA. 2010. P/Q and N channels control baseline and spike-triggered calcium levels in neocortical axons and synaptic boutons. *The Journal of neuroscience* 30:11858–11869. doi:10.1523/jneurosci.2651-10.2010

Zeng X-H, Xia X-M, Lingle CJ. 2005. Divalent Cation Sensitivity of BK Channel Activation Supports the Existence of Three Distinct Binding Sites. *J Gen Physiology* 125:273–286. doi:10.1085/jgp.200409239

Zhou Y, Xia X-M, Lingle CJ. 2015. Cadmium–cysteine coordination in the BK inner pore region and its structural and functional implications. *Proc National Acad Sci* 112:5237–5242. doi:10.1073/pnas.1500953112

Supplementary Figures

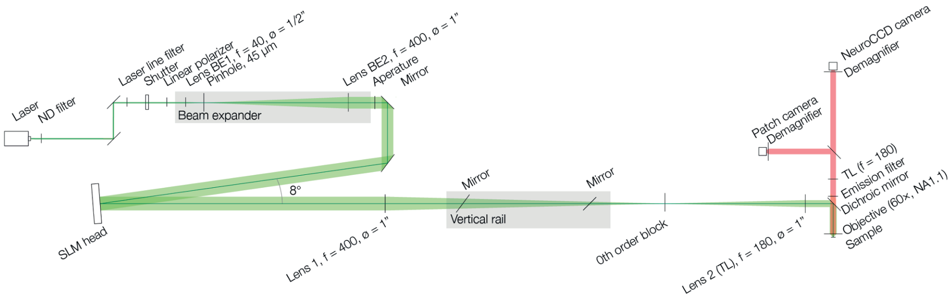
Laser
ND filter
Laser line filter
Shutter
Linear polarizer
Lens BE1, f = 40, ø = 1/2"
Pinhole, 45 µm
Beam expander
Lens BE2, f = 400, ø = 1"
Aperature
Mirror
8°
SLM head
Lens 1, f = 400, ø = 1"
Mirror
Vertical rail
Mirror
0th order block
Lens 2 (TL), f = 180, ø = 1"
Patch camera
Demagnifier
NeuroCCD camera
Demagnifier
TL (f = 180)
Emission filter
Dichroic mirror
Objective (60×, NA1.1)
Sample

Supplemental Figure 1. Optical system

A schematic of the optical elements in the fluorescence light path. See methods for more details. Elements, starting left: laser (500 mW laser emitting at 532 nm), ND: neutral density filters (OD range 0.1 – 4), laser line filter, a shutter controlling entry of the laser beam to the path, a polarization filter, BE: Beam Expander, consisting of two achromatic lenses ($f = 40$ mm and $f = 400$ mm) and a pinhole ($d = 45$ µm), aperture (15.8 × 12.6 mm), SLM: spatial light modulator, a telescope formed by two achromatic lenses ($f = 400$ mm and $f = 180$ mm), 0th order block (a glass slide with a small piece of black tape), single-edge dichroic mirror (cut wavelength 532 nm), objective (60×, NA1.1), stopline emission filter (stopped wavelength 532 nm), a tube lens, demagnifier (0.35×), CCD Camera

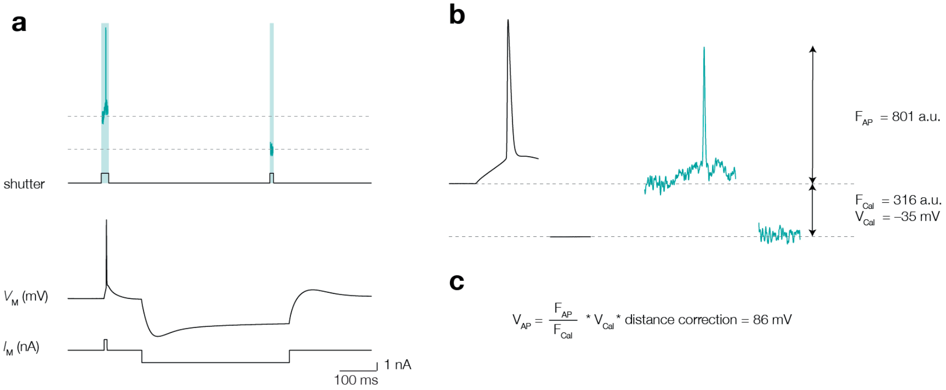

Supplemental Figure 2. Calibration of optical signal

a. The calibration approach used in this study, adopted from Cohen et al., *Cell*, 2020. A single AP was initiated by a positive current injection and a longer negative current injection hyperpolarized the membrane. Fluorescence was recorded during the AP and a short period during the hyperpolarization. Left, from top to bottom, the recorded fluorescence (blue), the closed and open states of the shutter, V_M, the injected current. **b.** The electrically V_M (black) and optically (blue) recorded traces during the two open shutter periods. **c.** Optical V_M was calibrated used the difference in fluorescence during baseline and the calibration pulse (F_{Cal}), the fluorescence of the AP (F_{AP}), the difference in somatic membrane potential (V_{Cal}) and a correction of the hyperpolarization pulse over distance.

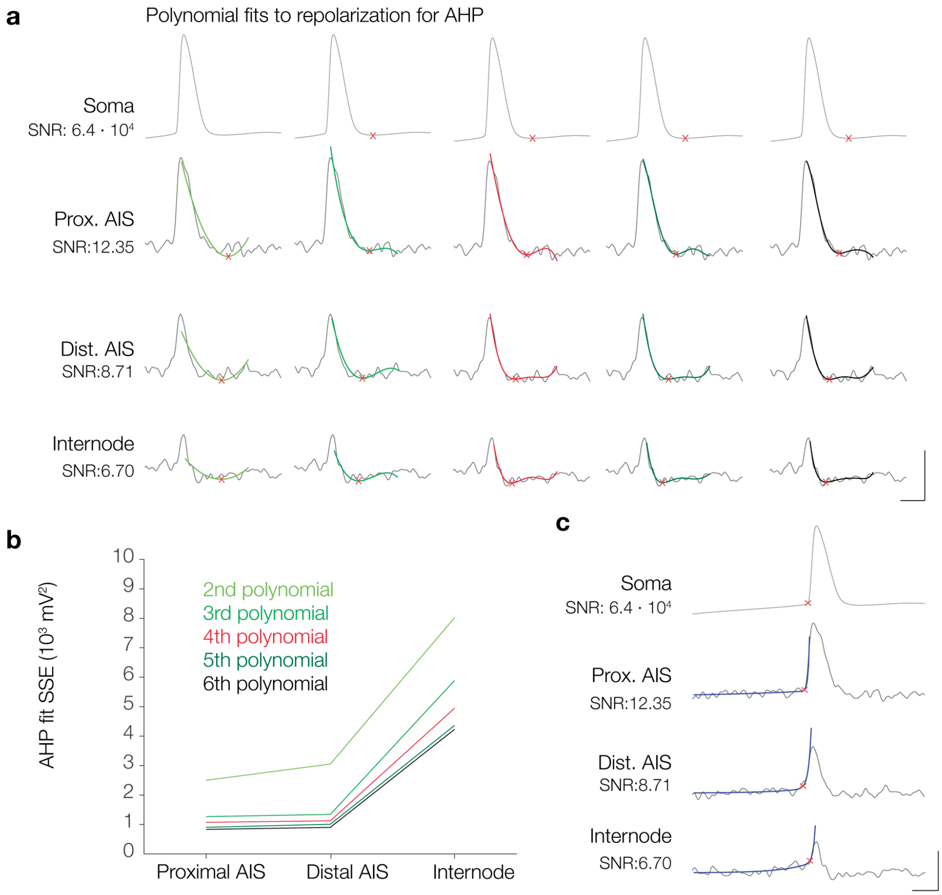

Supplemental Figure 3. Fitting de- and repolarization phase of the AP to measure AP threshold and fAHP

a. Electrically and optically recorded V_{M} of an example cell, with SNR close to the median SNR of our recordings. Polynomial fits with increasing number of degrees are fit to the repolarization phase of the AP (left to right: 2 – 6). The estimated fAHP is marked by a red cross. Note that the speed of the repolarization phase is not well captured in the fit with polynomials with 2 and 3 degrees. Scale bars from top to bottom are 50 mV and 1 ms. **b.** The sum of squared errors of the fit and the recorded traces. Note the decreasing error with increasing degrees. The error is largest in the internode, where SNR is lowest. The additional reduction from a polynomial with 4 degrees to fits with 5 or 6 degrees is marginal. **c**. The same data as **a**, with a double exponential used to fit the depolarization phase and the threshold indicated with red crosses. A double exponential is necessary to capture the steep acceleration of the V_{M}. Scale bars from top to bottom are 50 mV and 1 ms.

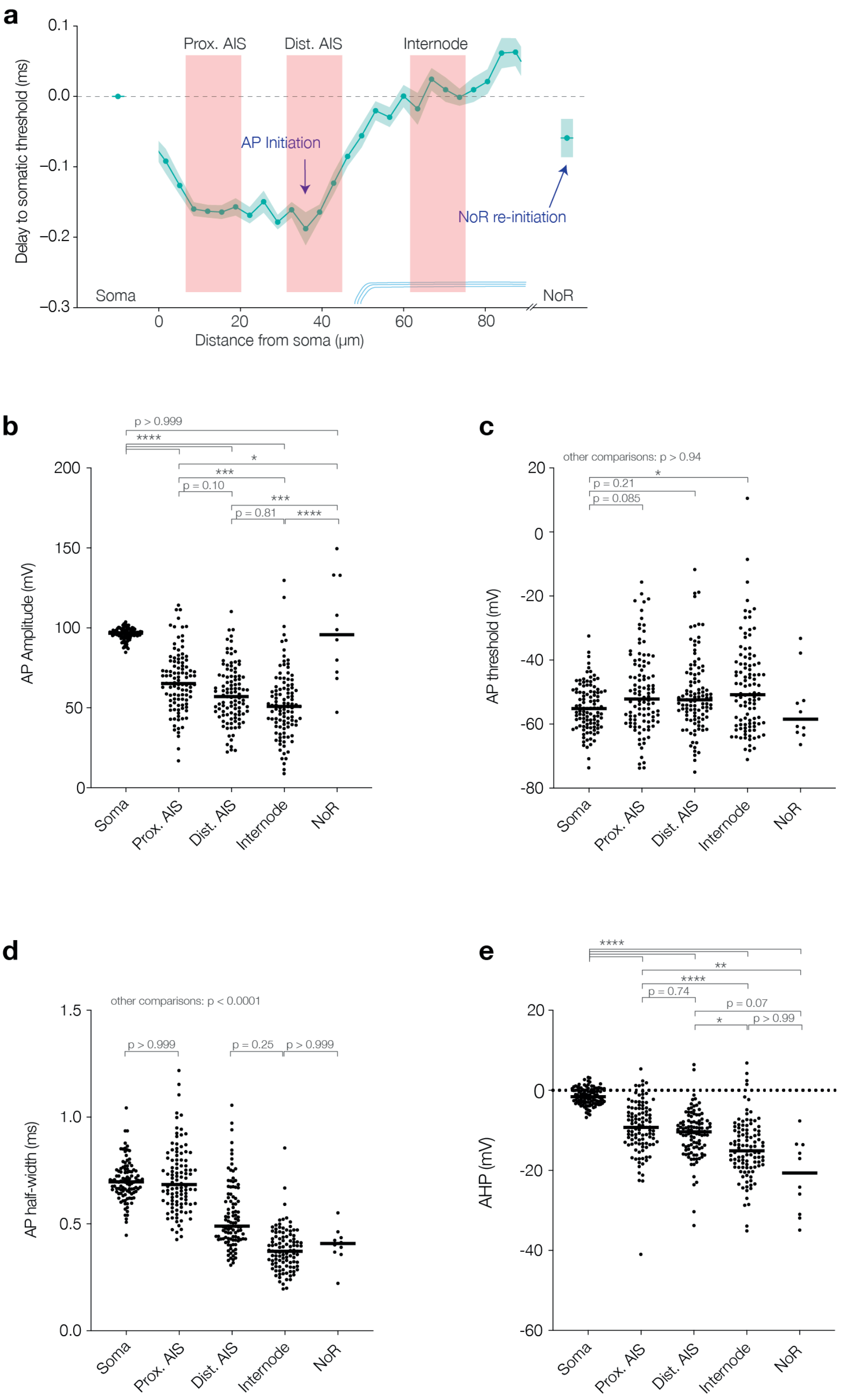
a
Delay to somatic threshold (ms)
0.1
0.0
−0.1
−0.2
−0.3
Prox. AIS
Dist. AIS
Internode
AP Initiation
NoR re-initiation
Soma
NoR
0
20
40
60
80
Distance from soma (μm)
b
AP Amplitude (mV)
p > 0.999
****
*
***
p = 0.10
***
p = 0.81
****
200
150
100
50
0
Soma
Prox. AIS
Dist. AIS
Internode
NoR
c
AP threshold (mV)
other comparisons: p > 0.94
*
p = 0.21
p = 0.085
20
0
-20
-40
-60
-80
Soma
Prox. AIS
Dist. AIS
Internode
NoR
d
AP half-width (ms)
other comparisons: p < 0.0001
p > 0.999
p = 0.25
p > 0.999
1.5
1.0
0.5
0.0
Soma
Prox. AIS
Dist. AIS
Internode
NoR
e
AHP (mV)
****
**
****
p = 0.74
p = 0.07
*
p > 0.99
20
0
-20
-40
-60
Soma
Prox. AIS
Dist. AIS
Internode
NoR

Supplemental Figure 4. AP parameters are different in soma and axonal regions
a. Same as Figure 2e: delay from somatic threshold plotted over distance from the soma. The spatially averaged regions used in this study (prox. AIS, dist. AIS and internode) are indicated by red squares and contain 4 pixels and ~16 µm. **b-e.** Population data of all control recordings (soma and AIS: n = 105, node: n = 9) for **b** AP amplitude **c** AP threshold **d** AP half-width and **e** fAHP. Note that the soma is recorded electrically, and the axonal regions are recorded optically. The parameters are significantly affected by locations (Kruskal-Wallis test, AP amplitude: $p < 0.0001$, AP threshold: $p = 0.01$, AP half-width: $p < 0.0001$, fAHP: $p < 0.0001$. Results from multiple comparisons are indicated in the graphs.

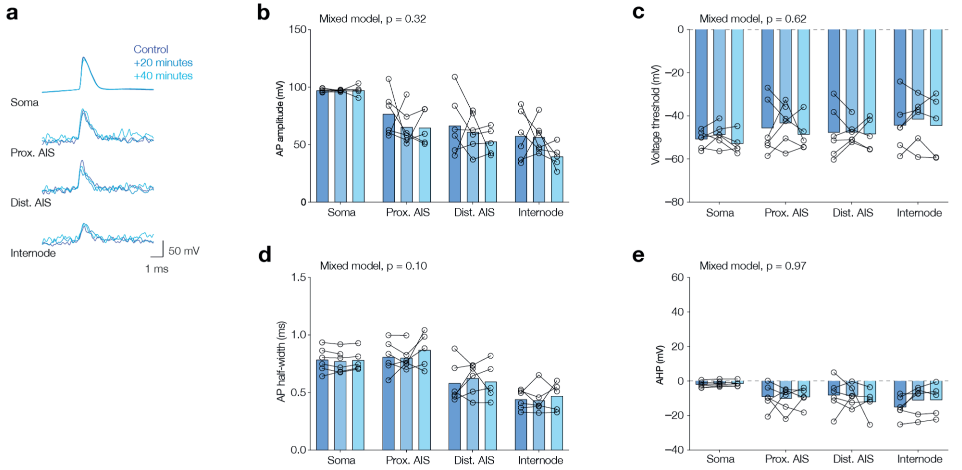

Supplemental Figure 5. Electrical and optical recordings are stable over time
a. Example traces of a cell recorded in control conditions with 20- and 40-minutes delay. **b-e.** The effect of 20 and 40 minutes waiting on **b** AP Amplitude **c** AP threshold **d** AP half-width and **e** fAHP. The results of mixed model comparisons are indicated in the graphs.

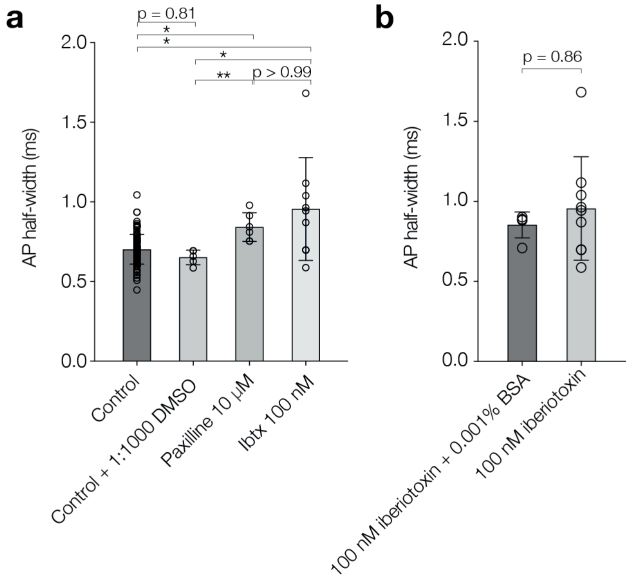

Supplemental Figure 6. Paxilline and IbTx similarly increase AP width
a. AP half-width in control and pharmacological treatments. Paxilline was dissolved in DMSO, but an equimolar concentration did not alter AP half-width. The AP half-width after Paxilline and IbTx application was not different. Statistical test was a Kruskas-Wallis test: p =0.0002, results of multiple comparisons are indicated in the graphs. **b.** Same as **a** but for IbTx with or without 0.001% BSA. Mann-Whitney test: p = 0.86.

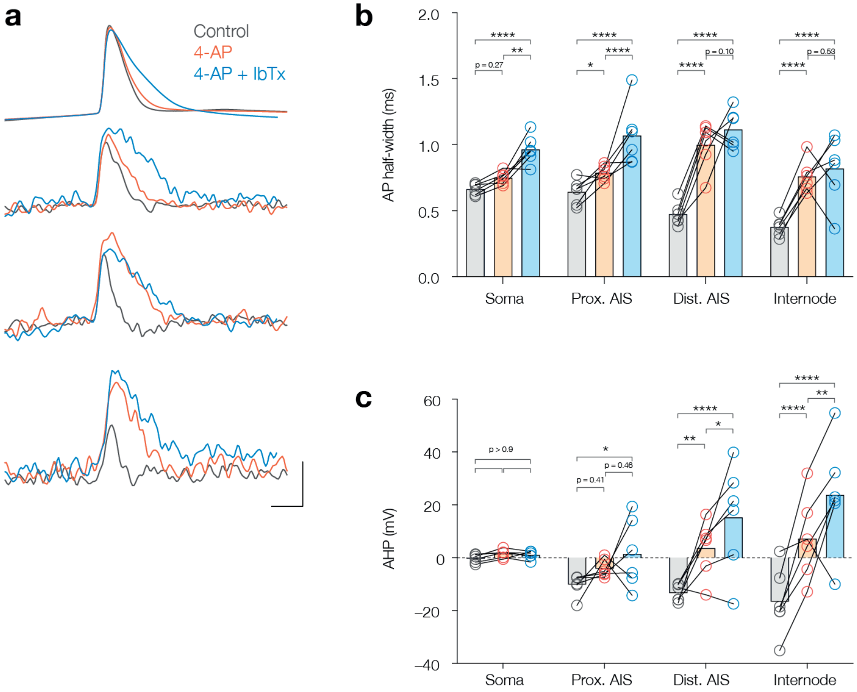

Supplemental Figure 7. IbTx additively affects 4-AP mediated wider APs

a. Example traces from the electrically recorded V_M in the soma and optically recorded V_M in the axon in Control (grey), after bath application of 100 µM 4-AP (red) and after a combined bath application of 100 µM 4-AP and 100 nM IbTx (blue). Scale bars are 1 ms and 50 mV. **b.** Population data for the AP half-width. Paired recordings indicated with grey lines. Two-way ANOVA, condition effect p = 0.0002, interaction location x condition p < 0.0001, multiple comparison statistics indicated by stars, n = 6 cells. **c.** Same as **b** for the fAHP. Two-way ANOVA, condition effect: p = 0.0020, interaction between location and condition: p < 0.0001, multiple comparison statistics indicated by stars, n = 6 cells.

Materials and Methods

Ethical approval

All animal experiments were performed in compliance with the European Communities Council Directive 2010/63/EU effective from 1 January 2013. They were evaluated and approved by the national CCD authority (license AVD8010020172426) and by the KNAW animal welfare and ethical guidelines and protocols (IvD NIN 17.21.01, 21.21.03 and 21.21.06).

Tissue collection for electrophysiology

Young adults Wistar rats (P21 – P42, median 28 weeks old, Janvier Labs) were deeply anaesthetized by inhalation of 3% isoflurane or intraperitoneal injection of 60 mg/kg pentobarbital, prior to decapitation or transcardial perfusion with ice-cold ACSF followed by decapitation (see below), respectively. The hemispheres were removed from the skull and transferred to ice cold carbogenated (95% O_2, 5%CO_2) artificial cerebral spinal fluid (ACSF), containing (in mM): 125 NaCl, 25 $NaHCO_3$, 1.25 NaH_2PO_4, 3 KCl, 25 Glucose, 1 $CaCl_2$ and 6 $MgCl_2$. Parasagittal slices of 300 µm thickness containing the primary somatosensory cortex were cut with a vibratome (VT1200S, Leica Microsystems, Germany). The slices were incubated at 35°C for 35 min, after which they were stored at room temperature in the same solution for at least 30 min.

Electrophysiological recording

For patch-clamp and optical voltage recordings, slices were transferred to the recording chamber of an upright microscope (LNscope, Luigs & Neumann, Germany), perfused with carbogenated (95% O_2, 5% CO_2) ACSF, containing (in mM): 125 NaCl, 25 $NaHCO_3$, 1.25 NaH_2PO_4, 3 KCl, 25 Glucose, 2 $CaCl_2$ and 1 $MgCl_2$. The slices were visualized with transmitted with 850 nm light emitting diode (LED, LZ1-10R602, LED Engin, CA), collimated with an an aspheric condenser lens (ACL50832U-B, Thorlabs, Germany) and adapted to the microscope lamp port using a custom 3D printed adapter and a condenser (U-UCD8-2, Olympus) with a diffuser (DG10-1500, Thorlabs, Germany) in one port turned slightly out of the light path to create Dodt contrast. The top 50 µm of the slice was visualized using a 60× water immersion objective (N.A. 1.1, LUMPLFLN60XW, Olympus, the Netherlands), 2× intermediate zoom attachment (U-ECA, Olympus), camera splitter (U-TRU, Olympus) with inbuilt 180 mm tube lens on the back port and a 0.63× demagnifier (U-TV0.63XC, Olympus) projected the final image onto a high resolution CCD camera (1392×1040 pixels, CoolSNAP-EZ, Photometrics), which was operated using μManager (Edelstein et al., 2014).

Layer 5 pyramidal neurons near the slice surface (< 40 μm) with an axon with a parallel orientation relative to the slice surface and an intact dendrite and axon were selected. Somatic whole-cell recordings were made with patch pipettes pulled to an open tip resistance of 4-5 MΩ. The intracellular solution (ICS) contained (in mM): 130 K-Gluconate, 10 KCl, 10 HEPES, 4 Mg-ATP, 0.3 Na_2-GTP, 10 Na_2-phosphocreatine, adjusted to a pH of 7.25 with KOH. For morphological reconstruction, 5 mg ml^{-1} biocytin was routinely added to the intracellular solution. About half of the pipette taper was filled with dye-free intracellular solution and the pipette was backfilled with ICS without biocytin containing 0.8 mM voltage-sensitive dye JPW3028 (Potentiometric Probes, USA). Current and voltage-clamp recordings were made with the Multiclamp 700B (Molecular Devices, US), run by the Multiclamp 700B commander software (version 2.2.2.2), low-pass filtered at 10 kHz (Bessel), digitized using a HEKA LIH 8+8 Data Acquisition System (HEKA, Harvard Bioscience, US) and sampled at 100 kHz using Axograph X (v.1.7.1 and 1.7.6, Axograph Scientific, NSW, Australia). Bridge balance, pipette capacitance and the liquid junction potential (–13.5 mV) were corrected. Neurons were filled at room temperature for maximum 1 hour (average filling time ~45 min), during which the resting membrane potential and bridge balance were monitored. If the resting membrane potential depolarized and the overall health of the cell decreased, the filling of this cell was stopped. If the bridge balance exceeded 25 MΩ, the cell was repatched with a new pipette. After filling, the patch pipette was carefully retracted, the position of the cell in the slice was noted and the slice was returned to the cutting medium for at least 1 hour and maximum 5 hours (average filling time ~150 min), to let the dye spread equally into the neurites.

Voltage-sensitive-dye (VSD) imaging

JPW excitation was performed with a frequency-doubled 500 mW diode-pumped Nd:YVO4 continuous wave laser emitting at 532 nm (MLL532, Changchun New Industries

Optoelectronics Tech. Co., Ltd., Changchun, China). The light intensity was attenuated by neutral density filters (OD range 0.1 – 4) in a filter wheel (FW212C, Thorlabs, Germany) and passed through a laser line filter (LL01-532-12.5, Semrock). A high-speed mechanical shutter (LS6SZMO Uniblitz, US) connected to a shutter driver (VCM-D1 Uniblitz, US) controlled the laser beam. After the shutter, the beam passed a polarization filter (LPVISA050-MP2, Thorlabs, Germany) and entered a beam expander, consisting of two achromatic lenses ($f = 40$ mm, AC254-040-A and $f = 400$ mm, AC254-0400-A, Thorlabs, Germany) and a pinhole ($d = 45$ µm). The expanded beam passed an aperture (15.8 × 12.6 mm), which cut the beam to the size of the active area of a spatial light modulator (X13138-04, Hamamatsu, Japan), which was controlled by the accompanied software (LCosControl). The reflected hologram was demagnified by a telescope formed by two achromatic lensed ($f = 400$ mm AC254-0400-A, Thorlabs, Germany and $f = 180$ mm). In the shared focal plane of these lenses, a glass slide with a small piece of black tape blocked the 0th order. The blind spot in the sample plane fell laterally just outside the field of view of the NeuroCCD camera used for voltage imaging. The beam was reflected to the sample by a single-edge dichroic mirror (Di03-R532-t1-25x36, Semrock). The emitted fluorescence passed through the dichroic mirror and was filtered by a stopline emission filter (NF01-532U-25, Semrock). The light passed through a tube lens (U-TLUIR, Olympus) and was demagnified (0.35×, U-TV0.35XC-2, Olympus) before it fell on a fast data-acquisition camera (up to 20 kHz) with relatively low spatial resolution (80 × 78 pixels, 26 × 4 pixels on high acquisition rates) but high dynamic range (14 bits) and low read noise (NeuroCCD-SM, RedShirtImaging LLC, Decatur, GA). In combination with the 60× objective, the 78 × 80 chip area corresponded to a focal plane of 89.1 × 91.4 µm and a pixelsize of 1.1 × 1.1 µm^2. For high frame rates (20 kHz) only the subarea of the chip was active and pixels were binned 3 × 3, resulting in a chip area of 26 × 4 pixels, a field of view of 89.1 × 13.7 µm and a pixelsize of 3.4 x 3.4 µm^2. The camera was controlled by NeuroPlex software (version 10.2.1, RedShirtImaging LLC, Decatur, GA), running on IDL (version 7.1.1).

The temperature of the bath was increased to 35°C before the slices containing JPW-filled cells were transferred back to the imaging setup. The filled cell was patched with a pipette containing dye-free ICS with biocytin. The SLM was used to illuminate the sample with a rectangle of light, approximately corresponding to the field of view of the NeuroCCD camera, which we term pseudo-widefield illumination. The stage was positioned so that the soma was just outside the field of view of the NeuroCCD camera and the 26 × 4 pixel chip area contained the first ~90 μm of axon (see Figure x). Next, an image of the fluorescent axon was taken on the high spatial resolution camera. This image was imported in the custom-written matlab GUI *IntensityPattern.fig* (available on https://github.com/Kolelab), which can be used to select a polygon ROI around the axon, based on an imported .tif file, for which we used an image of the fluorescent cell excited in pseudo-widefield illumination. The script creates the desired light intensity profile, which restricts light only to the ROI and counterbalances the non-uniform laser intensity, so the result is a pattern that excites the sample relatively uniform inside the ROI. This pattern was loaded into the software accompanying the SLM (LCosControl), where an iterative Fourier transform algoritm (IFTA) with 100 rounds calculated the required hologram to display onto the SLM. Light exposure to the cell was minimized by using low laser intensity and slow frame rates for focusing and creating the pattern (~2.5 nW/ μm^2). During the experiment, higher laser intensities were used (3-10 μW/ μm^2) and light exposure was kept to a minimum.

The electrophysiological protocol consisted of an 8 ms long positive current injected that faithfully elicited a single AP (current amplitude was adjusted for each cell) and a 400 ms long negative current injection of 1 nA or 1.5 nA, which was used to calibrate the fluorescent signals posthoc. Fluorescence was recorded for 20 ms during the AP and for 10 ms during the calibration pulse. To minimize bleaching, trials were interrupted by at least 30 seconds. The focus of the axon was checked every 3 trials (or 1 minute). Small adjustments in z were sometimes necessary. Per condition generally 12 trials were averaged.

Pharmacology

Pharmacological blockers were added to the appropriate solution (see Table 1). If blockers were dissolved in DMSO (ryanodine and paxilline), equal parts DMSO were also added to the ACSF in the control condition. In all optical recordings, pharmacological data is paired to a control recording. Blockers were present in the recording chamber for at least 10 minutes, before the recording was started. The IbTx experiments were a combination of bath (n = 9 recordings) and puff (n = 4 recordings) application, with a 10× higher concentration in the latter (bath application: 100 nM, puff application: 1 μM). In the puffing experiments, we puffed the solution after 3 trials in 5 applications of 100 ms at 2 psi and ~15 µm distance from the middle of the AIS and checked in the brightfield image that we saw movement of the tissue (Picospritzer). BSA is sometimes added o solutions with toxins, to prevent non-specific binding of the toxin to the tubing and thus an underestimation of the concentration of the drug at the sample. We did not add BSA to the ACSF, because in our experience the solution foams and these bubbles occasionally enter the recording chamber, which can be very inconvenient in an imaging experiment. To ensure that we did not underestimate the concentration of IbTx, we compared the effect of 100 nM IbTx to 100 nM IbTx + 0.001% BSA on the half width of the AP in the soma. We did not observe a difference (IbTx: 956 µs, n = 10, IbTx + BSA: 853 µs, n = 5, Mann-Whitney test, p = 0.70), therefore we were certain that IbTx reached the sufficient bath concentration. The extracellular Ca^{2+} was lowered by bath application of 2.5 mM EGTA and using the online maxchelator tool (https://somapp.ucdmc.ucdavis.edu/) we calculated the remaining Ca^{2+} to be 437 nM, with temperature = 35℃, pH = 7.4 and ionic strength = 0.15 M (Bers et al., 2010). To limit hyperexcitability in the presence of EGTA, we added synaptic blockers to the ACSF (20mM CNXQ and 50mM D-AP5). In EGTA, cells generally required –100 pA holding current to stop spontaneous firing.

Table 1. Pharmacological blockers used in this study

Blocker	Blocks	Concentration	Added to	note
4-aminopyridine (4-AP)	K_V1, K_V3	100 µM	ACSF	
Iberiotoxin	BK channels	100 nM (bath) 1 µM (puff)	ACSF	Washed in, >10 min in bath before first recording, should be enough to block to >90% (Meera et al, 2000, PNAS)
Cadmium	L-type Ca_V	200 µM	ACSF	
Nickel	T-type Ca_V	100 µM	ACSF	Use phosphate free ACSF, increase NaCl to 126.25 mM
ω-conotoxin MVIIC	P/Q, N-type Ca_V	1 µM	ACSF	
Ryanodine	ER Ca^{2+} release	10 µM	ACSF	+ 1:1000 DMSO
Paxilline	BK channels	10 µM	ACSF	+ 1:1000 DMSO

BAPTA	Ca^{2+} buffer	10 mM	ICS	Reduce K-Gluconate to 90 mM and replace by 10 mM K_4-BAPTA
EGTA	Ca^{2+} buffer	10 mM (ICS) 2.5 mM (ACSF)	ICS, ACSF	ICS: Reduce K-Gluconate to 125 mM ACSF: add 20 µM CNX and 50 µM D-AP5.

Data analysis

All data was stored according to the FAIR guidelines. For JPW recordings, only trials with a single action potential were included. Data was analyzed with the custrom-writted *DaMatlab.m* script that is available on github.com/Kolelab. Briefly, the script imports the electrophysiological and optical recordings, along with an ROI defined in the Neuroplex software. The electrophysiological recordings are aligned temporally on the threshold (defined as the moment when dVdt > 50 V/s) and averaged. The following parameters are quantified: threshold, resting membrane potential, AP amplitude (threshold to peak), AP half-width (defined at the half-max amplitude), hyperpolarization during calibration pulse. The temporal jitter of the somatic AP is used to align the optical traces temporally. Non-ROI pixel data is discarded. The data is averaged over trials and the two periods with laser light on are defined (AP pulse and calibration pulse). A single exponential decay is fitted to the optical data, in the calibration pulse to the entire trace and the AP pulse to the trace before the onset of the current injection. The data are divided by the normalized exponential fit to correct for bleach decay. The aligned, averaged and bleach corrected AP traces and the mean intensity during the calibration pulse data are imported into a second script: *ExtractParameters.m* (available on github.com/Kolelab). Traces from prox. AIS (~7 – 21 µm distance from the soma), distal AIS (~31 – 45 µm distance from the soma) and the internode (62 – 71 µm distance from the soma) were spatially averaged and parallelly analyzed. Pixels with an SNR below 2 were excluded. JPW intensity is highly linear over a large voltage range (see Figure 5 Supplement 1 in Hanemaaijer, Popovic et al., 2020) and can be calibrated using the response to a negative stimulus (see Figure S5 in Cohen et al., Cell, 2021). The traces were calibrated with the following calculation:

$$V(F) = \frac{\Delta F_{AP}}{|F_{cal}|}\Delta V_{cal}e^{-x/k}$$

With V(F) being the calibrated fluorescent data, ΔF_{AP} the fluorescent traces relative from baseline, $|F_{cal}|$ the absolute fluorescence intensity during the calibration pulse relative from baseline, ΔV_{cal} is the hyperpolarization of the membrane potential in response to the calibration pulse measured in the soma, x is the distance from the soma and k is the steady state attenuation of voltage, determined be 1.18 mm in Cohen et al., Figure S5, Cell, 2021. The distance from the soma is calculated from the first pixel, which is associated with a certain error. The soma was always placed just outside the CCD field of view and the CCD camera has a relatively low spatial resolution (we focus in widefield illumination and with ~1.1 µm pixels). In posthoc confocal scans of a subset of the recorded AISs, we quantified the AIS distance from the soma at 3.0 ± 0.34 µm and the AIS length at 45.2 ± 1.2 µm (n = 25). Since the variability of these parameters is less than the length of 1 pixel, we assume we make an error in distance from the soma of maximally 1 pixel. Since the width of a pixel (3.4 µm) is much larger than we variance in the AIS onset and length, we did not realign the voltage recordings to the AIS morphology. After calibration, the data was filtered three times with a binomial filter with a window of 3. For each condition and each pixel, the following parameters were extracted: AP peak, AP amplitude, threshold, AP onset, AP half-width, AHP, SNR. Parameters that were unphysiological were excluded, specifically: AP onset < –0.5 ms or > 1 ms, AP width > 1.75 ms. To obtain the BK channel effect (∫ΔV in **Figure 4** and BK onset, delay to peak and peak amplitude in **Figure 5**), the calibrated optical data and the somatic data were filtered with 10 rounds of binomial filter, window 3. Then, the toxin trace was subtracted from the control trace. A double exponential function was fitted to the onset of BK channels effect to obtain the delay to onset in **Figure 5**. In 2 cells, the onset could not be fitted and these were ignored. Membrane potential (Figure 1 and 2) was plotted using the perceptually uniform 'Vik' color sceme (Crameri et al., 2020).

Viral Injections

Viral injections (AAV1 containings Kcnma1 smFP HA ORANGE KI - hSyn_GFP) were performed on adult H11$^{\text{LSL-Cas9}}$ x Rbp4-Cre mice. Mice were deeply anaesthetized via 3% isoflurane and received subcutaneous injection of 5mg/kg Metacom. Body temperature was monitored and maintained at 37 °C. Eye ointment was used to prevent eyes from drying out during the surgery and the head was shaved. Mice were placed in a stereotaxic frame and an incision was made along the midline. Xylocaine was applied before removing the periost. Small (<1 mm) bilateral craniotomies were made at 1.5 mm caudally from Bregma and -0.5 and 0.5 mm laterally from the midline without damaging the dura mater. A sharp glass pipet attached to Nanoject III was used to inject 25 and 50 nl of AAV1 ORANGE KCNMA1 at a depth of -0.450 mm at 1nl/second. 5 minutes after injection, the glass pipette was slowly removed, and bone wax was applied to the craniotomies. The skin was sutured, and animals were allowed to recover.

Tissue Collection and immunohistochemistry

Three weeks post injection, mice were deeply anesthetized via IP injection of pentobarbital and perfused with 4% PFA. Brains were then removed from the skull and received 1 hr post fixation in 4% PFA before being transferred to successive rinses in 10% and 30% sucrose in PBS. Next, 50 µm thick sections were taken using the Leica CM3050 cryostat. Slices were incubated for 2 hr in blocking solution containing 10% NGS and 0.3% Triton-X. Sections were then stained with primary mouse anti-HA antibody (sigma H9658) in 5% NGS and 0.3% Triton-X overnight at room temperature. Slices were then washed with PBS before incubation with secondary antibodies in PBS (1:500 of goat α-mouse Alexa 647 (Invitrogen). Sections were again washed with PBS before being mounted on slides and cover slipped with Vectashield fluorescent mounting medium with DAPI. Slides were then sealed and scanned.

Histochemistry and immunofluorescence

Tissue that was used for optical recordings was generally fixed in 4% PFA for 20 minutes at room temperature on a shaker, before stored in PBS at 4ºC. This tissue was stained for biocytin, MBP and ßIV-spectrin or AnkyrinG. Staining procedures were as follows: a blocking buffer was prepared containing 2% Triton-X and 10% NGS. The tissue was blocked in blocking buffer for 2 hours, the first hour at 37ºC and the second hour on a shaker at room temperature, after it was incubated for 30 minutes at 37ºC and subsequently on a shaker at room temperature overnight in the blocking buffer with the following primary antibodies: 1:500 mouse anti-MBP (Biolegend), 1:1000 rat anti-BIV spectrin (Engelhardt) or 1:500 guineapig anti-ankG (Synaptic Systems). Subsequently, the tissue was washed once for 10 minutes in PBS, before it was incubated for two hours, the first hour at 37ºC and the second hour on a shaker at room temperature, in the blocking buffer containing the following secondary antibodies: 1:500 Streptavidin, Alexa Fluor 488 conjugate (Thermofischer), 1:500 goat anti-guinea pig Alexa 555 (Invitrogen), or 1:500 goat anti-rat Alexa 555 (Invitrogen), 1:500 goat anti-mouse Alexa 647 (Invitrogen). Afterwards, the tissue was washed once for 10 minutes in PBS and the tissue was mounted on a glass slide (Superfrost plus, Thermoscientific). Excess liquid was absorbed with paper and the tissue was immediately coverslipped (Menzel-Gläser). Images were collected on an SP8X (DM6000 CFS; acquisition software Leica Application Suite AF v. 3.2.1.9702) confocal laser-scanning microscope (Leica Microsystems GmbH). Confocal images were acquired on 1048 × 256 pixels (~0.55 μm z-step) using a 40× (N.A. 1.3; 0.75–1.0 digital zoom) oil-immersion objective, corresponding to a region of ~280 × 80 μm. The number of z steps depended on the angle of the axon relative to the optical plane: all steps including axon were scanned. To avoid bleed through between emission wavelengths, multiple channels were sequentially acquired. The data saved as uncompressed LIF format and analyzed in FIJI (Schindelin et al., 2012). Interestingly, we observed an axon-carrying dendrite in 7/68 scanned cells, which is a smaller percentage than of the total population of ~33% (Hamada et al., 2016). It is likely that the careful inspection of the flatness of the AIS in brightfield, before selecting it for recording, introduced a bias against axons originating from the dendrite. In some cells (10/68 scanned), we observed a bleb within the field of view of the confocal scan (mean distance 189 μm from the soma).

Statistics

All statistical tests were performed in Graphpad Prism (version 9.2.0). Electrophysiological data was tested for normality and tested with parametric or non-parametric test based on the normality (**Figure 6** and **Supplemental Figure 6**). Parameters that were analyzed for control conditions (AP amplitude, threshold, AP half-width, AHP, **Figure 2** and **Supplemental Figure 4**) showed similar variance in electrically and optically required data. In all parameters the variance of the electrically recorded potential was smaller than the optically recorded potential, the latter was generally ~2× larger (half-width and AHP) and maximally 1 order of magnitude (AP amplitude), Since these parameters tested the same dependent variable and the variance was similar, they were combined for statistical purposes. For all parameters at least one location (soma, prox. AIS, distal AIS and internode) showed non-normally distributed data, hence Kruskas-Wallis tests were used.

Pharmacological data was analyzed with two-way ANOVA's or mixed models with Location and Condition as the two factors (**Figure 3, 4, 5** and **Supplemental Figure 4, 5 and 7**). Mixed models were used when data was missing, for example if the SNR in 1 location was below 2, which was an exclusion criterium, see *Data analysis*. Posthoc the normality of the residuals was checked in a QQ-plot. Pharmacology in the NoRs was tested using a Mann-Whitney test (**Figure 4**). Data are represented as mean ± the standard error of the mean. Cutoff for statistical significance is p = 0.05.

Code availability

All codes used are available at github.com/Kolelab.

Chapter 4

Robust adaptive optics for localization microscopy deep in complex tissue

Marijn E. Siemons[1], Naomi A.K. Hanemaaijer[1,2], Maarten H.P. Kole[1,2], Lukas C. Kapitein[1]

Published in *Nature Communications* 12:3407 (2021)

Affiliations

[1]Cell Biology, Neurobiology and Biophysics, Department of Biology, Faculty of Science, Utrecht University, Padualaan 8, 3584 CH Utrecht, the Netherlands

[2]Department of Axonal Signaling, Netherlands Institute for Neuroscience, Royal Netherlands Academy for Arts and Sciences (KNAW), Meibergdreef 47, 1105 BA Amsterdam, the Netherlands

Abstract

Single-Molecule Localization Microscopy (SMLM) provides the ability to determine molecular organizations in cells at nanoscale resolution, but in complex biological tissues, where sample-induced aberrations hamper detection and localization, its application remains a challenge. Various adaptive optics approaches have been proposed to overcome these issues, but the exact performance of these methods has not been consistently established. Here we systematically compare the performance of existing methods using both simulations and experiments with standardized samples and find that they often provide limited correction or even introduce additional errors. Careful analysis of the reasons that underlie this limited success enabled us to develop an improved method, termed REALM (Robust and Effective Adaptive Optics in Localization Microscopy), which corrects aberrations of up to 1 rad RMS using 297 frames of blinking molecules to improve single-molecule localization. After its quantitative validation, we demonstrate that REALM enables to resolve the periodic organization of cytoskeletal spectrin of the axon initial segment even at 50 μm depth in brain tissue.

Introduction

Single-Molecule Localization Microscopy (SMLM) (Betzig et al., 2006; Hess et al., 2006; Rust et al., 2006) enables the investigation of the nanoscale organization of cellular structures through repetitive localization of different sparse subsets of fluorophores. SMLM has provided key insights into the nanoscale organization of molecules in cultured cells, including the discovery of sub-membranous actin-spectrin rings in axons (Leterrier et al., 2015; Xu et al., 2013). Cultured cells, and neurons in particular, have limitations as model systems, because they lack most of the three-dimensional cellular organization and neurochemical conditions that are present *in vivo,* including extracellular matrix proteins and nutritional support from glial cells. On the other hand, performing SMLM deep inside tissue or organoids has remained challenging due to sample-induced aberrations. Accurate localization requires sufficient signal to noise and a non-aberrated point-spread-function (PSF) (Barna et al., 2016; Heller et al., 2020; Hou et al., 2015), both of which are compromised when imaging in biological tissue, in which a range of distinct cellular components cause complex light scattering (Liu et al., 2020).

One solution is to perform low-depth (~10 μm) imaging in thin sections) (Barna et al., 2016; Heller et al., 2020; Hou et al., 2015). However, in such experiments most cells within imaging range have been sectioned to some extent, precluding live-cell experiments in such preparations. In contrast, acutely cut >250 μm thick serial sections from the brain preserve most of the characteristics of the neuronal cytoarchitecture and allow the *ex vivo* study of electrophysiological properties. This brain slice preparation is one of the most widely used preparations in neuroscience and facilitates structure-function studies of intact and electrically active brain cell microcircuits. For these reasons, there is a clear need to perform optical nanoscopy deep inside these aberrating samples.

An important methodology to overcome tissue-induced aberrations is the use of intensity-based Adaptive Optics (AO), which uses a deformable mirror in the emission path to compensate for wave-front distortions. The required shape of the mirror can be found by iteratively optimizing the contrast of the image (or guide star when possible) (Booth et al., 2015). However, in SMLM the acquisitions are noisy and contain a strongly fluctuating amount of signal photons, rendering traditional approaches unusable. Various SMLM-specific AO-methods have been proposed to overcome these issues (Burke et al., 2015; Mlodzianoski et al., 2018; Tehrani et al., 2017), but the exact performance of these different AO-methods has not been consistently demonstrated and it has remained unclear what level of aberrations these methods can correct and under which conditions.

Here, we systematically compare the performance of existing methods using both simulations and experiments with standardized samples. We find that for realistic total signal and background ratios these methods provide only limited correction or introduce additional errors. Careful analysis of the reasons that underlie this limited success enabled us to develop an improved method, termed REALM (Robust and Effective Adaptive Optics in Localization Microscopy), which corrects aberrations of up to 1 rad RMS using 297 frames of blinking molecules, thereby enabling robust SMLM at 50 μm depth and even up to 80 μm depth when pre-correcting spherical aberration.

Results

Aberrations alter the point spread function (PSF), decreasing contrast and the spatial frequency support (see **Figure 1a-d**). The key for intensity-based AO is to find a relevant metric, a quality measure computed from the acquisitions, in combination with an optimization algorithm to efficiently and robustly optimize the metric (Booth, 2007). To reduce the effect of strongly fluctuating signal levels of the acquisitions, all existing methods propose a weighted sum of the Fourier transform of the acquisition as metric, while differing in the specific weighting of the spatial frequencies and in normalization (see insert **Figure 1d**). We termed these methods 1, 2 and 3, with metrics M1, M2 and M3, corresponding to Burke et al., Tehrani et al., and Mlodzianoski et al., respectively. Because SMLM acquisitions are comprised of pseudo-random point sources, these methods effectively probe and optimize the Magnitude Transfer Function (MTF). As optimization algorithm to maximize the value of the metrics, Burke et al. use model-based optimization, Tehrani et al. use particle-swarm optimization, and Mlodzianoski et al. use downhill simplex optimization.

In order to systematically compare between different methods, we first sought to establish a standardized sample with tunable signal and background values. Therefore, we used a DNA-PAINT-based sample where molecules transiently bind to the coverslip, mimicking blinking (Schnitzbauer et al., 2017) (see **Figure 1a**). This sample maintains stable signal and noise levels during the complete experimental sequence of several hours (see Methods and **Supplementary Figure 1**). Using a setup with a carefully calibrated deformable mirror (see Methods and **Supplementary Figures 2&3**) we introduced 25 random aberration of Zernike modes, which are polynomials that describe surface shapes. In theory, any wave-front can be described by the sum of infinite Zernike polynomials or modes. Wave-fronts that travel through an optical system or biological tissue undergo alterations or wave-front error and Zernike modes are often used in optics to describe the wave-front errors. Using we deformable mirror, we introduced configurations of 0.75 rad RMS wave-front error, consisting of random combinations of Zernike modes up to the fourth radial order (excluding piston, tip, tilt and defocus) and assessed how well the various methods were able to correct these aberrations (see **Figure 1e,f**). We quantified the Strehl ratio: a measure between 0 and 1 with 1 being a hypothetical unaberrated system. In order to achieve a realistic signal and background level, we tuned the emitter density and intensity to around 20 emitters per frame and 2500 signal photons per emitter. Transmission brightfield illumination was used to substantially increase the background level to 20 photons per pixel in the 400×400 pixel field of view, resulting in a total signal background ratio (SBR) of

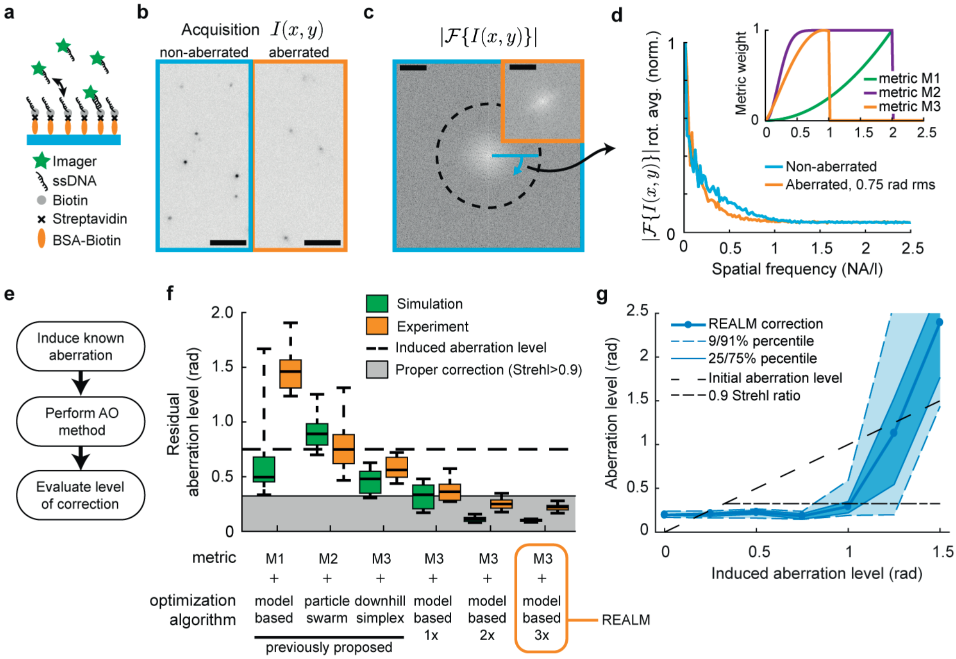

Figure 1. Systematic comparison between different AO methods reveals that only REALM achieves robust correction.

a. DNA-PAINT test sample: imager strands bind transiently to the coverslip, mimicking single-molecule blinking with consistent signal levels for many hours. **b**. Representative acquisition of a non- and 0.75 rad RMS aberrated acquisition (*I(x,y)*) corresponding to **f** (n = 625). Scale bar indicates 5 μm. **c**. Absolute value of the 2D Fourier transform of a non-aberrated acquisition and aberrated acquisition of **b** (orange insert, center crop) (|*F{I(x,y)}*|). Dashed line indicates 2NA / λ. Scale bars indicate NA / λ. **d**. The rotational average of **c** shows that noise dominates spatial frequencies above 1 NA / λ. The major decrease in the MTF due to aberrations occurs between 0.25 and 1 NA / λ. Insert shows the spatial frequency weights of the different proposed metrics. **e**. Strategy for comparing AO methods by inducing known aberrations in a well-corrected system. **f**. Performance of different AO metrics and optimization algorithms. Metric 3 in combination with model-based optimization leads to robust correction in 3 correction rounds (297 acquisitions), and we termed this approach REALM. Boxplot indicates 9/91-percentile, 25/75-percentile and median for 25 random aberration configurations of 0.75 rad rms wave-front error consisting of random combinations of Zernike modes up to the fourth radial order (excluding piston, tip, tilt and defocus). Each frame (400×400 pixels, 26×26 μm) contains on average 13 emitters, emitting 2500 photons with a background of 20 photons per pixel. See Supplementary Figure 1 for more details. **g**. Performance of REALM as function of induced aberration level (10 random aberration configurations). Each frame (400×400 pixels, 26×26 μm) contains on average 17 emitters, emitting 2465 photons with a background of 40 photons per pixel.

0.016 (2500 signal photons × 20 emitters / (20 background photons × 400×400 pixels)). In addition, we tested the performance of the methods on simulated data sets (see Methods).

In both the standardized experiments and the simulations, we found that the previously proposed methods were unable to meaningfully correct the aberrated wave-front. For example, method 1 and method 2 increased the aberration level in 100% and 48% of the experimental cases, respectively, whereas method 3 decreased the aberration level only by 20% (0.16 rad RMS) on average. The experimentally achieved corrections deviated to some extent from the simulation results (**Figure 1f**), likely due to additional noise sources such as read noise and fixed pattern noise from the camera, which are not included in the simulation. Furthermore, the small initial aberration introduced by the DM limited the experimentally achievable aberration level to 0.2 rad RMS (**Supplementary Figure 1e**). Nonetheless, both simulations and experimental data show that none of the three methods robustly achieves proper correction (here taken as a Strehl-ratio of 0.9).

To understand why correction often fails, we next examined how the different metrics depend on noise levels and aberrations. The spatial frequency content of acquisitions in non-aberrated and aberrated conditions revealed that, in both cases, spatial frequencies above 1 NA/λ are dominated by noise (see **Figure 1d**). Metric M1 and M2 have the highest weights for these frequencies, which includes a large amount of noise in the metric value. In contrast, M3 only weights the low spatial frequencies (<1 NA/λ), where signal levels are much higher. This makes metric M3 the most robust measure of the MTF and explains why M3 enables consistent correction, albeit without reaching diffraction-limited imaging.

We wondered whether the limited correction obtained using metric M3 could be caused by the use of simplex optimization. The simplex optimization is sensitive to local noise in the parameter space as it only compares two values per optimization parameter. In contrast, model-based optimization iteratively corrects Zernike modes by applying a sequence of biases for each Zernike mode to be corrected. The metric values for these series of acquisitions are then fitted to a curve (the model or so-called metric curve) to find the optimum (see **Supplementary Figure 4**) (Facomprez et al., 2012). This procedure reduces noise and therefore appears more suitable for AO in SMLM, as originally proposed by

Burke et al. To test this, we implemented metric M3 in combination with model-based optimization. We first simulated aberrated acquisitions to assess the metric curve and found that it could be approximated by a Gaussian function with offset within a range of ± 1 rad per Zernike mode (see **Supplementary Figure 5**). Next, we used a series of simulations to optimize our method in terms of maximum bias range, the number of biases per Zernike mode, and the number of correction rounds (see **Supplementary Figure 6**).

These simulations provided two key insights. First, they revealed the importance of varying the bias over a sufficiently large range to confidently estimate the optimal bias (see **Supplementary Figure 6a-c**). In order to estimate the optimal bias with a high precision, the contrast in the metric value has to be as large as possible and needs to be probed ~0.5-0.75 rad around the optimum. We found that using a maximum bias range of ± 1 rad resulted in the best correction, which is in line with previous work on model-based modal aberration correction (Facomprez et al., 2012). Secondly, these simulations revealed that the precision of the estimated optimal bias depends on the amount of aberration in the other modes, i.e. the contrast in the obtained metric values for the Zernike mode that is being corrected improves when the overall level of aberration is lower. Consequently, the use of multiple correction rounds improves the correction (see **Figure 1f** and **Supplementary Figure 6d-f**). The optimization analysis indicated that there are two efficient correction strategies: either 3 correction rounds, with 9 biases per Zernike mode (3×9×11=297 acquisitions) or 2 correction rounds with 13 biases per Zernike mode (2×13×11=286 acquisitions). The latter option appeared to perform slightly more robust in the conditions with low SBR, whereas the first option achieved slightly better correction if the aberration profile was very unevenly distributed between Zernike modes. In all cases, it was beneficial to first correct the Zernike modes expected to dominate, such as spherical aberration, because for any mode the correction precision depends on the amount of aberration in the other modes.

We experimentally verified this approach using the DNA-PAINT sample and were able to consistently reduce the induced wave-front error of 0.75 rad RMS by a factor of two in the first correction round (99 acquisitions). The second correction round (another 99 acquisitions) yielded further improvement and achieved diffraction-limited imaging in 21 out of 25 cases, whereas after the third correction round (297 acquisitions in total) all induced aberrations were corrected (see **Figure 1f**). We termed this method REALM (Robust and Effective Adaptive Optics in Localization Microscopy) and implemented it as a freely available and open source Micro-Manager plugin (Edelstein et al., 2014) (see Methods). The performance of REALM was evaluated further by measuring the aberration correction for increasing amounts of induced aberrations and different signal background ratios. This revealed that our method was able to robustly correct aberrations of up to 1 rad RMS (see **Figure 1g** and **Supplementary Figure 7**) for various signal and noise levels. Even with very low signal levels (6 emitters on average, 1745 signal photons per emitter and 216 background photons, 0.0003 SBR) REALM was able to correct significant aberrations (see **Supplementary Figure 7c**).

We next aimed to test this approach for SMLM using more complex experimental samples. Previously, Mlodzianoski et al. used a water-filled cavity to validate their method (Mlodzianoski et al., 2018). However, such a sample does not fully capture the complexity of complex tissue, where cell bodies, capillaries and nerve fibers all may act as obstacles for light and distort the wave-front. Others have tested their AO method using fluorescent beads imaged through the nematode C. elegans (Tehrani et al., 2017). While this assay features a richer aberration profile, the beads are bright and do not exhibit blinking dynamics. In an effort to better mimic deep-tissue localization microscopy, we performed SMLM on COS-7 cells stained for microtubules (a staple reconstruction test in SMLM), but imaged these cells through brain sections of 50 and 80 μm thickness (see **Figure 2** and **Supplementary Figure 8**). We chose this sample over stained tissue for our first analyses, because these microtubule immunostainings are highly reproducible and result in recognizable structures. To address the scattering induced by the sample we mounted the brain sections in a glycerol-based buffer instead of a water-based buffer, similar to previous work (Hou et al., 2015). This reduces scattering by reducing the local differences in refractive index between the subcellular content and the mounting medium. Slices mounted in this buffer appear almost transparent in regions such as the cortex, indicating that scattering is indeed reduced. We estimated that the refractive index of brain sections in this buffer is around 1.48 (assuming an overall refractive index of 1.4 and a water content of 70% before incubation in the glycerol buffer). We therefore used a 1.49 NA oil objective

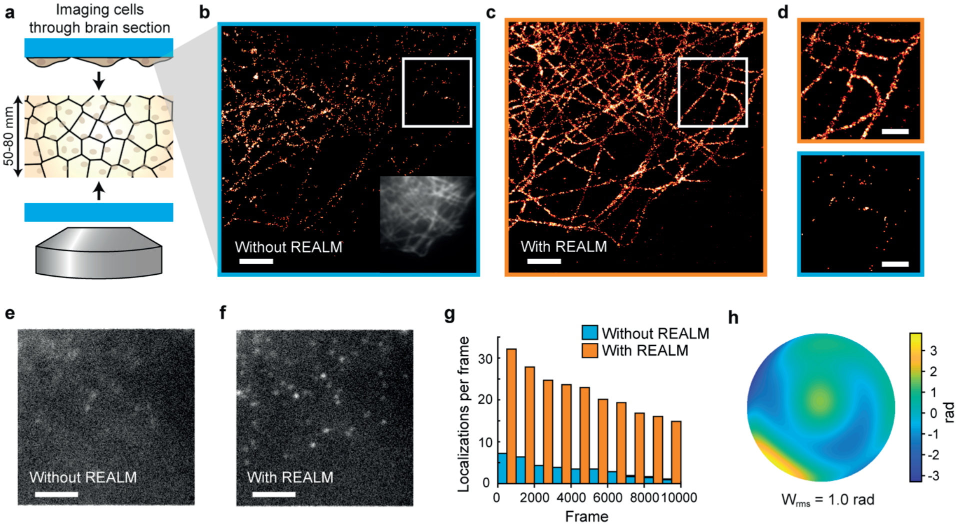

Figure 2. Improved single-molecule imaging through brain sections using REALM
a. Illustration of the sample. A 50 µm brain slice is mounted in between two cover glasses, on one of which COS-7 cells were grown. These cells were stained for microtubules (aTub) and imaged through the brain section, to mimic deep-tissue imaging. **b**-**c**. SMLM reconstruction of microtubules in COS-7 cells through a 50 µm thick brain section with 5000 frames without AO sample correction (without REALM, panel **b** and with sample-based correction (with REALM, panel **c**). Insert in panel **b** shows the widefield image prior to correction. FRC resolution is 196 nm and 127 for **b** and **c** respectively. Scale bars indicate 2 µm. **d**. zoom of **b** and **c** indicated by white square. Scale bars indicate 1 µm. **e**-**f**. Representative single acquisitions corresponding to the reconstruction of **b** and **c** respectively. Scale bars indicate 4 µm. **g**. Number of localizations in the acquisition series during which the DM alternated between the system-corrected state (without REALM) and sample-corrected state (with REALM) every 500 frames. **h**. Estimated wave-front distortion as estimated using REALM, of which 0.55 rad was used as initial guess for primary spherical aberration. Repeated n =10 times in 3 distinct samples.

to ensure larger collection efficiency and less sample-induced spherical aberrations compared to a silicon immersion objective lens (see **Supplementary Figure 9**).

With this assay, we performed a systematic comparison between REALM and no-AO conditions by switching between the system-corrected state (without REALM) and the sample-corrected state (with REALM) every 500 frames during the SMLM acquisition (see **Supplementary Movie 1**). We found that REALM increased the number of successful localizations (see methods for classification details) up to 6-fold, resulting in a strongly improved reconstruction (see **Figure 2**). The resolution estimated using Fourier Ring Correlation (FRC) improved by 35% when using REALM. For the 80 µm thick slices, we estimated the spherical aberration to be around 100 nm and used this for precorrection. We switched the DM between this pre-corrected state and the sample-corrected state and again found an improvement in both the number of detected events when using REALM as well as the FRC (24% improvement) (see **Supplementary Figure 8**), indicating that non-spherical aberrations contribute considerably to image deterioration as well.

We found that without AO blinking events are detectable only if the events are bright and perfectly in focus. This approach still yielded recognizable features in the reconstruction (see **Figure 2b**), but with much lower number of localizations. This was caused by the aberrated PSF, which quickly broadened when molecules were slightly out of focus (±100-200nm) and therefore significantly hampered detection (see **Figure 2e** and **Supplementary Movie 1**). With REALM, the PSF is more symmetric and remains focused along the focal depth of the objective. This increases the detection of dim blinking events as well as the detection of molecules inside the complete depth of focus. Therefore the reconstruction with REALM also contains microtubule structures that are not visible in the reconstruction without AO (see **Figure 2d**). Although the ground-truth aberrations were unknown, the increase in the number of detected events, as measured using the exact same fluorescent structures, demonstrates the success of the AO algorithm.

We next used a similar sample (COS-7 cells imaged through 60 μm thick brain slices) to directly compare REALM to the method proposed by Mlodzianoski et al., (see **Supplementary Figure 10**). This revealed that REALM was more effective in restoring the PSF, which consequently improved detection and localization. Overall, this resulted in a 2.2× increase (median) in number of localizations with a localization precision below 20 nm and an 8.6× increase in the number of localizations with a precision below 5 nm. Even when we extended the previously published method by including more Zernike modes than originally proposed, it could not achieve the same correction as REALM. The FRC resolution improved from 150 nm (median) when using the method of Mlodzianoski et al. to 120 nm (median) when using REALM. On average, REALM estimated the aberrations to be around 1 rad RMS, whereas the method of Mlodzianoski et al. resulted in a 3-fold lower estimate, leaving an average residual aberration of around 0.7 rad RMS. These results demonstrate that REALM achieves a 3-fold improvement in aberration correction over previous methods and enables robust single-molecule imaging at 60 µm depth through brain tissue with improved resolution.

Next, we aimed to image structures stained within the tissue itself and focused on the axon initial segment (AIS) of cortical layer 5 pyramidal neurons in rat brain slices of 300-400 µm thickness. Landmark SMLM experiments have used neurons cultured on coverslips to reveal that axons display a ~190 nm actin-spectrin based periodic structure called the membrane-associated periodic scaffold (MPS), which at the AIS includes βIV-spectrin (Leterrier et al., 2015; Xu et al., 2013). However, due to the limited imaging depth of conventional SMLM, correlating these structures to functional recordings of neurons in brain slices is not possible. In acute brain slices healthy neurons are typically located at >30 µm depth from the slice surface and can be reliably targeted by a patch pipette up to 100 µm depth (Stuart et al., 1993). Using REALM, we could perform multiplane 3D astigmatic SMLM imaging on βIV-spectrin stained brain sections up to a depth of 50 µm (**Figure 3**). We resolved the periodic patterning of this scaffolding protein in 3D and revealed a periodicity of 203 ± 10 nm (mean ± s.d., **Figure 3**, **Supplementary movie 2&3** and **Supplementary Figure 11**). For details of the estimated aberrations see **Supplementary Figure 12**. Beyond 50 µm depth, the increase background levels hindered both REALM and single-molecule detection.

To further examine the improvement achieved by REALM we imaged βIV-spectrin in slices and switched between uncorrected and corrected mirror states during the acquisition, which resulted in an improved reconstruction upon correction (76 nm FRC with AO, 100 nm FRC without AO, see **Supplementary Figure 13a**). In addition to improving the number of detections and the FRC, the use of Adaptive Optics also corrected the loss of ellipticity when performing astigmatic 3D SMLM (Mlodzianoski et al., 2018; Siemons et al., 2020). We observed a depth-dependent increase in aberrations (see **Supplementary Figure 13d**) and have shown in previous work (Siemons et al., 2020) that this loss of ellipticity is due to (higher order) spherical aberration, revealing why the applied astigmatism level has to increase when imaging in tissue even with using AO. Without such an increased level of astigmatism, the z-encoding is lost, rendering volumetric multiplane astigmatic 3D SMLM unattainable because individual focal planes cannot be stitched (see

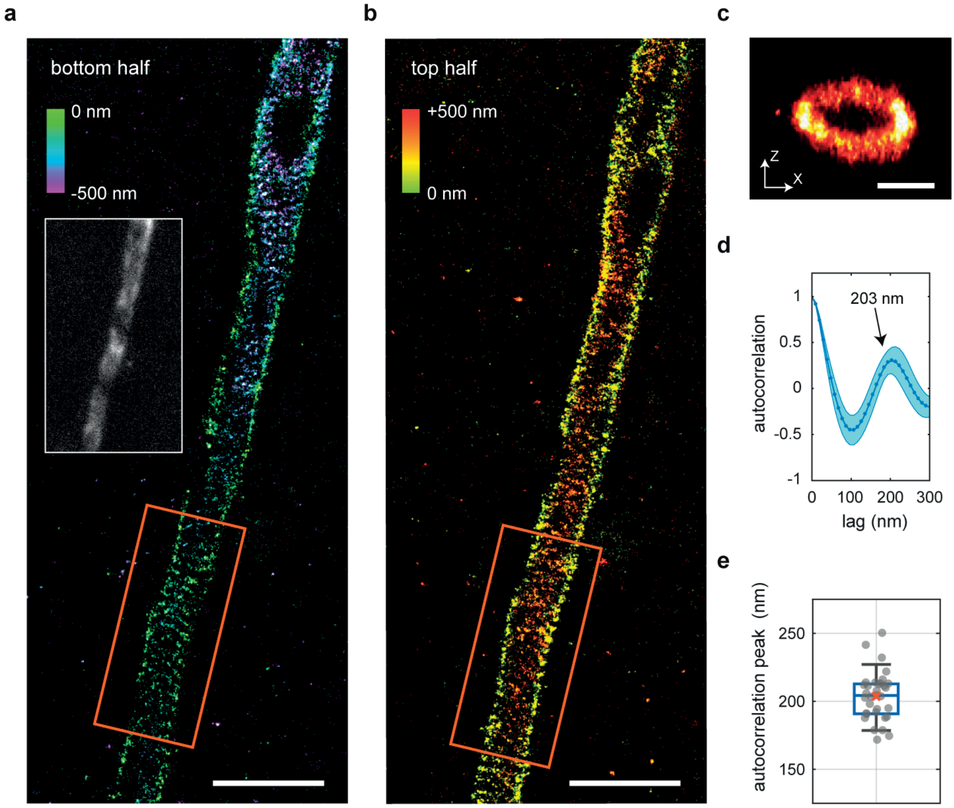

Figure 3. Resolving the nanoscale spectrin organization in axons at 50 µm depth. **a**-**b**. SMLM reconstruction of the upper half (panel **a**) and lower half (panel **b**) of a layer 5 pyramidal neuron AIS stained for ßIV spectrin in a rat brain slice at 50 µm depth. Color encoding indicates the z-position. Scale bars indicates 2 µm. Insert with white rim shows the widefield image prior to aberration correction. The holes in ßIV spectrin pattern are likely sites of synaptic connections. Scale bar indicates 2 µm. **c**. z-x cross-section of the rectangular orange area indicated in (**a**-**b**). Scale bar indicates 500 nm (both directions). **d**. The average autocorrelation (blue line) of 30 line segments in the reconstruction of 3(a,b) and Supplementary Figure 11 shows a peak at 203 ± 10 nm. Shaded region indicates the standard deviation. **e**. Distribution of the estimated autocorrelation peaks of the individual line segments of reconstructions of a,b and Supplementary Figure 11. Boxplot indicates 9/91-precentile, 25/75-precentile and median. Red cross indicates the mean autocorrelation distance. See also Supplementary Figure 11. Repeated n=12 times in 4 distinct samples with similar results.

Supplementary Figure 13b,c). Using PSF simulations described in our previous work (Siemons et al., 2020) we could determine the theoretical required astigmatism level at each depth to obtain a constant calibration curve. Application of these estimated levels of

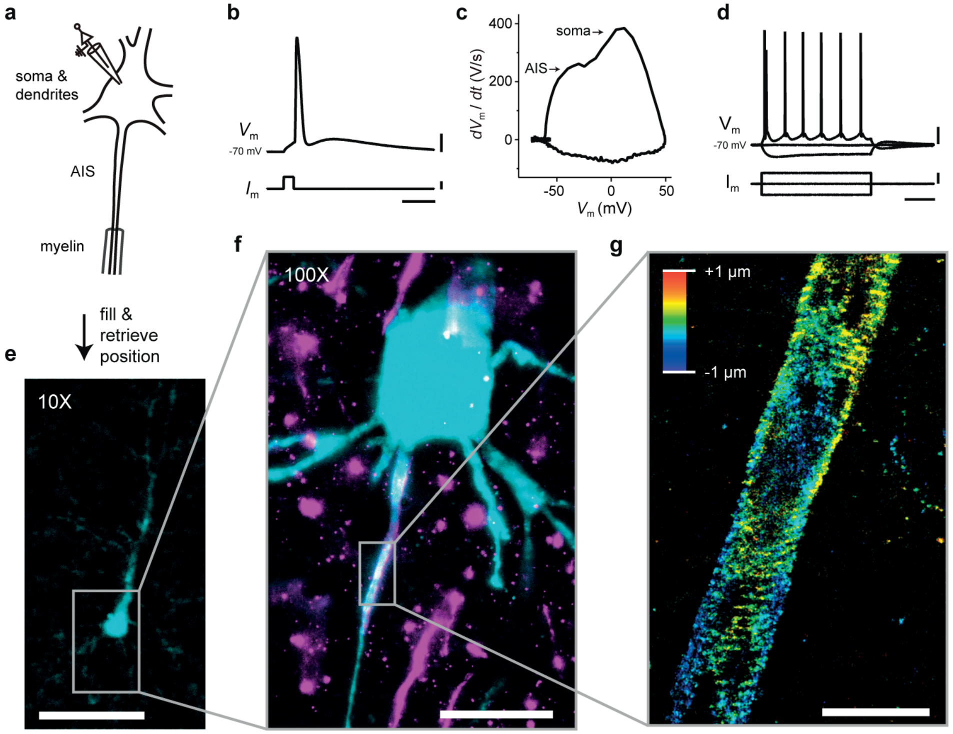

Figure 4. Proof-of-principle for following up electrophysiological recordings with 3D SMLM in brain sections.

a. Schematic of electrophysiological whole-cell patch clamp recording. **b**. An action potential of a layer 5 pyramidal neuron in an acute brain slice patched at 35 µm depth. V_M, membrane potential and IM, injected current. Scale bars indicate from top to bottom: 20 mV, 500 pA and 10 ms. **c**. Phase-plane plot (dV_M /dt versus V_M) of the action potential shown in **b** showing separate peaks from the AIS and the somatodendritic compartment. **d**. The membrane potential (V_M) in response to negative and positive current injections (I_M). Scale bars indicate from top to bottom: 20 mV, 200 pA, 200 ms. **e**. Widefield image (10×) of the whole-cell recorded and biocytin-filled pyramidal neuron **b-d** labelled with streptavidin-Alexa488. Scale bar indicates 100 mm. **f**. Same as **e** but with a 100× objective. Magenta shows the ßIV spectrin-Alexa647 staining. Scalebar indicates 20 µm. **g**. 3D SMLM reconstruction of the ßIV spectrin at the AIS of the same whole-cell patch clamped neuron (**b-f**). Single-molecule localizations of four focal planes are merged. Color depicts z-position. Scalebar indicates 2 µm.

astigmatism restored proper z-encoding and allowed volumetric multiplane astigmatic 3D SMLM (**Figure 3** and **Supplementary Figures 11, 13 & 14**).

Finally, we also successfully resolved the βIV-spectrin structure of a functionally identified pyramidal neuron in a brain section (**Figure 4**). First, electrophysiological recordings were performed on a layer 5 pyramidal neuron (**Figure 4a-d**), after which the neuron was filled with biocytin, fixed and stained. After mounting of the brain section and application of the SMLM buffer, the position of the patched neuron was retrieved using the stained biocytin fill and a 10× objective. Subsequently, SMLM in combination with REALM was used to resolve the nanoscale architecture of βIV-spectrin, demonstrating the possibility to directly correlate functional studies and nanoscopic organization.

Discussion

In this work, we systematically analyzed the performance of different AO techniques for SMLM using standardized samples. Comparing different methods in an objective and robust manner is challenging, because signal and background levels can vary dramatically between samples and often also rapidly change during acquisitions. To overcome this, we first used DNA-PAINT in combination with a well-calibrated deformable mirror to compare and validate the performance of previously published methods in identical signal and background levels, while systematically varying the levels and types of aberrations. We augmented these experiments with simulations to further compare how different methods perform in identical conditions. Furthermore, we imaged densely-labeled cells through brain slices of varying thickness, enabling the side-by-side evaluation of different methods in identical conditions with physiological aberrations. Together, these assays revealed that previously proposed AO methods provide only limited correction or in some cases introduced additional aberrations. Careful analysis of the reasons that underlie this limited success enabled us to develop REALM. We demonstrated that REALM can robustly correct aberration levels up to 1 rad RMS in realistic signal and noise levels and using less than 300 acquisitions. Compared to standard imaging (non-AO) and earlier AO methods, REALM detects more molecules and obtains better FRC resolutions.

Next to these idealized samples, we also tested the performance of REALM in stained brain slices. We demonstrated multiplane 3D astigmatic SMLM imaging on βIV-spectrin stained brain sections up to a depth of 50 μm and resolved the periodic structure in 3D. Importantly, we also resolved this structure in a functionally identified pyramidal neuron, demonstrating the feasibility of directly correlating functional studies to nanoscopic organizations. While imaging βIV-spectrin, typical background levels ranged between 200-300 photons per pixel, resulting in a SBR of around 0.005 (depending on the imaging depth, size of the AIS, and labeling), which is in the range in which REALM can achieve significant correction (see **Supplementary Figure 7**).

Beyond 50 mm depth, we found that not the aberration level, but the increase in background fluorescence hampered both aberration correction and localization. In preliminary experiments we noticed that at lower glycerol concentrations (50%), less laser power was required to switch fluorophores to a dark state, which reduced the background levels (to ~50 background photons per pixel) at the expense of more spherical aberration and scattering. The best imaging buffer in tissue might therefore depend on the required imaging depth, the abundance of the staining throughout the sample and the number of fluorophores blinking inside the field of view. To further reduce background, light-sheet based illumination could be considered. In addition, the use of cell-specific *in vivo* knock-in (KI) approaches in brain tissue, such as ORANGE [20], enables tagging endogenous proteins in only a subset of cells (~1-10%) within the tissue, thereby further reducing background. We anticipate that REALM can enable 80 or 100 µm deep imaging in tissue when combined with approaches that limit out-of-focus fluorescence by either light-sheet illumination or sparse labeling using an *in vivo* knock-in approach (Willems et al., 2020).

REALM can be combined with other z-localization techniques such as PSF engineering (Pavani et al., 2009; Shechtman et al., 2014) or self-interference (Bon et al., 2018). Our approach also complements the recently introduced INSPR (In Situ Point Spread function Retrieval) localization method, which demonstrated accurate 3D localization in aberrated conditions when imaging below 20 µm depth (Xu et al., 2020). Thus, we anticipate that the open source micromanager plug-in REALM that we provide will enable new avenues for SMLM in deep tissue and facilitate correlative functional and nano-structural research.

References

Barna L, Dudok B, Miczán V, Horváth A, László ZI, Katona I. 2016. Correlated confocal and super-resolution imaging by VividSTORM. *Nat Protoc* 11:163–183. doi:10.1038/nprot.2016.002

Betzig E, Patterson GH, Sougrat R, Lindwasser OW, Olenych S, Bonifacino JS, Davidson MW, Lippincott-Schwartz J, Hess HF. 2006. Imaging Intracellular Fluorescent Proteins at Nanometer Resolution. *Science* 313:1642–1645. doi:10.1126/science.1127344

Bon P, Linarès-Loyez J, Feyeux M, Alessandri K, Lounis B, Nassoy P, Cognet L. 2018. Self-interference 3D super-resolution microscopy for deep tissue investigations. *Nat Methods* 15:449–454. doi:10.1038/s41592-018-0005-3

Booth M, Andrade D, Burke D, Patton B, Zurauskas M. 2015. Aberrations and adaptive optics in super-resolution microscopy. *Microscopy* 64:251–261. doi:10.1093/jmicro/dfv033

Booth MJ. 2007. Adaptive optics in microscopy. *Philosophical Transactions Royal Soc Math Phys Eng Sci* 365:2829–2843. doi:10.1098/rsta.2007.0013

Burke D, Patton B, Huang F, Bewersdorf J, Booth MJ. 2015. Adaptive optics correction of specimen-induced aberrations in single-molecule switching microscopy. *Optica* 2:177–185. doi:10.1364/optica.2.000177

Chazeau A, Katrukha EA, Hoogenraad CC, Kapitein LC. 2016. Chapter 5 Studying neuronal microtubule organization and microtubule-associated proteins using single molecule localization microscopy. *Methods Cell Biol* 131:127–149. doi:10.1016/bs.mcb.2015.06.017

Edelstein AD, Tsuchida MA, Amodaj N, Pinkard H, Vale RD, Stuurman N. 2014. Advanced methods of microscope control using μManager software. *Journal of Biological Methods* 1:10–10. doi:10.14440/jbm.2014.36

Facomprez A, Beaurepaire E, Débarre D. 2012. Accuracy of correction in modal sensorless adaptive optics. *Opt Express* 20:2598. doi:10.1364/oe.20.002598

Heller JP, Odii T, Zheng K, Rusakov DA. 2020. Imaging tripartite synapses using super-resolution microscopy. *Methods San Diego Calif* 174:81–90. doi:10.1016/j.ymeth.2019.05.024

Hess ST, Girirajan TPK, Mason MD. 2006. Ultra-High Resolution Imaging by Fluorescence Photoactivation Localization Microscopy. *Biophys J* 91:4258–4272. doi:10.1529/biophysj.106.091116

Hou Y, Jayasinghe I, Crossman DJ, Baddeley D, Soeller C. 2015. Nanoscale analysis of ryanodine receptor clusters in dyadic couplings of rat cardiac myocytes. *J Mol Cell Cardiol* 80:45–55. doi:10.1016/j.yjmcc.2014.12.013

Leterrier C, Potier J, Caillol G, Debarnot C, Boroni FR, Dargent B. 2015. Nanoscale Architecture of the Axon Initial Segment Reveals an Organized and Robust Scaffold. *Cell Reports* 13:2781–2793. doi:10.1016/j.celrep.2015.11.051

Liu S, Huh H, Lee S-H, Huang F. 2020. Three-Dimensional Single-Molecule Localization Microscopy in Whole-Cell and Tissue Specimens. *Annu Rev Biomed Eng* 22:1–30. doi:10.1146/annurev-bioeng-060418-052203

Mlodzianoski MJ, Cheng-Hathaway PJ, Bemiller SM, McCray TJ, Liu S, Miller DA, Lamb BT, Landreth GE, Huang F. 2018. Active PSF Shaping and Adaptive Optics Enable Volumetric Localization Microscopy through Brain Sections. *Nat Methods* 15:583–586. doi:10.1038/s41592-018-0053-8

Pavani SRP, Thompson MA, Biteen JS, Lord SJ, Liu N, Twieg RJ, Piestun R, Moerner WE. 2009. Three-dimensional, single-molecule fluorescence imaging beyond the diffraction limit by using a double-helix point spread function. *Proc National Acad Sci* 106:2995–2999. doi:10.1073/pnas.0900245106

Rust MJ, Bates M, Zhuang X. 2006. Sub-diffraction-limit imaging by stochastic optical reconstruction microscopy (STORM). *Nat Methods* 3:793–796. doi:10.1038/nmeth929

Schnitzbauer J, Strauss MT, Schlichthaerle T, Schueder F, Jungmann R. 2017. Super-resolution microscopy with DNA-PAINT. *Nat Protoc* 12:1198–1228. doi:10.1038/nprot.2017.024

Shechtman Y, Sahl SJ, Backer AS, Moerner WE. 2014. Optimal Point Spread Function Design for 3D Imaging. *Phys Rev Lett* 113:133902. doi:10.1103/physrevlett.113.133902

Siemons M, Cloin BMC, Salas DM, Nijenhuis W, Katrukha EA, Kapitein LC. 2020. Comparing strategies for deep astigmatism-based single-molecule localization microscopy. *Biomed Opt Express* 11:735. doi:10.1364/boe.382023

Siemons M, Hulleman CN, Thorsen RØ, Smith CS, Stallinga S. 2018. High precision wavefront control in point spread function engineering for single emitter localization. *Biorxiv* 267864. doi:10.1101/267864

Stallinga S, Rieger B. 2010. Accuracy of the Gaussian Point Spread Function model in 2D localization microscopy. *Opt Express* 18:24461. doi:10.1364/oe.18.024461

Stuart GJ, Dodt HU, Sakmann B. 1993. Patch-clamp recordings from the soma and dendrites of neurons in brain slices using infrared video microscopy. *Pflügers Archiv - European Journal of Physiology* 423:511–518. doi:10.1007/bf00374949

Tehrani KF, Zhang Y, Shen P, Kner P. 2017. Adaptive optics stochastic optical reconstruction microscopy (AO-STORM) by particle swarm optimization. *Biomed Opt Express* 8:5087. doi:10.1364/boe.8.005087

Willems J, Jong APH de, Scheefhals N, Mertens E, Catsburg LAE, Poorthuis RB, Winter F de, Verhaagen J, Meye FJ, MacGillavry HD. 2020. ORANGE: A CRISPR/Cas9-based genome editing toolbox for epitope tagging of endogenous proteins in neurons. *Plos Biol* 18:e3000665. doi:10.1371/journal.pbio.3000665

Xu F, Ma D, MacPherson KP, Liu S, Bu Y, Wang Y, Tang Y, Bi C, Kwok T, Chubykin AA, Yin P, Calve S, Landreth GE, Huang F. 2020. Three-dimensional nanoscopy of whole cells and tissues with in situ point spread function retrieval. *Nature Methods* 17:1–36. doi:10.1038/s41592-020-0816-x

Xu K, Zhong G, Zhuang X. 2013. Actin, spectrin, and associated proteins form a periodic cytoskeletal structure in axons. *Science* 339:452–456. doi:10.1126/science.1232251

Supplementary Information for:

Robust adaptive optics for localization microscopy deep in complex tissue

Marijn E. Siemons[1], *Naomi A.K. Hanemaaijer*[1,2], *Maarten H.P. Kole*[1,2], *Lukas C. Kapitein*[1]

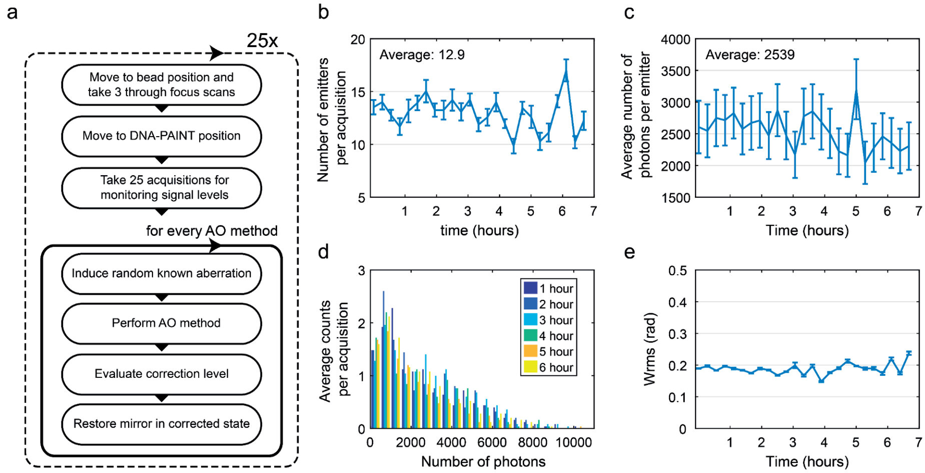

Supplementary Figure 1. DNA-PAINT sample and deformable mirror remain stable during the experiment of Figure 1f.

a. Schematic of the experimental procedure, consisting of a monitoring part (first 3 blocks) and a correction part (bottom 4 blocks). For all AO methods tested, the stage moves to a position with a bead and acquires 3 through-focus scan. Next, 25 frames were acquired at the DNA-PAINT position (without a bead in the FOV) with the system-corrected DM state. From these acquisitions the number of emitters **b**, number of photons per emitter **c** and distribution of photon counts were measured **d**. This revealed that the signal levels remained constant for the full 7 hour duration of the experiment. The acquired through-focus scans (in system corrected state) are analyzed with a phase retrieval algorithm [25] to check for possible drift in the mirror. The aberration level (**e**) remained at a level of 0.2 rad RMS during the whole experiment. Error bars indicate the standard error of mean in the number of emitters (**b**), number of photons (**c**) of the 25 frames and estimated aberration level (**e**) measured from 3 through focus scans.

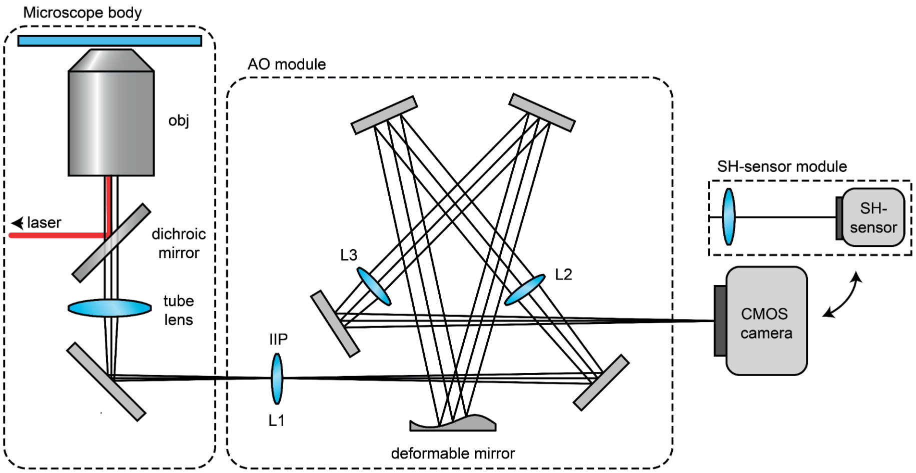
Microscope body
obj
laser
dichroic mirror
tube lens
AO module
L3
L2
IIP
L1
deformable mirror
SH-sensor module
SH-sensor
CMOS camera

Supplementary Figure 2. Illustration of the set up.

The AO module consists of a 4F system (lenses L2 and L3, f = 500 mm), where the deformable mirror (DM) is placed in the back focal plane of L2. Another lens (L1, f = 750 mm) is placed in the intermediate image plane (IIP), which conjugates the pupil plane of the objective to the DM. This lens is needed as the tube lens and objective inside the microscope body are placed approximately 5 cm too close to each other to form a 4F system. For calibration of the DM, the CMOS camera is replaced with the SH-sensor module, which consists of a lens (f = 100 mm) and a Shack-Hartman sensor.

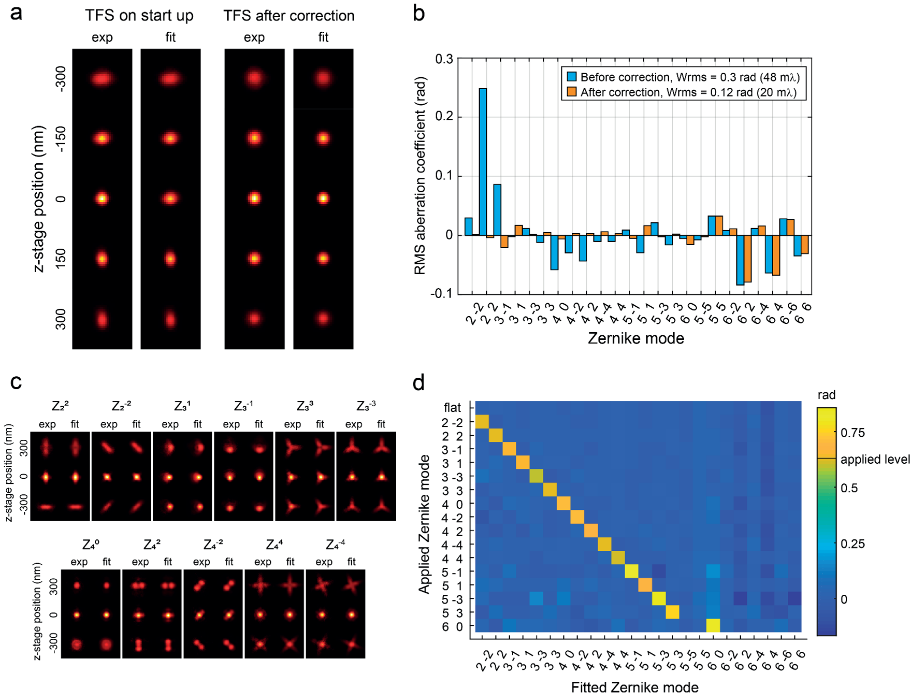

Supplementary Figure 3. Verification of the DM-calibration.

a. On start-up the experimental PSF (exp) is aberrated due to drift in the deformable mirror. A phase retrieval algorithm (fit) (see methods) estimated the specific Zernike modes as shown in (**b**). The inverse Zernike coefficients of modes Z2 ±2, Z3 ±1, Z3 ±3, Z40, Z4 ±2, Z4 ±4, Z5 ±1, Z5 ±3 and Z60 were subsequently applied by the mirror, which improves the PSF (TFS after correction). Phase retrieval revealed that all major contributing Zernike modes were nullified. **c.** PSFs and phase retrieval fits corresponding to Zernike modes Z2 ±2, Z3 ±1, Z3 ±3, Z40, Z4 ±2, Z4 ±4 with an amplitude of 0.63 rad (100 mλ). **d**. phase retrieval of (**c**) revealed that this DM is capable of accurately modulating Zernike modes up to the fourth order with little crosstalk. Higher order modes such as Z5 ±1, Z5 ±3 and Z60 appear to have crosstalk with lower modes.

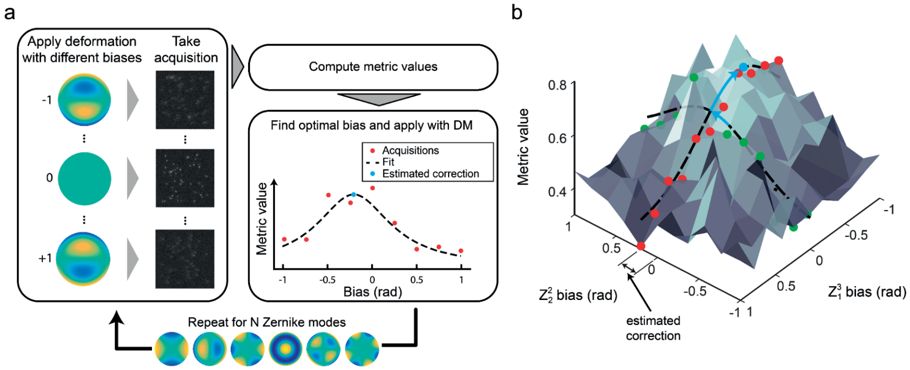
a
Apply deformation with different biases
Take acquisition
-1
0
+1
Compute metric values
Find optimal bias and apply with DM
Acquisitions
Fit
Estimated correction
Metric value
Bias (rad)
-1
-0.5
0
0.5
1
Repeat for N Zernike modes
b
Metric value
0.8
0.6
0.4
1
0.5
0
-0.5
-1
Z_2^2 bias (rad)
estimated correction
1
0.5
0
-0.5
-1
Z_1^3 bias (rad)

Supplementary Figure 4. **Schematic of model-based optimization.**

a. For each Zernike mode a series of frames is acquired with different biases (amplitude of the Zernike mode). From these acquisitions the metric value is computed. Next, the optimal bias is determined by fitting an appropriate function (the metric curve) to these points, after which the estimated correction is applied. This is performed for multiple Zernike modes. **b.** The optimum correction for Zernike modes can be more easily estimated when the contrast in metric value is improved. Therefore, it is beneficial to first correct major expected types of aberrations, such as spherical aberration. For the same reason, multiple correction rounds also yield additional improvement.

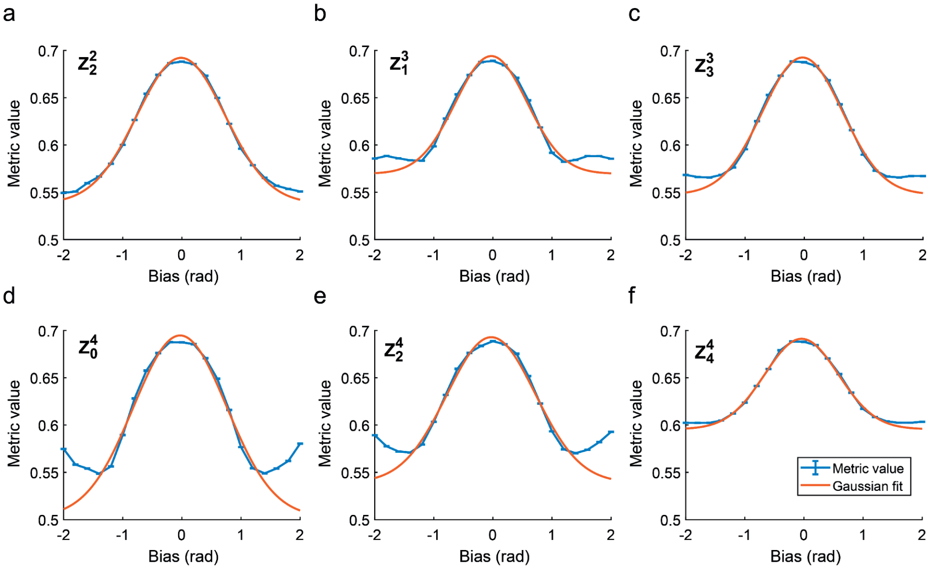

Supplementary Figure 5. Metric curves for different Zernike modes

a-f. Metric value as function of applied bias for different Zernike modes. These values were obtained by simulating single-molecule acquisitions (see methods) with different biases for each Zernike mode. A Gaussian function with offset properly describes the metric values to all Zernike modes up to the 4th order in a ± 1 rad range and was therefore used as the metric curve. Increasing the bias beyond ± 1.5 rad results in an increase in the metric value for some Zernike modes. This inversion of the metric value occurs due to contrast inversion at (specific) spatial frequencies.

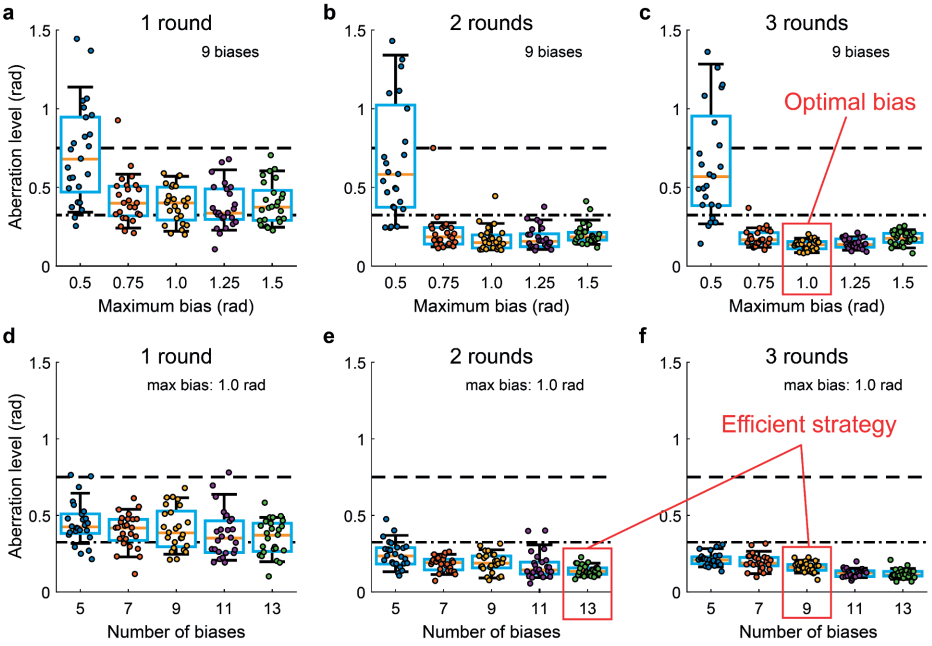

Supplementary Figure 6. Simulation-based optimization of REALM

a-c. Residual aberration level for different maximum applied biases and correction rounds, using 9 biases per Zernike mode (11 Zernike modes in total). Dashed line indicates induced aberration level (0.75 rad RMS). Residual aberrations are minimal when using a bias of 1 rad. **d-f**. Residual aberration level for different number of biases and correction rounds. Approaches with 13 biases in 2 correction rounds (total of 286 acquisitions for 11 Zernike modes) or 9 biases in 3 correction rounds (total 297 acquisitions for 11 Zernike modes) both constitute efficient strategies to achieve robust correction. All simulations contain 25 random aberration configurations (n = 25) for each optimization configuration. Box plot indicates 9/91-percentile, 25/75-percentile and median.

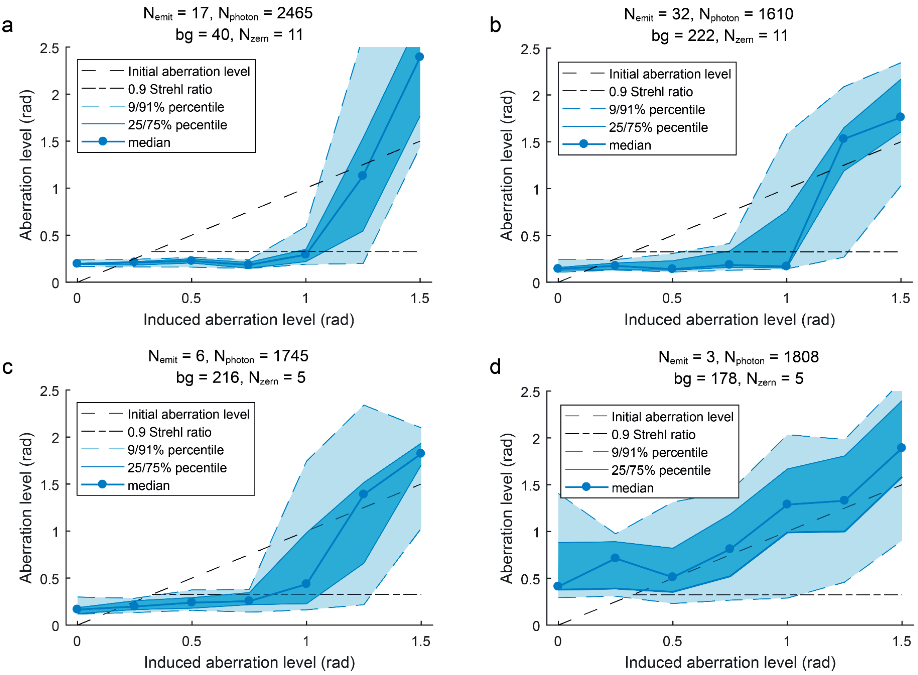

Supplementary Figure 7.

a-d. Experimental performance of REALM as function of induced aberration level using a DNA-PAINT sample in different signal to background ratio's (SBR). Here 2 correction rounds with 13 biases per Zernike mode with a maximum bias of 1 rad is used. For each aberration level, 10 random aberration configurations were induced by the deformable mirror and subsequently corrected. Results below the initial aberration level (dashed line) indicate improvement, results below 0.9 Strehl-ratio (dashed-dotted line) indicate proper imaging conditions. For (**a**) and (**b**) these aberration configurations consisted of 11 Zernike modes (astigmatism, coma, primary spherical aberration, trefoil, second order astigmatism and quadrafoil) and for (**c**) and (**d**) these consisted of 5 Zernike modes (astigmatism, coma and primary spherical aberration). The measured total signal to background ratio (SBR) was 0.0065 (**a**), 0.0015 (**b**), 0.0003 (**c**) and 0.0002 (**d**). The signal and background level are estimated from 25 pre-acquisitions before an aberration is induced. N_{emit}, N_{photon}, *bg* and N_{zern} indicate the average number of emitters per frame, the average number of emitted photons of each emitter, the background photon count and the number of applied Zernike modes present in the aberration configuration. Error bands indicate 9/91% and 25/75% percentile in all panels. REALM was capable of correcting up to 1 rad RMS of wave-front error when the aberration was completely random for all but the lowest SBR. In practice, a major contribution is due to spherical aberration, which can be roughly pre-corrected, significantly increases the aberration level which can be corrected by REALM.

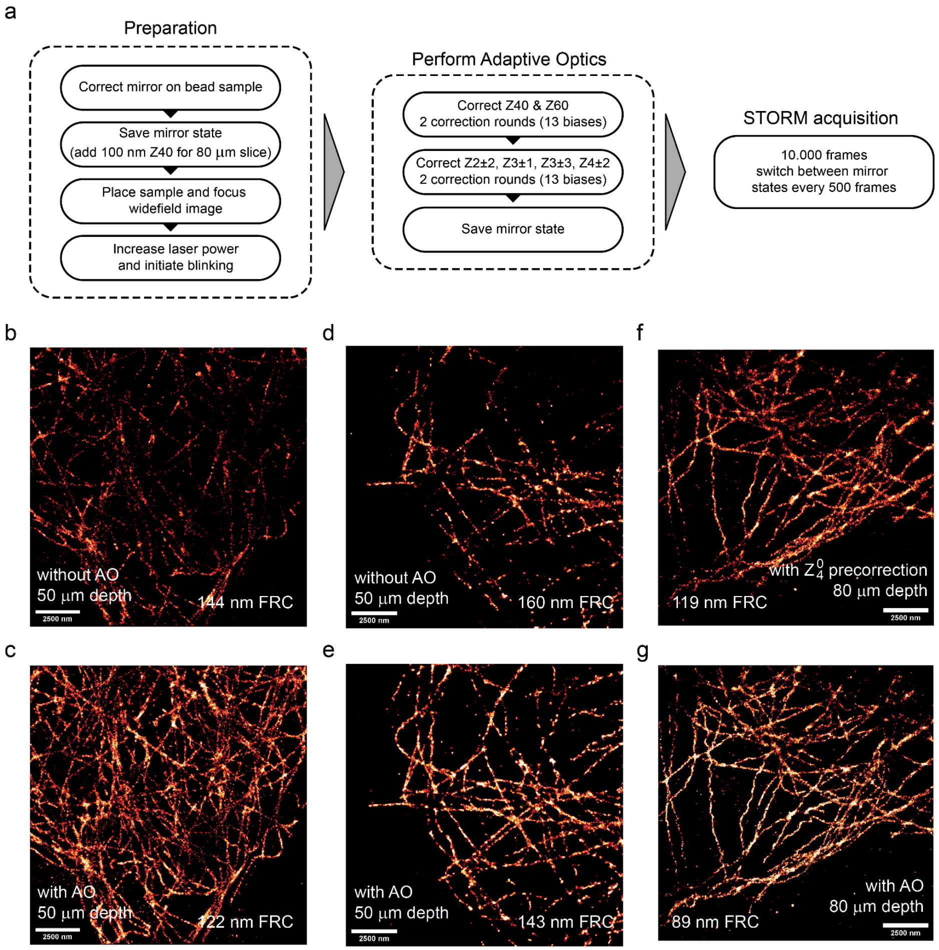
a
Preparation
Correct mirror on bead sample
Save mirror state
(add 100 nm Z40 for 80 µm slice)
Place sample and focus
widefield image
Increase laser power
and initiate blinking
Perform Adaptive Optics
Correct Z40 & Z60
2 correction rounds (13 biases)
Correct Z2±2, Z3±1, Z3±3, Z4±2
2 correction rounds (13 biases)
Save mirror state
STORM acquisition
10.000 frames
switch between mirror
states every 500 frames
b
without AO
50 µm depth
144 nm FRC
2500 nm
d
without AO
50 µm depth
160 nm FRC
2500 nm
f
with Z_4^0 precorrection
80 µm depth
119 nm FRC
2500 nm
c
with AO
50 µm depth
122 nm FRC
2500 nm
e
with AO
50 µm depth
143 nm FRC
2500 nm
g
with AO
80 µm depth
89 nm FRC
2500 nm

Supplementary Figure 8.

a. Experimental procedure for comparing SMLM with and without adaptive optics. First, the mirror was used to correct all system induced aberrations using a bead sample (see **Supplementary Figure 2**). This mirror state was saved and later used as the system-corrected DM state. For the 80 µm slice we pre-corrected spherical aberration by applying this mode with an amplitude of 100 nm (0.9 rad) (RMS normalized amplitude). Next, the sample was mounted and focused using widefield imaging, while trying to keep the illumination minimal. Subsequently, the laser power was increased to initiate the blinking and spherical aberration was corrected, followed by the other Zernike modes. After correction the mirror state was saved as sample-corrected state and the SMLM acquisition was started. During this acquisition the mirror switches between the system- or *Z*40 pre-corrected and sample-corrected state every 500 frames. **b**. SMLM reconstruction of microtubules in COS-7 cells imaged through a 50 μm thick brain section using the frames with the DM in system-corrected state (without AO). Image contains a total of 34K successful localizations with a localization precision <20 nm. **c**. SMLM reconstruction of **b** using frames with sample-corrected DM state. The estimated aberration level was 0.81 ± 0.02 rad RMS and 123K events were successfully localized with a precision <20 nm. d&e) Another example as **b** and **c**, consisting of 17K localizations (without AO) and 53K localizations (with AO) with a localization precision <20 nm. Estimated aberration level was 1.07±0.08 rad RMS. **f**. SMLM reconstruction of microtubules in COS-7 cells imaged through an 80 μm thick brain section using the frames with a precorrection of spherical aberration (35K localizations with a localization precision <20 nm). **g**. as (**f**) but with frames with the DM in sample corrected state (79K localizations with a localization precision <20 nm). Estimated aberration level was 0.91 ± 0.04 rad RMS (on top of 0.9 rad pre-corrected spherical aberration). Repeated n=10 times in 3 distinct samples with similar results.

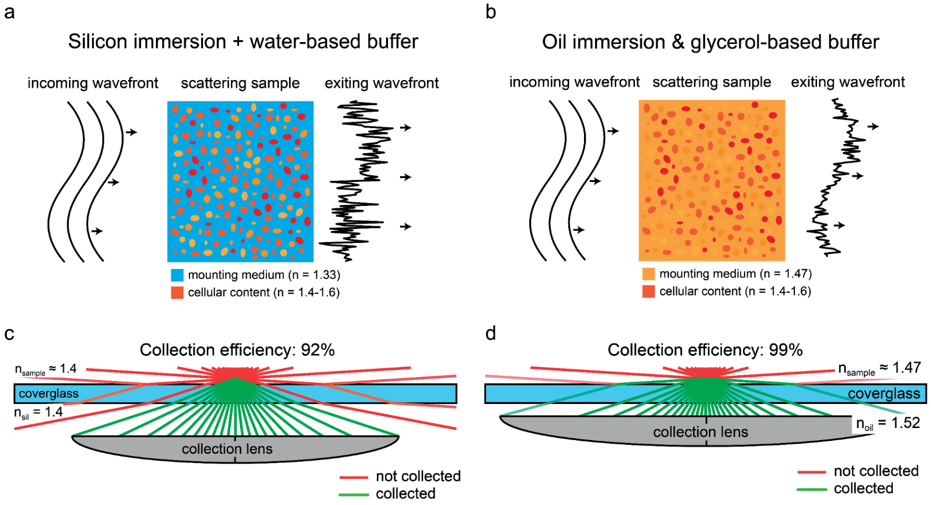
a
Silicon immersion + water-based buffer
incoming wavefront
scattering sample
exiting wavefront
mounting medium (n = 1.33)
cellular content (n = 1.4-1.6)
b
Oil immersion & glycerol-based buffer
incoming wavefront
scattering sample
exiting wavefront
mounting medium (n = 1.47)
cellular content (n = 1.4-1.6)
c
Collection efficiency: 92%
n_sample ≈ 1.4
coverglass
n_sil = 1.4
collection lens
not collected
collected
d
Collection efficiency: 99%
n_sample ≈ 1.47
coverglass
collection lens
n_oil = 1.52
not collected
collected

Supplementary Figure 9. Illustration of the effect of a high refractive index buffer and objective choice.

a. When using a water-based buffer the subcellular content of the tissue (organelles, DNA) has a large refractive index mismatch with the buffer. This rapid local change in refractive index drowns the gradually aberrated wave-front, thereby rendering AO less useful. **b**. By mounting the sample in a higher refractive index buffer using glycerol, the subcellular content causes less scattering and AO becomes more useful. **c**. A silicon immersion lens is the objective of choice when using a water buffer as the average refractive index of (brain) tissue is around 1.4. This matches the refractive index of the silicon oil, minimizing sample induced spherical aberration. However, the collection efficiency is only 92% as the largest available NA (1.35) is smaller than the refractive index. **d**. The glycerol-based buffer increases the average to around 1.48 (assuming a water content of 70%, which is replaced by the glycerol blinking buffer). Therefore a 1.49 NA oil immersion lens has a smaller refractive index mismatch than silicon oil and a higher collection efficiency as it collects the complete 2 π sr solid angle and is therefore the objective of choice. For the computation of the collection efficiency we incorporated the Fresnel reflection at each interface.

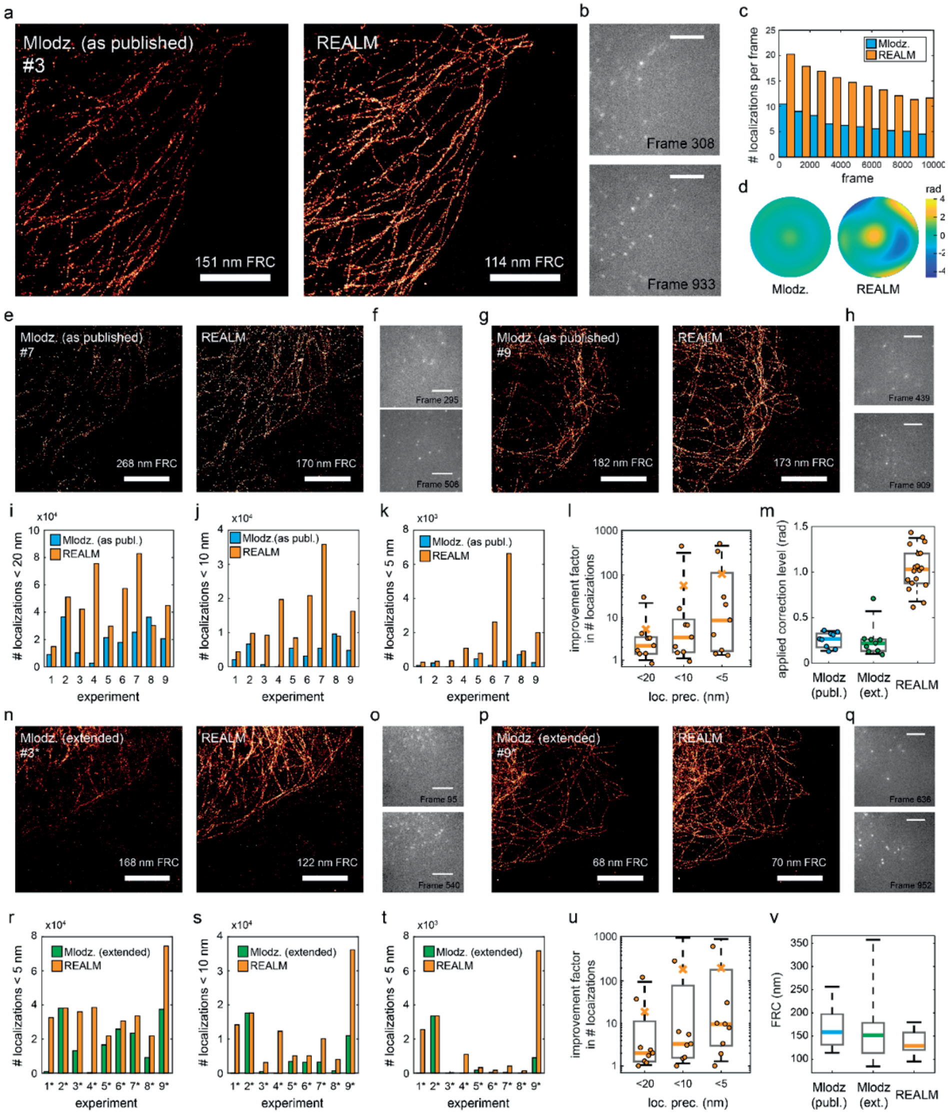

Supplementary Figure 10.

Direct comparison between the method proposed by Mlodzianoski et al. (here shortened to Mlodz.) and REALM by imaging COS-7 cells through 60 μm thick slices (repeated 2 × 9 times). We first performed both correction methods and performed SMLM while switching between mirror states during the acquisition every 500 frames. Mlodz. (as published) indicates the implementation as published, including a separate simplex routine with a different metric for primary and secondary spherical aberration, after which a secondary simplex routine corrects astigmatism and coma. Mlodz. (extended) denotes the method as published, except that trefoil and secondary astigmatism are also included in the second simplex routine. REALM was implemented as in **Supplementary Figure 9**. **a**. Reconstruction of Mlodz. (as published) and REALM for experiment #3. **b**. Representative single acquisition for Mlodz. and REALM corresponding to the image shown in **(a)**. Spots appear more confined and round with REALM. **c**. Average number of localization per frame for Mlodz. and REALM for (**a**). **d**. Estimated wave-front by Mlodz. (W_{rms} = 0.36 rad) and REALM (W_{rms} = 1.3 rad) for (**a**). **e-h**) Same as (**a,b**) but for experiment #7 & #9. **i-k**) Total number of successful localizations with a localization precision below 20 nm, 10 nm and 5 nm resp. for Mlodz. (as published) compared to REALM. l) Improvement factor in the number of localizations below 20 nm (2.2×, median), 10 nm (3.4×, median), and 5 nm (8.6×, median) with REALM compared to Mlodz. (as published). m) Applied correction level for Mlodz. (as published), Mlodz. (extended) and REALM. REALM applies a larger correction, indicating that simplex optimization remains in a noise induced local minimum **n-u**. Same as (**e-l**) but with Mlodz. (extended). **v**. Box plot of the calculated FRC of Mlodz. as published (151 nm median), Mlodz. Extended (145) and REALM (122 nm). The median FRC for all reconstruction with Mlodz. is 150 nm. All experiments were performed on three distinct samples. All scale bars indicate 5 µm. All box plots (**l,m,u,v**) indicate 9/91-percentile, 25/75-percentile and median. All reconstruction pairs are shown with the same contrast.

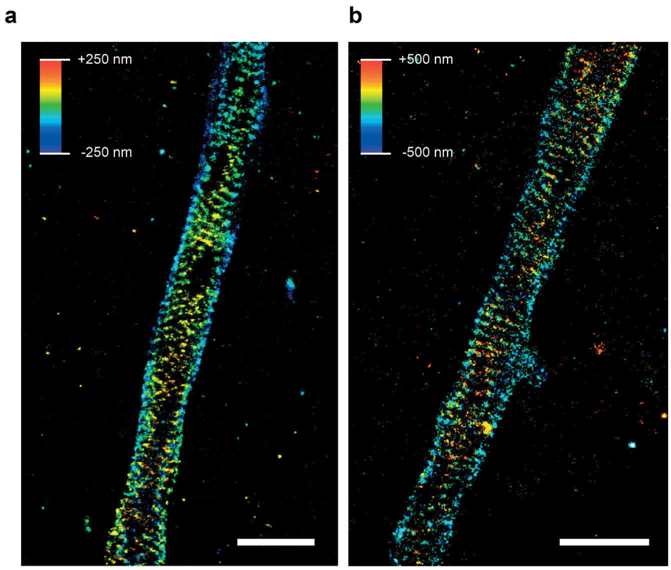

Supplementary Figure 11.

Example 3D SMLM reconstructions of ßIV-spectrin in the AIS of layer 5 axons at a depth of 40 µm (**a**) and 50 µm (**b**). Scalebar indicates 2 µm. Repeated n=12 times in 4 distinct samples with similar results.

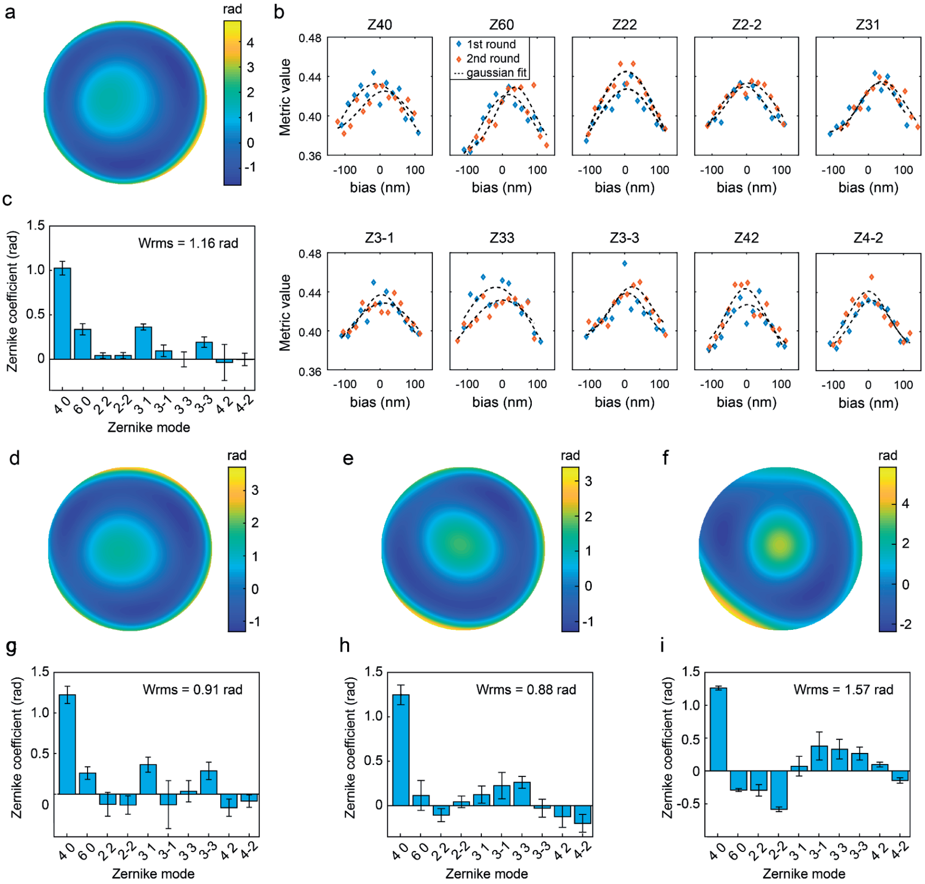

Supplementary Figure 12. Estimated aberrations by REALM

a. Aberration profile corresponding to the ßIV-spectrin reconstruction of **Figure 3**. **b**. Metric values and Gaussian fits of (**a**) of the model-based optimization algorithm of REALM. **c**. Estimated Zernike coefficients of (**a**) and (**b**). Error bars indicate the standard deviation based on the goodness of fit to the metric values. **d-f**. Aberration profiles corresponding to ßIV-spectrin reconstructions of **Supplementary Figure 11a,b** and **Figure 2** respectively. **g-i** Estimated Zernike coefficients of (**d-f**), respectively. Error bars indicate the standard deviation based on the goodness of fit to the metric values.

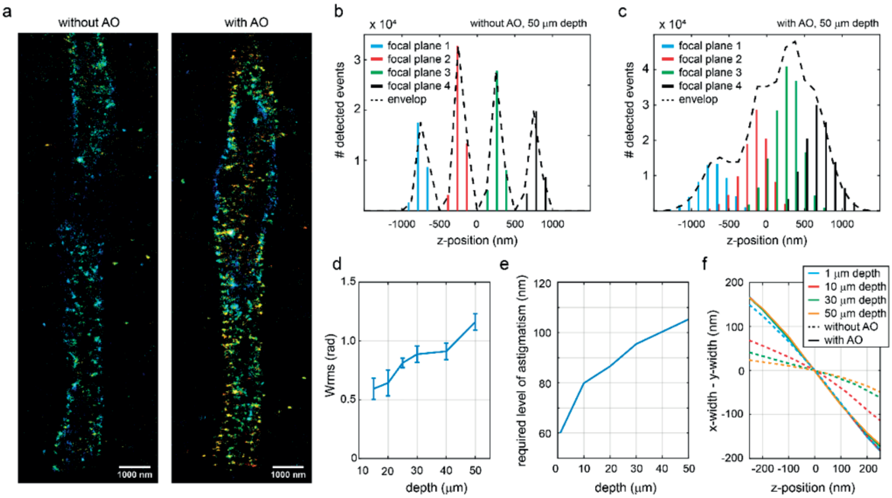

Supplementary Figure 13. REALM improves 3D multiplane astigmatic SMLM.

a. SMLM reconstruction of a single-plane astigmatic imaging experiment using ßIV-spectrin at a depth of 50 µm. Every 500 frames the DM state was switched to system-corrected (without AO, 100 nm FRC) and sample-based correction (with AO, 76 nm FRC) (repeated n=3 times with similar results). **b**. Due to spherical aberration, the ellipticity of the PSF and therefore the z-encoding is lost without AO. This prevents multiplane astigmatic SMLM reconstructions to be ‘stitched’ together. **c**. Using REALM for aberration correction, z-encoding is restored allowing for 3D multiplane astigmatic SMLM. **d**. Measured aberration level using REALM on ßIV-spectrin stained slices at different depths. Data comprised of estimated aberration levels in 3 samples. Error bars indicate standard deviation of REALM. Correction was performed once (n=1). **e**. Required level of astigmatism to maintain a similar calibration curve for astigmatic z-encoding, based on PSF simulations and a refractive index of 1.48. **f**. Theoretical calibration curve with and without AO with astigmatism levels of (**e**) as a function of depth. Without AO the ellipticity of lost, resulting in failure of 3D multiplane astigmatic SMLM as shown in (**b**).

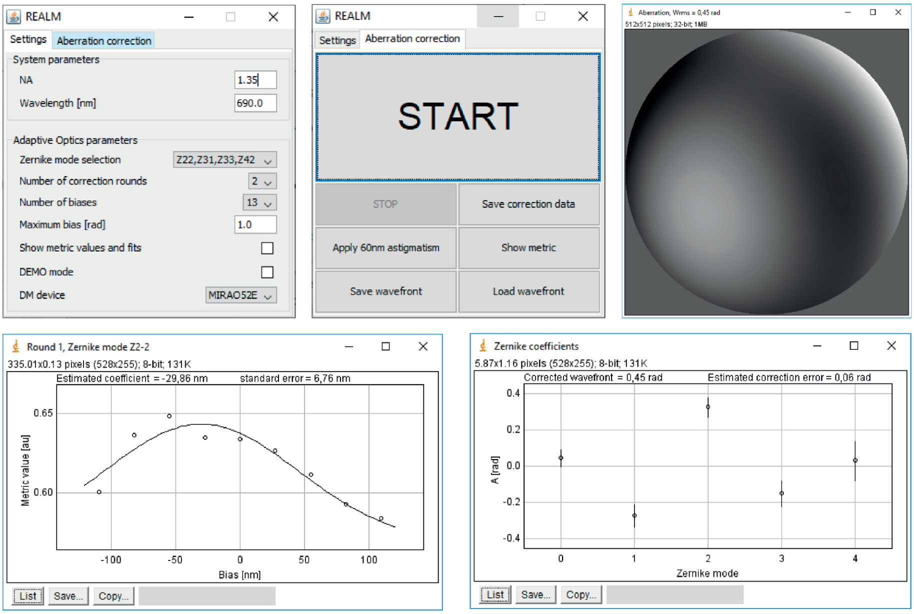

NA: 1.35
Wavelength [nm]: 690.0
Zernike mode selection: Z22,Z31,Z33,Z42
Number of correction rounds: 2
Number of biases: 13
Maximum bias [rad]: 1.0
Show metric values and fits ☐
DEMO mode ☐
DM device: MIRAO52E

Estimated coefficient = -29,86 nm standard error = 6,76 nm

Corrected wavefront = 0,45 rad Estimated correction error = 0,06 rad

REALM
Settings
Aberration correction
System parameters
Adaptive Optics parameters
START
STOP
Save correction data
Apply 60nm astigmatism
Show metric
Save wavefront
Load wavefront
Aberration, Wrms = 0,45 rad
512x512 pixels; 32-bit; 1MB
Round 1, Zernike mode Z2-2
335.01x0.13 pixels (528x255); 8-bit; 131K
0.65
0.60
Metric value [au]
-100
-50
0
50
100
Bias [nm]
List
Save...
Copy...
Zernike coefficients
5.87x1.16 pixels (528x255); 8-bit; 131K
0.4
0.2
0.0
-0.2
-0.4
A [rad]
0
1
2
3
4
Zernike mode
List
Save...
Copy...

Supplementary Figure 14.

Images of the opensource Micro-Manager plugin REALM (https://github.com/MSiemons/REALM). Relevant parameters can be tuned (Zernike modes, number of biases, maximum bias, number of correction rounds). REALM requires only little input parameters (NA and wavelength), resulting in a clear and user-friendly interface.

Materials and Methods

Set up

Experiments were performed using a Nikon Ti Eclipse body with a 100× 1.49 NA objective and a quad-band filter cube (containing a ZT405/488/561/640rpc dichroic and ZET405/488/561/640m emission filter, Chroma), to which a MICAO adaptive optics module containing a MIRAO52E (Imagine Optics) deformable mirror was mounted (Siemons et al., 2020) (see Supplementary Figure 2). Detection is performed with a CMOS camera (Orca Flash v4.0, Hamamatsu). For excitation we used a single mode 647nm laser (140mW, LuxX, Omicron) and 405nm laser (60mW LuxX, Omicron) which can be used for normal widefield and TIRF illumination.

Calibration of the DM

In order to ensure accurate modulation of the Zernike modes, the deformable mirror needs to be properly calibrated. The DM was calibrated by replacing the camera with a Shack-Hartmann sensor (HASO, Imagine Optics) to directly measure the wave-front, using the provided software. A 1 µm bead (TetraSpeck, ThermoFisher, T7282, dilution 1:1000) dried on a coverslip and mounted in glycerol was used as a point source. Mounting in glycerol reduces apodization in the pupil plane due to possible super-critical angle fluorescence, ensuring a homogeneously filled pupil. We blocked other beads in the FOV by placing an iris in the intermediate image plane. The wave-front deformation of each actuator was measured with 10 push-pull cycles to obtain the interaction matrix, which was then converted into the Zernike-based control matrix. We perform this calibration once a year.

The calibration was verified using a phase retrieval algorithm (Siemons et al., 2018) in combination with through-focus scans of 175 nm green fluorescent beads (PS-speck, ThermoFisher, P7220, dilution 1:500) mounted in PBS. This revealed that upon startup the shape of the mirror is imperfect due to thermal drift and needs to be corrected (see Supplementary Figure 3). The inverse estimated Zernike coefficients from the phase retrieval algorithm were subsequently applied by the mirror, after which a second through-focus scan was acquired. This revealed that this approach was able to correct the complete system within 0.1-0.2 rad RMS (15-30 mλ) wave-front error. Prior to each experiment we performed this calibration step to ensure that the system was properly corrected. Next, we modulated individual Zernike modes and acquired through-focus scans of these PSFs.

Phase retrieval indicated that all modes up to the 4th order could be accurately modulated with little crosstalk between Zernike modes (see Supplementary Figure 3).

DNA-PAINT sample and imaging protocol

Sample chambers were prepared using double sided tape to create two cavities of 10 µl between a microscope slide and a plasma-cleaned #1.5 high-precision cover glass. Next, 10 µl of a solution of BSA-biotin (1 mg/ml in ultra-pure water MQ, Sigma Aldrich, A8549) was incubated for 5 min after being washed with 50 µl washing buffer (1× PBS containing 10 mM $MgCl_2$). 10 µl of streptavidin (1 mg/ml in MQ, Sigma Aldrich, 434302) was then flushed in and incubated for 5 minutes and washed with washing buffer. Next, biotin conjugated to the complementary DNA-strand P1 (1 mg/ml in MQ) (Schnitzbauer et al., 2017) was incubated for 5 minutes and washed away. Finally, washing buffer containing 500 pM of Atto645 conjugated to DNA-strand I1 and green fluorescent beads (PS-speck, ThermoFisher, dilution 1:1000) was flushed in, after which the cavity was sealed with grease and nail polish. The fluorescent beads were used to monitor the stability of the deformable mirror and if needed to correct for thermal drift in between experiments.

For each AO correction, a random aberration configuration consisting of Zernike modes $Z2\pm2$, $Z3\pm1$, $Z3\pm3$, $Z40$, $Z4\pm2$ and $Z4\pm4$ (11 modes) was induced by the DM. The amplitudes of these modes were chosen uniformly random and normalized to 0.75 rad RMS. Next, the adaptive optics method was performed (see below for implementation details). Afterwards the residual aberration level W_{rms} was evaluated as

$$W_{\mathrm{rms}} = \sqrt{\sum_{j=1}^{11}\left(A^{j}_{\mathrm{induced}} - A^{j}_{\mathrm{estimated}}\right)^2} \tag{1}$$

with A^{j}_{induced} being the induced known Zernike coefficient of Zernike mode j and the $A^{j}_{\mathrm{estimated}}$ the coefficient of Zernike mode j estimated by the AO method. Prior and during the experiment the signal levels and state of the DM were monitored to ensure equal comparison between these methods (see **Supplementary Figure 1** for experimental details).

Single-molecule acquisition simulations

The single-molecule acquisitions were simulated using a vector PSF model to capture the full complexity of the aberration configurations (Stallinga and Rieger, 2010). Blinking dynamics play a large role in the variability of the metric value and needed to be incorporated in the simulation. We mimicked these blinking dynamics by introducing a variability in the number of emitters in each frame and in the number of photons each emitter emits. The parameters for these distributions corresponded to the experimental signal levels of the DNA-PAINT sample (see Supplementary Figure 1). The number of emitters per frame was randomly chosen from a Poisson-distribution (with an average of 13 emitters), and the number of photons of each emitter followed an exponential distribution (with an average of 2500 photons). The emitters were randomly positioned with uniform probability across in the field of view (400 × 400 pixels, 65 nm pixel size) with a uniform background of 20 photons per pixel. Lastly, Poisson noise was added to represent the shot-noise.

The performance of the AO methods was evaluated similar to the procedure described above. Known aberration configurations were induced, followed by AO-based corrections using the different approaches. For comparison with our DNA-PAINT experiment all emitters were placed in focus (z-position = 0 nm) and simulated with a 1.49 NA objective, while for the metric curve and optimization of our method (see **Supplementary Figures 3&4**) the emitters were uniformly random positioned in the z-direction between ±200 nm at a depth of 20 μm with a 1.35 NA silicon immersion objective with refractive index matching.

AO methods

Model-based optimization iteratively corrects Zernike modes by applying a sequence of biases of the Zernike mode that is to be corrected. The metric values of these acquisitions are computed and a metric curve is fitted to find the optimum (see Supplementary Figure 4). Metric curve fitting was implemented by least-squares fitting with a Gaussian function with an offset (4 fit parameters). The width and center of the fitted Gaussian were constrained to prevent that occasional outliers in the metric values resulted in extreme fit values. The width was constrained to [0.4, 1] rad and the center to [-0.5, 0.5] rad. This greatly improved the performance of the previously proposed method (Burke et al., 2015) as the noise-sensitive metric M1 often led to extreme fit-values when not constrained. For Figure 1, the model-based optimization by Burke et al. was implemented with 11 biases per Zernike mode, whereas REALM used 9 biases per Zernike mode.

The downhill-simplex algorithm uses simplexes (higher dimensional triangles) to find an optimum in the parameter space. We implemented this optimization algorithm via the MATLAB function fmincon with the initial simplex size set to 0.2 rad, which was found to work optimally. Metric M3 was used for all Zernike modes as we did not induce secondary spherical aberration. Therefore, a separate simplex routine with a different metric for primary and secondary spherical aberration as originally proposed (Mlodzianoski et al., 2018) could not be implemented. We did not find any reduced correction ability for primary spherical aberration using metric M3. However, we noticed that when correcting more than 4 Zernike modes, the simplex optimization was unable to converge in this larger noisy parameter space. Therefore, optimization was stopped after 300 acquisitions and the state with the best obtained metric value was taken as the estimated correction.

Particle-swarm optimization uses a collection of solutions moving through solution space, where their movement is affected by the individually best solution it found so far, as well as the groups best solution. Particle-swarm optimization was implemented via the MATLAB function particleswarm with a swarm size of 25 as suggested (Tehrani et al., 2017) with a maximum of 20 iterations for a maximum of 300 acquisitions. We used an initial swarm spansize of 0.1 rad and a maximum spansize of 0.75 rad. Other settings for particleswarm were set to standard values (InertiaRange, SelfAdjustment and SocialAdjustment set to 1).

COS7 staining

COS-7 cells for Figure 2a-e were seeded onto 25 mm coverslips. After 24 hours, cells were pre-extracted with 0.1% glutaraldehyde and 0.2% Triton-X100 in PEM80 (80 mM Pipes, 1 mM EGTA, 4 mM $MgCl_2$, pH 6.8) for one minute. The cells were subsequently fixed with 4% PFA in PEM80 for 10 minutes. After washing in PBS (3×5 min) cells were permeabilized in 0.2% Triton-X100 in PEM80 for 15 minutes. After washing (3×5 min) blocking was performed in 3% BSA in PEM80 for 45 minutes and incubated overnight with a primary antibody against αTub (mouse IgG1, Sigma Aldrich, B-5-1-2, dilution 1:500). The cells were again washed with PBS (3×5 min) and incubated with secondary antibody (goat, anti-Mouse IgG (H+L), AlexaFluor647, Life Technologies, dilution 1:500) for 1 hour at RT. The coverslip was then placed on a microscope slide with the cells facing upwards, after which a 50 or 80 µm thick rat brain section (see below for details) was placed on the coverslip. The surplus of PBS was removed with a tissue and 70 µl of glycerol blinking buffer (see below) was deposited on the slice. Next, a 25 mm #1.5 high precision coverslip was placed on top of the slice and the assembly was sealed with nail polish. For the blinking buffer 10 µl of 1M MEA, together with 2,5 µl of 20% glucose and 1 µl of gloxy buffer (70 mg/ml glucose oxidase, 4 mg/ml catalase in MQ), were mixed with 86 µl of a mixture of 95% glycerol and 5% Tris 20 mM, pH 8.0.

Slice preparation and ßIV-spectrin staining

All animal experiments were performed in compliance with the European Communities Council Directive 2010/63/EU effective from 1 January 2013. They were evaluated and approved by the national CCD authority (license AVD8010020172426) and by the Royal Netherlands Academy of Arts and Science (KNAW) animal welfare and ethical guidelines and protocols (IvD NIN 17.21.01 and 19.21.11).

To obtain sections with a fixed thickness (**Figure 2a-e**), adult rats were deeply anaesthetized by an i.p. injection of pentobarbital (50 mg/kg) and transcardially perfused with PBS and 4% PFA. The brains were removed and post-fixed in PFA for 24 hours after which the tissue was stored in PBS. Coronal sections of 50 µm thick were cut on a vibratome (VT1200S, Leica Microsystems).

For ßIV-spectrin staining (Figure 2f-i), adult rats were deeply anaesthetized by 3% isoflurane inhalation and decapitated, after which the brains were moved to ice-cold artificial cerebral spinal fluid containing (in mM): 125 NaCl, 3 KCl, 25 glucose, 25 $NaHCO_3$, 1.25 $Na_2H_2PO_4$, 1 $CaCl_2$, 6 $MgCl_2$, saturated with 95% O_2 and 5% CO_2 (pH 7.4). 300-400 µm thick parasagittal brain sections containing the primary somatosensory cortex were cut on a vibrotome (1200S, Leica Microsystems). Following a recovery period at 35 °C for 35–45 minutes slices were stored at room temperature in the ACSF. For whole-cell filling with biocytin (Figure 4), the slice was transferred to a customized upright microscope (BX51WI, Olympus Nederland BV). The microscope bath was perfused with oxygenated (95% O_2, 5% CO_2) ACSF consisting of (in mM): 125 NaCl, 3 KCl, 25 glucose, 25 $NaHCO_3$, 1.25 $Na_2H_2PO_4$, 2 $CaCl_2$, and 1 $MgCl_2$. Patch pipettes were pulled from borosilicate glass (Harvard Apparatus, Edenbridge, Kent, UK) pulled to an open tip of 3 – 6 MΩ resistance. The intracellular solution contained (in mM): 130 K-Gluconate, 10 KCl, 4 Mg-ATP, 0.3 Na_2-GTP, 10 HEPES, 10 Na_2-phosphocreatine and 5 mg ml^{-1} biocytin (pH 7.25 adjusted with KOH, 280 mOsmol kg^{-1}). An Axopatch 200B (Molecular Devices) was used to obtain whole-cell configuration. The cell was left to fill for 30 min, during which the bridge balance was monitored and stayed below 15 mΩ. Slices were fixed in 4% PFA (20 minutes) and blocked with 5% NGS and 2% Triton (2 hours) before incubation with rabbit anti-ßIV-spectrin antibody in blocking buffer (1:1000, 24 hours, gift from M. Engelhardt). Slices were washed (3×15 minutes), incubated with goat anti-rabbit Alexa 647 (1:500 or 1:1000, 2 hours, ThermoFisher) and in the case of biocytin filling, with Streptavidin Alexa-488 conjugate (1:500, Invitrogen) and washed again. During all steps, the slices were at room temperature and on a shaker. The slices were stored in PBS (4°C). Before imaging, slices were incubated for at least 15 minutes in 95% glycerol and 5% Tris 20 mM after which they were mounted between a microscope slide and #1.5 high precision coverslip with two 120 µm spacers (Secure-Seal Spacer, Thermofisher, S24735) in the blinking buffer described above.

SMLM detection, localization and reconstruction

The detection, localization and reconstruction was performed with the ImageJ plugin DoM (Detection of Molecules) (Chazeau et al., 2016) (see https://github.com/ekatrukha). DoM detects single molecules events by convolving images with a combination of a Gaussian and Mexican hat kernel. Localization is performed by an unweighted nonlinear 2D Gaussian fit with Levenberg–Marquardt optimization. The detection PSF size was set to 150 nm. Localizations with a width larger than 130% of this size (195 nm) are regarded as false positives. A localization is classified as successful if it is non-false positive and has a positive integrated intensity. SMLM reconstructions were rendered by plotting each molecule as a 2D or 3D Gaussian with standard deviations in each dimension equal to the corresponding localization errors. For astigmatic 3D localization the *z*-position was estimated from the difference in x- and y-width of the spot, where we corrected for depth-induced loss of astigmatism (Siemons et al., 2020) using a simulated required astigmatism level at each depth (see Supplementary Figure 13e-f). Drift was corrected by 2D cross-correlation of intermediate reconstructions consisting of 500 or 1000 frames. The FRC resolution was computed by splitting the localizations in two batches every other 500 frames. The corresponding reconstructions where then used the calculate the FRC resolution using the ImageJ Fourier Ring Correlation plugin.

REALM

REALM (Robust and Effective Adaptive optics in Localization Microscopy) is a free open-source Micro-Manager plugin (github.com/MSiemons/REALM) where the method described in this work is implemented (see Supplementary Figure 5). It offers a compact and intuitive user interface suitable for non-experts. It currently supports two types of DMs: MIRAO52E (Image Optics) and DMH40-P01 (Thorlabs, see github.com/HohlbeinLab/Thorlabs_DM_Device_Adapter for the device adapter) and we encourage others to build device adapters for other DM manufacturers to interface with REALM. The Fourier transform needed for the metric evaluation is implemented via the 2D Fast Hartley Transform (FHT), where the image is padded with the mode value of the acquisition to a size of $2^n \times 2^n$ (with n in integer), usually resulting in a size of 256 × 256 or 512 × 512. All aberration corrections for Figure 2 and 3 are performed with REALM.

Data availability

The data that support the findings of this study are available from the corresponding author upon reasonable request. Source data are provided as a Source Data file with this paper.

Code availability

The code for REALM is publicly available at github.com/MSiemons/REALM. The custom code for analysis that support the findings of this study are available from the corresponding author upon reasonable request.

Acknowledgements

The authors thank Allard Mosk, Giulia Sereni and Ivo Vellekoop for useful discussion on aberration in brain tissue, Roderick Tas and Chiung-Yi Chen for help with the DNA-PAINT assays and Audrius Jasaitis (Imagine Optic) for help in controlling the Deformable Mirror. This work was funded by the Dutch Research Council (NWO) through the FOM program Neurophotonics.

Author Contributions

L.K and M.S. conceived research. M.S. developed the method presented in this work, performed the simulations, the DNA-PAINT and sandwich assays, analyzed the SMLM data and made the figures. N.H. prepared the brain sections for the sandwich assay, the ßIV stainings and performed the electrophysiological recording, under supervision of M.K. M.S. and N.H. performed the SMLM imaging on ßIV-spectrin. M.S and L.K. wrote the manuscript with input from N.H. and M.K. L.K. supervised the project.

Competing Interests

The authors declare no competing interests.

Chapter 5

General Discussion

Fifty years ago, the first optical recording of neural activity was performed using the molecule aequorin, showing depolarization-dependent Ca^{2+} entry in the squid giant axon (Baker et al., 1971). Since then, the optical toolkit has expanded tremendously and it is now possible to record Ca^{2+}, Na^{+} and voltage optically from subcellular neuronal regions, at kHz resolution (Filipis and Canepari, 2021; Jaafari et al., 2015; Popovic et al., 2015). Optical recordings of Ca^{2+} have become a standard technique in the field and voltage recordings are gaining ground as an insightful tool. In addition, the development of superresolution microscopy has provided detailed insights about the molecular skeleton of neurons on the scale of tens of nanometers. The aim of this thesis was to employ and optimize advanced optical approaches to identify properties of ionic signaling in the mammalian axon and in particular the AIS.

AIS Ca^{2+} signaling pathways

In **Chapter 2**, we studied the Ca^{2+} signaling pathways in the AIS of L5 rat pyramidal neurons. We used a combination of axonal Ca^{2+} imaging and pharmacology to identify three Ca^{2+} entry routes in the AIS: Ca^{2+} release from internal stores and Ca^{2+} entry through Cav and, surprisingly, Nav channels (**Figure 1**). Despite early reports of Ca^{2+} conductance by Nav channels in the squid giant axon and in cardiac cells (Baker et al., 1971; Meves and Vogel, 1973), the role of Nav channels in AIS Ca^{2+} signaling was unexpected. To test our hypothesis, we optically recorded the Ca^{2+} current in the AIS by using high-speed Ca^{2+} imaging of the low-affinity Ca^{2+} indicator, OGB-5N. The activation kinetics of the Ca^{2+} current showed a fast activation and inactivation, as well as a persistent component, which resemble Nav channel gating, suggestive for the entry of Ca^{2+} through Nav channels. We calibrated the ratiometric Ca^{2+} indicator bis-Fura-2 to obtain an absolute measure of the $[Ca^{2+}]$ rise in the AIS and implemented a simulation to calculate the Ca^{2+} permeability of Nav channels to be 0.38%. Due to the high density of Nav channels at the AIS, even this slight Ca^{2+} permeability of the Nav channels was sufficient to make Nav channels a major and rapid source for Ca^{2+} in the AIS.

To reach this conclusion, we used various imaging approaches in Chapter 2. To support the notion that Ca^{2+} entered the AIS through Nav channels, we needed to isolate the Ca^{2+} and Na^{+} current and compare the kinetics of these currents. We first considered

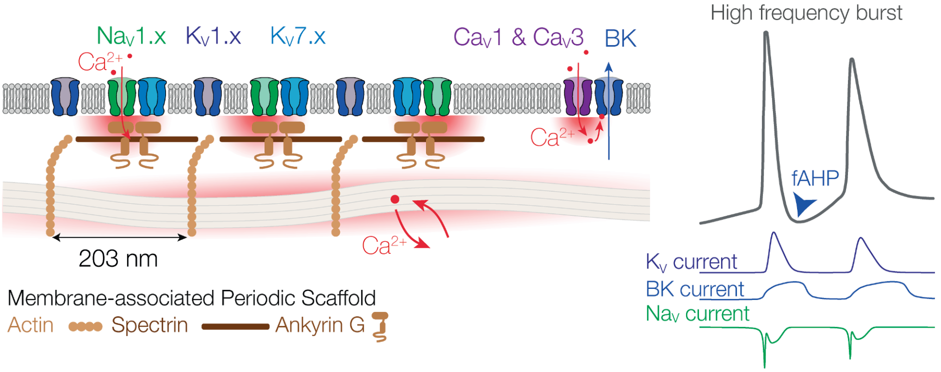

Figure 1. Optical Ca^{2+} and voltage recordings reveal a BK-Ca_V complex at AIS
Left, the Membrane-associated Periodic Scaffold in the L5 rat pyramidal neuron AIS shows a 203 nm periodicity (Chapter 4). AP firing raises AIS Ca^{2+} levels through Ca^{2+} release from the intracellular stores and by Ca^{2+} entry through $Ca_V1.x$, $Ca_V3.x$ and Na_V channels (Chapter 2). Ca_V channels form nanodomains with BK channels and provide the Ca^{2+} to activate them, but how this complex is anchored to the AIS is not yet know (Chapter 3). Right, the Ca_V - BK channel complex mediates the fAHP and burst firing (Chapter 3). AP depolarization is mediated by the Na_V channel mediated inward current, whereas AP repolarization is mediated by both K_V and BK channel mediated outward currents. Depending on the location within the AIS and the local AP width, BK currents are most prominent during AP repolarization or during the fAHP, which mediates high-frequency burst firing in the L5 pyramidal axon.

various electrophysiological approaches to isolate the currents. Because the Nav mediated Na^+ current and the Nav mediated Ca^{2+} current enter the AIS through the same channel, a pharmacological approach would however block both currents equally. An alternative approach to isolate Nav mediated Ca^{2+} current is by replacing extracellular Na^+ with equimolar concentration of NMDG to balance the intra- and extracellular concentration of Na^+ and thereby abolish the driving force for Na^+ fluxes (Santana et al., 1998). Any remaining current would be Nav mediated Ca^{2+} current and this could provide evidence of Ca^{2+} permeating the Nav channel. However, changes in ion concentrations can alter the membrane surface charge and influence the channel conduction, so it would neither provide evidence for Nav mediated Ca^{2+} permeation under physiological conditions nor allow the estimation of conductance ratio (Lewis, 1979). Therefore, electrophysiologically isolating Nav mediated Na^+ current and Ca^{2+} current in the AIS was not possible and instead, we took advantage of the Ca^{2+} selectivity of a fluorescent Ca^{2+} indicator, specifically the low-affinity dye OGB-5N, and optically recorded the Ca^{2+} current. Since we hypothesized that the Ca^{2+} currents were mediated by Nav channels, we expected currents with activation kinetics in the range of a few hundred microseconds and required a sufficiently high acquisition frame rate of 20 kHz, translating to a pixel dwell time of 50 μs (Filipis and Canepari, 2021; Jaafari et al., 2014; Ouares et al., 2016). Short dwell times put major constraints on other imaging parameters. In imaging, ‘photons are sacred’. An increasing number of photons per recording increases the size of the signal relative to the noise and vice versa. Many parameters determine the number of photons that are recorded, such as pixel dwell time, dye brightness, excitation amplitude, phototoxicity, pixelsize and the light collection efficiency of the optical system. Most imaging experiments benefit a certain *sweet spot* of these parameters. When we wanted to optically record Na_V mediated Ca^{2+} currents, we were restricted by the shortest possible dwell time of 50 μs and in order to obtain a sufficient number of photons in this short time window, we needed to find optimal settings, and sometimes compromise, for the other parameters. To optimize light collection efficiency, we used a high NA objective with a working distance that still allowed a patch pipette to reach the sample (NA1.1). In addition, we selected superficial cells to minimize the path of photons traveled through the tissue, hence minimizing the loss of photons through light scattering. Additionally, we kept the light exposure to a minimum so we could use higher light intensities during our recordings. We were able to obtain sufficient signal to record the Ca^{2+} current from the AIS and observed activation speed of ~450 μs, resembling Na_V channel gating (see Chapter 2). This optical approach enabled us to isolate the Na^+ and Ca^{2+} currents and compare their kinetics, which formed a paramount building block of our hypothesis.

Additionally, to estimate the Ca^{2+} conductivity ratio of Na_V channels in Chapter 2, we needed to measure the absolute increase in $[Ca^{2+}]$ in the AIS. Not all indicators are fit for calibration, because generally changes in dye intensity are always related to the dye concentration, which is not equal between experiments or even subcellular regions, so it is not possible to convert the changes in fluorescence to changes in concentration of the ion. Some dyes however, such as Fura-2, have a bidirectional change in excitation or emission when they bind Ca^{2+} (Helmchen, 2011). When excited in a certain wavelength, they might decrease intensity, whereas the intensity increases when excited with another wavelength. Because these relative changes are not dependent on dye concentration, it is possible to calibrate the ratio to absolute concentration changes and we employed this feature in Chapter 2. Ratiometric imaging requires specific hardware to measure the response of two wavelengths, which can either be separated by a dichroic mirror and recorded on two cameras or requires sequential triggering the two wavelengths, which is the approach we used (Miyazaki and Ross, 2015; Miyazaki et al., 2019). Optical recording of $[Ca^{2+}]_i$ allowed us to then simulate the $[Ca^{2+}]_i$ without any dye present and subsequently optimize the ratio of Ca^{2+} entry through Na_V channels. The need for the simulation without a dye points towards the main disadvantage of fluorescent ion indicators: they inherently buffer the ion that they report and therefore influence ionic signaling in the cell. We evaluated the buffering capacities of the dyes used in this study in the NEURON simulation software and the effect on free $[Ca^{2+}]$ is significant. Even with a low affinity dye more than 50% of the Ca^{2+} in the AIS was buffered. This needs to be taken into consideration when the focus of the study is an interaction between the imaged ion and a down-stream process, for example when the relationship between Ca^{2+} influx and synaptic signals is investigated. Since we did not investigate the downstream effects of Ca^{2+} levels in the AIS in Chapter 2, we could employ Ca^{2+} imaging techniques and its advantages.

Ca^{2+} signaling in the AIS has been studied in various species, brain regions and cell types (Bender and Trussell, 2009; Clarkson et al., 2017; Schiller et al., 1995; Yu et al., 2010), and Ca^{2+} entry through Na_V channels had been described previously in the squid giant axon and in cardiac cells (Baker et al., 1971; Santana et al., 1998), but whether Na_V channels contribute to neuronal Ca^{2+} levels was not previously investigated. The selectivity of Na_V channels over other ions is dependent on the amino-acid composition of the selectivity filter and a single point mutation can alter the Na^+/Ca^{2+} selectivity of the Na_V channel (Heinemann et al., 1992). One of such mutations, missense variant SCN2A p.K1422E, is associated to developmental delay, spasms, and features of autism spectrum disorder (Echevarria-Cooper et al., 2022). The mutated channel differs from the wildtype channel by a single-point mutation that leads to an alternative amino acid in the selectivity filter of the channel. This mutated channel showed reduced overall conductance and lowered Na^+ specificity over Ca^{2+}. The altered biophysical properties of the channels led to slower AP kinetics on a cellular level, in addition to rare seizures, altered response to induced seizures and altered social and anxiety-related behavior. These results show how a single point mutation on a Na_V channel can have large behavioral impacts and emphasizes how critical the selectivity filter of ion channels is.

In Chapter 2, we described that the selectivity filter of wildtype Na_V channels has a 0.4% Ca^{2+} conductivity ratio, which endows the L5 rat somatosensory cortex AIS with a rapid Ca^{2+} signaling pathway. In 2021, Lipkin et al. used a combination of electrophysiology, two-photon imaging and pharmacology to study the Ca^{2+} signaling at the AIS of prefrontal mouse L5 pyramidal neurons (Lipkin et al., 2021). Similar to our findings described in Chapter 2, Lipkin et al. found a contribution of Ca^{2+} release from internal stores and from T-type Ca_V channels to Ca^{2+} levels in the AIS. However, they did not observe a contribution of L-type Ca_V channels and unlike in rat S1, they did observe a contribution of P/Q, N and R-type Ca_V channels. Finally, they used an optical approach to compare the onset of the Na^+ and Ca^{2+} rise temporally in the AIS and found that the Na^+ signal consistently rose before the peak of the AP, while the Ca^{2+} signal rose ~1 ms later, during the fall of the AP. This experiment showed that Ca^{2+} in the AIS did not enter the AIS simultaneously with Na^+ and they concluded that Ca^{2+} did not enter through Na_V channels.

What could underly the differences between the findings in Chapter 2 and the study from Lipkin et al.? It is probably a combination of technical and biological factors: first, the two studies used a different model organism (rat and mouse, respectively), so it is possible that the relative ion channel compositions in the AIS differ between species. Secondly, in Lipkin et al., a cocktail of Ca_V channel blockers decreased Ca^{2+} entry in the AIS by 65% in response to three APs. This leaves room for a smaller Na_V channel mediated fraction, which was not investigated further. So while both studies identified AIS Ca^{2+} signaling pathways depending on a complex interaction between the internal stores and ion channels, the exact fraction of Na_V mediated Ca^{2+} signaling may be species-dependent and requires further investigation.

A technical difference could further explain the differences of the two studies. Interestingly, Lipkin et al. studied AIS Ca^{2+} signaling at the microscale using ~500 nm wide two-photon line- and point scanning at 30 µm from the soma. They described microdomains of T-type Ca^{2+} channels coupled to ryanodine receptors (RyR) that were responsible for local (~500 nm) hotspots of Ca^{2+} increase, which they suggested may correspond to $K_V2.1$ and RyR hotspots observed in the AIS previously (King et al., 2014). Such microdomains would have been missed by our widefield imaging experiments from Chapter 2, but their presence may suggest highly specialized Ca^{2+} signaling domains, potentially involved in BK channel activation, as discussed in more detail below. Interestingly, a recent study using ultrafast wide-field voltage, Na^+ and Ca^{2+} imaging and a $Na_V1.2$ specific toxin did describe a $\mathrm{Na_V}1.2$ dependent Ca^{2+} entry in L5 pyramidal mouse AIS (Filipis et al., 2022, preprint at the time of writing). This confirms that technical details could be important in differentiating between various Ca^{2+} entry pathways and may suggest that widefield illimitation, which provides higher signal amplitudes, might be necessary to measure $\mathrm{Na_V}$ mediated Ca^{2+} signaling. The authors of this preprint further described that Ca^{2+} entry through $\mathrm{Na_V}$ channel mediates Ca^{2+} dependent BK channel activation, which was also studied in chapter 3.

Holographic voltage imaging revealed $\mathrm{Ca_V}$ - BK channel signaling at the AIS

In **Chapter 3**, we further investigated AIS Ca^{2+}, by studying possible downstream targets of Ca^{2+} entry in AIS on Ca^{2+} sensitive BK channels. Based on single-cell RNA-sequencing, BK channels are expressed in L5 pyramidal neurons, but this technique does not provide information on subcellular expression patterns (Yao et al., 2021). Combined patch-clamp and pharmacological experiments revealed that BK channels are present in the soma and dendrites and the somatic BK channels actively participate in shaping the AP, whereas dendritic BK channels attenuated local Ca^{2+} spikes (Bock and Stuart, 2016). In the AIS of ferret L5 pyramidal neurons, BK channels also contributed to AP repolarization, but whether this extended to other species and other axonal domains was unknown (Yu et al., 2010).

To examine the role of BK channels in AP repolarization in various regions of the axon, we needed to record the axonal AP shape with high temporal resolution, since the axonal AP width is ~ 300 µs (Kole et al., 2007). To optically record voltage with maximal accuracy and temporal resolution, we incorporated a spatial light modulator in the excitation path, which allowed holographic illumination or light patterning onto the sample (Foust et al., 2015; Tanese et al., 2017). With patterned excitation, we were able to obtain accurate measurements with minimal interference of the signal from out-of-focus neurites or regions outside of our interest. Light patterning decreased background signals and increased the SNR of our optical voltage recordings. As a result, features of the AP were more discernable from the noise, with the peak appearing sharper and the fAHP becoming more apparent. We used this optical voltage imaging setup to study the effect of $\mathrm{K_V}$ and BK channels on AP repolarization and found spatially distinct contributions of the two channels, with K_V channels' contribution being most prominent in the distal AIS and internode. BK channels contributed to the AP repolarization in all regions tested, however during different phases of the AP trajectory. The delay to the maximum BK contribution was constant between axonal regions (~1.2 ms), but in regions with a wider AP (~700 µs in the soma), BK channels contributed mainly to AP width, whereas in distal axon where the AP was narrow (~350 µs in the internode), BK channels contributed to the fAHP. In addition, BK channels were necessary to fire in high-frequency bursts and were activated by Ca^{2+} entering the axon through nanodomain coupled Ca_V channels (**Figure 1**). Together, using advanced optical approaches we resolved complex ion channel interactions in the mammalian axon.

Technical advances in voltage imaging

Optical voltage recordings have been vital during investigations into axonal signaling, for example by provided spatial information about AP initiation (Palmer and Stuart, 2006) or about the temporal saltation of AP conduction (Cohen et al., 2020). In combination with pharmacology, optical voltage recordings have also complemented electrophysiological approaches to identify K_V channels as the major contributors to AP width in the distal axon (Foust et al., 2011; Kole et al., 2007; Sabater et al., 2021). In Chapter 3, we optimized optical voltage recordings by applying light patterning and calibration and developing a data fitting approach, together providing enough increase in signal accuracy to quantify subtle features of the AP. The major benefit of light patterning is that non-ROIs are not excited, which reduces light scattering and interference of the signal from other neurites. Light patterning could also be beneficial in other optical recordings, such as Ca^{2+} imaging, because Ca^{2+} transients are depended on local AP shape and ion channels in the membrane and are thus highly different between neurites (see Chapter 2). Light patterning isolates the signal specifically from the ROI and may be a valuable tool for future investigation of subcellular Ca^{2+} transients.

One major constraint in the holographic imaging approach as described in Chapter 3 is the 2D focal plane. While a spatial light modulator can excite tissue with 3D holograms, the light collection is limited to the 2D focal plane. Recordings are therefore limited to neurites that are relatively parallel to the optical plane, which is feasible with certain cell types such as pyramidal neurons, given the right slicing angle (Kole and Popovic, 2016). However, the axon collaterals of pyramidal neurons axons are far more morphologically complex, much like the entire axonal arbor of other cell types such as parvalbumin-expressing interneurons, without long straight stretches of neurites nor a standard orientation relative to a slicing plane. To study axonal Ca^{2+} or AP shape in anatomically complex cells, one approach would be to excite the dye with scanning two-photon excitation, which is compatible with most Ca^{2+} dyes and some voltage dyes, such as di-2-AN(F)EPPTEA (Acker et al., 2011; Rowan et al., 2016). Holographic imaging is increasingly challenging in two-photon microscopy, because the speckles present in a hologram are proportionally much larger with two versus one-photon excitation, due to the quadratic-dependence of two-photon fluorescence on excitation. Various technical solutions to overcome the speckle pattern do exist and light patterning is gaining ground in *in vivo* two-photon microscopy (Papagiakoumou et al., 2010; Ronzitti et al., 2017). An alternative for imaging in morphologically complex cells is offered by Light-Field microscopy, which enables optical sectioning and posthoc focusing in wide-field illumination (Levoy et al., 2006; Quicke et al., 2020). Taken together, while light patterning initiated the possibility to study AP repolarization in great detail in Chapter 3, it is certain that the technological developments will continue to expand the possibilities to measure AP shape and Ca^{2+} in various cell types and neurites, offering an exciting outlook to study subcellular electrical and ionic signaling.

Functional implications of Ca_V - BK coupling

In **Chapter 3**, we identified a Ca_V - BK channel complex at the AIS contributing to AP repolarization. What is the functional implication of BK channels contributing to the fAHP in the distal AIS? The fAHP limits inactivation of Na_V and activation of K_V channels (Gu et al., 2007), which makes the membrane more excitable, a somewhat counterintuitive example of hyperpolarization with an excitatory effect. Indeed, as we showed in **Chapter 3**, BK channels critically contributed to spiking at high frequency (>100 Hz). The cell type that we studied, the L5 pyramidal neuron, uses these high frequency bursts to encode whisker touch in vivo (Kock et al., 2021; Manns et al., 2004). The effect of a BK-mediated high frequency burst on the postsynaptic cell is complex, because it depends on the AP width and the interspike interval (ISI). Firstly, the width of each AP relates to the amplitude of each individual postsynaptic response, secondly, a short ISI will cause temporal summation of the signals and thirdly, the ISI can bidirectionally influence whether two spikes cause paired-pulse facilitation or depression (Debanne et al., 1996). In 2018, Roshchin et al. studied the effect of BK channels on the postsynaptic signal, by recording the EPSPs of two connected L5 pyramidal neurons of a train of two spikes before and after blocking BK channels with Iberiotoxin (Roshchin et al., 2018). Both spikes in the trains were wider after Iberiotoxin application, and the increase of the second spike was relatively larger. Notably, they fixed the ISI of the burst to 10 ms in control and Iberiotoxin condition, so they did not study the effect of ISI on the EPSP. Postsynaptically, they observed an increase in the second EPSP and a switch from paired-pulse depression to paired-pulse facilitation after Iberiotoxin application. They assumed BK channels in the axon contributed to AP width and increased the EPSP amplitude. However, in Chapter 3, we showed that BK channels do not contribute to AP width in all regions. In addition, BK channels in the mossy fiber bouton do not mediate AP width under physiological conditions when the AP lasts ~ 1ms (Alle et al., 2011). Given the narrow AP width in boutons in the L5 pyramidal neuron (Ritzau-Jost et al., 2021), we hypothesize that BK channels in the terminals do not contribute to AP width, but instead that the postsynaptic effect of BK channels is dominated by their contribution to the ISI, so postsynaptic temporal summation. Exactly how axonal BK channels shape the EPSPs and whether it involves BK channels in the AIS, terminals or both remains to be studied, for which voltage imaging may be an excellent tool.

Structure-function relations at the nanoscale

Ion channels at the AIS are anchored to a complex molecular organization, which has been investigated on a molecular level, or nanoscale, since the development of superresolution microscopy. STORM and other superresolution imaging approaches have been of vital importance in the investigation of the AIS architecture. In 2013, Xu et al. for the first time observed a ~190 nm periodic presence of the cytoskeletal molecules building the axon: actin and spectrin (Xu et al., 2013). They described the anti-phase presence of both molecules and provided a model for the axon cytoskeleton existing of actin rings, spaced

190 nm apart by spectrin tetramers. Shortly thereafter, the same periodicity was described for additional cytoskeletal molecules and ion channels (Leterrier et al., 2015), in living cells (D’Este et al., 2015), in a wide variety of brain regions and cell types (D’Este et al., 2016), in nodes of Ranvier (D’Este et al., 2017) and in other neuronal regions, such as dendrites and spines (He et al., 2016). Taken together, the development of superresolution has expanded the knowledge about the membrane-associated periodic skeleton (MPS), the backbone of the AIS, tremendously in the last decade (Leterrier, 2018).

Most of the initial work was carried out in cultured neurons, which grow in a single layer on a glass slide. This preparation is beneficial for microscopy, because scattering of light is minimized, and molecule localization is hence more precise. However, cultured cells develop under very different conditions than cells *in vivo*, lacking neurochemical signaling, support by glial cells and the presence of an extracellular matrix. A next step would be to correlate functional and structural research of the MPS, but this comes with challenges, because it requires superresolution microscopy in tissue fit for functional investigation, generally > 200 μm thick sections. Microscopy in deep tissue is difficult because biological tissue is opaque and light scattering increases as light travels through the tissue. To overcome this obstacle, we introduced REALM in Chapter 4: a combination of STORM and adaptive optics to correct for the aberrations that are caused by imaging deep in tissue. REALM enables superresolution reconstruction of cells used for patch clamp recordings at ~50 μm depth in thick sections. We also performed REALM on a cell that was used for patch-clamp recording, showing the feasibility to correlate functional recordings with superresolution reconstructions. Finally, we used REALM to resolve the nanostructure of the AIS in the L5 rat pyramidal neuron and observed a periodicity of 203 ± 10 nm, in range with previously published ~200 nm periodicity in axon of cultured cortical and hippocampal neurons (D’Este et al., 2016). REALM would be an ideal bridge between functional and superresolution structural research of AIS proteins.

What could be the functional implication of the MPS? Several putative roles of the MPS have been proposed (Unsain et al., 2018). Firstly, the MPS is a barrier for transmembrane diffusion of proteins and is involved in maintaining neuronal polarity. This is supported by work showing that the lack of AnkyrinG causes axons to obtain dendrite-resembling characteristics (Hedstrom et al., 2008; Huang and Rasband, 2018; Rasband, 2010; Sobotzik et al., 2009). Using computational simulations of a coarse-grain molecular dynamics model, Zhang et al. showed that the MPS is indeed restricting diffusion of membrane proteins on the inner leaflet of the membrane (Zhang et al., 2019), confirming a role of the MPS in maintaining neuronal polarity. Secondly, spectrin-lacking animals show fragile axons that are prone to breaking during movement of the animal (Hammarlund et al., 2007) and atomic force microscopy showed that the axonal membrane has higher stiffness than its somatodendritic counterpart (Zhang et al., 2017), suggesting that the MPS provides rigidity to the axonal membrane and protection during mechanical stress. Thirdly, the MPS allows high-density clustering of voltage-gated ion channels. Nav and Kv7.x channels share an AnkyrinG binding motif that clusters them at the AIS and are observed in the same phase as AnkyrinG (Garrido et al., 2003; Pan et al., 2006; Zhou et al., 1998). Interestingly, Kv7 channels are inhibited by Ca^{2+} through Calmodulin, which may be a role of the Nav -mediated Ca^{2+} entry (Delmas and Brown, 2005; Gamper and Shapiro, 2003; Selyanko and Brown, 1996). Kv1.1 and 1.2 channels are anchored at the AIS by a molecular complex including Postsynaptic Density-93 and cluster at actin rings, anti-phase to Nav channels and AnkyrinG (D'Este et al., 2017; Ogawa et al., 2008). Kv2.1 channels do not follow the MPS periodicity, but instead localize to AnkyrinG-deficient sites in the AIS where they colocalize with the cisternal organelles (King et al., 2014). How and whether Cav and BK channels are anchored at the AIS is not yet known.

Aside from the MPS enabling a polarity, rigidity and a high-density of ion channels, could there be a direct consequence of the periodicity of ion entry? Nav channels are restricted to the MPS, meaning that Na^{+} entry occurs at 190 nm spaced hotspots. Could this influence electrical signaling at the AIS? The electrical space constant is dependent on the temporal frequency of the signal and the diameter and time constant of the membrane. For steady-state signals, the electrical space constant is in the range of tens to hundreds of micrometers (Alle and Geiger, 2006; Cohen et al., 2020; Rall, 1969; Shu et al., 2006). The electrical space constant is smaller for signals with higher temporal frequencies, such as an AP, however we do not expect it to be on a nanometer scale and therefore we do not expect electrical periodicity in the AIS. However, the length constant of chemical signaling is shorter: concentration gradients are strong around channels and can fall within tens of nanometers, depending on endogenous buffering capacities (Fakler and Adelman, 2008; Naraghi and Neher, 1997). Phase or anti-phase coupling of two channels in the MPS increases the distance between two channels from almost zero to ~95 nm, respectively. The Nav mediated Ca^{2+} entry described in Chapter 2 suggests that there are domains of Ca^{2+} entry in phase with the AnkyrinG, but not actin, regions of the MPS. We do not yet know if this periodic Nav mediated Ca^{2+} influx activates a specific downstream partner, but based on our observations in Chapter 3, that AIS BK channels are exclusively activated by Cav mediated Ca^{2+}, we hypothesize that BK channels do not co-localize with Na^{+} channels. Directly visualizing Cav and BK channels through immunohistochemistry has proven challenging, potentially due to their relatively low expression levels, therefore the localization of the Cav - BK complex within the AIS and whether it anchors to the MPS, to the Kv2 rich / AnkyrinG-deficient spots or through an alternative mechanism is unknown. An exciting development that may provide new opportunities to visualize ion channels are CRISPR/Cas9 approaches to tag endogenous channels (Gao et al., 2019; Willems et al., 2020). Indeed, using an ORANGE knock-in approach, we were able to visualize BK channels in the soma and axon of transgenic mice (Chapter 4). In combination with multiplexed gene tagging (Droogers et al., 2022) and REALM, this introduces a new avenue of advanced functional and nanoscale experiments, where subcellular ion activity and AP shape is first investigated using imaging (Chapter 2 and 3) and subsequently the ion channel presence could be reconstructed on the nanoscale (Chapter 4). Such combinatory research would greatly contribute to our understanding of the subcellular electrical properties.

The methods and findings described in this thesis identify various subcellular ion signaling mechanisms that contribute to the electrical behavior of the neuron as a whole. The nanoscale organization of the AIS critically determines the neurons excitability. Indeed, mutations in ion channel subtypes and AIS proteins are involved in a wide spectrum of diseases, such as epilepsy and autism spectrum disorder (Huang and Rasband, 2018). This emphasizes the importance of neuroscience on all scales, from genetics and subcellular nanoscale interactions to behavior and clinical research. Technical advancements provide increasingly complex information about neuronal signaling, for example, single-cell RNA sequencing enables the identification of the expected protein expressing of specific neuronal subtypes. In addition, in vivo imaging and electrophysiology are rapidly increasing our knowledge on neuronal network dynamics. At the same time, subcellular investigation is required to describe the exact function of each protein and the role of a single neuron in a network. The work presented in this thesis emphasizes the importance of investigating ionic signaling in subcellular compartments and the strength of optical approaches in this endeavor.

References

Acker, C.D., Yan, P., and Loew, L.M. (2011). Single-Voxel Recording of Voltage Transients in Dendritic Spines. Biophysical Journal *101*, L11–L13.

Alle, H., and Geiger, J.R.P. (2006). Combined analog and action potential coding in hippocampal mossy fibers. Science *311*, 1290–1293.

Alle, H., Kubota, H., and Geiger, J.R.P. (2011). Sparse But Highly Efficient Kv3 Outpace BKCa Channels in Action Potential Repolarization at Hippocampal Mossy Fiber Boutons. J Neurosci *31*, 8001–8012.

Baker, P.F., Hodgkin, A.L., and Ridgway, E.B. (1971). Depolarization and calcium entry in squid giant axons. J Physiology *218*, 709–755.

Bender, K.J., and Trussell, L.O. (2009). Axon Initial Segment Ca2+ Channels Influence Action Potential Generation and Timing. Neuron *61*, 259–271.

Bock, T., and Stuart, G.J. (2016). The Impact of BK Channels on Cellular Excitability Depends on their Subcellular Location. Frontiers in Cellular Neuroscience *10*, 914–918.

Clarkson, R.L., Liptak, A.T., Gee, S.M., Sohal, V.S., and Bender, K.J. (2017). D3 Receptors Regulate Excitability in a Unique Class of Prefrontal Pyramidal Cells. Journal of Neuroscience *37*, 5846–5860.

Cohen, C.C.H., Popovic, M.A., Klooster, J., Weil, M.-T., Möbius, W., Nave, K.-A., and Kole, M.H.P. (2020). Saltatory Conduction along Myelinated Axons Involves a Periaxonal Nanocircuit. Cell *180*, 1–28.

Debanne, D., Guérineau, N.C., Gähwiler, B.H., and Thompson, S.M. (1996). Paired-pulse facilitation and depression at unitary synapses in rat hippocampus: quantal fluctuation affects subsequent release. J Physiology *491*, 163–176.

Delmas, P., and Brown, D.A. (2005). Pathways modulating neural KCNQ/M (Kv7) potassium channels. Nat Rev Neurosci *6*, 850–862. https://doi.org/10.1038/nrn1785.

D’Este, E., Kamin, D., Göttfert, F., El-Hady, A., and Hell, S.W. (2015). STED Nanoscopy Reveals the Ubiquity of Subcortical Cytoskeleton Periodicity in Living Neurons. Cell Reports *10*, 1246–1251.

D’Este, E., Kamin, D., Velte, C., Göttfert, F., Simons, M., and Hell, S.W. (2016). Subcortical cytoskeleton periodicity throughout the nervous system. Sci Rep-Uk *6*, 22741.

D’Este, E., Kamin, D., Balzarotti, F., and Hell, S.W. (2017). Ultrastructural anatomy of nodes of Ranvier in the peripheral nervous system as revealed by STED microscopy. Proceedings of the National Academy of Sciences *114*, E191–E199.

Droogers WJ, Willems J, MacGillavry HD, Jong APH de. (2022). Duplex Labeling and Manipulation of Neuronal Proteins Using Sequential CRISPR/Cas9 Gene Editing. Eneuro *9*

Echevarria-Cooper, D.M., Hawkins, N.A., Misra, S.N., Huffman, A.M., Thaxton, T., Thompson, C.H., Ben-Shalom, R., Nelson, A.D., Lipkin, A.M., George, A.L., et al. (2022). Cellular and behavioral effects of altered NaV1.2 sodium channel ion permeability in Scn2aK1422E mice. Hum Mol Genet ddac087. https://doi.org/10.1093/hmg/ddac087.

Fakler, B., and Adelman, J.P. (2008). Control of KCa Channels by Calcium Nano/Microdomains. Neuron *59*, 873–881.

Filipis, L., and Canepari, M. (2021). Optical measurement of physiological sodium currents in the axon initial segment. Journal of Physiology *599*, 2020.07.20.211839.

Filipis, L., Blömer, L.A., Montnach, J., De Waard, M. and Canepari, M. (2022). Nav1.2 and BK channels interaction shapes the action potential in the axon initial segment. bioRxiv.

Foust, A.J., Yu, Y., Popovic, M.A., Zecevic, D., and McCormick, D.A. (2011). Somatic Membrane Potential and Kv1 Channels Control Spike Repolarization in Cortical Axon Collaterals and Presynaptic Boutons. Journal of Neuroscience *31*, 15490–15498.

Foust, A.J., Zampini, V., Tanese, D., Papagiakoumou, E., and Emiliani, V. (2015). Computer-generated holography enhances voltage dye fluorescence discrimination in adjacent neuronal structures. Neurophotonics *2*, 021007.

Gao, Y., Hisey, E., Bradshaw, T.W.A., Erata, E., Brown, W.E., Courtland, J.L., Uezu, A., Xiang, Y., Diao, Y., and Soderling, S.H. (2019). Plug-and-Play Protein Modification Using Homology-Independent Universal Genome Engineering. Neuron *103*, 583-597.e8.

Garrido, J.J., Giraud, P., Carlier, E., Fernandes, F., Moussif, A., Fache, M.-P., Debanne, D., and Dargent, B. (2003). A Targeting Motif Involved in Sodium Channel Clustering at the Axonal Initial Segment. Science *300*, 2091–2094.

Gamper, N., and Shapiro, M.S. (2003). Calmodulin Mediates Ca2+-dependent Modulation of M-type K+ Channels. J Gen Physiology *122*, 17–31. https://doi.org/10.1085/jgp.200208783.

Gu, N., Vervaeke, K., and Storm, J.F. (2007). BK potassium channels facilitate high-frequency firing and cause early spike frequency adaptation in rat CA1 hippocampal pyramidal cells. J Physiology *580*, 859–882.

Hammarlund, M., Jorgensen, E.M., and Bastiani, M.J. (2007). Axons break in animals lacking β-spectrin. J Cell Biology *176*, 269–275.

He, J., Zhou, R., Wu, Z., Carrasco, M.A., Kurshan, P.T., Farley, J.E., Simon, D.J., Wang, G., Han, B., Hao, J., et al. (2016). Prevalent presence of periodic actin–spectrin-based membrane skeleton in a broad range of neuronal cell types and animal species. Proc National Acad Sci *113*, 6029–6034.

Hedstrom, K.L., Ogawa, Y., and Rasband, M.N. (2008). AnkyrinG is required for maintenance of the axon initial segment and neuronal polarity. J Cell Biology *183*, 635–640.

Heinemann, S.H., Terlau, H., Stühmer, W., Imoto, K., and Numa, S. (1992). Calcium channel characteristics conferred on the sodium channel by single mutations. Nature *356*, 441–443.

Helmchen, F. (2011). Calibration of Fluorescent Calcium Indicators. Cold Spring Harbor Protocols *2011*, pdb.top120-pdb.top120.

Huang, C.Y., and Rasband, M.N. (2018). Axon initial segments: structure, function, and disease. Ann Ny Acad Sci *1420*, 46–61.

Jaafari, N., Waard, M.D., and Canepari, M. (2014). Imaging Fast Calcium Currents beyond the Limitations of Electrode Techniques. Biophysical Journal *107*, 1280–1288.

Jaafari, N., Marret, E., and Canepari, M. (2015). Using simultaneous voltage and calcium imaging to study fast Ca(2+) channels. Neurophotonics *2*, 021010.

King, A.N., Manning, C.F., and Trimmer, J.S. (2014). A unique ion channel clustering domain on the axon initial segment of mammalian neurons. Journal of Comparative Neurology *522*, 2594–2608.

Kock, C.P.J. de, Pie, J., Pieneman, A.W., Mease, R.A., Bast, A., Guest, J.M., Oberlaender, M., Mansvelder, H.D., and Sakmann, B. (2021). High-frequency burst spiking in layer 5 thick-tufted pyramids of rat primary somatosensory cortex encodes exploratory touch. Commun Biology *4*, 709.

Kole, M.H.P., and Popovic, M.A. (2016). Patch-Clamp Recording from Myelinated Central Axons. (Springer New York), pp. 123–138.

Kole, M.H.P., Letzkus, J.J., and Stuart, G.J. (2007). Axon Initial Segment Kv1 Channels Control Axonal Action Potential Waveform and Synaptic Efficacy. Neuron *55*, 633–647.

Leterrier, C. (2018). The Axon Initial Segment: An Updated Viewpoint. Journal of Neuroscience *38*, 2135–2145.

Leterrier, C., Potier, J., Caillol, G., Debarnot, C., Boroni, F.R., and Dargent, B. (2015). Nanoscale Architecture of the Axon Initial Segment Reveals an Organized and Robust Scaffold. Cell Reports *13*, 2781–2793.

Levoy, M., Ng, R., Adams, A., Footer, M., and Horowitz, M. (2006). Light field microscopy. Acm Transactions Graph Tog *25*, 924–934.

Lewis, C.A. (1979). Ion-concentration dependence of the reversal potential and the single channel conductance of ion channels at the frog neuromuscular junction. The Journal of Physiology *286*, 417–445.

Lipkin, A.M., Cunniff, M.M., Spratt, P.W.E., Lemke, S.M., and Bender, K.J. (2021). Functional Microstructure of Ca V -Mediated Calcium Signaling in the Axon Initial Segment. J Neurosci *41*, 3764–3776.

Manns, I.D., Sakmann, B., and Brecht, M. (2004). Sub- and suprathreshold receptive field properties of pyramidal neurones in layers 5A and 5B of rat somatosensory barrel cortex. J Physiology *556*, 601–622.

Meves, H., and Vogel, W. (1973). Calcium inward currents in internally perfused giant axons. The Journal of Physiology *235*, 225–265.

Miyazaki, K., and Ross, W.N. (2015). Simultaneous Sodium and Calcium Imaging from Dendrites and Axons. ENeuro *2*, 1–10.

Miyazaki, K., Lisman, J.E., and Ross, W.N. (2019). Improvements in Simultaneous Sodium and Calcium Imaging. Frontiers in Cellular Neuroscience *12*, ENEURO.0050-15.2016-10.

Naraghi, M., and Neher, E. (1997). Linearized Buffered Ca2+ Diffusion in Microdomains and Its Implications for Calculation of [Ca2+] at the Mouth of a Calcium Channel. J Neurosci *17*, 6961–6973.

Ogawa, Y., Horresh, I., Trimmer, J.S., Bredt, D.S., Peles, E., and Rasband, M.N. (2008). Postsynaptic Density-93 Clusters Kv1 Channels at Axon Initial Segments Independently of Caspr2. J Neurosci *28*, 5731–5739.

Ouares, K.A., Jaafari, N., and Canepari, M. (2016). A generalised method to estimate the kinetics of fast Ca2+ currents from Ca2+ imaging experiments. J Neurosci Meth *268*, 66–77.

Palmer, L.M., and Stuart, G.J. (2006). Site of action potential initiation in layer 5 pyramidal neurons. The Journal of Neuroscience *26*, 1854–1863.

Pan, Z., Kao, T., Horvath, Z., Lemos, J., Sul, J.-Y., Cranstoun, S.D., Bennett, V., Scherer, S.S., and Cooper, E.C. (2006). A Common Ankyrin-G-Based Mechanism Retains KCNQ and Na V Channels at Electrically Active Domains of the Axon. J Neurosci *26*, 2599–2613.

Papagiakoumou, E., Anselmi, F., Bègue, A., Sars, V. de, Glückstad, J., Isacoff, E.Y., and Emiliani, V. (2010). Scanless two-photon excitation of channelrhodopsin-2. Nat Methods *7*, 848–854.

Popovic, M.A., Carnevale, N.T., Rozsa, B., and Zecevic, D. (2015). Electrical behaviour of dendritic spines as revealed by voltage imaging. Nature Communications *6*, 1–12.

Quicke, P., Howe, C.L., Song, P., Jadan, H.V., Song, C., Knöpfel, T., Neil, M., Dragotti, P.L., Schultz, S.R., and Foust, A.J. (2020). Subcellular resolution three-dimensional light-field imaging with genetically encoded voltage indicators. Neurophotonics *7*, 1–19.

Rall, W. (1969). Time Constants and Electrotonic Length of Membrane Cylinders and Neurons. Biophys J *9*, 1483–1508.

Rasband, M.N. (2010). The axon initial segment and the maintenance of neuronal polarity. Nature Reviews Neuroscience *11*, 1–11.

Ritzau-Jost, A., Tsintsadze, T., Krueger, M., Ader, J., Bechmann, I., Eilers, J., Barbour, B., Smith, S.M., and Hallermann, S. (2021). Large, Stable Spikes Exhibit Differential Broadening in Excitatory and Inhibitory Neocortical Boutons. CellReports *34*, 108612.

Ronzitti, E., Ventalon, C., Canepari, M., Forget, B.C., Papagiakoumou, E., and Emiliani, V. (2017). Recent advances in patterned photostimulation for optogenetics. Journal of Optics *19*, 0–0.

Roshchin, M.V., Matlashov, M.E., Ierusalimsky, V.N., Balaban, P.M., Belousov, V.V., Kemenes, G., Staras, K., and Nikitin, E.S. (2018). A BK channel–mediated feedback pathway links single-synapse activity with action potential sharpening in repetitive firing. Sci Adv *4*, eaat1357.

Rowan, M.J.M., DelCanto, G., Yu, J.J., Kamasawa, N., and Christie, J.M. (2016). Synapse-Level Determination of Action Potential Duration by K+ Channel Clustering in Axons. Neuron *91*, 370–383.

Sabater, V.G., Rigby, M., and Burrone, J. (2021). Voltage-gated potassium channels ensure action potential shape fidelity in distal axons. J Neurosci *41*, JN-RM-2765-20.

Santana, L.F., Gómez, A.M., and Lederer, W.J. (1998). Ca2+ Flux Through Promiscuous Cardiac Na+ Channels: Slip-Mode Conductance. Science *279*, 1027–1033.

Schiller, J., Helmchen, F., and Sakmann, B. (1995). Spatial profile of dendritic calcium transients evoked by action potentials in rat neocortical pyramidal neurones. Journal of Physiology *487 (Pt 3)*, 583–600.

Selyanko, A.A., and Brown, D.A. (1996). Intracellular Calcium Directly Inhibits Potassium M Channels in Excised Membrane Patches from Rat Sympathetic Neurons. Neuron *16*, 151–162. https://doi.org/10.1016/s0896-6273(00)80032-x.

Shu, Y., Hasenstaub, A., Duque, A., Yu, Y., and McCormick, D.A. (2006). Modulation of intracortical synaptic potentials by presynaptic somatic membrane potential. Nature *441*, 761–765.

Sobotzik, J.-M., Sie, J.M., Politi, C., Turco, D.D., Bennett, V., Deller, T., and Schultz, C. (2009). AnkyrinG is required to maintain axo-dendritic polarity in vivo. Proc National Acad Sci *106*, 17564–17569.

Tanese, D., Weng, J.-Y., Zampini, V., Sars, V.D., Canepari, M., Rozsa, B., Emiliani, V., and Zecevic, D. (2017). Imaging membrane potential changes from dendritic spines using computer-generated holography. Neurophotonics *4*, 031211.

Unsain, N., Stefani, F.D., and Cáceres, A. (2018). The Actin/Spectrin Membrane-Associated Periodic Skeleton in Neurons. Frontiers Synaptic Neurosci *10*, 10.

Willems, J., Jong, A.P.H. de, Scheefhals, N., Mertens, E., Catsburg, L.A.E., Poorthuis, R.B., Winter, F. de, Verhaagen, J., Meye, F.J., and MacGillavry, H.D. (2020). ORANGE: A CRISPR/Cas9-based genome editing toolbox for epitope tagging of endogenous proteins in neurons. Plos Biol *18*, e3000665.

Xu, K., Zhong, G., and Zhuang, X. (2013). Actin, spectrin, and associated proteins form a periodic cytoskeletal structure in axons. Science *339*, 452–456.

Yao, Z., Velthoven, C.T.J. van, Nguyen, T.N., Goldy, J., Sedeno-Cortes, A.E., Baftizadeh, F., Bertagnolli, D., Casper, T., Chiang, M., Crichton, K., et al. (2021). A taxonomy of transcriptomic cell types across the isocortex and hippocampal formation. Cell *184*, 3222-3241.e26.

Yu, Y., Maureira, C., Liu, X., and McCormick, D.A. (2010). P/Q and N channels control baseline and spike-triggered calcium levels in neocortical axons and synaptic boutons. The Journal of Neuroscience *30*, 11858–11869.

Zhang, Y., Abiraman, K., Li, H., Pierce, D.M., Tzingounis, A.V., and Lykotrafitis, G. (2017). Modeling of the axon membrane skeleton structure and implications for its mechanical properties. Plos Comput Biol *13*, e1005407.

Zhang, Y., Tzingounis, A.V., and Lykotrafitis, G. (2019). Modeling of the axon plasma membrane structure and its effects on protein diffusion. Plos Comput Biol *15*, e1007003.

Zhou, D., Lambert, S., Malen, P.L., Carpenter, S., Boland, L.M., and Bennett, V. (1998). AnkyrinG Is Required for Clustering of Voltage-gated Na Channels at Axon Initial Segments and for Normal Action Potential Firing. J Cell Biology *143*, 1295–1304.

Appendix

Summary

Enlightening axonal signaling

Our thoughts and actions are generated by a network of billions of neurons that communicate through electrical and chemical signals. Neurons are anatomically complex cells and have distinct regions for receiving and sending signals. Information is received on multiple branched structures called dendrites and when the integrated information surpasses a certain threshold, a large electrical signal is initiated and distributed to downstream cells along the axon, a structure with complex arborization spanning vast distances in the brain. To generate electrical impulses neurons actively maintain and alter ionic gradients across their membrane, generating a voltage potential. Classic electrophysical work has established how the precisely timed, sequential opening of sodium and potassium channels generates the rapid de- and repolarization of the membrane: an *action potential*. Action potentials are the primary mean to transmit information through the neuronal network and originate in the proximal region of the axon: the axon initial segment (AIS), which contains a high density of sodium and potassium channels. AIS calcium levels also rise in response to activity, but how calcium ions enter the AIS and locally influence electrical signaling is not yet known. A putative calcium target is the BK channel, a special type of potassium channel that is important for the repolarization of the action potential and depends on calcium binding. The AIS is an anatomically thin structure which makes it hard to record with electrophysiological means. However, voltage and ion transients along the axon can be recorded optically using fluorescent dyes, enabling live measurement of ionic signaling. Furthermore, recent advances in microscopy revealed that ion channels at the AIS follow a nanoscale periodic structure. In this thesis we asked the questions how ion signaling and the periodic organization at the AIS shape the generation of action potentials. In order to answer these questions, we need to bridge functional investigations with high resolution structural reconstructions.

In **Chapter 2**, we used optical calcium recordings and identified three calcium entry pathways in the AIS. As expected, calcium is released from internal stores and enters through calcium channels, however, surprisingly, we also observed calcium entering through sodium channels. We estimated that the conductivity ratio of sodium channels for calcium is small, but because they are present at a high density at the AIS, they do form a major and rapid source of calcium.

In **Chapter 3**, we investigated whether the calcium-dependent BK channel was a downstream target for calcium in the AIS. We implemented a novel technique to use light patterning of a fluorescent voltage reporter to obtain highly accurate measures of the action potential shape in the axon. BK channels were indeed activated during the action potential at the AIS, forming a link between calcium entry and action potential repolarization. Together, the complex of calcium and BK channels mediated high-frequency burst firing, an important feature of the cell type that we studied.

In **Chapter 4**, we developed a novel optical method to perform high resolution microscopy deep inside tissue, where the neurons are in an intact three-dimensional context. Because biological tissue is not transparent, light traveling through tissue suffers from distortions, which makes microscopy at depth problematic. To overcome this obstacle, we used a deformable mirror to counteract the light distortions and enable high resolution microscopy inside biological tissue. We used this method to perform both live experiments and high-resolution microscopy from the same neuron, demonstrating that this method can bridge the structure-function relationship in neurons.

Together, the experiments in this thesis shed light on the biophysical properties of axonal ion fluxes and how they are tuned to regulate proper neuronal excitability.

The work presented in this thesis shows that optical approaches provide valuable tools in neuroscientific research and open novel avenues for future investigation of the biophysical properties of the neuronal membrane.

Samenvatting

Axonale activiteit belichten

Onze gedachten en acties worden gegenereerd door een netwerk van biljoenen neuronen die met elkaar communiceren door middel van elektrische en chemische signalen. Neuronen zijn anatomisch complexe cellen en hebben gescheiden regio's voor het ontvangen en verzenden van signalen. Informatie wordt ontvangen op verschillende vertakte structuren die dendrieten worden genoemd, en wanneer de geïntegreerde informatie een bepaalde drempelwaarde overstijgt, wordt een groot elektrisch impuls geïnitieerd en uitgezonden naar de verbonden cellen door het axon, een structuur met een complex netwerk van vertakkingen dat grote afstanden in het brein overspand. Om elektrische impulsen te genereren, onderhouden neuronen actief gradiënten van ionen over hun membraan, wat zorgt voor een voltage potentiaalverschil. Klassiek elektrofysiologisch werk heeft vastgesteld hoe de precies getimede en opeenvolgende opening van natrium en kalium kanalen zorgt voor een snelle de- en repolarisatie van het membraan: een *actiepotentiaal*. Actie potentialen zijn het belangrijkste middel waarmee informatie door het neuronale netwerk wordt verzonden en starten in het proximale deel van het axon: het axon initieel segment (AIS), welke een hoge dichtheid van natrium en kaliumkanalen bevat. Calcium niveaus in het AIS stijgen ook na activiteit, maar hoe calcium het AIS betreedt en lokaal invloed uitoefent op het elektrische signaal is niet bekend. Een mogelijk doel van calcium is het activeren van het BK kanaal, een bijzonder type kalium kanaal dat belangrijk is voor de repolarisatie van het actiepotentiaal en afhankelijk is van calcium. Het AIS is een anatomisch dunne structuur, wat het moeilijk maakt om het met elektrofysiologische middelen te bestuderen. Maar elektrische en ionische signalen langs het axon kunnen ook optisch gemeten worden met behulp van fluorescente stoffen, wat het mogelijk maakt om *live* de ion signalen te meten. Daarnaast hebben recente ontwikkelingen in de microscopie onthuld dat ion kanalen in het AIS periodisch zijn verdeeld op de nanoschaal. In dit proefschrift vragen we ons af hoe ion signalen en de periodische organisatie in het AIS bijdragen aan de ontwikkeling van actie potentialen. Om deze vragen te kunnen beantwoorden, moeten we een brug slaan tussen functionele onderzoeken en structurele reconstructies op hoge resolutie.

In **Hoofdstuk 2** hebben we optisch calcium gemeten en drie toegangspaden voor calcium in het AIS geïdentificeerd. Zoals verwacht wordt calcium losgelaten uit intracellulaire calcium bufferende organellen en komt calcium de cel binnen door calcium kanalen. Daarnaast, verrassend genoeg, observeerden we dat calcium de cel ook binnenkwam door natriumkanalen. We berekenden dat de geleidingsratio van natriumkanalen voor calcium klein is, maar omdat deze kanalen in zeer hoge dichtheid aanwezig zijn in het AIS, vormen ze een belangrijke en snelle bron voor calcium.

In **Hoofdstuk 3** onderzochten we of de calcium-afhankelijke BK kanalen een activatie doel waren voor het calcium in het AIS. We implementeerden een nieuwe techniek om een fluorescente voltage indicator met lichtpatronen te exciteren waarmee we zeer accurate metingen van het actiepotentiaal in het axon konden verkrijgen. BK kanalen waren inderdaad actief tijdens een actiepotentiaal in het AIS en vormen dus een link tussen de binnenkomst van calcium en de repolarisatie van het membraan. Het complex van calcium en BK kanalen bevorderde het vuren op een hoge frequentie, wat een belangrijke eigenschap is van het type neuron dat we bestudeerden.

In **Hoofdstuk 4** hebben we een nieuwe optische methode ontwikkeld om microscopie op hoge resolutie uit te voeren diep in weefsel, waar neuronen zich in een intacte driedimensionale context bevinden. Omdat biologisch weefsel niet transparant is, wordt licht dat door weefsel reist vertekend en dat maakt microscopie diep in weefsel moeilijk. Om dit probleem op te lossen, hebben wij gebruik gemaakt van een vervormbare spiegel die de vertekeningen corrigeert en daardoor microscopie met hoge resolutie mogelijk maakt diep in biologisch weefsel. We gebruikten deze methode om zowel functionele experimenten als hoge resolutie microscopie in dezelfde neuron uit te voeren, om te demonstreren dat deze methode een brug kan slaap tussen kennis van structuur en functie in neuronen.

Concluderend, de experimenten in dit proefschrift belichten biofysische eigenschappen van axonale ion stromen en hoe deze zijn afgestemd om neuronale communicatie te reguleren. Het werk beschreven in dit proefschrift toont aan dat optische methodes zeer waardevolle technieken zijn in neurowetenschappelijk onderzoek en opent nieuwe paden voor toekomstige bestudering van de biofysische eigenschappen van het neuronale membraan.

Curriculum Vitae

Birthplace	Leiden, The Netherlands, April 1st, 1991
Nationality	Dutch

Education

2017 – 2021	Netherlands Institute for Neuroscience / Utrecht University PhD Neuroscience
2015 – 2017	University of Amsterdam MSc Brain and Cognitive Sciences
2011 – 2015	Leiden University BSc Biology

Research Experience

2017 – 2022	Netherlands Institute for Neuroscience / Utrecht University *Enlightening axonal activity: optical approaches to identify ion channels and their function*
2017	Kavli Institute for Systems Neuroscience / Centre for Neural Computation under supervision of Dr. Jonathan Whitlock *Validation and quantification of opto- and chemogenetic silencing approaches to investigate the neural circuits underlying action representation in the rodent posterior parietal cortex.*
2016	Netherlands Institute for Neuroscience under supervision of Dr. Marko Popovic *A quantitative measurement of sodium influx in the axon during action potential initiation and propagation*

Poster presentations

Submillisecond rapid axonal Ca^{2+} signaling generated by voltage-gated Na^{+} channels
Axons in the Hills Meeting, Heidelberg, Germany, October 4th, 2018

Submillisecond rapid axonal Ca2+ signaling generated by voltage-gated Na^{+} channels
ONWAR Annual meeting, Woudschoten, The Netherlands, November 22nd, 2018

Submillisecond rapid axonal Ca^{2+} signaling generated by voltage-gated Na^{+} channels
Dutch Neuroscience Meeting, Lunteren, The Netherlands, June 20th, 2019

Ca^{2+} entry through Na_V channels generates submillisecond axonal Ca^{2+} signaling
Dutch BioPhysics Meeting, Veldhoven, The Netherlands, October 7th , 2019

Ca^{2+} entry through Na_V channels generates submillisecond axonal Ca^{2+} signaling
FENS, virtual, July 11th, 2020

Ca^{2+} entry through Na_V channels generates submillisecond axonal Ca^{2+} signaling
Dutch BioPhysics meeting, virtual, October 20th, 2020

Optical voltage recordings reveal multiple gradients in action potential repolarization in the proximal axon
EMBO Axons Meeting, virtual, October 5th, 2021

Optical voltage recordings reveal multiple gradients in action potential repolarization in the proximal axon
Society for Neuroscience Meeting, virtual, November 9th, 2021

Oral Presentations

Holographic Illumination for live-cell imaging
NIN – Donders Meeting, Nijmegen, The Netherlands, November 28th, 2019

Holographic voltage imaging to study electrical signaling at the axon initial segment
Invited Lecture at the Donders Institute, virtual, November 12th, 2020

High-speed imaging of large-conductance calcium-activated (BK_{Ca}) potassium channels at the axon initial segment
Dutch Neuroscience Meeting, virtual, July 10th, 2021

Holographic illumination reveals micrometer-precise subcellular diversity of action potentials
Dutch Neuroscience Meeting, virtual, July 11th, 2021

Publications

Naomi A. K. Hanemaaijer $^{\#}$, Marko A. Popovic $^{\#}$, Xante Wilders, Sara Grasman, Oriol Pavón Arocas and Maarten H. P. Kole, *Ca^{2+} entry through Na_V channels generates submillisecond axonal Ca^{2+} signaling.* eLife 9:353–32 (2020)

Marijn E. Siemons, Naomi A.K. Hanemaaijer, Maarten H.P. Kole, Lukas C. Kapitein, *Robust adaptive optics for localization microscopy deep in complex tissue*. Nature Communications 12:3407 (2021)

Naomi A.K. Hanemaaijer, Kieran P. Higgins, Koen Kole, Arthur P.J. de Jong, Harold D. MacGillavry, Maarten H.P. Kole, *Axonal BK-channel mediated action potential repolarization revealed by holographic voltage recordings, in preparation*

Acknowledgements

This thesis would not have been possible without the support of many amazing people. First and foremost, I want to thank Maarten for being an incredible mentor and for giving me the opportunity to work in his group. Thanks for challenging me, for giving me so much responsibility and at the same time, for always being available on short notice. I never ceased to be amazed by your encyclopedia-ness. Your eagerness and curiosity are contagious, and I wish you all the best for the science to come.

Marko, the last few years would not have been the same if it weren't for you. You were there for my first neuroscience lecture, and it is an honor to have you as my co-promotor many years later. Thanks for teaching me about optics, about art-and-crafts in the lab, about wiggling cables and about picking the right dish in a Chinese restaurant. It was a blast to work with you.

I also want to thank all members of the Kole group, former and current. Arne, Mustafa, Charles, Sharon, Mohit, Nora, Naomi, Koen, Amélie, David, Viktor, Kieran, this thesis certainly was a team effort and I want to thank you all for your endless support and feedback throughout the years. And, of course, thanks for all the happy times in the lab. I have enjoyed working with you all a lot. My students Tom, Jorik, Tijn and Merijn, thank you for your hard work and dedication. A special shoutout to Sharon, Marcus, Paloma, David, Nora and Koen for being wonderful colleagues and friends.

Thanks to all the kind people working at the Netherlands Institute for Neuroscience and without whom this work would not have been possible. Marian and all the animal caretakes, thanks for taking good care of all the animals. Maurice, Mike, Joop and all the other guys from the workshop, thanks for many nice chats and for helping me with the endless adjustments to the microscope. Elvis, thank you for your happy presence at the institute.

One very nice part of my PhD was the Neurophotonics consortium and I want to thank you all: Marijn, Jelmer, Lotte, Guilia, Pegah, Lukas, Harold, Allard, Corette, Ivo and Hans. Thank you for sharing your expertise and for helping me with the setup. I enjoyed our consortium meetings and I always felt inspired after. Marijn and Lukas, I really enjoyed working with you and want to thank you both for our collaboration. Marijn, I had so much fun working together on your and my setup. Lukas, it was an honor to have you as my second promotor.

I'd like to thank Arthur and Harold for the very nice and fruitful collaboration. The tools that you've developed strongly complement our investigations and I'm certain that they will prove valuable in the future.

In addition, I'd like to thank Christiaan the Kock for being a kind and involved mentor. From the neuroscience course I took many years ago up to the end of my PhD, you've been a very kind and pleasant mentor. Thanks for the many trips to the NIN and for checking in on me from time to time.

I want to thank my incredible friends for their support, kindness and sometimes crazy questions. And no, I have not named an ion channel the Hanemaaijannel.

I also want to thank Judith and Emma, for being the sweetest sisters I could wish for. Thanks for your endless support and I hope you know how much that has meant.

A special thanks to my parents, to which I'd like to dedicate this thesis. Mom, you clearly passed your interest in the brain on to me. Dad, I probably inherited your determination for accuracy. You have always given me the opportunity to develop myself any way I wanted and when I had doubts, you encouraged me to just give it a go.

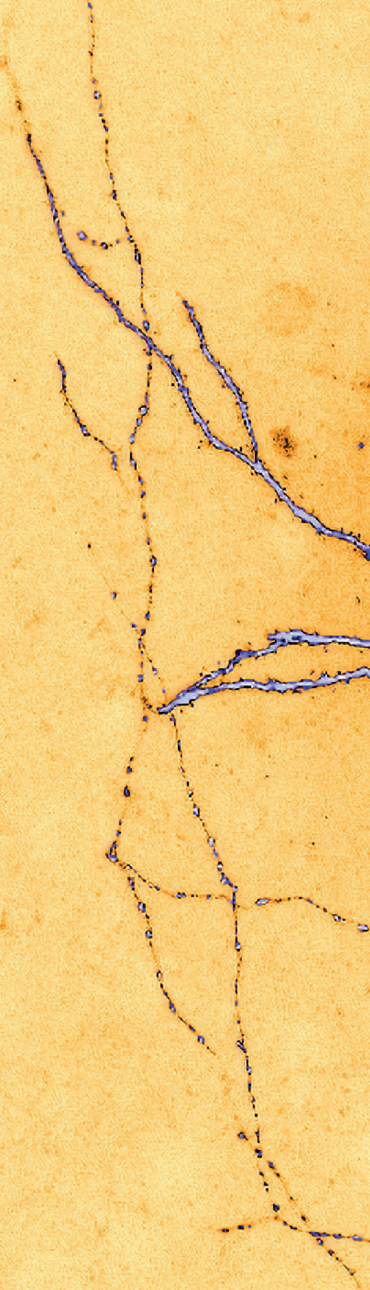The biggest thanks go to my love Tobias, for being the most amazing and supporting person in my life. There are a million things that I could thank you for and the most important one is this: I don't think anyone believes in me as much as you do.